Agip

Amoco

ARCO

Chevron

Exxon

Halliburton

Marathon

Mobil

Radian

Silicon Graphics

Shell

Stratamodel

Texaco

Unocal

Final Report

Reservoir Characterization Research Laboratory

Characterization of Reservoir Heterogeneity in Carbonate-Ramp Systems, San Andres/Grayburg, Permian Basin

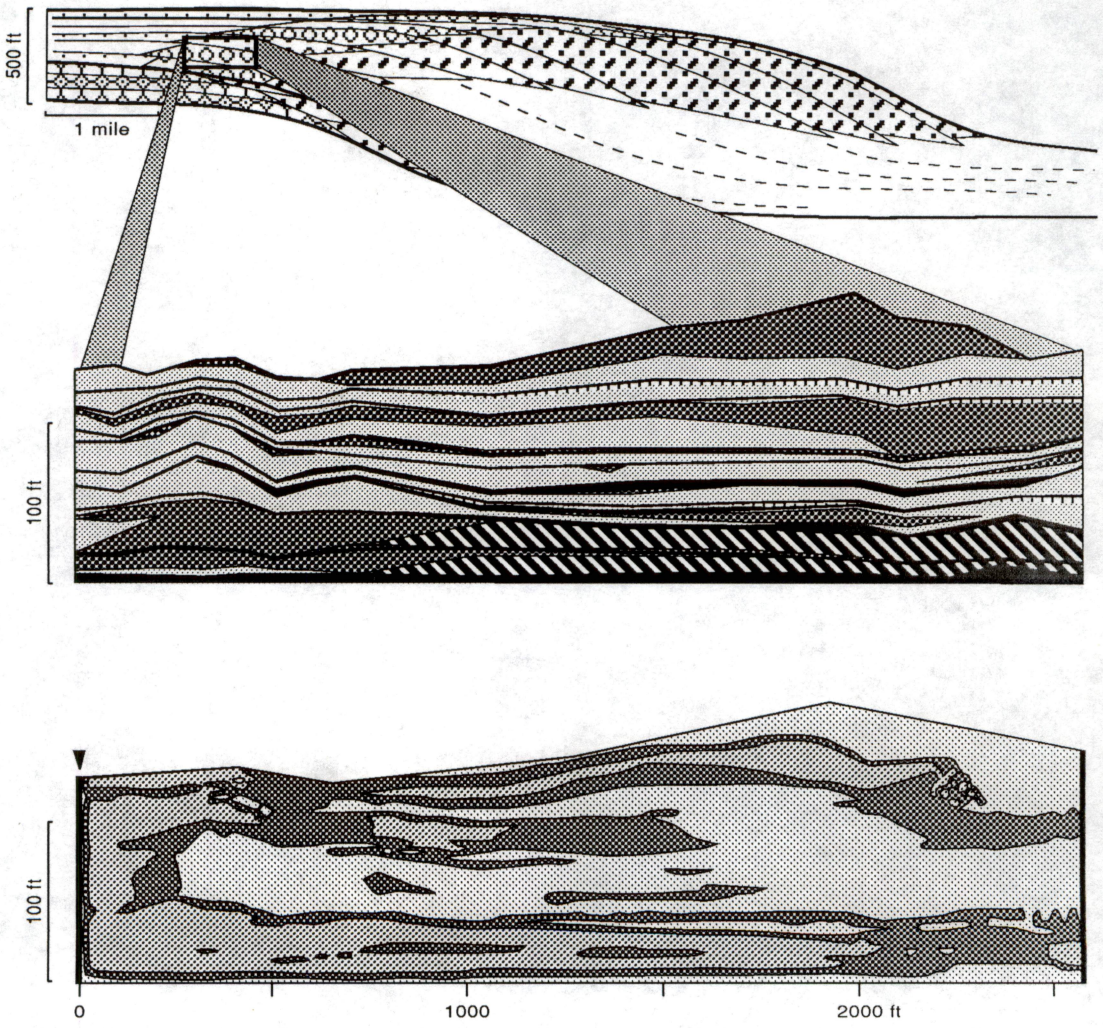

Prepared by the
Bureau of Economic Geology
W. L. Fisher, Director
The University of Texas at Austin
Austin, Texas 78713-7508

Reservoir Characterization Research Laboratory

Characterization of Reservoir Heterogeneity in Carbonate-Ramp Systems, San Andres/Grayburg, Permian Basin

FINAL REPORT

Charles Kerans, F. J. Lucia, R. K. Senger, G. E. Fogg, H. S. Nance,
Ekrem Kasap, and S. D. Hovorka

Assisted by A. P. Czebieniak, W. M. Fitchen, M. A. Ferris, and R. S. Single

Bureau of Economic Geology
W. L. Fisher, Director
The University of Texas at Austin
Austin, Texas 78713-7508

March 1991

CONTENTS

EXECUTIVE SUMMARY

More than 13 billion barrels of mobile oil and 17 billion barrels of residual oil will remain in San Andres and Grayburg reservoirs at abandonment if current development practices continue to be followed. Through development and application of new advanced recovery technology, a large part of this resource can be recovered. We have focused our research on developing and testing new techniques for improving recovery efficiency of this resource. Outcrop and subsurface geological and engineering data were utilized to develop new methodologies for integrating geologic observations with engineering data in order to improve numerical models that predict reservoir performance more accurately.

Key results of the study area:

- Reservoir Framework: Extensive regional measuring of sections and oblique aerial photomosaic mapping of the 14-mi by 1,200-ft San Andres outcrop demonstrates that the San Andres carbonate-ramp complex, like many thick carbonate-platform units, is composed of multiple depositional sequences that have significant basinward shifts in reservoir-quality facies tracts occurring across sequence boundaries.

- Reservoir Architecture: Detailed geological and petrophysical mapping of a 2,500-ft-long by 160-ft-thick window demonstrates that the fundamental scale of geologic description for reservoir characterization is the parasequence and its component rock-fabric-based facies. This is also true in the subsurface, as shown by descriptions of cores from Seminole (San Andres) field.

- Petrophysical Quantification: Outcrop and subsurface petrophysical data show that the parasequence framework can be quantified in petrophysical terms through rock-fabric-based transforms. Three basic rock-fabric/petrophysical classes, each having distinct petrophysical characteristics, can be used to quantify the geologic framework. These three classes can be distinguished in the subsurface using wireline log transforms.

- Geostatistical Modeling: Geostatistical analysis of closely spaced permeability data within a facies/rock-fabric type (bar-crest grainstone) shows a high degree of local variability, which appears random in nature. Statistically significant differences in permeability occur between facies/rock-fabric types.

- Conditional Simulation: Fine-scale finite-difference flow modeling within a single parasequence using conditional simulations of outcrop permeability data based on variogram-derived continuity functions demonstrates that fluid flow within a rock-fabric facies can be represented by the geometric mean permeability.

- Finite Element Modeling: Finite element modeling of the multi-parasequence outcrop window demonstrates the importance of accurately representing the geometry of both high- and low-permeability elements. Simulation of water injection shows that high-permeability grainstone beds are major flow conduits, whereas injection into lower permeability packstones and mud-dominated fabrics lags behind. Discontinuous mudstone layers provide barriers to cross flow between parasequences.

ACKNOWLEDGMENTS

We would like to acknowledge the strong support of our industry sponsors, Agip, Amoco, ARCO, Chevron, Exxon, Halliburton, Marathon, Mobil, Radian, Silicon Graphics, Shell, Stratamodel, Texaco, and Unical. We are especially indebted to Shell Oil Company, and Rob Mathis and John Treckman specifically, for providing us with Paul Hindrich's original data from his pioneering work on the San Andres of the Algerita Escarpment. The aerial photographs of the Algerita Escarpment were particularly useful in the initial phases of this project. We also wish to thank Marathon Oil Company for the XRD data on the core from Amerada No. 2505 and for the core analysis of the plug samples from selected whole-core samples, Chevron Oil Company for processing color photographs of the Algerita Escarpment, and Shell for providing funds to run spectral gamma-ray logs in the boreholes. The data contributed greatly to the success of the project. Finally, Amerada Hess provided us with cores, core data, logs, and production data from Seminole field, without which carrying out the subsurface part of this study would have been impossible.

The report was designed by Jamie H. Coggin. Melissa Snell completed the word processing under the supervision of Susann Doenges, Editor-in-Charge. Lana Dieterich and Bobby Duncan edited the report, and Tucker F. Hentz was the technical editor. Joel L. Lardon, Kerza A. Prewitt, Ed Banks, Jana S. Robinson, Michele LaHaye, and Maria E. Saenz drafted illustrations under the supervision of Richard L. Dillon, Chief Cartographer. Lana Dieterich coordinated the production of the publication.

INTRODUCTION

This report summarizes research carried out by the Bureau of Economic Geology's San Andres/Grayburg Reservoir Characterization Research Laboratory (RCRL) from September 1988 through September 1990. The goal of the RCRL program was to develop advanced approaches to reservoir characterization for improved recovery of the substantial remaining mobile oil in San Andres and Grayburg reservoirs. Emphasis was placed on developing an outcrop analog for San Andres strata that could be used as (1) a guide to interpreting the regional and local geologic framework of the subsurface reservoirs and (2) a data source illustrating the scales and patterns of variability of rock-fabric facies and petrophysical properties, particularly in lateral dimension, and on scales that cannot be studied during subsurface reservoir characterization.

Areas selected for study were the San Andres exposures of the Algerita Escarpment in the northern Guadalupe Mountains and the Seminole San Andres Unit on the northern margin of the Central Basin Platform. The outcrop-analog research was emphasized because it had received little attention before this study by either industry or academe.

Reports in this summary involve (1) outcrop and subsurface geological characterization of the Algerita Escarpment San Andres and the Seminole San Andres Unit (Kerans), (2) correlation of detailed outcrop mapping in order to research cored wells at Lawyer Canyon, Algerita Escarpment (Nance), (3) diagenetic/petrographic analysis of selected upper San Andres facies focusing on the origin of moldic porosity (Hovorka), (4) geologic engineering description of the upper San Andres carbonates at Lawyer Canyon and the upper producing interval at Seminole (Lucia), (5) geostatistical analysis of permeability patterns and stochastic-based finite-difference modeling of the upper San Andres parasequence window (Senger and Fogg), and (6) deterministic finite element modeling of the upper San Andres parasequence window (Kasap).

Availability of basic data for these studies is summarized in the appendix.

GEOLOGIC CHARACTERIZATION OF SAN ANDRES RESERVOIRS: OUTCROP-ANALOG MAPPING, ALGERITA ESCARPMENT, GUADALUPE MOUNTAINS, AND SEMINOLE SAN ANDRES UNIT, NORTHERN CENTRAL BASIN PLATFORM

by Charles Kerans

OUTCROP-ANALOG GEOLOGIC MAPPING: SAN ANDRES OUTCROP OF ALGERITA ESCARPMENT

Geologic Setting of the San Andres Formation, Algerita Escarpment

Outcrop studies for the San Andres/Grayburg Reservoir Characterization Research Laboratory (RCRL) were located in the northern Guadalupe Mountains where excellent complete exposures of the San Andres Formation lie in this northwest corner of the Northwest Shelf (figs. 1 and 2). The Algerita Escarpment was the key exposure, containing a 1,200-ft-thick San Andres section spanning 17 mi of oblique-dip carbonate-ramp profile including a diverse array of carbonate-ramp facies (figs. 3 and 4). The combination of superb exposure on the Algerita Escarpment and proximity of these outcrops to their equivalent reservoirs (fig. 1) made the spot ideal for evaluating the utility of outcrop heterogeneity models used for interpreting equivalent reservoirs.

Sequence-Stratigraphic Studies for Reservoir Framework Analysis

The application of sequence-stratigraphic concepts, first developed for exploration and basin evaluation applications, proved useful for constructing both regional and interwell-scale geologic models used in production-geology studies. The depositional sequence provided a conceptual model that can be tested and also lent a predictive capability to the data collected. Table 1 provides a list of sequence-stratigraphic terminology adapted from Van Wagoner and others (1988) and is annotated to include some relevant aspects of each term/feature from a production geologist's perspective. Terms describing different scales of stratigraphic packaging

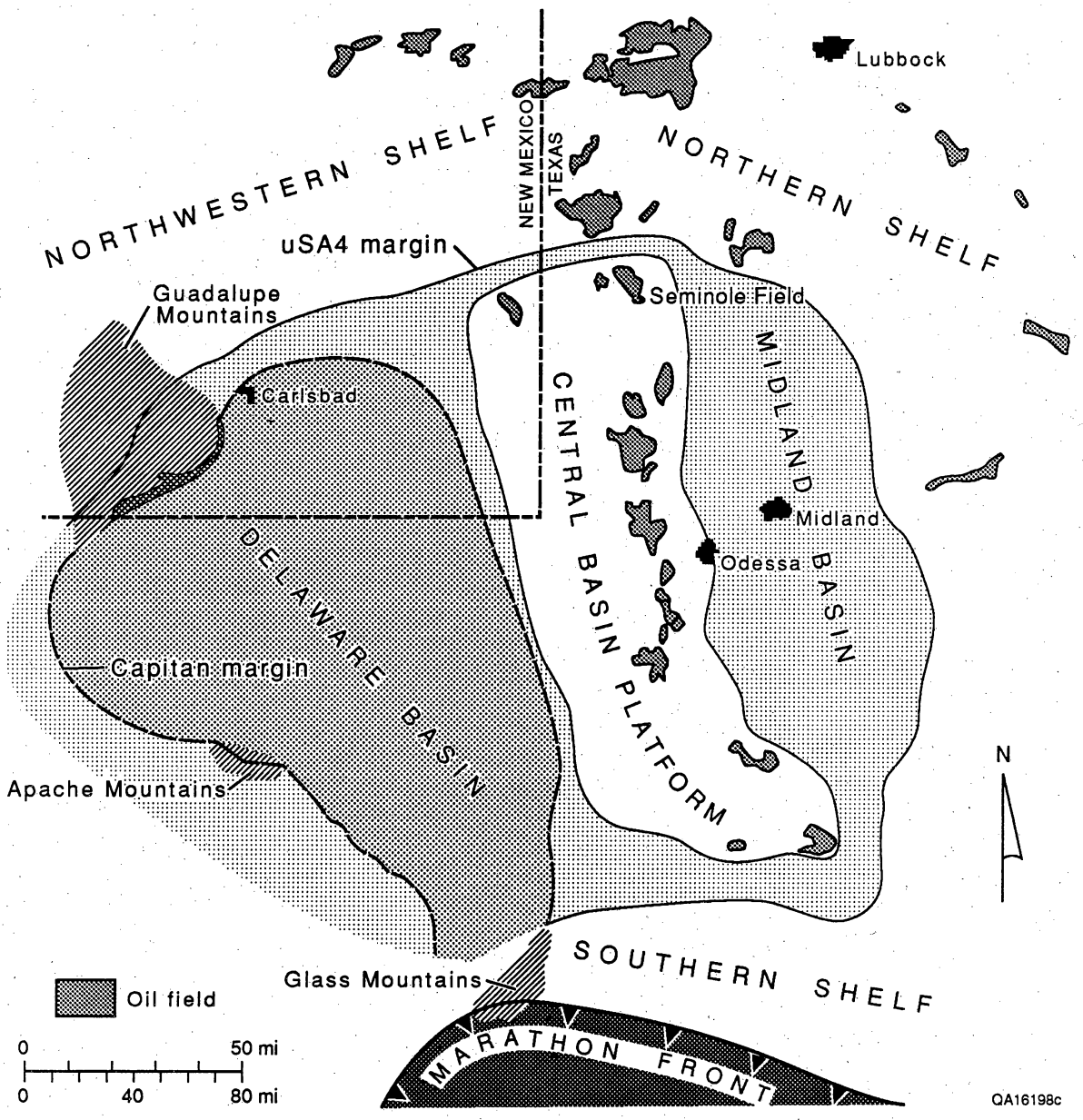

Figure 1. Generalized paleogeographic setting of the San Andres Formation, Permian Basin, showing San Andres reservoirs that have produced more than 10 million barrels of oil. Also shown are the Guadalupe Mountain outcrop area and Seminole field.

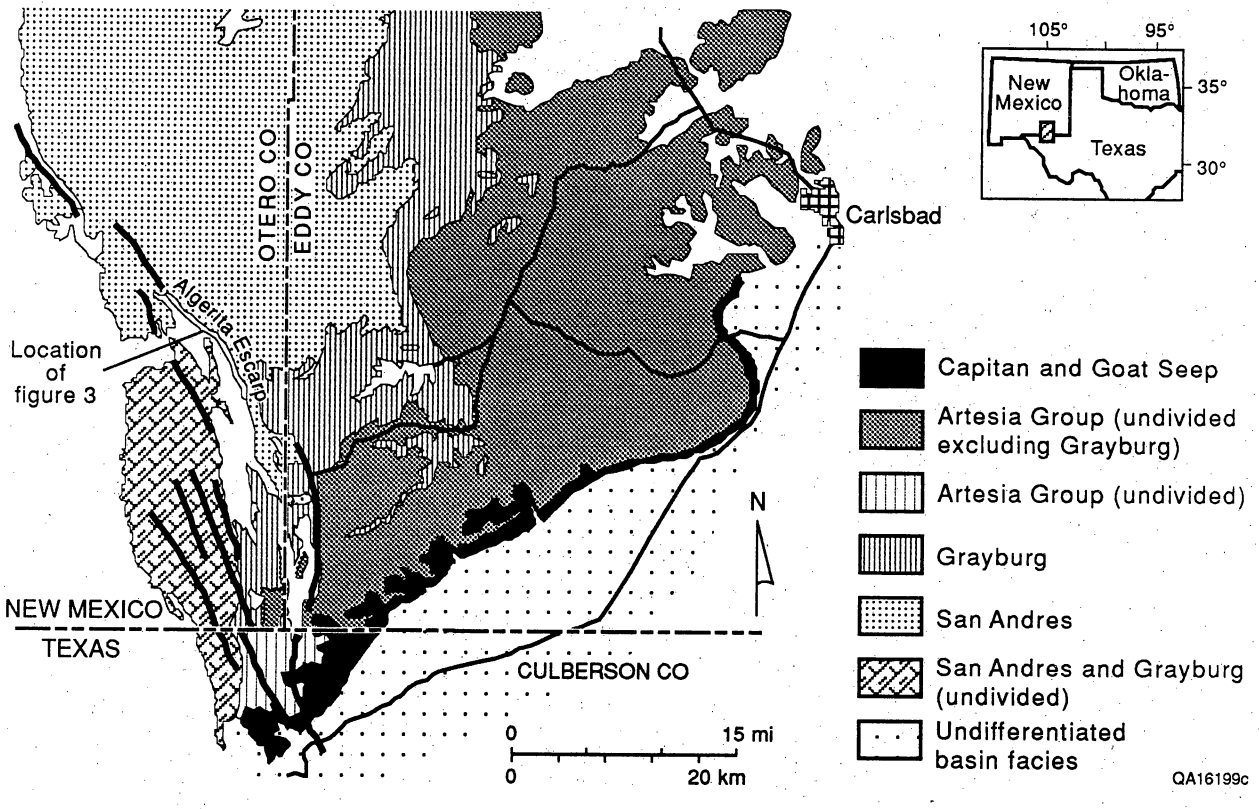

Figure 2. Geologic map of the Guadalupe Mountains compiled from Hayes (1964) and King (1948) showing Algerita Escarpment study area in the northern Guadalupe Mountains.

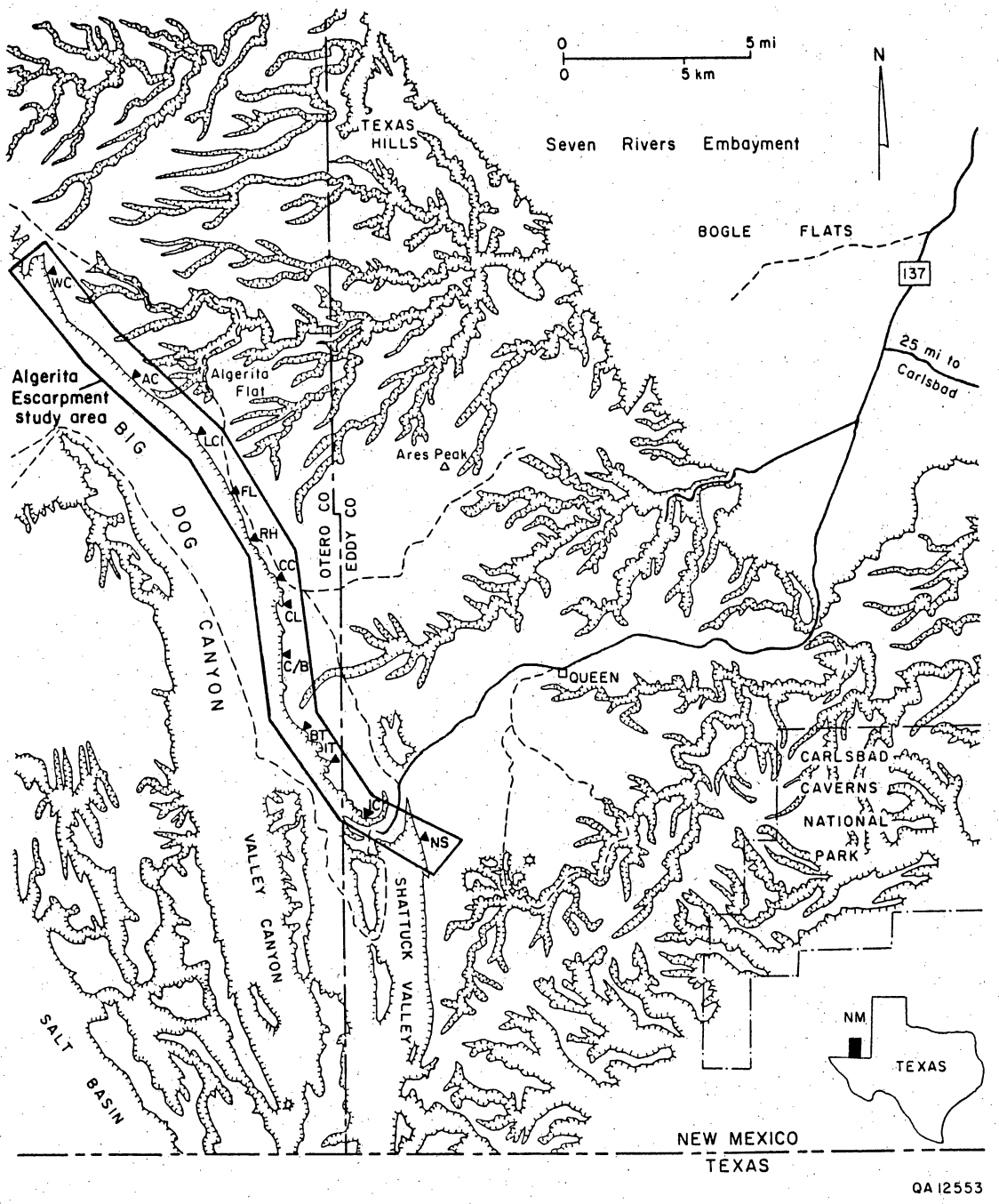

Figure 3. Physiographic map of the Algerita Escarpment and surrounds showing regional measured sections in figures 4 and 5 and detailed study areas. Modified from Moore and Wilde (1986). Measured sections indicated are WC - Woods Canyon, AC - Algerita Canyon, LC - Lawyer Canyon, FL - Fenceline, RH - Rawhide, CC - Cougar Canyon, CL - Coats Lake, C/B - Coats/Brister Intermediate, BT - Brister Tank, IT - Irabarne Tank, IC, Irabarne Canyon, NS - North Shattuck Valley.

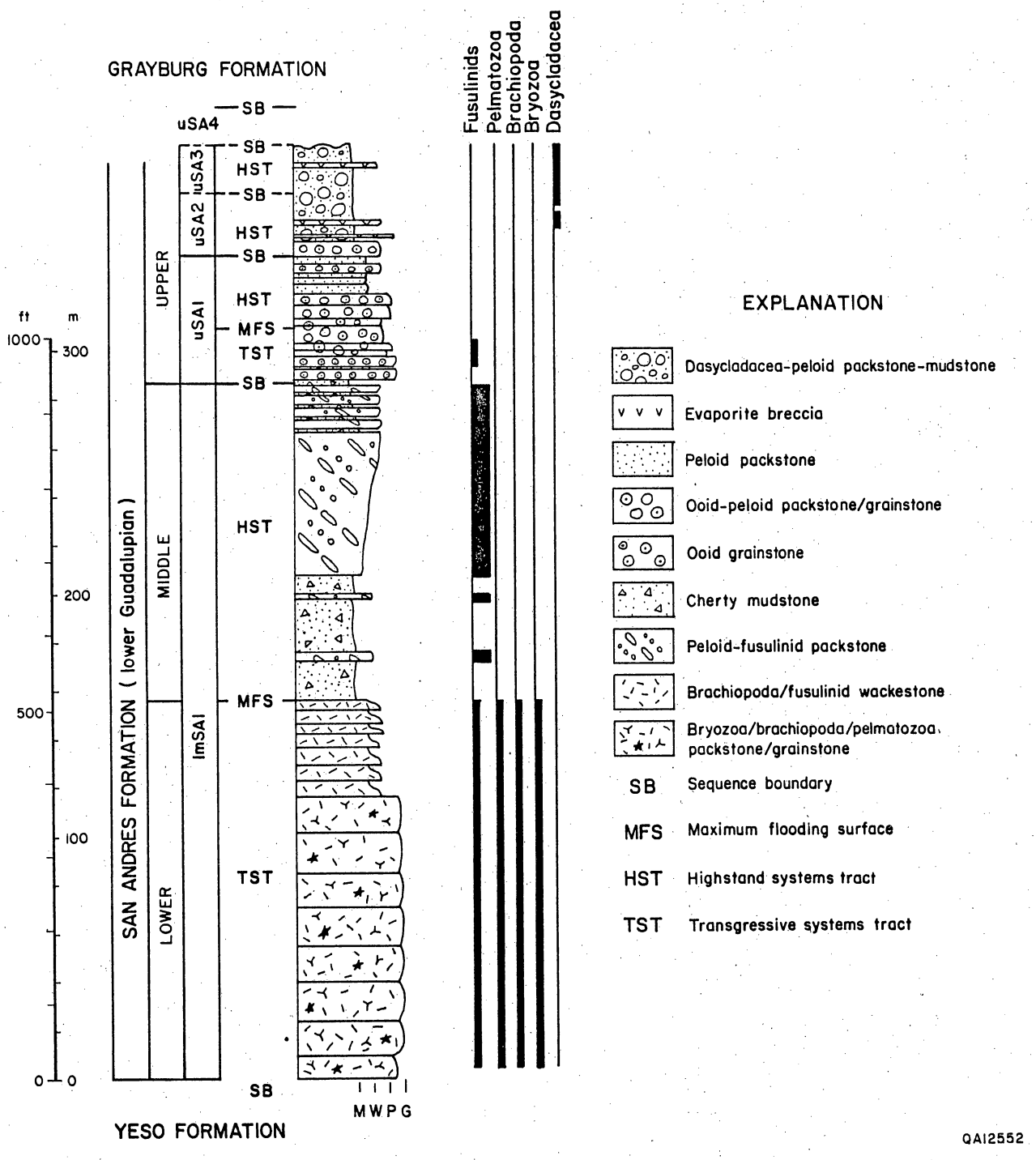

Figure 4. Measured section of the San Andres Formation at Lawyer Canyon displaying lithologic and sequence terminology.

TABLE 1. Sequence-stratigraphic terminology and its relation to production geologic studies.

TERM		DEFINITION	RESERVOIR APPLICATION
Sequence stratigraphy		Study of rock relationships within a chronostratigraphic framework of repetitive, genetically related strata bounded by surfaces of erosion or nondeposition or their correlative conformities	Reservoir framework
Sequence		Relatively conformable succession of genetically related strata bounded by unconformities and their correlative conformities	Total reservoir interval
Sequence boundary	SB	Surface of erosion or nondeposition that separates younger strata above from older strata below	Strata below SB in platform areas may display enhancement of porosity; may or may not separate reservoir zones
Parasequence	ps	Relatively conformable succession of genetically related and generally progradational beds and bed sets bounded above and below by marine flooding surfaces and their correlative surfaces	Basic reservoir mapping unit; may be closely related to flow units
Marine-flooding surface		Surface that separates older strata below from younger above, across which there is evidence of abrupt increase in water depth	Potentially critical as intrareservoir flow barrier
Depositional system		Three-dimensional assemblage of lithofacies	Classic style of geologic reservoir description; example: delta
Systems tract	ST	Linkage of contemporaneous depositional systems. Three systems tracts can be recognized within a sequence: lowstand (or shelf margin if type-2 sequence), transgressive, and highstand	Recognition of systems tract within sequence lends predictability to vertical and lateral trends of reservoir strata

TABLE 1 (cont.)

TERM		DEFINITION	RESERVOIR APPLICATION
Lowstand systems tract	LST	Basal systems tract of type-1 sequence, developed basinward of precursor shelf edge during sea-level fall and maximum regression. Composed of complex aggradational to progradational parasequences in lowstand fan and wedge facies tracts	Common siliciclastic reservoir settings; Permian Basin examples; Spraberry siliciclastics and Bone Spring fields
Shelf margin systems tract	SMST	Basal systems tract of type-2 sequence, developed atop and seaward of old shelf margin	May represent separate shingled reservoir zone within overall progradational sequence set
Transgressive systems tract	TST	Middle systems tract of either type-1 or type-2 sequence, separated from LST or SMST by transgressive surface. Deposited during sea-level rise with component parasequences onlapping underlying sequence boundary and stacking in aggradational or retrogradational sets	Retrogradational package; can form separated reservoir draped by condensed section deposits; example, Holt (lower San Andres) reservoirs at North Cowden, Penwell
Transgressive surface	TS	First significant marine-flooding surface across the precursor shelf	
Downlap surface	DS	Marine flooding surface onto which the toes of clinoforms of overlying highstand tract downlap	May form top seal of reservoir; key seismically resolvable mapping surface; typically separates distinctly different reservoir styles
Maximum flooding surface	MFS	Time-transgressive surface marking the position of deepest water encroachment across the platform	May form top seal of TST reservoir in distal areas; in proximal areas may form thief zone
Condensed section	CS	Starved sediment deposit at DS	Can serve as source bed and/or intrasequence reservoir seal

TABLE 1 (cont.)

TERM		DEFINITION	RESERVOIR APPLICATION
Highstand systems tract	HST	Widespread uppermost systems tract of sequence containing aggradational and/or progradational parasequence sets, onlapping SB toward shelf and downlapping TST or LST basinward in clinoformal geometry, and capped by type-1 or type-2 SB	Contains high-energy shoal-type reservoir strata

or the hierarchy within this general sequence-stratigraphic framework have recently proliferated. Table 2 compares the terminology used in this study with some of the published terminologies both on the Guadalupe Mountain outcrop and in general application.

Previous Framework

In early studies of the San Andres in outcrop and in the subsurface, most workers (for example, Hindrichs and others, 1986) thought this formation recorded a single upward-shallowing unit. A regional stratigraphic analysis by Sarg and Lehmann (1986) of the San Andres and associated units in the Guadalupe Mountain outcrop significantly revises this framework, introducing sequence-stratigraphic concepts into the analysis of the San Andres ramp complex.

Sarg and Lehmann (1986) divided the San Andres into two major third-order depositional sequences, (1) a lower sequence resting unconformably on the Leonardian Yeso Formation and comprising the lower and middle lithologic units of the San Andres and (2) an upper sequence approximately equivalent to the upper San Andres of Hayes (1964). Sarg and Lehmann suggested that these sequences, which were defined on the Algerita Escarpment on the basis of a subtle downward shift in onlap, could be correlated with the Last Chance Canyon area. Here the sequences would be separated by the Cherry Canyon tongue, which represents the lowstand systems tract (LST) of the upper San Andres sequence. Sarg and Lehmann also demonstrated that the upper San Andres sequence was unconformably overlain and onlapped by the Grayburg Formation (table 3).

Sequence Framework Developed by RCRL

Regional stratigraphic data collected along the Algerita Escarpment (fig. 3) have led to refinement of the Sarg and Lehmann (1986) sequence-stratigraphic framework, particularly in the upper San Andres sequence—the focus of the RCRL detailed studies (table 3). As a result of

Table 2. Terminology of stratigraphic hierarchies and their application to the San Andres Formation of the Guadalupe Mountains.

Goldhammer and others (1990)	Exxon general	Sarg and Lehmann (1986), Guadalupe Mtns.	This study, Algerita Escarpment	Sonnenfeld (1990), Last Chance Canyon
2nd order	Megasequence			
3rd-order (1–10 m.y.) cycle	Sequence	Lower-to-middle San Andres and upper San Andres 3rd-order sequences	lmSA1 3rd-order sequence	Lower San Andres and upper San Andres 3rd-order sequences (≅uSA3 and uSA4 4th-order sequences of present study)
4th-order (0.1–1 m.y.) cycle	High-frequency sequence		uSA1, uSA2, uSA3, uSA4 4th-order sequences	Genetic sequences 1-19 (≅parasequences of this study)
5th-order (0.01–0.1 m.y.) cycle	Parasequence	Parasequence	Parasequence	

Table 3. Lithostratigraphic terminology of the San Andres Formation in the Algerita Escarpment/Last Chance Canyon area.

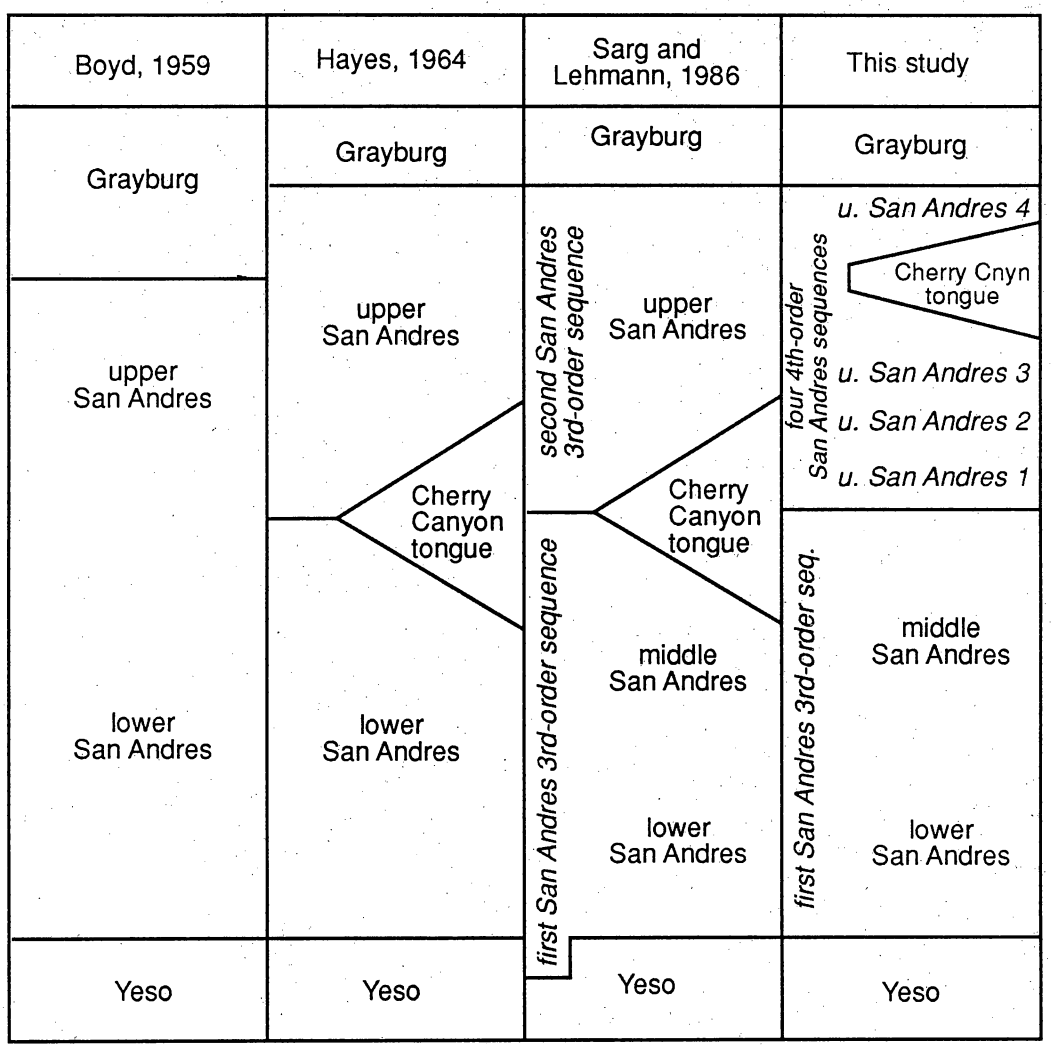

this focus, Sarg and Lehmann's upper San Andres third-order sequence was subdivided into four fourth-order sequences, and a similar analysis in the lower to middle San Andres third order sequence would probably yield a further subdivision there as well. The data for this sequence framework came from measured sections along the Algerita Escarpment in a dip-oriented cross section (figs. 3 and 5; pl. 1).

Lower-Middle San Andres Third-Order Sequence (lmSA1)

The lower-middle San Andres sequence (lmSA1) as defined by Sarg and Lehmann (1986) and as used in this report ranges in thickness from 400 ft basinward to 800 ft in Lawyer Canyon, where it is most completely exposed (fig. 4). At Lawyer Canyon the sequence consists of an open-marine transgressive bank (lower San Andres unit, 500 ft thick) succeeded by a prograding restricted ramp system (middle San Andres) that includes a landward-tapering cherty mudstone tongue (less than 1 to 500 ft thick) that shallows upward into 280 ft of cyclic fusulinid-peloid wackestone/packstone (upper middle San Andres) (figs. 4 and 5). Middle San Andres facies on this portion of the Algerita Escarpment are entirely of outer ramp origin (fig. 5; pl. 1)

The San Andres/Yeso sequence boundary is open to interpretation and depends on whether the uppermost tidal-flat cycles of the Yeso are included in the lmSA1 transgressive systems tract (Sarg and Lehmann, 1986) or in the youngest Yeso highstand systems tract (HST). Either interpretation indicates a type-1 sequence boundary between the Yeso and San Andres.

The boundary between the the lmSA1 sequence and the first upper San Andres sequence (uSA1) is apparently conformable as exposed on the Algerita Escarpment. It is represented by a downward shift in facies tracts that, in the Lawyer Canyon area, has placed ramp-crest ooid-peloid grainstones on top of outer ramp fusulinid packstone. This downward shift probably not only represents a minor 30- to 50-ft shift in relative sea-level lowering, but also a significant lateral shift in facies tracts of several miles because of the gradual depositional slope.

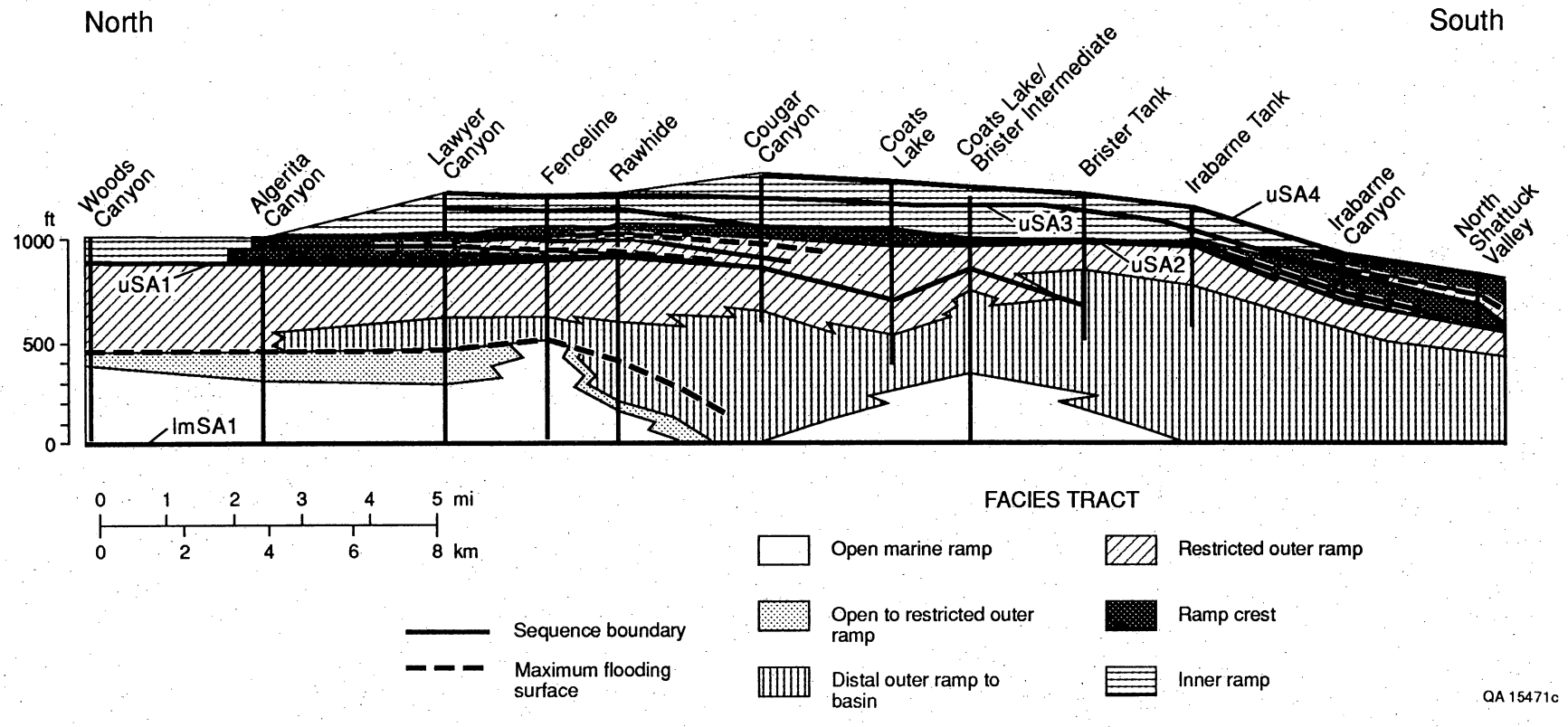

Figure 5. Sequence-stratigraphic model for the San Andres Formation of the Algerita Escarpment.

The sequence consists of transgressive-systems-tract (TST) (lower San Andres) and HST (middle San Andres) units. The lowstand record for this sequence must be entirely basinally restricted and is not exposed in the Algerita Escarpment area. The TST (lower San Andres) is an open-marine bank deposit that represents one of the major marine flooding events in the Permian Series of the Permian Basin. It places normal marine strata and faunas atop the strongly prograded uppermost Leonardian platform and pushes the shelf edge a minimum of 20 mi landward. In the 17-mi dip transect of the Algerita the TST forms a landward-thickening wedge from roughly 100 ft between the Rawhide section and the Cougar Canyon section to a maximum of 500 ft at the Fenceline section before leveling at 450 ft from north of the Fenceline section to the Woods Canyon section (fig. 5). Mounding in the TST is observed downdip of this major bank (Coats Lake/Brister section, fig. 5) and may represent an oblique cut through a lobate TST bank margin or a discrete buildup similar to that forming the Seminole San Andres unit (see later discussion).

On the Algerita Escarpment a minimum of 40 parasequences of skeletal wackestone to skeletal packstone/grainstone is recorded in the TST. The flora and fauna in the TST are markedly different from those found in the remainder of the San Andres section, containing a diverse assemblage of brachiopoda, bryozoa, rugose corals, pelmatozoa, calcareous algae, trilobites, and foraminifera. The TST has subtidal-dominated parasequences that only rarely shoal to intertidal conditions (three examples in several thousand feet of measured section). Vertical stacking is predominantly aggradational to retrogradational, reflecting the overall high accommodation potential during deposition of the TST.

Across most of the TST bank, sea-level rise began to outpace sediment accumulation in the upper third of the systems tract. This incipient drowning is recorded by an increase in fusulinids replacing corals and bryozoa in the upper 150 ft of the TST and the loss of high-energy cross-stratified skeletal grainstones upward. An exception occurs at the Fenceline section where thick crossbedded skeletal shoals record sedimentation within wave base for most of TST deposition, resulting in local thickening of the section here (fig. 5). The thick

crossbedded skeletal shoals at the Fenceline section and thinner equivalents at the Lawyer Canyon section and the Algerita Canyon section have excellent interparticle porosity and may be equivalent to Holt reservoir facies in the subsurface.

Downlap onto the TST generally cannot be readily detected using stratal geometry because the clinoform slopes of the lmSA1 HST are highly aggradational and define a low angle (<1 degree) relative to the TST. Distal outer ramp clinoform toes of the HST that drape it are of dark cherty mudstone that has thin allodapic fusulinid/pelmatozoan packstone beds. As the downlap surface is traced landward from Lawyer Canyon to Algerita Canyon, water depths at maximum flooding decrease, and eventually at Algerita Canyon cyclic pelmatozoan and fusulinid wackestones of the lower San Andres upper TST meld into fusulinid wackestones of the middle San Andres early HST without clear distinction; cherty mudstones of the lower part of the middle San Andres are absent (fig. 5).

The HST of the lower-to-middle San Andres sequence is equivalent to the middle San Andres unit of Sarg and Lehmann (1986) and this report (fig. 4 and table 3). It consists of a lower section less than 1 ft to 500 ft thick of dark-gray cherty spicule-bearing mudstone and an upper massive to cyclic fusulinid-peloid wackestone/packstone less than 1 ft to 400 ft thick. Cyclic sedimentation could not be discerned in the cherty mudstones, but shallow-water equivalents of the mudstone facies farther landward (Woods Canyon section) display well-developed cyclicity from fusulinid wackestone to fusulinid-pelmatozoan wackestone/packstone (pl. 1). The fusulinid-peloid wackestone/packstone facies that composes the upper half of the HST at Lawyer Canyon is made up of poorly defined 20- to 30-ft-thick cherty fusulinid wackestone to fusulinid-pelmatozoan-peloid packstone parasequences at the base, which pass upward to well-defined 10- to 20-ft-thick mudstone/fusulinid wackestone/fusulinid-pelmatozoan peloid packstone/grainstone parasequences in the upper 100 ft. Seaward of Lawyer Canyon, parasequences become increasingly mud rich, and lower parasequences pass into cherty mudstone. However, nowhere on the Algerita Escarpment can it be demonstrated that the entire highstand passes into distal outer ramp mudstones.

First Upper San Andres Fourth-Order Sequence (uSA1)

Subdivision of the upper San Andres third-order sequence of Sarg and Lehmann (1986) into four fourth-order sequences derives from detailed parasequence-scale mapping between Lawyer Canyon and north Sixshooter Canyon (table 3, fig. 5; pl. 1). The first upper San Andres sequence is best exposed at Lawyer Canyon where it is made up of nine parasequences (fig. 9) totaling 140 to 180 ft. Because a more detailed discussion of facies at Lawyer Canyon follows, only the major sequence-defining characteristics are outlined here.

The first upper San Andres fourth-order sequence boundary (uSA1-SB) appears conformable with the lmSA1 sequence in the study area as described previously. Ooid-peloid packstone/grainstone dominates the facies composition of uSA1 parasequences at Lawyer Canyon, suggesting a ramp-crest position for this sequence. An ideal parasequence in the ramp-crest area would be basal flooded-shelf mudstone followed by shallow-shelf peloid-wackestone/packstone, bar-flank ooid-peloid packstone/grainstone, and bar-crest peloid-ooid grainstone in an upward-shallowing succession. Parasequences 1 through 6 of uSA1 are aggradational to slightly backstepping, with successively higher parasequences containing less shallow-water high-energy facies. Parasequence 7 of the first upper San Andres sequence (ps7/uSA1) is a 35-ft-thick unit representing maximum flooding within uSA1. Indicators of maximum flooding during parasequence 7 are its anomalous thickness (suggesting greater accommodation space), the thick basal flooded-shelf mudstone, and fusulinid-peloid packstone near the base of the unit marking the updip maximum transgression of outer ramp facies in the upper San Andres. The maximum flooding surface for the uSA1 sequence is thus placed inside ps7 within the fusulinid packstone tongue.

The remaining upward-shallowing portion of ps7 and ps8 through 9b represent the highstand part of this sequence (60 to 90 ft thick). The upper sequence boundary of uSA1 is a karst surface containing pockets of solution collapse breccia and 1- to 2-ft deep solution dolines.

This karsted bar-top surface displays a minimum of 35 ft of depositional relief that was subaerially exposed and onlapped by uSA2 parasequences. At least 20 ft of this onlap is visible in the detailed study area of the Lawyer Canyon uSA1 parasequence window (see later discussion).

Updip from Lawyer Canyon the uSA1 sequence passes into peloid packstones and wackestones of a lower-energy lagoonal facies tract. Downdip of Lawyer Canyon the mudstone to grainstone upward-shoaling parasequences are replaced by mudstone/fusulinid wackestone to fusulinid wackestone/packstone parasequences of the outer ramp. Differentiation of the uSA1 and uSA2 sequences becomes difficult downdip of Lawyer Canyon because the sequence boundary passes into a paraconformable contact between outer ramp parasequences of uSA1 and uSA2 (fig. 5).

Second Upper San Andres Fourth-Order Sequence (uSA2)

The uSA2 sequence is recognized across the length of the Algerita study area and is best exposed in its ramp-crest position in the Rawhide to Cougar Canyon area. Here it is 120 ft thick and consists of nine to ten fusulinid-peloid packstone parasequences and five peloid grainstone parasequences. The uSA1/uSA2 sequence boundary is a microkarst surface recognizable from Lawyer Canyon to halfway between the Lawyer Canyon and Fenceline sections (fig. 5). In the Fenceline section (see appendix) a basal set of grainstone-dominated parasequences onlap the basal uSA1/uSA2 sequence boundary in the direction of Lawyer Canyon and pass downdip in the Cougar Canyon area into fusulinid-peloid packstone parasequences. These basal parasequences represent the TST of uSA2.

Above the TST grainstone parasequences at the Fenceline section and northward are dasyclad-peloid mudstone/wackestone/packstone parasequences deposited in an inner ramp lagoon behind an extensive grainstone complex in the Cougar Canyon–Irabarne Tank area (fig. 5 and pl. 1). The grainstone complex contains at least four stacked grainstone

parasequences that are either mudstone-based or amalgamated grainstone on grainstone. In the latter case parasequences are separated by microkarst surfaces. The dip width of the ramp-crest facies tract of the uSA2 HST is estimated to be 5 mi.

The uSA2/uSA3 sequence boundary is the most traceable karst surface on the Algerita Escarpment. The karst profile is best developed in the Cougar Canyon area where as much as 20 ft of collapse breccia containing minor quartz silt is preserved. Elsewhere the surface is represented by a more subtle, scalloped erosion surface having 0.5 to 2 ft of relief atop the thick (20 to 40 ft) grainstone complex.

Third Upper San Andres Fourth-Order Sequence (uSA3)

The uSA3 sequence is bounded below by the regionally mappable karst surface described in uSA2 and is capped by a ledge-forming amalgamated tidal-flat complex that is readily mapped on air photos and in the field from Coats Lake to Irabarne Tank. Updip of Coats Lake this tidal-flat complex changes facies to lagoonal mudstone, but the surface corresponds closely to the onset of siliciclastic sedimentation (Lovington sandstones and associated thin siltstone beds) and is thus carried at the base of these sandstones from Coats Lake north. The uSA3 thickens markedly on the Algerita Escarpment from 20 ft in the Fenceline area to 115 ft at Irabarne Tank 10 mi downdip (fig. 5). Approximately 5 transgressive parasequences and 10 highstand parasequences are recognized in the Irabarne area, with transgressive parasequences containing fusulinid wackestone/packstone marking significant flooding over the previously subaerially exposed uSA2 sequence boundary. Highstand parasequences are dominated by peloid packstone/grainstone and dasyclad-peloid packstone of largely inner ramp origin. Ramp-crest grainstones of the highstand tract are restricted to downdip of Irabarne Tank in the North Sixshooter and North Shattuck sections and define a 4-mi-wide belt.

Fourth Upper San Andres Fourth-Order Sequence (uSA4)

Sequence uSA4 is bounded below by the regionally mappable tidal-flat complex (Coats Lake to Irabarne Tank sections) and the Lovington sandstones (Cougar Canyon to Lawyer Canyon sections) and above by a variably developed karst surface that separates the San Andres and Grayburg Formations. This upper sequence boundary is exposed on the Algerita Escarpment from Cougar Canyon in the north to North Shattuck in the south (fig. 5) and is correlative to the karst event separating the San Andres and Grayburg Formations in the subsurface, such as the one found at Yates and Taylor Link fields, southern Central Basin Platform (Craig, 1988).

The uSA4 sequence is 115 ft thick in the area between the Brister and Irabarne Tank sections, where it is best exposed. A thin transgressive system tract includes two fusulinid-peloid-packstone-bearing parasequences immediately above the uSA3 sequence boundary. The siliciclastic-sand-based parasequences (Lovington Sandstones and two to four other locally occurring sands) are also interpreted as transgressive units, with sand being preserved on the shelf rather than bypassed because of overall high accommodation during TST deposition. Highstand deposits in the Fenceline to Irabarne Tank sections include some 10 to 12 thin (5 to 15 ft thick) mudstone to dasyclad-peloid wackestone/packstone parasequences that have locally developed tidal-flat caps. In the North Sixshooter and North Shattuck sections massive amalgamated ramp-crest peloid-ooid grainstone parasequences make up much of the HST, with thin mudstone-based, fenestral/tepee-capped parasequences forming the final four to five parasequences. The ramp-crest facies tract of the HST in uSA4 is at least 3.5 mi in dip dimension.

PARASEQUENCE WINDOW STUDY AREAS FOR INTERWELL MODELING

The priority of the outcrop part of the RCRL program was to develop deterministic images of geologic facies architecture and corresponding porosity/permeability structure at a scale ranging from 1 ft to tens of feet vertically and inches to hundreds of feet laterally (interwell scale). These images are useful for constraining both qualitative and quantitative interpretations of equivalent reservoir strata. The sequence analysis was conducted to provide a framework within which the detailed data could be collected and more meaningfully applied to the San Andres in other parts of the Permian Basin, and to similar carbonate-ramp systems worldwide.

The ramp-crest grainstone complex of the uSA1 sequence was selected as the first detailed parasequence window study area. This area was given high priority because a series of recent reservoir-characterization studies of San Andres and Grayburg reservoirs (Longacre, 1980; Harris and others, 1984; Bebout and others, 1987; Ruppel and Cander, 1988) demonstrated that this facies tract displayed the greatest inherent geologic heterogeneity and hence could benefit most from facies-variability data provided by continuous outcrops. Other areas selected for detailed study that are currently being analyzed geologically and petrophysically are the Lawyer Canyon lmSA1 outer ramp window and the Irabarne Tank uSA2 outer ramp window (fig. 6).

Parasequence Framework for Reservoir-Scale Mapping

Parasequences are the most significant stratigraphic elements in the San Andres Formation at the reservoir scale, both in outcrop and in reservoirs. A parasequence is defined as "a relatively conformable succession of genetically related beds or bedsets bounded by marine flooding surfaces and their correlative surfaces" (Van Wagoner and others, 1988, p. 39). These units are defined in a one-dimensional sense by the classic upward-shallowing cycles of Wilson (1975) and James (1977) that produce an ideal upward-coarsening profile of mudstone to

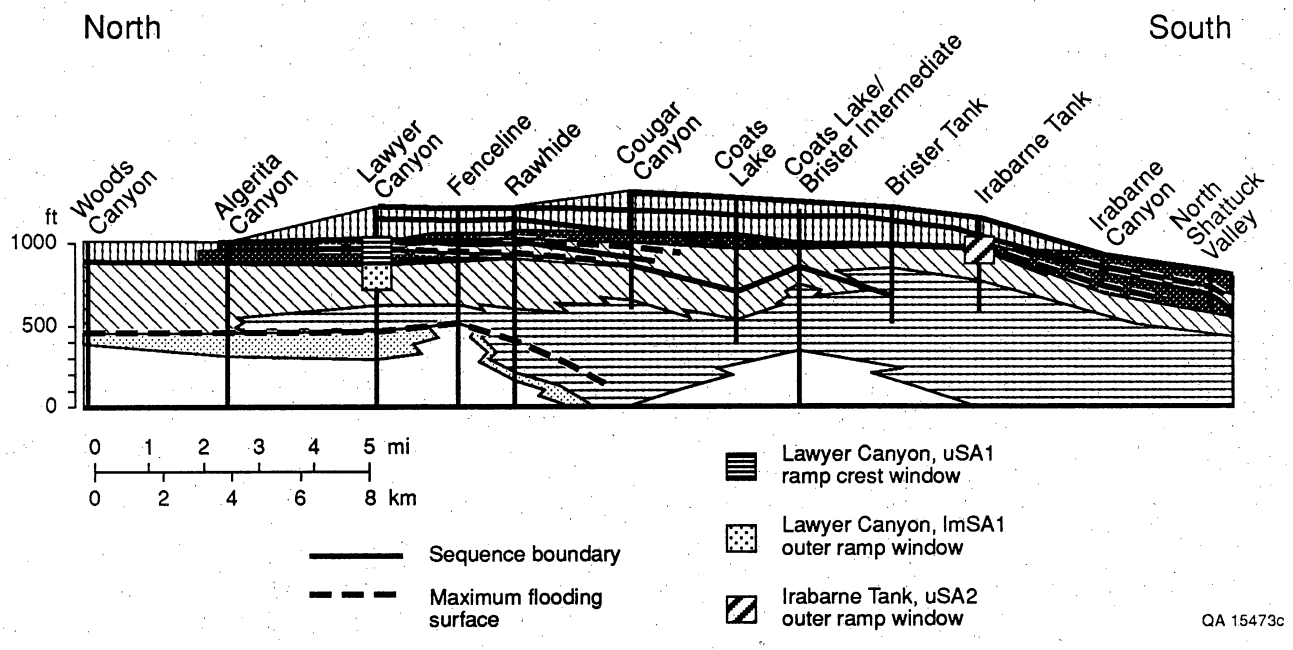

Figure 6. Location of detailed parasequence windows in Algerita sequence-stratigraphic framework.

wackestone/packstone to grainstone (with or without tidal-flat cap). However, the parasequence is a three-dimensional, time-bounded entity that is only partly described by the one-dimensional upward-shallowing profile. The two-dimensional parasequence windows described herein are a way of capturing the lateral variability within parasequences.

The parasequence concept has direct applications for reservoir characterization and flow-modeling studies in carbonate reservoir strata. First, the flooding surfaces and, locally, the tidal-flat caps that bound parasequences commonly are defined by low-permeability layers (mudstones, wackestones, and sulfate-cemented carbonate) that serve to stratify the reservoir vertically. Second, the upward change in rock fabrics from fine to coarse can, within the proper framework (Lucia, 1983), be translated into predictable petrophysically significant relationships that aid log interpretation of permeability. Finally, dividing the reservoir interval into smaller time-bounded units promotes accurate depositional and diagenetic facies measurement, which can form the basis of stochastic reservoir models. Earlier geologic facies-mosaic cross sections give little insight into dimensions of depositionally or petrophysically significant facies at the reservoir scale.

Lawyer Canyon uSA1 Ramp-Crest Window

The Lawyer Canyon uSA1 ramp-crest parasequence window contains a grid of 100- to 300-ft laterally spaced measured sections, each covering 120 to 180 ft of vertical section. The lateral dimension of this geologic grid is 2,600 ft, covering an area equivalent to several well spacings in a typical San Andres or Grayburg reservoir (figs. 7 and 8).

This window contains nine parasequences, each displaying variable development of the ideal upward-shallowing, upward-coarsening facies and rock-fabric succession (figs. 9 and 10). Parasequences average 15 ft in thickness and are continuous on the scale of the 2,600-ft cross section, but component depositional facies are not. Grainstone facies range from 5 to 38 ft in maximum thickness (average of 16 ft) and from less than 100 ft to greater than 2,600 ft in dip

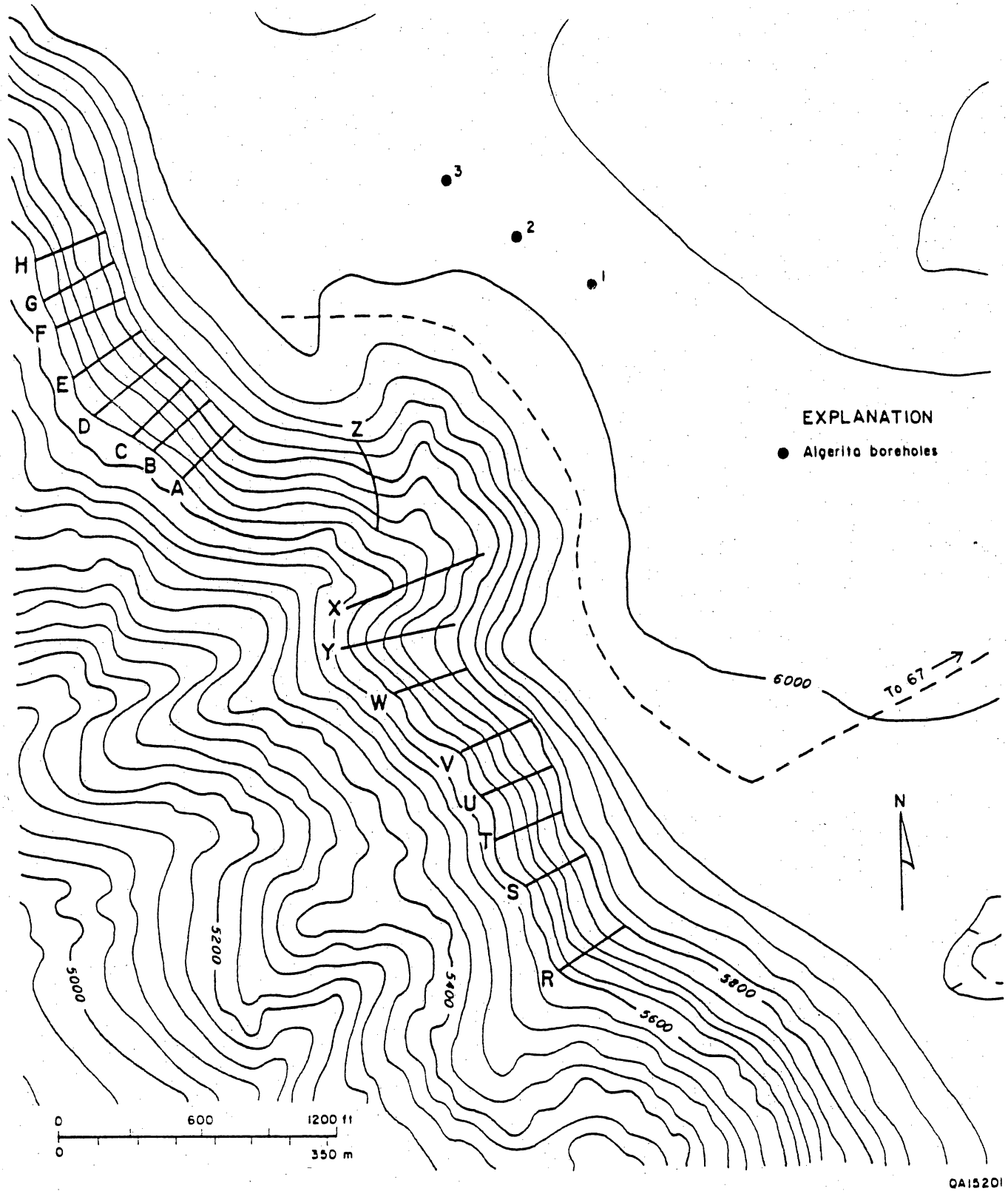

Figure 7. Topographic map showing detailed measured sections of Lawyer Canyon uSA1 ramp-crest parasequence window, in 21-23S-20E of the Algerita Canyon 7.5-minute topographic sheet. Contour interval is 200 ft.

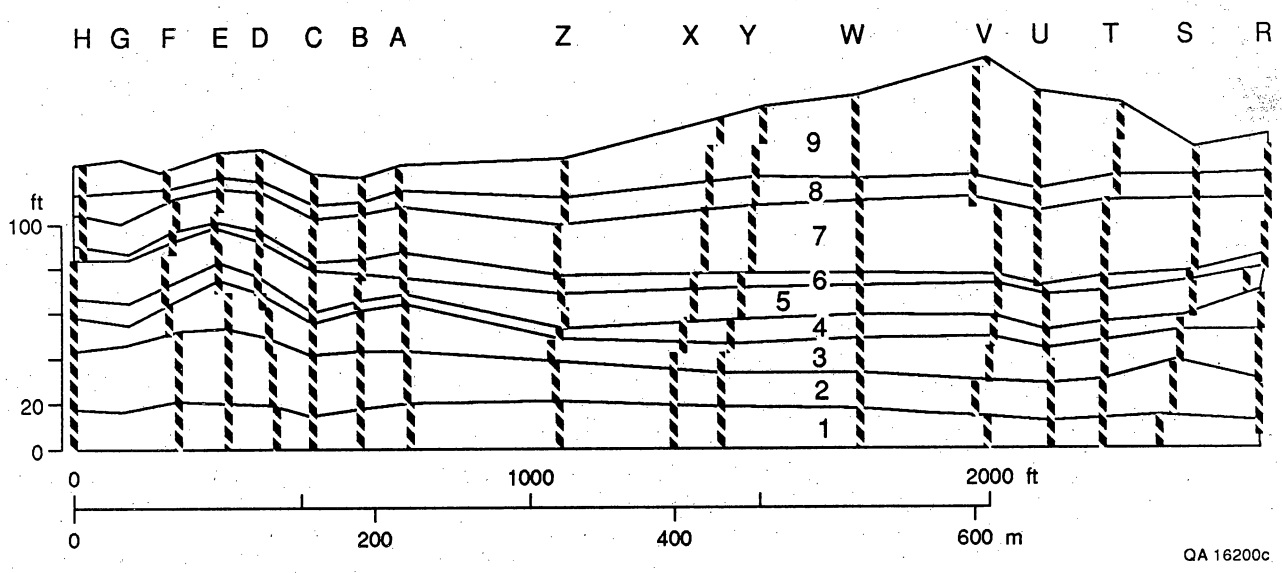

Figure 8. Cross section showing distribution of geologic measured sections in the Lawyer Canyon uSA1 ramp-crest parasequence window and parasequence outlines.

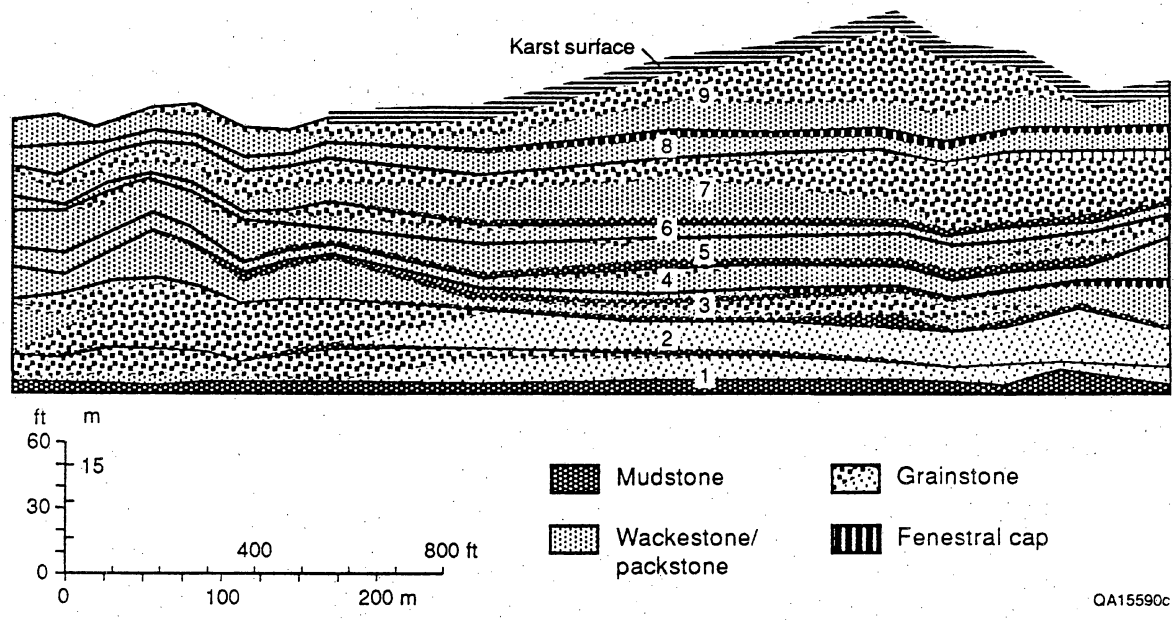

Figure 9. Simplified depositional facies version of the Lawyer Canyon uSA1 ramp-crest parasequence window.

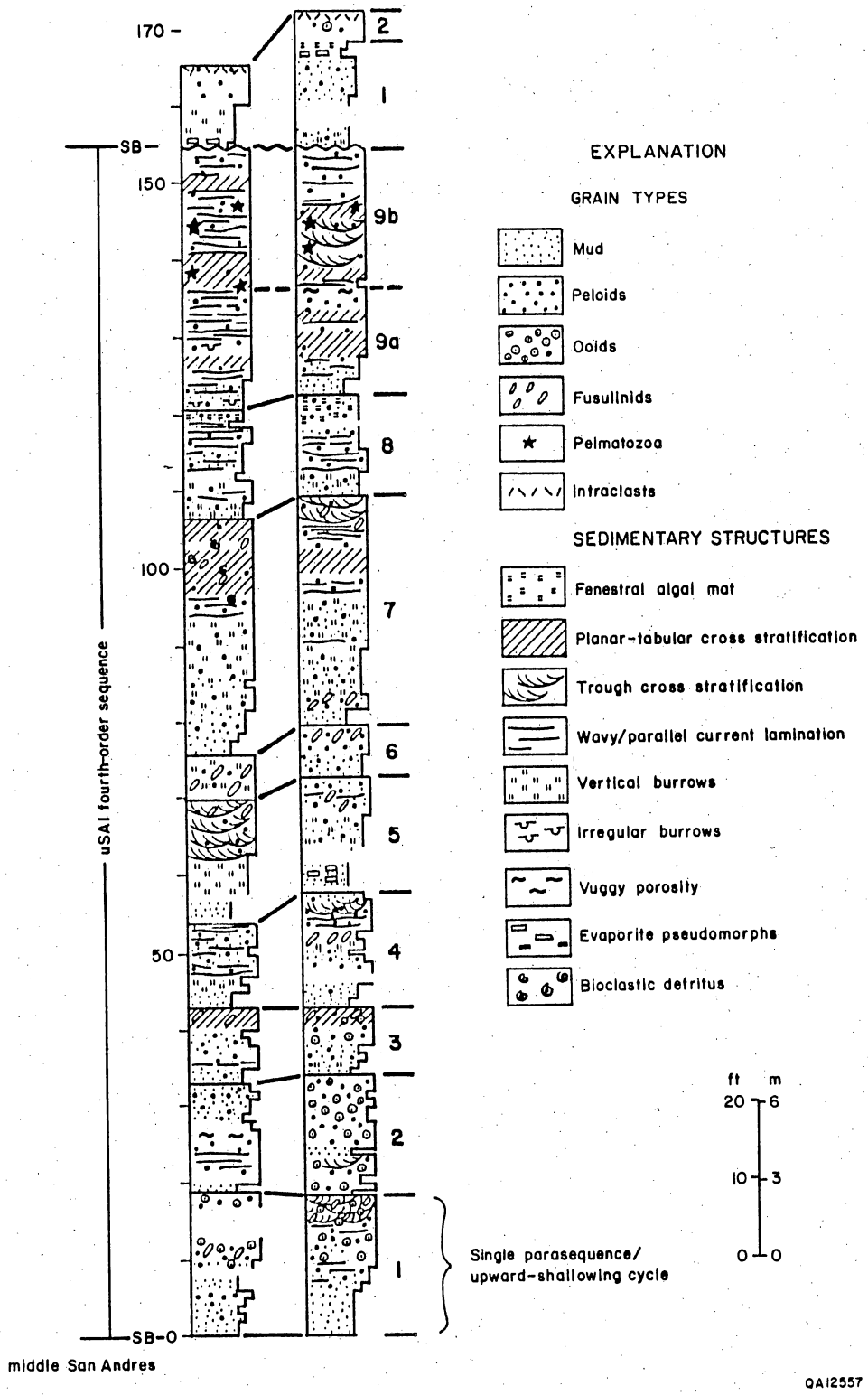

Figure 10. Detailed vertical sections showing the depositional cyclicity of the ramp-crest parasequences, Lawyer Canyon uSA1 ramp-crest parasequence window.

length (fig. 9). Wackestone/packstone facies are thinner and more continuous than the grainstone part of the parasequences. Mudstones range from less than 1 to 5 ft in thickness and from tens of feet to several miles in width (beyond the scope of the detailed study area) in dip dimension.

Examining a single parasequence for internal architecture (figs. 11 and 12; pl. 2) can show sedimentation to have been initiated by mudstone deposition interpreted to represent slow sedimentation after a rapid sea-level rise (flooded-shelf mudstone facies). After this transgressive event, the carbonate system established itself and built to sea level (as recorded by deposition of open-shelf, vertically burrowed to flaser/lenticular bedded wackestone/packstone), and finally bar-crest and bar-flank grainstones and packstones were established. Bar-crest grainstones exhibit abundant small-scale trough and planar-tabular cross-stratification, indicating active reworking within the zone of normal wave base and tidal influence. Bar-flank deposits contain parallel-laminated grainstones intercalated with thin wackestone/packstone layers that represent storm-dominated shelf sedimentation. Such sedimentation transports grainstones from the active bar crest to the bar flank, where they are intercalated with lower-energy shelf sediments.

Facies development within a parasequence is potentially highly variable. Note that in parasequence 9 (fig. 9), grainstones reach a thickness of 38 ft but quickly thin laterally. Generally in the ramp-crest facies tract, the thicker the parasequence, the more laterally variable the resultant facies mosaic, largely because the greater accommodation space allows a fuller range of depositional environments to develop.

Lawyer Canyon lmSA1 Outer Ramp Window

The outer ramp fusulinid-rich strata were mapped in detail both at Lawyer Canyon (lmSA1) and in a younger succession of outer ramp strata in the Irabarne Tank area (see later discussion). The impetus for detailed mapping in these generally more homogeneous facies is

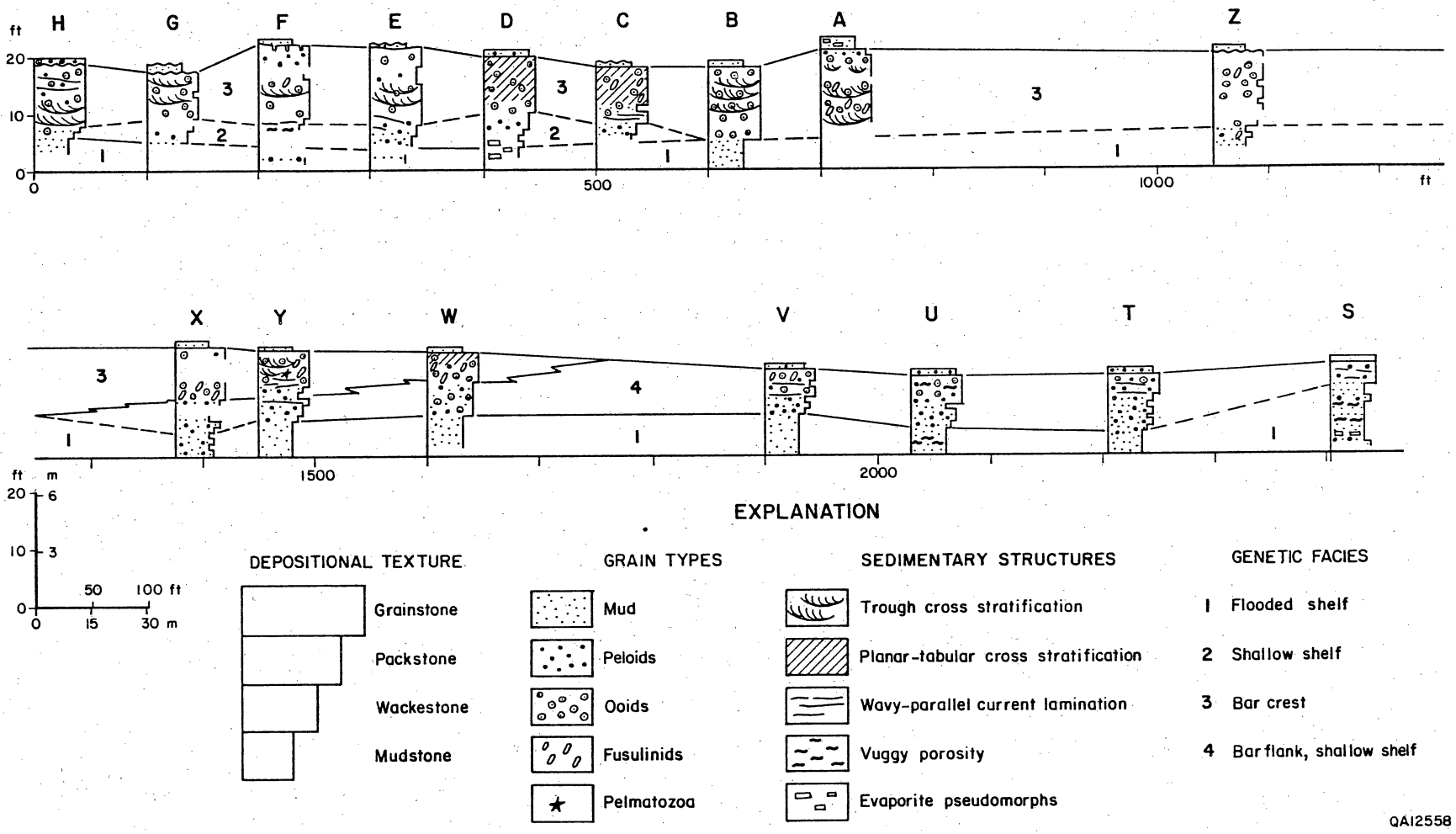

Figure 11. Lateral facies variations within parasequence 1, Lawyer Canyon uSA1 ramp-crest parasequence window. The basal flooded-shelf mudstone is continuous for the 2,600-ft dimension of the cross section but the bar-crest facies passes downdip into finer grained bar-flank deposits.

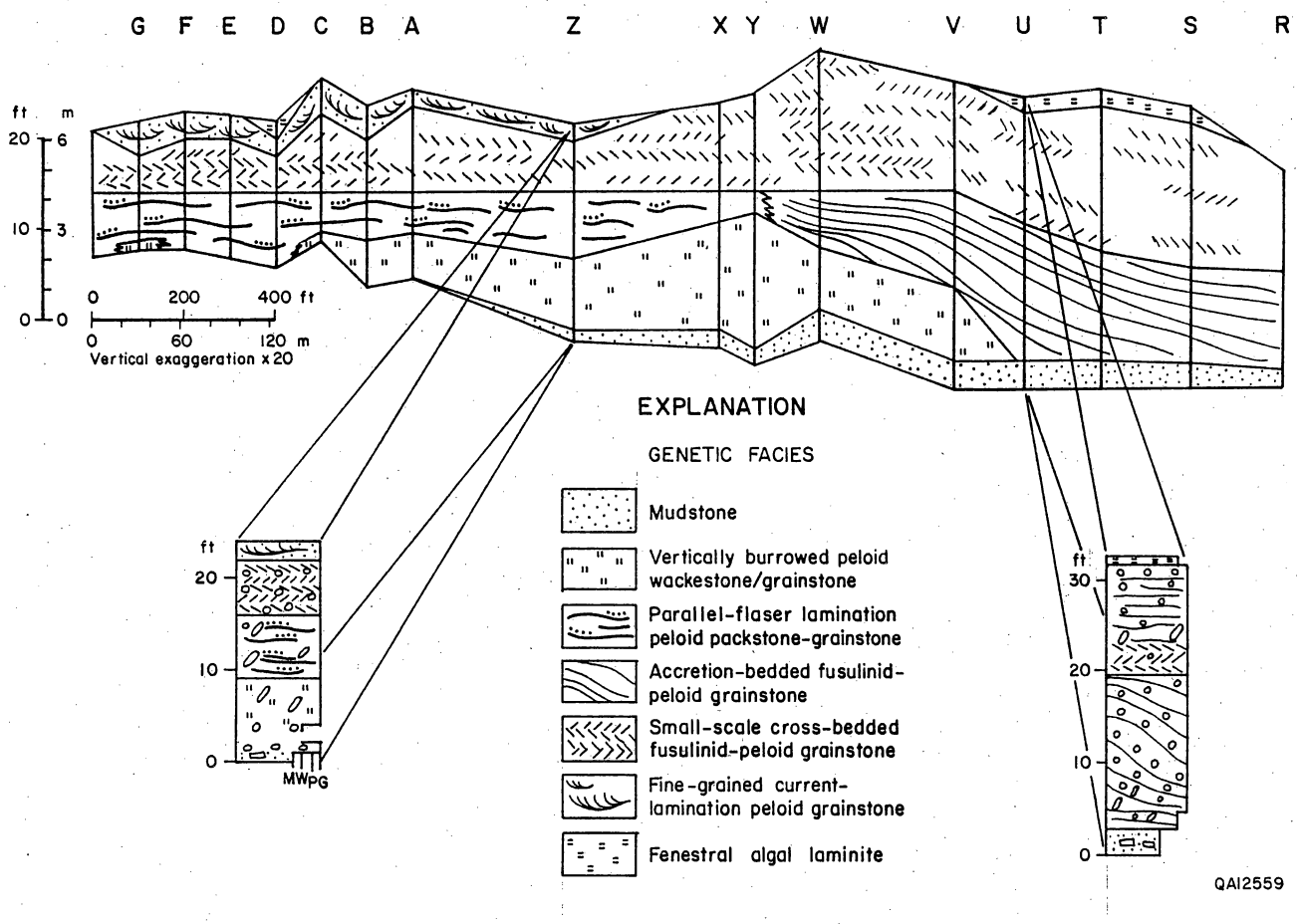

Figure 12. Lateral facies variations within parasequence 7, Lawyer Canyon uSA1 ramp-crest parasequence window. Parasequence 7 is one of the most complex of the parasequences in the study area, showing development of channel-filling(?) accretion stratification in addition to small-scale cross-stratified bar-crest deposits and a thin, locally developed tidal flat atop the bar-crest grainstones.

twofold. First, this subtidal fusulinid-dominated outer ramp section commonly accounts for more than 50 percent of the producing interval and contains a similar proportion of the remaining oil resource in most San Andres and Grayburg reservoirs. Second, core description of the outer ramp facies tract rarely leads to improved zonation or refined geologic structure, and it was felt that examination of this facies tract might help guide future reservoir descriptions.

Five sections were described in the lmSA1 outer ramp window, a 1,800- by 280-ft area (fig. 6 and pl. 3). These sections began in cherty fusulinid wackestone just above the cherty mudstone facies. Sections were weakly cyclic between moldic fusulinid wackestone/packstone and fusulinid peloid packstone in the basal 200 ft, becoming distinctively cyclic in the upper 80 ft.

The 280-ft section was subdivided into 15 parasequences from 12 to 40 ft in thickness, with individual parasequences displaying a constant thickness across the 1,800-ft map area. The lower parasequences are thicker (20 to 40 ft) and consist of cherty fusulinid wackestone to fusulinid-crinoid-peloid packstone. The upper four parasequences are thinner (15 to 20 ft) and have distinctive mudstone bases followed by fusulinid wackestone/packstone and fusulinid-crinoid-peloid packstone/grainstone caps. Within these upper two to three parasequences Hindrichs performed his pioneering studies of permeability distribution at Lawyer Canyon (Hindrichs and others, 1986).

The vertical progression from thick, cherty, mud-rich parasequences to thin, chert-free, grain-rich parasequences at the top of the middle San Andres records a steady progradation of this outer ramp facies tract. The high lateral continuity of parasequence thickness and internal facies composition across the study area is consistent with the deeper-water (30 to 200 ft) outer ramp depositional environment for this facies tract of the HST.

The Lawyer Canyon lmSA1 fusulinid packstone window is in the outer ramp facies tract of the lmSA1 HST (fig. 6) and thus was deposited on a gradual shelf-to-basin slope. However, using the top lmSA1 sequence boundary as an approximate horizontal datum, the dip defined by

parasequence stratification appears below the resolution of our mapping techniques and is probably less than 1 degree.

Irabarne Tank uSA2 Outer Ramp Parasequence Window

The Irabarne Tank outer ramp window is 12 mi downdip of the Lawyer Canyon windows, largely within the uSA2 sequence (figs. 6 and 13). Seven detailed geologic sections were taken at 200-ft sampling distances along east-northeast- and east-southeast-trending canyon walls, forming panels of a three-dimensional grid 1,300 ft on a side, approximating a 20-acre 5-spot pattern. Each section covers 100 ft of vertical section and contains eight clinoform parasequences, seven of which are continuous through all sections (fig. 14). Parasequences are upward-coarsening, grading from fusulinid-peloid wackestone to fusulinid-peloid-crinoid packstone/grainstone. Depositional dip on the clinoform units is 1 to 2 degrees, and whereas it is still gradual, it is clearly visible on outcrop and in the geometry defined by the measured sections. Petrophysical analysis of the Irabarne Tank window is ongoing.

RESERVOIR CHARACTERIZATION APPLICATION: SEMINOLE SAN ANDRES UNIT

Regional Setting of the Seminole San Andres Unit

The Seminole San Andres Unit lies on the northern Central Basin Platform immediately south of the San Simon Channel. Preliminary interpretation of regional seismic data suggests that Seminole is one of several isolated lower to middle San Andres buildups that became linked with the rest of the San Andres platform only during youngest phases of San Andres sedimentation. Other such buildups include West Seminole, East Seminole, and Hanford. Significantly, reservoir character and quality in the San Andres at Seminole should thus change toward the margins of the productive structure because this structure mimics original depositional geometry.

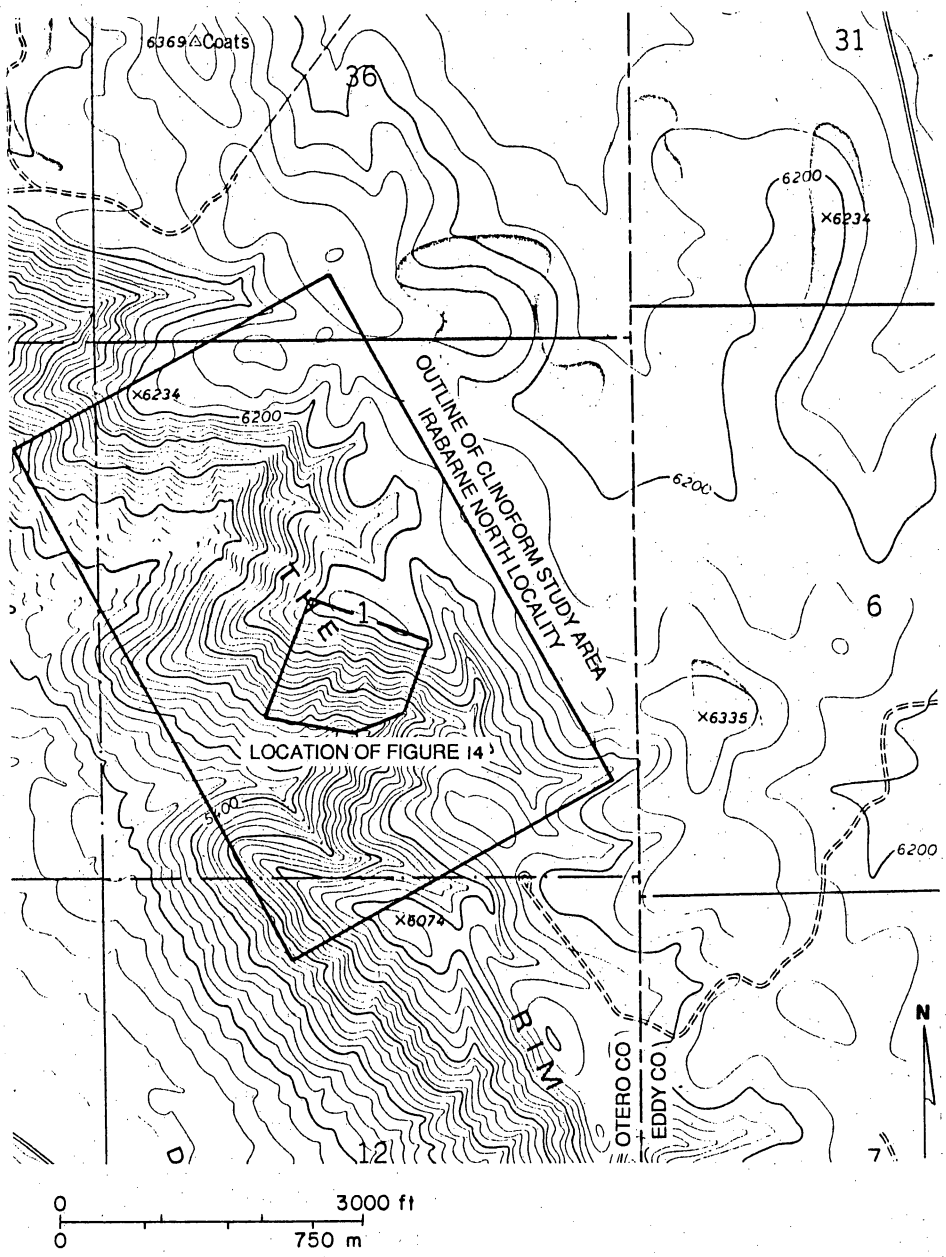

Figure 13. Topographic map showing the Irabarne Tank study area in 1-25S-20E of the Pickett Hill 7.5-minute topographic sheet.

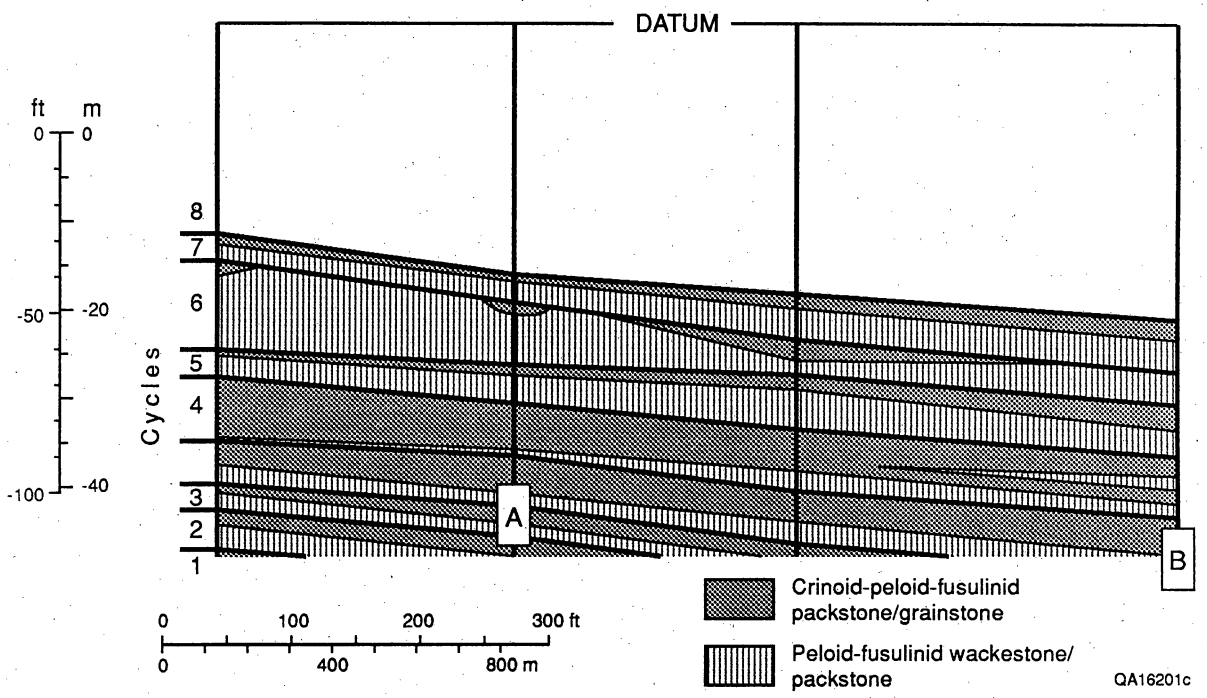

Figure 14. Generalized facies cross section of the north wall of the Irabarne Tank area canyon showing the continuity of parasequences and the approximately 2-degree basinward slope of these parasequences relative to the horizontal paleotopographic datum. Also shown are locations of detailed petrophysical sampling grids. Location of section shown in figure 13.

Initiation of the Seminole buildup followed flooding of the subaerially exposed uppermost Clearfork platform, in a manner analogous to the major flooding event observed atop the Yeso along the Algerita Escarpment. In a dip cross section from Seminole basinward toward the San Simon Channel, the San Andres lmSA1 platform margin stepped back 2 mi; the backstep to the contiguous San Andres margin of the Central Basin Platform is 9.5 mi. In the Guadalupe Mountain Northwest Shelf outcrop, the backstep of equivalent shelf margins, from latest Leonardian below (terminal Victorio Peak/Bone Spring facies contact) to earliest lmSA1 San Andres above (bioclastic shallow-shelf wackestone/packstone to distal outer ramp mudstones on the Algerita Escarpment) is 20 mi.

The sequence boundary between the upper Clearfork and the San Andres is not cored but is interpreted to be near the top of a series of stacked tidal-flat complexes in the position of the Glorieta gamma-ray pick. The only core at Seminole that penetrates the lower San Andres TST is the SSAU-5309 core. This core shows this interval to contain skeletal grainstones and packstones, and it has an open-marine fauna comparable to that of the lower San Andres TST of the outcrop. The TST, which is 750 ft thick, has high porosity and permeability, but it is in the water leg and thus nonproductive.

Maximum flooding is represented at Seminole by cherty fusulinid wackestones. No true cherty mudstone interval comparable to that seen in the middle San Andres at Lawyer Canyon, Algerita Escarpment, is developed. This transition from open-marine shallow-ramp wackestones and packstones to HST restricted-ramp wackestones and packstones is similar to the TST to HST transition in the north parts of the Algerita Escarpment (sections AC, WC, fig. 5).

The remainder of the cored interval is undivided highstand deposits that include approximately 450 ft of porous carbonates and 380 ft of largely anhydrite-cemented tidal-flat(?) cycles. The lower porous reservoir section is thought to contain highstand deposits of at least two sequences, the equivalent of the lmSA1 and uSA1 sequences of the Algerita outcrop model. The equivalents of the uSA2-uSA4 sequences are presumed to be equivalent to the upper tidal-flat section at Seminole.

Data for Geologic Analysis

Data for the sequence-scale geologic characterization at Seminole included (1) a regional log cross section from the outcrop in New Mexico to the San Simon Channel area (see Nance, this report), (2) a regional seismic grid, and (3) nine cores and associated well logs along a north-northwest-trending fieldwide cross section along the axis of the reservoir. For the detailed interwell study a two-section area in the north part of the reservoir (sections 230 and 231) was selected that contained (1) 62 wells and log suites, (2) 11 cored wells, 4 of them on the corners of a 10-acre 5-spot, and (3) per-well production data (fig. 15).

Detailed Geologic Mapping—the Parasequence Framework

The goal of the geologic characterization was to develop a three-dimensional framework that accurately portrays the distribution of geologic facies and that can be translated into petrophysical rock types for generating maps of such basic attributes as K/h, phi/h, Swi, and So/phi/h.

A key result of the integrated outcrop study was the recognition that the basic architecture of the San Andres is dominated by 10- to 30-ft upward-shallowing, upward-coarsening cycles or parasequences that are mappable on the scale of thousands of feet laterally and that can be related to petrophysical and flow properties via a rock-fabric facies mapping approach (see Lucia, this report). Although upward-shallowing cycles are widely recognized in carbonate deposits (Wilson, 1975; James, 1977), the role of these cycles in controlling fluid flow and recovery properties within a reservoir has not been quantified.

Using the results of the detailed parasequence window mapping from the outcrop as a guide, the Seminole cores from the main pay section were logged in detail and interpreted in terms of a series of upward-shallowing parasequences. The study focused on the upper 250 ft of

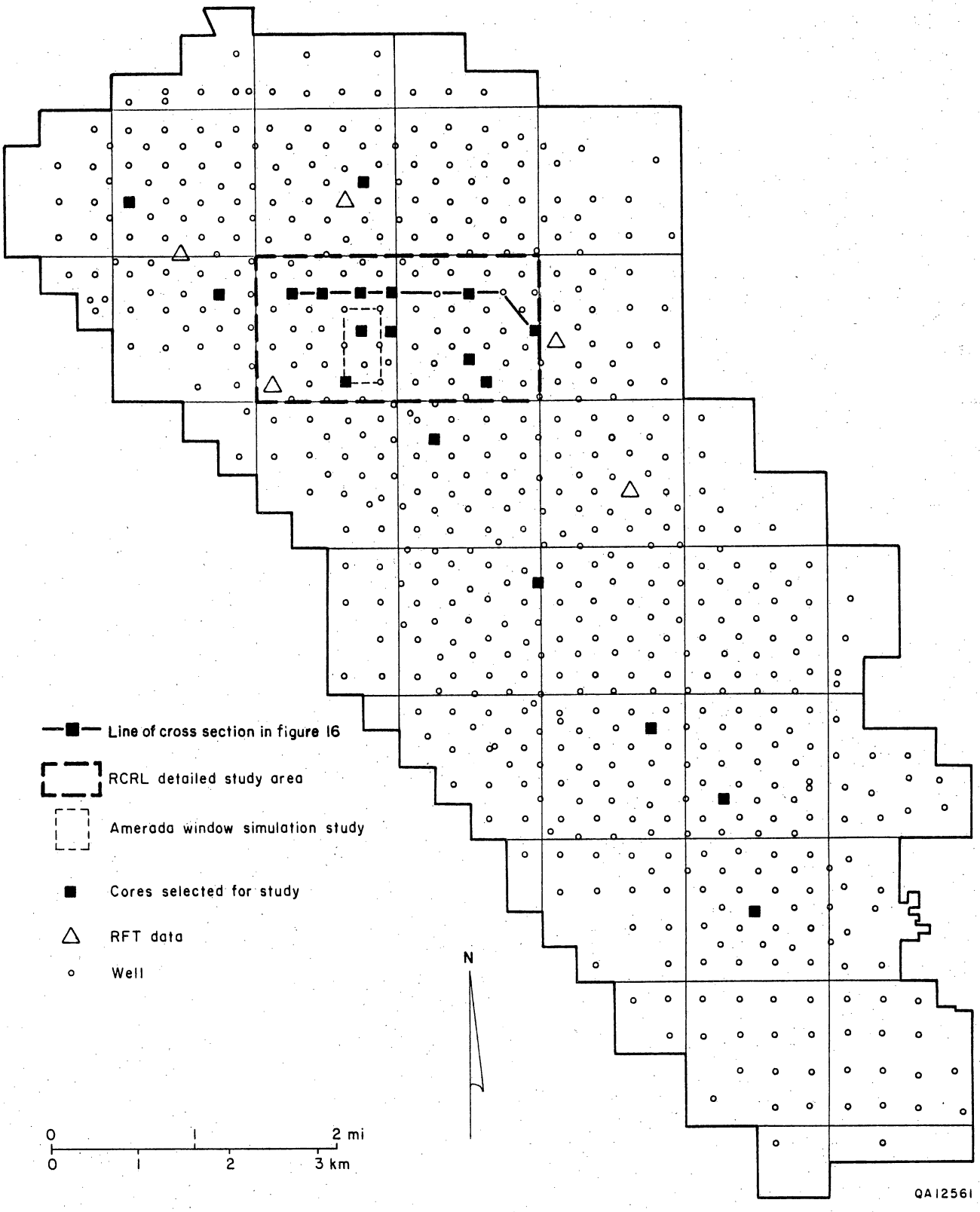

Figure 15. Well location map of Seminole San Andres Unit indicating cores used in this study and the two-section area selected for detailed geologic/petrophysical analysis. Detailed cross section in figure 16 also shown.

the Seminole reservoir because lower parasequences in the fusulinid-dominated section showed little rock-fabric variability. Cores were described on a foot-by-foot basis and linked to well log response (mainly gamma ray) before, during, and after core description. Through an iterative process of description and correlation, 11 parasequences were confidently identified in cored and uncored wells both in the detailed study area and on the reservoirwide cross section (fig. 16).

The lower three parasequences (10 through 12) are 20- to 30-ft-thick units containing dense moldic fusulinid-peloid wackestone/packstone coarsening upwards into skeletal-preserved crinoid-fusulinid-peloid packstone/grain-dominated packstone. The coarser grained upper portion of these parasequences typically displays high porosity values. However, little relationship between depositional fabric and permeability is seen in the fusulinid-dominated parasequences because the coarse dolomite-crystal size of the muddy matrix in these lower parasequences precludes a control by depositional fabric (see Lucia, this report).

Parasequences 6, 8, and 9 are transitional between the outer ramp fusulinid-dominated lower parasequences (10 through 12) and the inner ramp tidal-flat capped parasequences (1 through 5). They display laterally variable internal facies mosaics that include ramp-crest grain-dominated packstone to grainstone fabrics comparable to those of ps1/uSA1 at Lawyer Canyon. True crossbedded ooid grainstones are rare, however, and thick single-cycle grainstone bars such as ps9/uSA1 of Lawyer Canyon are not observed in the detailed section study area. Seminole parasequence 6 does show marked thickening of its grainstone facies in a southerly direction from 2 ft in the north to 20 ft about 5 mi south along the north-northwest fieldwide cross section.

Another difference between the Seminole ramp-crest grain-rich parasequences and their equivalents on the outcrop is the absence in the former of thick basal mudstone/peloid wackestone flooding surfaces. Instead, fusulinid-peloid wackestone/packstone typically marks parasequence flooding surfaces. This is significant for the flow-modeling perspective because

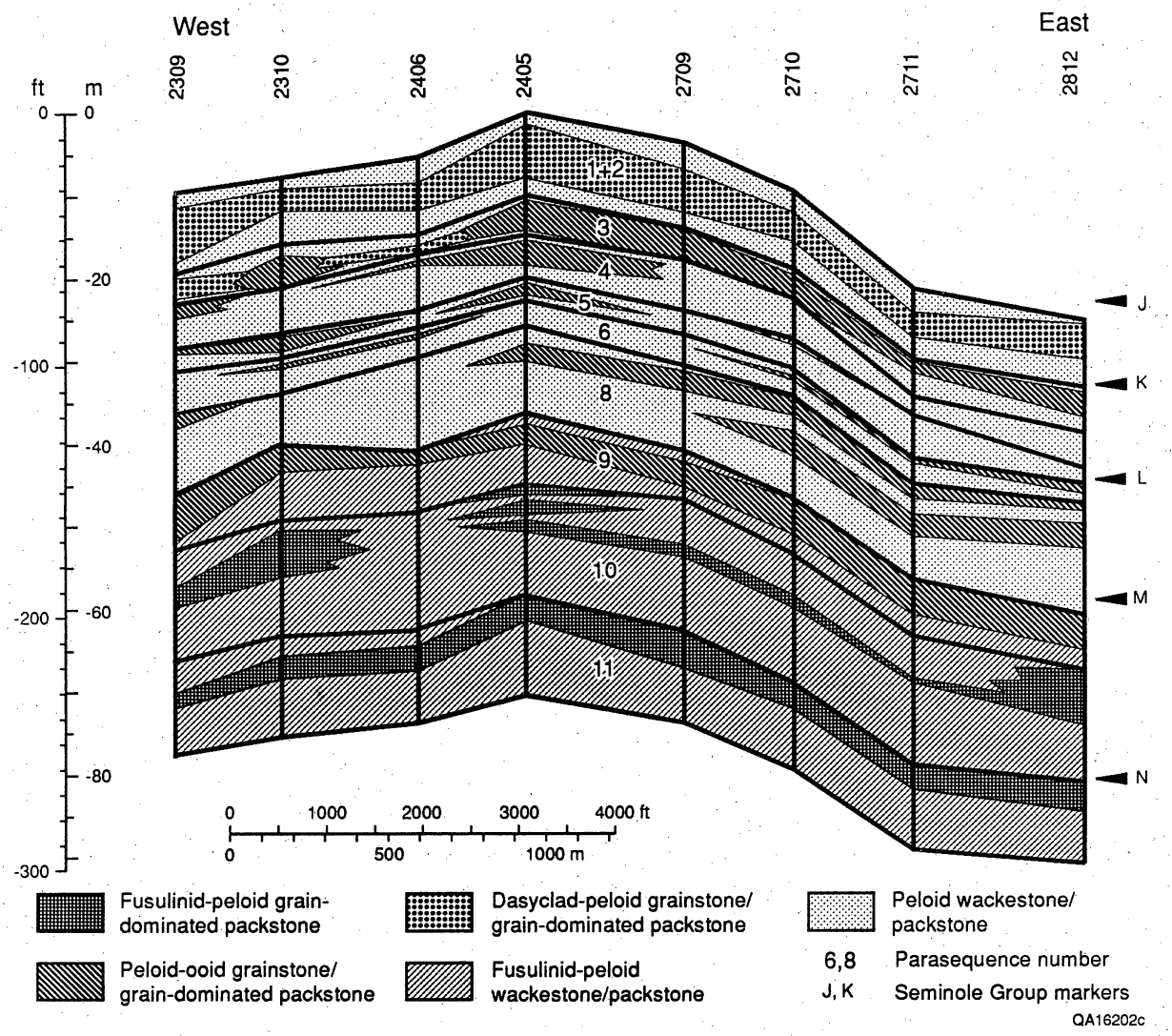

Figure 16. Simplified geologic west-east cross section through the detailed study area based on core data only. High-energy grain-dominated packstones and grainstones are indicated for both outer ramp and ramp-crest parasequences. Note upward thinning of parasequences. Line of section shown in figure 15.

some of the Seminole wackestone/packstones have moderate permeabilities and thus do not all act as flow barriers, as do those described at Lawyer Canyon.

The upper five parasequences (1 through 5) are thinner (5 to 20 ft) inner ramp units that all aggrade at least locally into fenestral peritidal deposits. Parasequences 2 through 5 have thin, laterally discontinuous grainstone intervals and are therefore analogous to Lawyer Canyon parasequences uSA1 ps3 and 5. Extension of detailed mapping outside the detailed two-section study area will probably demonstrate these upper parasequences to be most heterogeneous and therefore least efficiently swept. Tracing these upper parasequences from the detailed study area southward demonstrated that the top of porosity moved downward so that in the detailed study area it was at the top of ps1, whereas 3 mi south it was at the top of ps3.

CONCLUSIONS

Outcrop analysis for evaluating styles and scales of reservoir heterogeneity of the San Andres Formation has demonstrated that the most effective way to characterize these complex and heterogeneous carbonates is through a combination of regional and highly detailed descriptions at sequence and parasequence scales. The parasequence approach is particularly useful for providing a meaningful framework for describing facies variability on the scale of tens to hundreds of feet laterally and from 1 ft to tens of feet vertically. Specific results of the outcrop analysis are:

(1) The San Andres Formation of the Algerita Escarpment is divided into at least five sequences. The lower to middle San Andres is still considered a third-order sequence (lmSA1) as indicated by Sarg and Lehmann (1986). The upper San Andres third-order sequence is now divided into four fourth-order sequences (uSA1–uSA4). The lmSA1 sequence is strongly aggradational, whereas upper San Andres sequences become increasingly progradational upwards and have 3- to 5-mi basinward shifts in ramp-crest position between highstands.

(2) Within the sequence framework, subdividing geologic facies on the scale of tens to hundreds of feet laterally (interwell scale for most San Andres and Grayburg reservoirs) is most efficient using a parasequence framework.

(3) Nine parasequences averaging 20 ft in thickness could be mapped continuously across the Lawyer Canyon upper San Andres ramp-crest parasequence window (140 ft by 2,600 ft). Each parasequence recorded a distinct episode of flooding and aggradation. Within these parasequences the bar-crest and bar-flank facies showed best reservoir quality and marked lateral variability in thickness.

(4) In the Lawyer Canyon middle San Andres outer ramp parasequence window 15 upward-shallowing, upward-coarsening parasequences 15 to 40 ft thick were continuous across the 1,800-ft lateral dimension of the study area. The lower 10 parasequences were defined largely by subtle changes from wackestone to packstone, whereas the upper 5 have distinctive mud-rich wackestone to mudstone bases and packstone to grain-dominated packstone caps.

(5) Outer ramp parasequences of the Irabarne Tank upper San Andres parasequence window are comparable to those at Lawyer Canyon, consisting of fusulinid wackestones and packstones. These parasequences were deposited on an outer ramp surface that dipped 1 to 2 degrees basinward, but little change in depositional texture could be observed within parasequences across the 1,300-ft study area.

The geologic characterization methods developed in the outcrop phase of the study and used at the Seminole San Andres Unit showed that the parasequence framework could be used to develop a detailed genetically based zonation that uses both geologic facies and key log markers to subdivide the reservoirs. Specific conclusions related to the geologic part of the Seminole study are:

(1) The sequence-stratigraphic framework of the Seminole San Andres is comparable to that developed along the Algerita Escarpment, including development of a thick lower to middle San Andres sequence (minimum 850 ft) followed by a rapidly shallowing succession of

parasequences (800 ft) that are the record of the four upper San Andres sequences of the outcrop model.

(2) The 250-ft main pay interval contains 11 upward-shallowing parasequences that together define an upward-shallowing, upward-thinning parasequence set. This parasequence set probably contains parts of at least two of the San Andres sequences defined in outcrop, probably the uppermost lmSA1 and the uSA1.

(3) Greatest lateral heterogeneity of facies appears in the upper five parasequences of the reservoir, where grain-dominated intervals less than 1 to 20 ft thick are commonly not continuous for more than one or two well spacings.

REFERENCES

Bebout, D. G., Lucia, F. J., Hocott, C. R., Fogg, G. E., and Vander Stoep, G. W., 1987, Characterization of the Grayburg reservoir, University Lands Dune field, Crane County, Texas: The University of Texas at Austin, Bureau of Economic Geology Report of Investigations No. 168, 98 p.

Boyd, D. W., 1958, Permian sedimentary facies, central Guadalupe Mountains, New Mexico: New Mexico Bureau of Mines and Mineral Resources Bulletin 49, 100 p.

Craig, D. H., 1988, Caves and other features of Permian karst in San Andres Dolomite, Yates field reservoir, West Texas: *in* James, N. P., and Choquette, P. W., eds., Paleokarst: New York, Springer-Verlag, p. 342–363.

Goldhammer, R. K., Dunn, P. A., and Hardie, L. A., 1990, Depositional cycles, composite sea-level changes, cycle stacking patterns, and the hierarchy of stratigraphic forcing:

examples from Alpine Triassic platform carbonates: Geological Society of America Bulletin, v. 102, p. 535–562.

Harris, P. M., Dodman, C. A., and Bliefnick, D. M., 1984, Permian (Guadalupian) reservoir facies, McElroy field, West Texas, *in* Harris, P. M., ed., Carbonate sands—a core workshop: Society of Economic Paleontologists and Mineralogists Core Workshop No. 5, p. 136–174.

Hayes, P. T., 1964, Geology of the Guadalupe Mountains, New Mexico: U.S. Geological Survey Professional Paper 446, 69 p.

Hindrichs, P. D., Lucia, F. J., and Mathis, R. L., 1986, Permeability and reservoir continuity in Permian San Andres shelf carbonates, Guadalupe Mountains, New Mexico, *in* Moore, G. E., and Wilde, G. L., eds., Lower and middle Guadalupian facies, stratigraphy, and reservoir geometries, San Andres–Grayburg Formations, Guadalupe Mountains, New Mexico and Texas: Society of Economic Paleontologists and Mineralogists, Permian Basin Section, Publication No. 86-25, p. 37–47.

James, N. P., 1977, Facies models 8; shallowing upward sequences in carbonates: Geoscience Canada, v. 4, p. 126–136.

King, P. B., 1948, Geology of the southern Guadalupe Mountains, Texas: U.S. Geological Survey Professional Paper 480, 183 p.

Longacre, S. A., 1980, Dolomite reservoirs from Permian biomicrites, *in* Halley, R. B., and Loucks, R. G., eds., Carbonate reservoir rocks: Society of Economic Paleontologists and Mineralogists Core Workshop No. 1, p. 105–117.

Lucia, F. J., 1983, Petrophysical parameters estimated from visual descriptions of carbonate rocks: a new field classification of carbonate pore space: Journal of Petroleum Technology, v. 35, p. 629–637.

Moore, G. E., and Wilde, G. L., eds., 1986, Lower and middle Guadalupian facies, stratigraphy, and reservoir geometries, San Andres–Grayburg Formations, Guadalupe Mountains, New Mexico and Texas: Society of Economic Paleontologists and Mineralogists, Permian Basin Section, Publication No. 86–25, 144 p.

Ruppel, S. C., and Cander, H. S., 1988, Effects of facies and diagenesis on reservoir heterogeneity: Emma San Andres field, West Texas: The University of Texas at Austin, Bureau of Economic Geology Report of Investigations No. 178, 67 p.

Sarg, J. F., and Lehmann, P. J., 1986, Lower-middle Guadalupian facies and stratigraphy, San Andres–Grayburg Formations, Permian Basin, Guadalupe Mountains, New Mexico, *in* Moore, G. E., and Wilde, G. L., eds., Lower and middle Guadalupian facies, stratigraphy and reservoir geometries, San Andres–Grayburg Formations, Guadalupe Mountains, New Mexico and Texas: Society of Economic Paleontologists and Mineralogists, Permian Basin Section Publication No. 86-25, p. 1–36.

Sonnenfeld, M. D., 1990, High-frequency carbonate/siliciclastic reciprocal sedimentation within the upper San Andres depositional sequence (Permian, Guadalupian), Last Chance Canyon, Guadalupe Mountains, New Mexico (abs.): American Association of Petroleum Geologists Bulletin, v. 74, p. 768.

Van Wagoner, J. C., Posamentier, H. W., Mitchum, R. M., Jr., Vail, P. R., Sarg, J. F., Loutit, T. S., and Hardenbol, J., 1988, An overview of the fundamentals of sequence stratigraphy and

key definitions, *in* Wilgus, C. K., Hastings, B. S., Kendall, C. G. St. C., Posamentier, H. W., Ross, C. A., and Van Wagoner, J. C., eds., Sea-level changes: an integrated approach: Society of Economic Paleontologists and Mineralogists Special Publication No. 42, p. 39–46.

Wilson, J. L., 1975, Carbonate facies in geologic history: New York, Springer-Verlag, 471 p.

OUTCROP/SUBSURFACE CORRELATIONS: ALGERITA ESCARPMENT STUDY AREA, OTERO COUNTY, NEW MEXICO

by H. Seay Nance

INTRODUCTION

Many Guadalupian-age petroliferous reservoirs in the West Texas–New Mexico Permian Basin produce from carbonate grainstone complexes. Carbonate sand bodies characteristically are deposited at or near shelf margins or proximal to carbonate ramp crests (Ball, 1967; Ahr, 1973; Markello and Read, 1982). These complexes comprise grain-rich rocks, deposited as shoals, generally encased in finer grained transgressive and off-shoal deposits.

Core was taken in the Lawyer Canyon study area (Guadalupe Mountains, Otero County, New Mexico) to (1) investigate three-dimensional parasequence geometries and lithologies for San Andres grainstone complexes, (2) evaluate effects of near-surface weathering, and (3) develop a suite of core and well-log data similar to that used in reservoir evaluations. The laterally extensive exposures of the upper San Andres ooid/peloid grainstone, peloid packstones and wackestones, and mudstones on the Algerita Escarpment provide an opportunity to determine sizes, shapes, and porosity/permeability distributions of reservoir-analogous lithologic units.

Reservoir Characterization Research Laboratory boreholes have been correlated with the nearby outcrop. These correlations enable comparison of outcrop parasequence features (for example, weathering effects, thickness, and facies variations) with the features of stratigraphically equivalent intervals in core. The correlations also allow mapping of some rock properties (thickness and texture) in the third dimension.

Cross sections and maps are presented of the nine upper San Andres parasequences (P1u–P9u) defined on the outcrop. To date, the middle San Andres interval has been less intensively investigated, and only a brief discussion of its features in core and a cross section between the

cores and outcrop are included. A regional cross section correlates the outcrop study interval across the Northwest Shelf and San Simon Channel with equivalent productive hydrocarbon-bearing intervals at the Seminole San Andres Unit (Gaines County, Texas) on the northern Central Basin Platform.

DATA AND METHODS

The data include 16 measured sections from the upper San Andres outcrop, 2 stratigraphically equivalent cores from the No. 1 and No. 2 Algerita wells that are approximately 1,000 ft east of the nearest outcrop measured section (X), and logs from these 2 wells (fig. 1). Also included is one measured section from the middle San Andres outcrop, 63 ft of uppermost middle San Andres core from No. 1 Algerita, and 225 ft of middle San Andres core from No. 3 Algerita (660 ft north of No. 1 Algerita). Core materials were analyzed for porosity and permeability by Rotary Engineers Laboratories, Midland, Texas.

For near-outcrop borehole correlations, Schlumberger Natural Gamma Ray tool (NGT) and Gamma Ray/Lithodensity tool (LDT) logs were acquired from the No. 2 and No. 3 Algerita and one outcrop gamma-ray log was acquired by using a Scintrex GAD-6 gamma-ray spectrometer coupled with a GSP-3 portable gamma-ray sensor. No geophysical logs were acquired from the No. 1 Algerita because of compromised borehole conditions. Additionally, 42 gamma-ray/porosity logs from Eddy and Lea Counties, New Mexico, and Gaines County, Texas, were used for regional correlation. Delineation of one of the San Andres shelf margins in New Mexico (fig. 2) was drawn on the basis of updip pinch-outs of Delaware Mountain sandstone or its stratigraphic equivalents as illustrated in published cross sections or measured sections. The shelf margin near Seminole field was interpreted from seismic data.

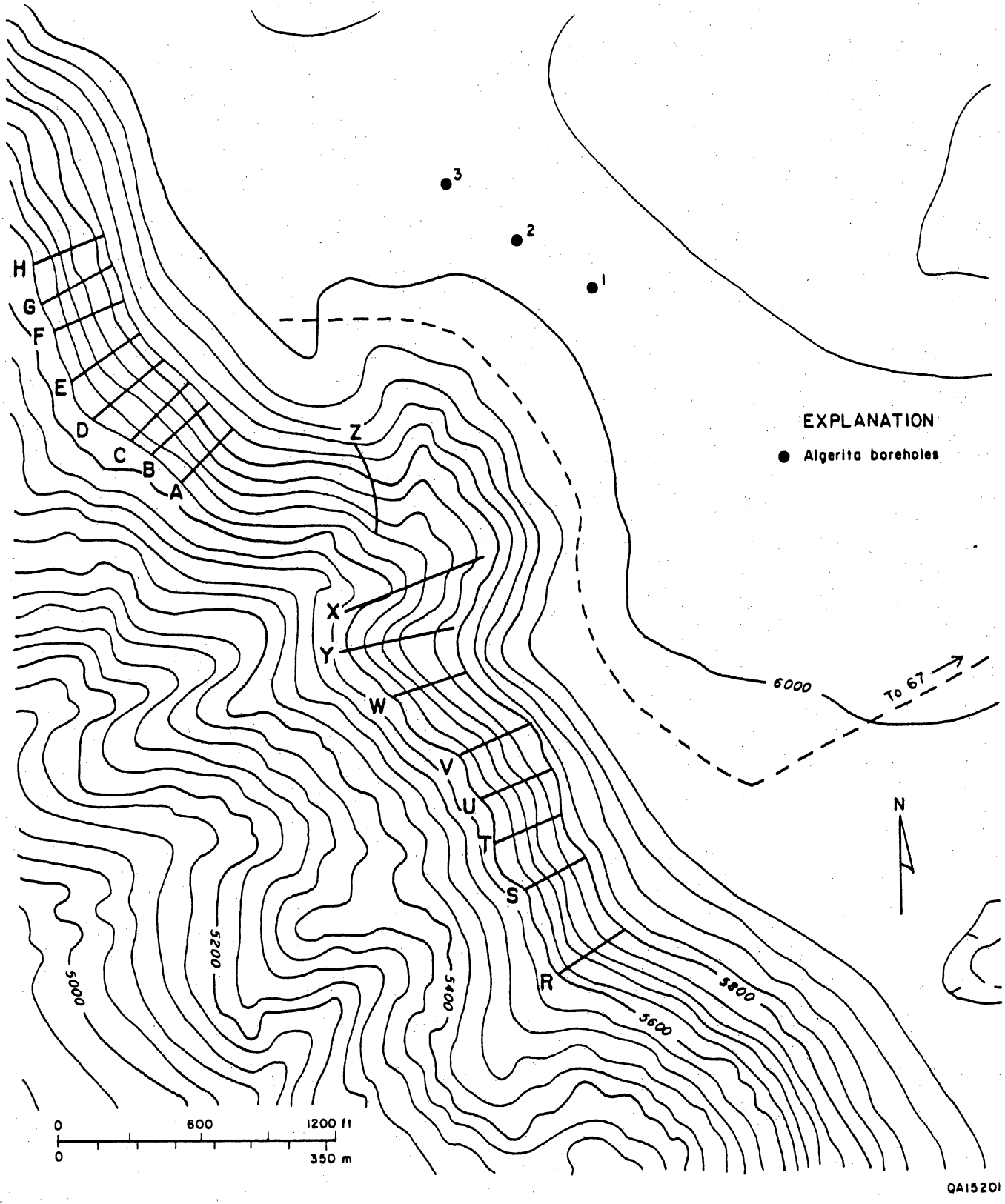

Figure 1. Location map for outcrop measured sections and exploratory boreholes, Algerita Escarpment study area.

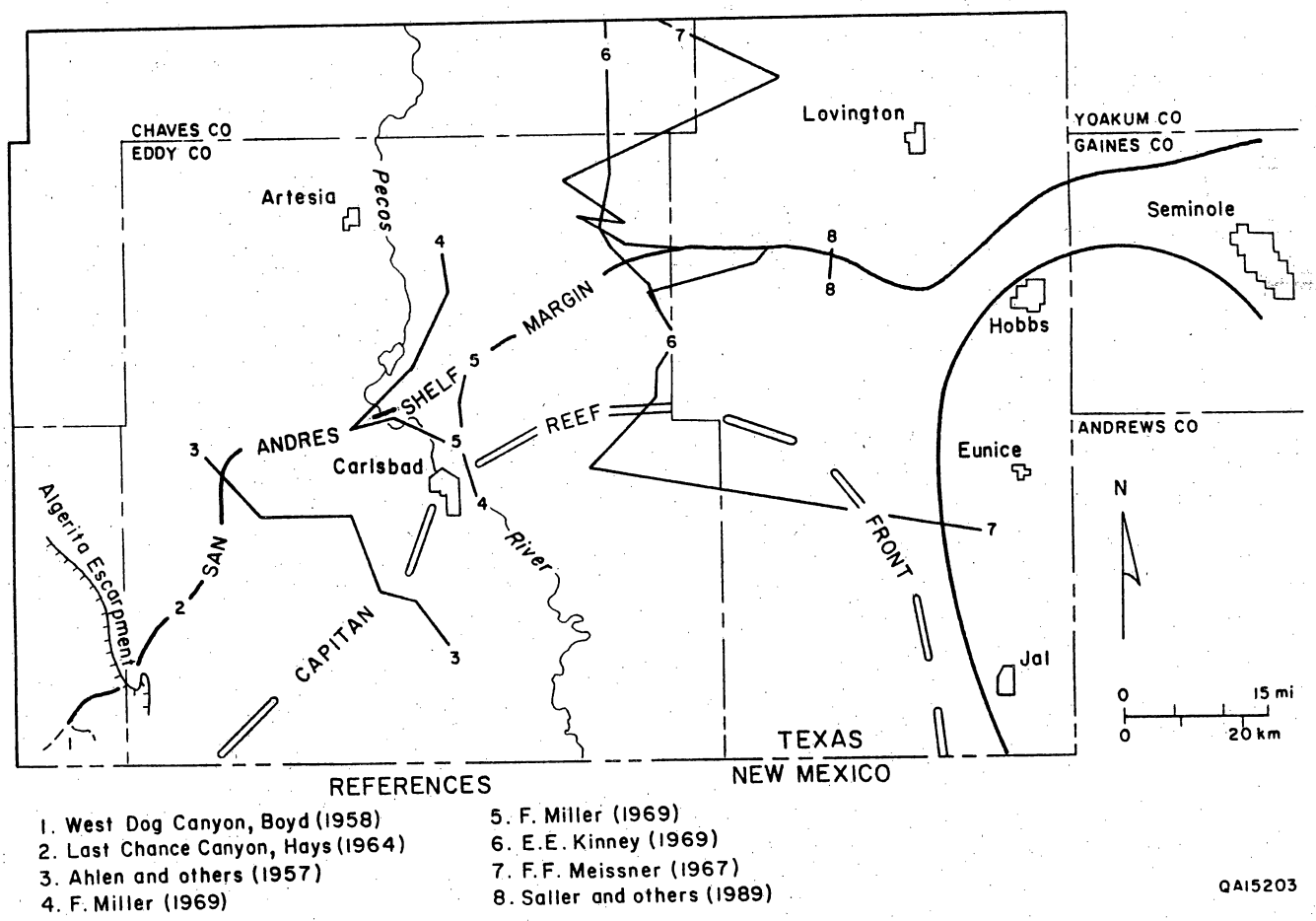

Figure 2. San Andres Shelf Margin (Sequence SA 2C). Based on pinch-outs of Delaware Mountain Sandstone equivalents shown on published measured sections and cross sections. Margin in Seminole area based on seismic data.

DRILLING HISTORY AND CORE SAMPLING

The No. 1 Algerita was cored March 27, 1989, to May 10, 1989, from the surface (approximately 100 ft below the top of the San Andres Formation) to 403 ft (uppermost middle San Andres Formation) by Byrl Binkley Drilling Company, using a slim-hole wireline coring rig and mud circulation. Core recovery (approximately 90 percent) and quality were generally insufficient for detailed analysis but were generally better than that of core recovered from subsequent boreholes (fig. 3). The continual need for water delivery to the site and repeated cementing of fractured intervals to maintain circulation resulted in excessive downtime and borehole conditions that precluded well logging. From the 350 ft of upper San Andres and 33 ft of middle San Andres core, 97 whole-core and 57 plug samples were tested for porosity and permeability.

The No. 3 Algerita was drilled and cored from August 30, 1989, to September 21, 1989, by W. Perry Smith Exploration/Homco Coring Services, using air-drilling methods. Air drilling was selected to avoid downtime experienced in the No. 1 Algerita and to provide a full-diameter (6.125-inch) uncemented borehole. Because the uppermost San Andres mudstone-dominated interval had been cored at the No. 1 Algerita and was not the focus of this study, the upper 170 ft of the No. 3 Algerita was not cored. When core recovery (less than 35 percent) and quality proved insufficient, the decision was made to drill from 270 to 370 ft (approximate base of the upper San Andres) and then resume coring in the middle San Andres. Middle San Andres recovery was better than 90 percent, with generally good quality (fig. 3). From the No. 3 Algerita core, 67 whole-core and 139 plug samples were tested for porosity and permeability. Only spectral gamma-ray and LDT logs were acquired because the borehole could not retain fluid for the operation of other logging tools.

The No. 2 Algerita was drilled to 606 ft from September 22, 1989, to October 12, 1989, by Smith/Homco. The section was cored from 170 ft (approximate top of the upper San Andres

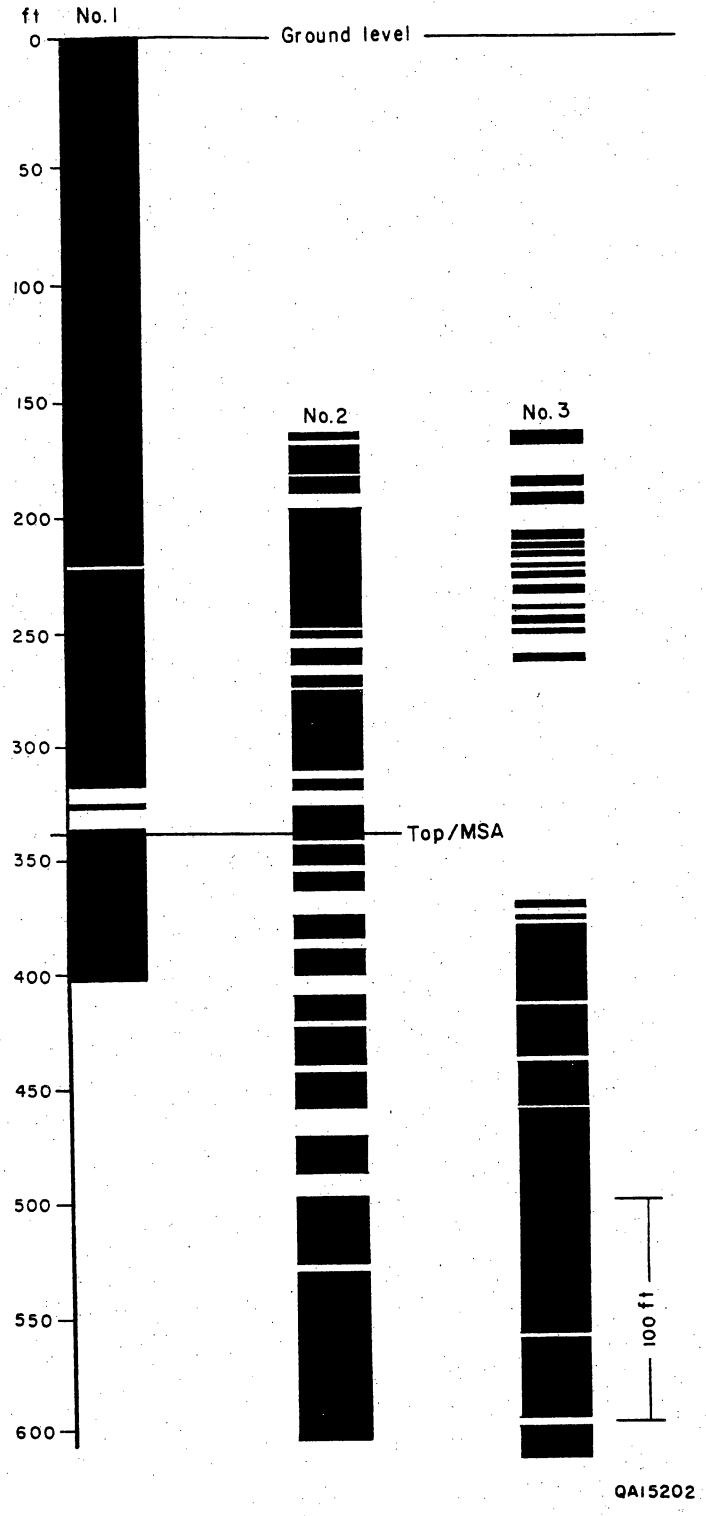

Figure 3. Core recovery at exploratory boreholes, Lawyer Canyon area.

grainstone complex) to 606 ft, the base of the middle San Andres fusulinid interval. Upper San Andres core recovery (81 percent, fig. 3) and quality were generally acceptable and of use for preparing basic lithologic cross sections and maps. The middle San Andres core was less well recovered (76 percent) and used only for porosity/permeability testing. From the No. 2 Algerita core, 25 whole-core and 187 plug samples were tested for porosity and permeability. Only spectral gamma-ray and LDT logs were acquired from this borehole.

Although the cores used for this study are approximately continuous, few of the core pieces fit together, suggesting that some sections are missing. Mudstones observed on the outcrop were severely fractured and most core loss was probably in finer grained rocks that jammed in the core barrel, preventing their complete recovery.

A summary of drilling/coring operations is listed in the table.

CORE DESCRIPTIONS AND PARASEQUENCE BREAKS

The descriptions of cores from the No. 1, No. 2, and No. 3 Algerita wells are shown in figures 4, 7, and 8. These descriptions and their relation to the outcrop are summarized in the following sections.

No. 1 Algerita

Upper San Andres

The No. 1 Algerita (fig. 4) was cored from ground surface to 403 ft. Rocks include dolomitic siltstone and sandstone, dolomudstones, pellet grainstone, packstone, wackestone, peloid dolograinstone, and fossiliferous peloid dolograinstone (fig. 5A–G). Core samples recovered from the No. 1 Algerita include an approximately continuous section of the upper San Andres minus most of parasequence 1 (P1u) and the basal part of P2u. The uppermost 63 ft of the middle San Andres was also recovered. An important regional marker bed, the Lovington Sandstone

Table. Summary of drilling and coring operations: Algerita exploratory boreholes.

Well	Co.	Method	Drilling dates	Interval drilled	Interval cored	Recovery	Logs
No. 1	Binkley	mud, 2.5 in. core	3/27/89 to 5/10/89	—	0–403 ft	90%	—
No. 2	Smith/ Homco	air, 6.5-in. hole, 4-in. core	9/22/89 to 10/12/89	0–165 ft	165–606 ft	77%	NGT, GR/LDT
No. 3	Smith/ Homco	air, 6.5-in. hole, 4-in. core	8/30/89 to 9/21/89	0–170 ft 270–370 ft	170–270 ft 370–615 ft	39% 22%	NGT, GR/LDT

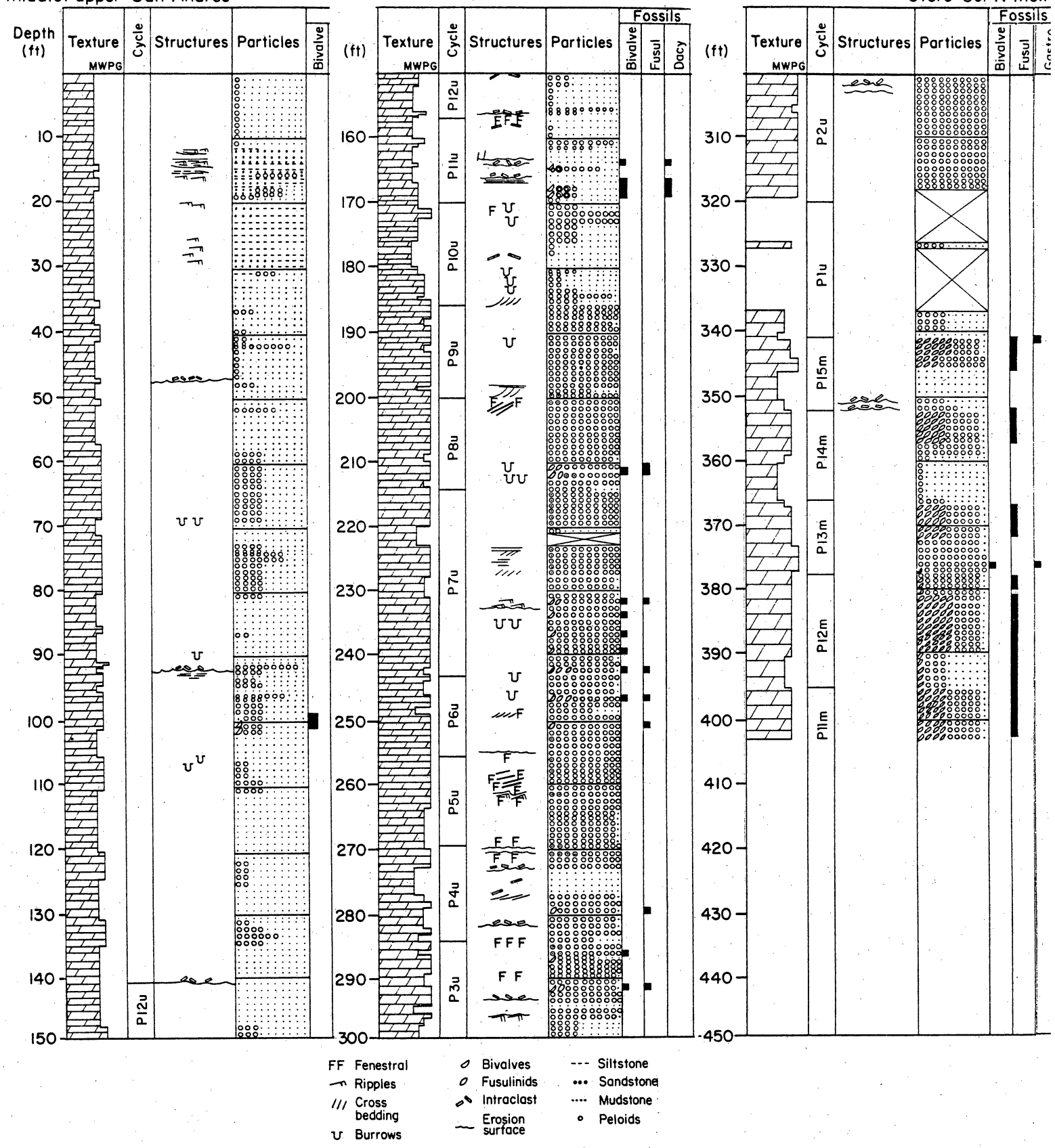

Figure 4. Core description, No. 1 Algerita.

Figure 5. Thin-section photomicrographs, No. 1 Algerita: A. Lovington Sandstone, 14.3 ft; B. mudstone-to-pellet wackestone, 8.8 ft; C. pellet grainstone, 105.6 ft; D. peloid packstone, 266.7 ft, P5u; E. peloid grainstone, 210.6 ft, P8u; F. oo-peloid grainstone, 212.1 ft, P8u; G. peloid grainstone, 197.2 ft, P3u; H. moldic skeletal peloid grainstone, 236.8 ft, P7u. Long dimensions of photomicrographs are 2.8 mm.

Member of the San Andres Formation (Sheldon, 1954), was sampled at 10 to 30 ft (fig. 5A) In this core the Lovington Sandstone comprises dolomitic medium- to coarse-grained siltstone and very fine-grained, cross-laminated sandstone. From 30 to 184 ft the cored section is dominated by mudstones and wackestones. In places these rocks include evaporite molds, possible fecal pellets (fig. 5C), and mudstone rip-up clasts, suggesting deposition in lagoonal environments landward of grainstone shoal complexes. On the basis of the presence of fenestral fabrics, 157 to 185 ft has been divided into two parasequences (P10u and P11u). Parasequences composing the mud-rich lagoonal interval above P11u have not been delineated.

The base of the upper San Andres grainstone-dominated interval (185 to 341 ft) was selected at the top of middle San Andres fusulinid packstone. In addition to intercrystalline porosity, rocks in the No. 1 Algerita display interparticle and moldic porosity. Upper San Andres grainstones in the No. 1 Algerita, except for P7u, are dominated by interparticle porosity (fig. 5D–5G). P7u grainstone, however, is dominated by moldic porosity (fig. 5H). Pore types are discussed further in other chapters of this volume. Parasequence boundaries and criteria for their delineation are illustrated in figure 5.

In terms of grainstone abundance (on average the most porous and permeable facies), the seven continuously cored parasequences (P3u-P9u) have the following composition:

Parasequence	Grainstone content
P3u	53%
P4u	27%
P5u	64%
P6u	75%
P7u	76%
P8u	86%
P9u	83%

A few observations on the presence of several parasequences are pertinent:

1. Fenestral tidal caps present at the tops of P3u, P4u, and P8u on outcrop extend to No. 1 Algerita; generally thinner fenestral caps seen at the top of P7u and P9Au on outcrop are not found at the No. 1 Algerita; tidal caps exist within, not just at the top of, P3u and P5u.

2. P5u has 6 ft (43 percent) of fenestral strata in the upper half of the parasequence, with a possible exposure surface at the top that suggests a topographically elevated area developed at this well location during later phases of P5u deposition. Outcrop sections D and G have only 1 ft of fenestral cap at each location. Apparently, thicker tidal caps are not necessarily more laterally extensive.

3. P4u has the lowest relative abundance of grainstone and includes 4 ft (27 percent) of evaporite-mold-bearing mudstone, also observed on the outcrop, probably deposited in a restricted lagoon landward of shoals. P4u may record more upslope deposition than that recorded at this location for the other parasequences.

4. P9u rocks show no exposure surface in the core although the outcrop shows abundant evidence for exposure on top of P9u, with at least two onlapping parasequences above that surface. Although it is possible that core showing exposure was not recovered, karst on top of P9u is localized areally and only a few feet in lateral dimension on outcrop; a borehole is not expected to intersect such a feature.

Among the observations cited above, the most relevant to reservoir analysis are (1) the relatively local distribution of tidal-cap facies and (2) the localization of exposure features and the difficulty in identifying, in core, parasequences that onlap exposure surfaces. Correlation of tidal-flat caps observed in reservoir wells separated by as little as several hundred feet could cause errors in parasequence correlation. Similarly, without evidence of parasequence onlap, it is probable that two or more individual parasequences would be correlated as a single parasequence. This could result in interpretation of several separate productive intervals as a single laterally continuous interval.

Middle San Andres

The middle San Andres part of this core comprises 62 ft of dolomudstone, fusulinid peloid dolowackestone to dolopackstone, and dolograinstone. Parasequence breaks were made in core,

as on the outcrop, at major textural breaks. Middle San Andres parasequences in the study area include mudstones or wackestones at the base, and packstones to grainstones in their upper parts. Strata observed in this core include one incomplete and four complete parasequences, each consisting of basal mudstone to fusulinid peloid wackestone overlain by fusulinid peloid packstone to peloid grainstone. Middle San Andres parasequences in the No. 1 Algerita average 14 ft in thickness. Correlations (fig. 6) indicate that these parasequences are equivalent to middle San Andres parasequences P11m–P15m on the outcrop. The most significant aspect of these strata is that these parasequences change little in character or thickness from outcrop to borehole, a minimum distance of 1,200 ft.

No. 2 Algerita

Upper San Andres

The No. 2 Algerita (fig. 7) was cored from 165 to 614 ft and includes a partial section of upper San Andres grainstone-dominated strata as well as an incomplete middle San Andres section. Recovery of the upper San Andres interval was sufficient for parasequence identification, however. Recovery of the middle San Andres interval was sufficient only for porosity/permeability testing.

Within the upper San Andres grainstone-dominated interval, the base of P1u (335.5 ft) was selected on the top of middle San Andres fusulinid-bearing rocks. The tops of P1u–P9u and criteria for their selection are illustrated in figure 7. Above P9u, 25 ft of mud-dominated strata from the upper San Andres lagoonal interval was recovered but was not delineated into parasequences.

Because of incomplete recovery of several of the parasequences, comparisons of grainstone content are not appropriate. However, observations of several of the parasequences are pertinent:

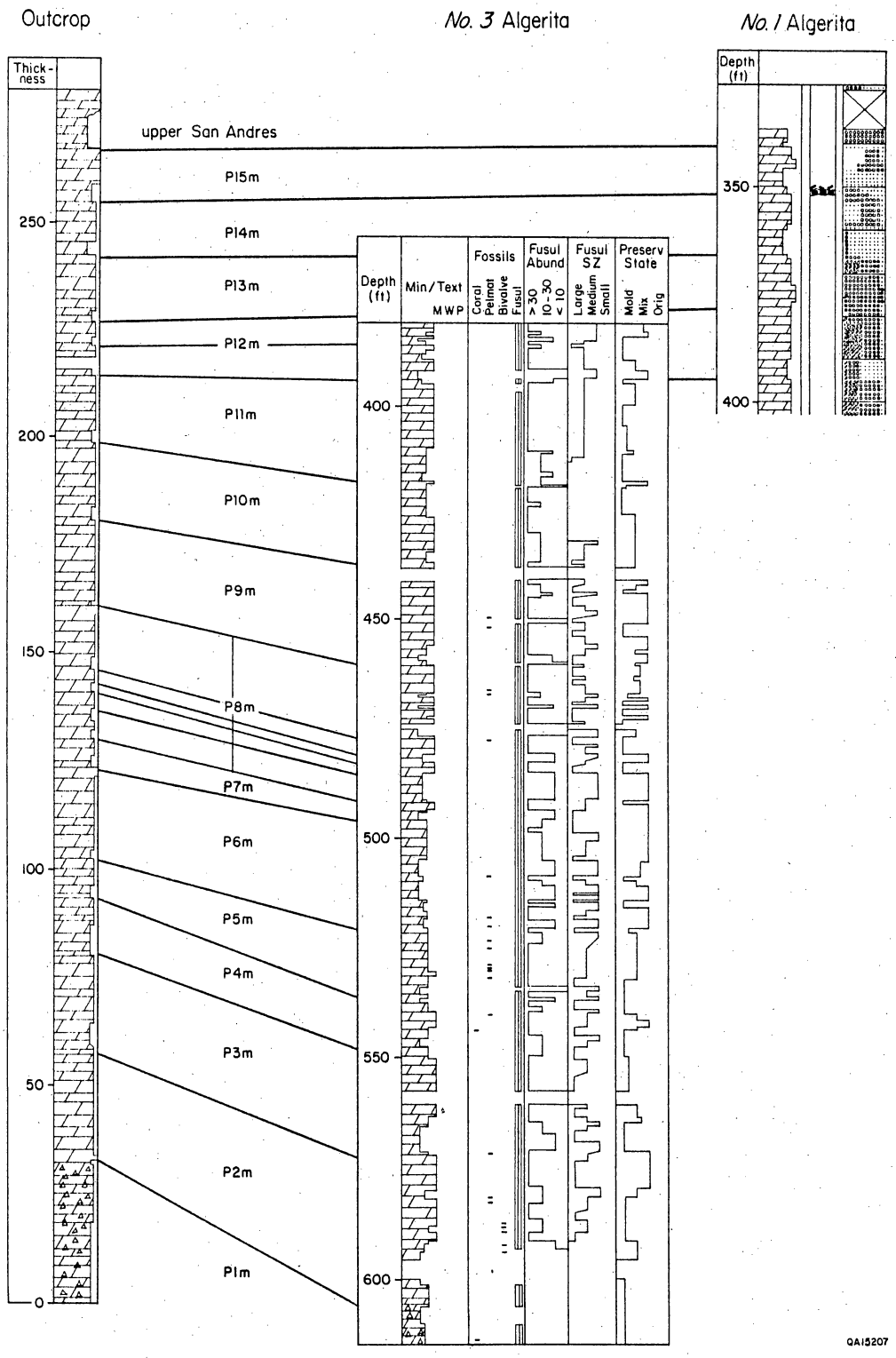

Figure 6. Lithologic correlation of 15 middle San Andres outcrop parasequences to No. 1 and No. 3 Algerita. Parasequences are laterally of consistent thickness and lithology.

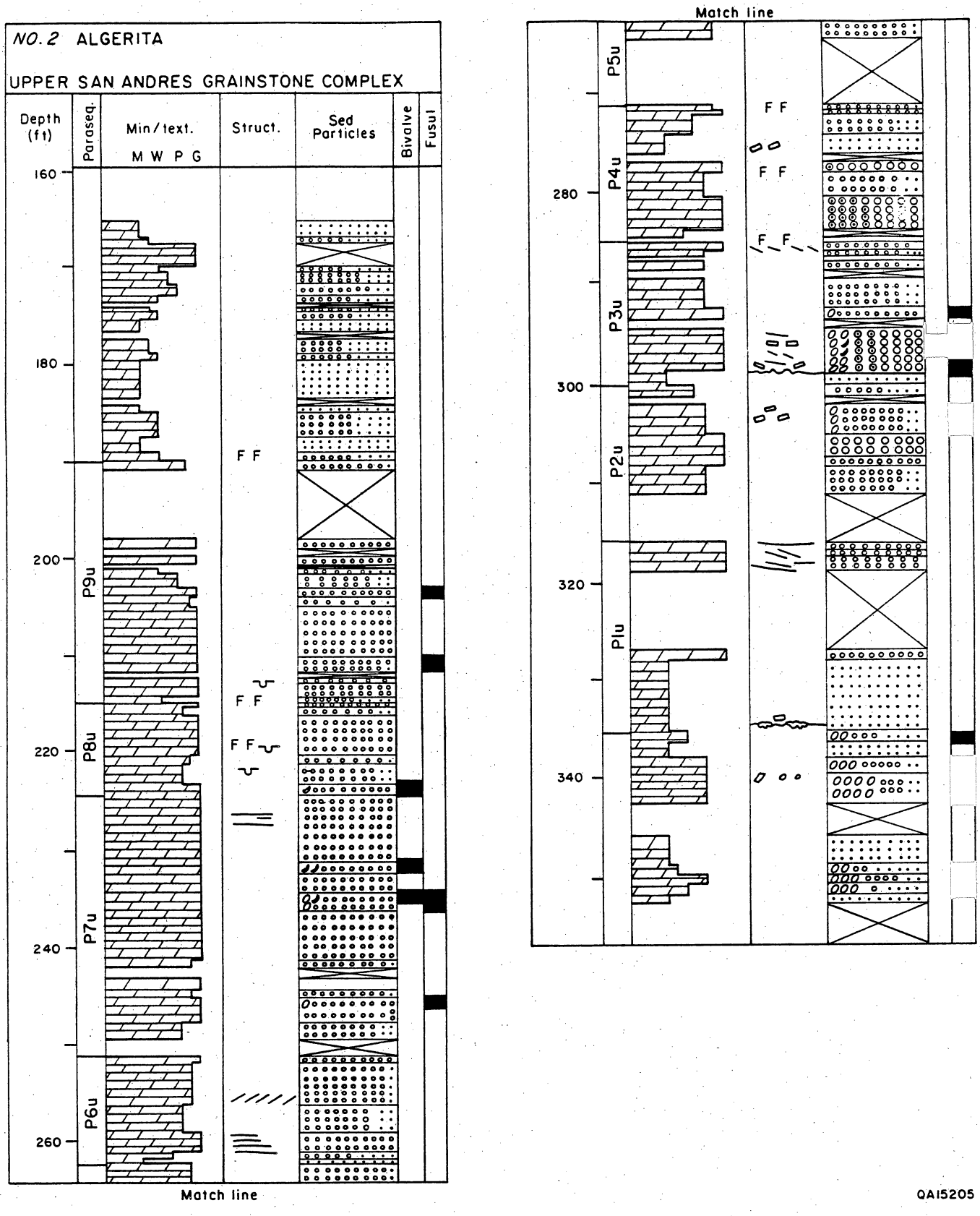

Figure 7. Core description, No. 2 Algerita.

1. The extensive fenestral caps found at the top of P3u, P4u, and P8u on outcrop and in the No. 1 Algerita extend to the No. 2 Algerita; P3u and P8u also have the thickest tidal-cap intervals on outcrop, suggesting that thicker tidal caps generally are more widespread than thinner caps, although the very local thick cap on the top of P5u is an exception.

2. The thick fenestral interval observed in P5u at the No. 1 Algerita was not identified at No. 2 Algerita; it was only 1 ft thick on the outcrop and at only one location (section D). Apparently the interpreted topographic high associated with the fenestral tidal cap was a very local feature (around the No. 1 Algerita), or it extended from the study area to locations not investigated.

3. P4u includes 2 ft of recovered evaporite-mold-bearing mudstone of probable lagoonal origin similar to that seen in P4u at the No. 1 Algerita and also observed on the outcrop.

No. 3 Algerita

Middle San Andres

Only the middle San Andres fusulinid-bearing interval was sufficiently recovered at the No. 3 Algerita (fig. 8) for study. This core comprises dolomudstone, and fusulinid peloid dolowackestone, dolopackstone, and dolograinstone arranged in upward-coarsening para-sequences similar to those observed on the outcrop.

Middle San Andres core recovery was 95 percent and extended nearly to the base of the fusulinid interval. Depositional components were easier to observe than on the outcrop, probably because the outcrop was proximal to faults and suffered extensive fracturing. For these reasons this core was described in greater detail than either the outcrop or equivalent core from the No. 1 Algerita. Descriptions of the core as grainstone, packstone, wackestone, and mudstone were based upon examination with a binocular microscope and reflect the relative ease with which component allochems could be observed. Muddier rocks were interpreted where allochems were harder to detect, although differences in cementation might

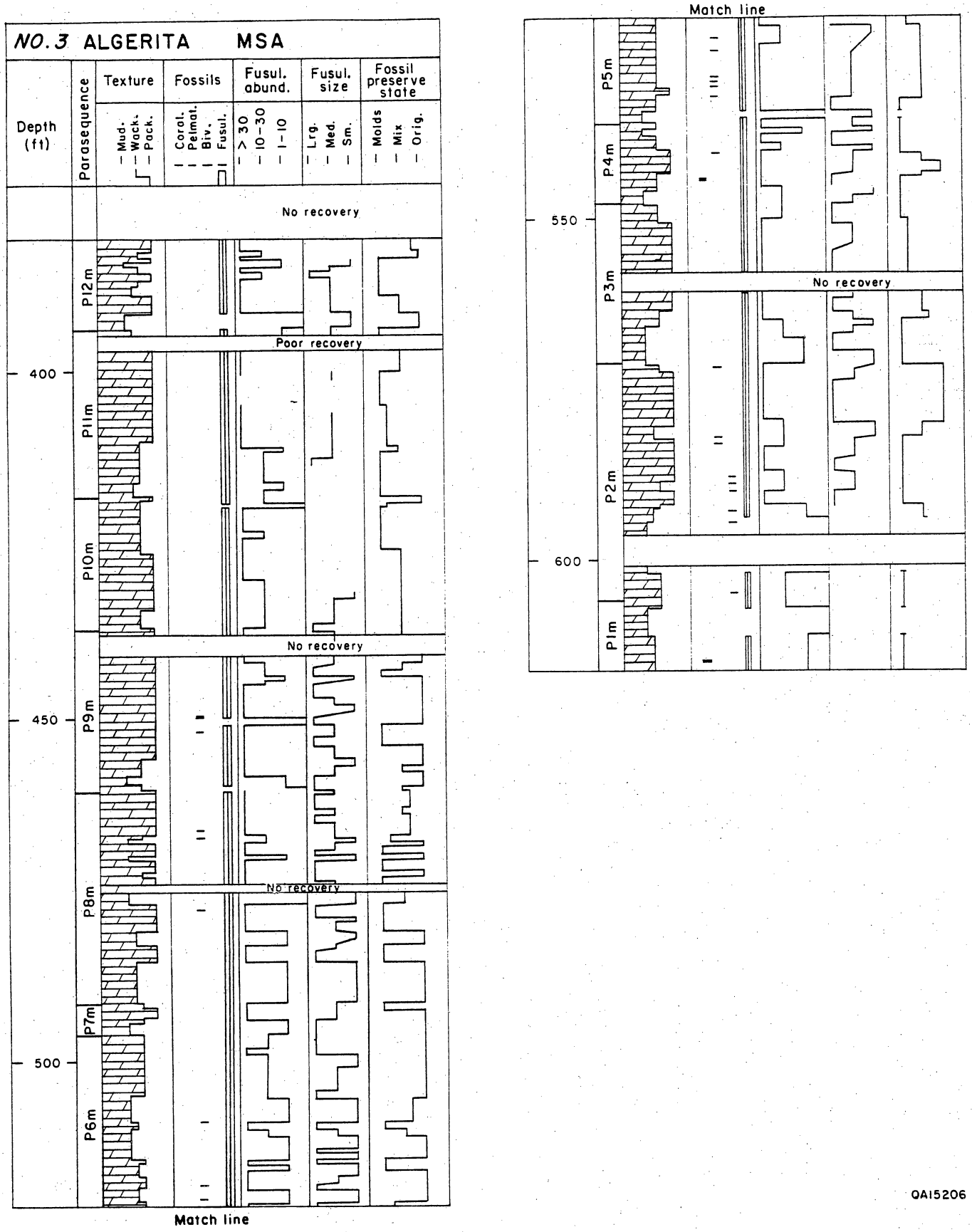

Figure 8. Core description, No. 3 Algerita.

have similar effects. Rigorous thin-section analysis was not included in this investigation, although cursory examination of thin sections suggests compositions ranging mainly from mud-dominated packstone to wackestone. Many components that appear to be pellets or peloids in thin section may actually be the mud casts preserved after total dissolution of fusulinid tests. True mudstone beds probably are present only in the upper three parasequences of the middle San Andres.

Parasequence boundaries were selected in the core, as on the outcrop, at significant textural breaks in the vertical sequence. Where, in core, several textural breaks were observed in an outcrop-equivalent interval but which were not observed in outcrop, the textural break was chosen that best maintained the parasequence thickness observed in outcrop. The tops of the middle San Andres parasequences cored in this well and criteria for their selection are illustrated in figure 8.

In addition to texture, features described are the relative abundance, relative size, and the state of preservation of fusulinids in the core. In the core descriptions of preservation-state, the term "original" refers to preservation of both original material and calcite-filled molds. The mode of preservation of fusulinids is important because it relates directly to the distribution of moldic porosity. In a reservoir setting molds may contain a significant proportion of the hydrocarbons. No consistent trends in the state of preservation of fusulinids within parasequences is observed (fig. 8). Intervals dominated by given modes of preservation often transgress parasequence boundaries. In general, intervals dominated by moldic porosity are vertically separated from intervals dominated by interparticle porosity by transitional intervals characterized by mixed-porosity types.

Fusulinid length fell within a narrow range of 0.25 mm to 1 cm. Judgments on the relative sizes and abundance of fusulinids were based on visual estimates and averaging and thus were not quantitatively rigorous. Therefore, results of this survey are preliminary.

Fusulinids in this core tend to be fairly well sorted. With respect to abundance and size, finer grained rocks tend to have fewer and smaller fusulinids; only exceptionally do the smaller

fusulinids dominate in packstones. Overall, where smaller fusulinids dominate the fauna, they tend to be in low abundance. P6m, P7m, and the lower half of P8m are characterized by an overall smaller sized fusulinid than the other parasequences examined; these parasequences, along with P4m and P5m, are also the finest textured. This suggests that size and abundance of fusulinids result from hydraulic sorting; smaller fusulinids were probably winnowed from the total population and widely distributed in relatively calm water (hence, their lower abundance), whereas larger individuals accumulated in higher energy environments. The above considerations suggest that P4m, P5m, P6m, P7m, and the lower part of P8m in the study area were deposited in calmer environments than were the other parasequences. Given that fauna other than fusulinids are rare in P6m, P7m, and the lower part of P8m (possible drowning of former habitat), it may be that P4m through the lower part of P8m represent a temporary transgressive interlude in the development of the progradational fusulinid bank.

The most pertinent conclusion drawn from study of the middle San Andres is that the parasequences are remarkably continuous laterally, both in texture and thickness. Because of possible errors incurred in outcrop measurements due to structural dip variations, the small parasequence thickness changes observed in outcrop-to-core correlations are probably not significant.

OUTCROP-TO-CORE CROSS SECTIONS: UPPER SAN ANDRES PARASEQUENCES P3u–P9u

Core recovery from the No. 1 and the No. 2 Algerita was sufficient to identify parasequences correlative to those described on the outcrop. Figure 9 illustrates the facies distributions from outcrop sections X and Y to borehole cores within P3u–P9u.

Several conclusions about lateral continuity of upper San Andres parasequences can be made. Parasequences P1u–P8u show thickness changes of 0 to 57 percent over the 1,400 ft between outcrop section Y and the borehole (No. 1 Algerita), averaging 16.2 percent overall (fig. 9). P6u and P9u show the greatest thickness changes of 57 and 53 percent, respectively.

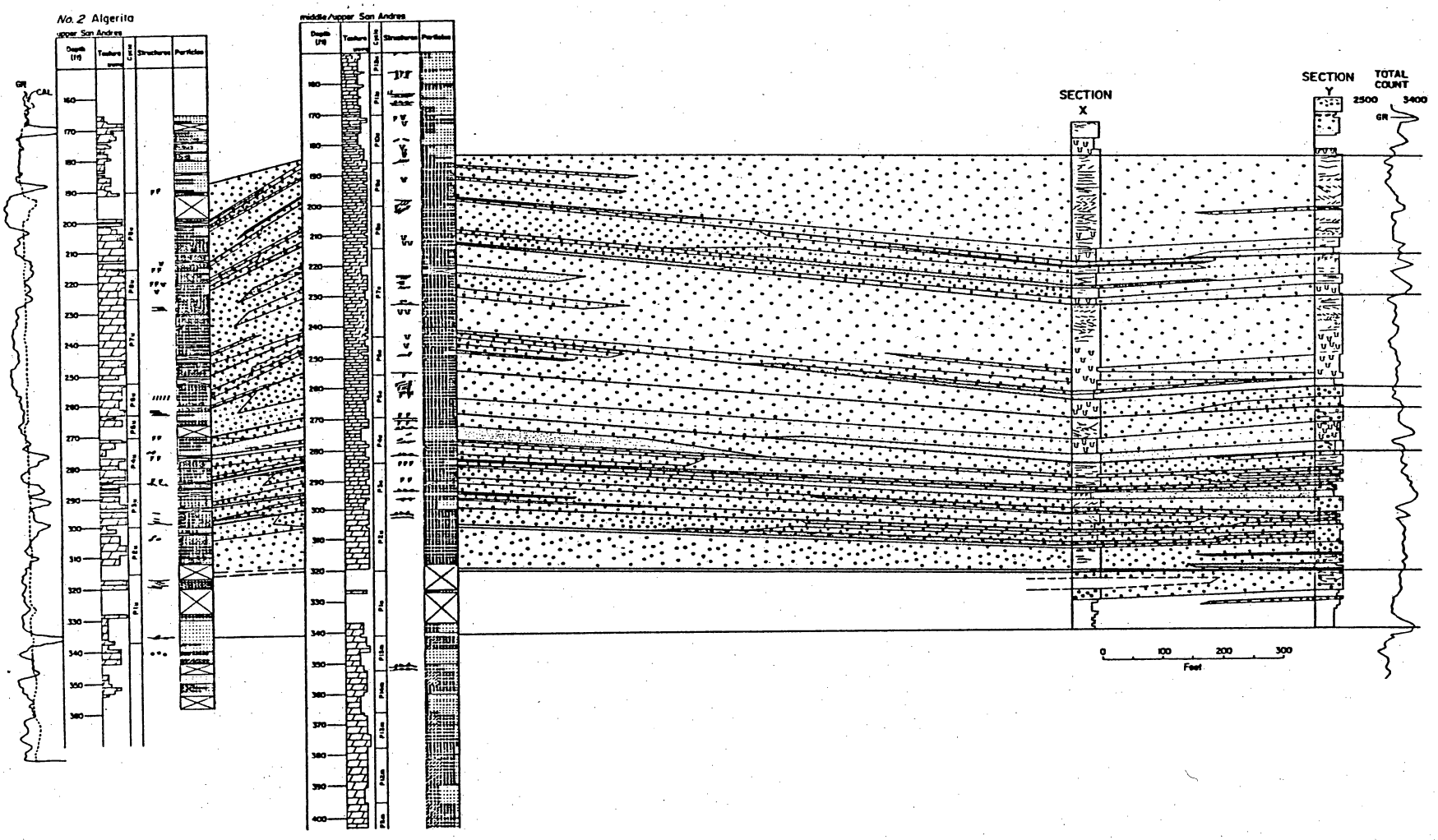

Figure 9. Outcrop borehole parasequence correlations. Parasequences are finer grained at bases and coarsen upwards. Note exception where parasequence 6 grainstone overlies parasequence 5 grainstone at outcrop section Y and No. 1 Algerita.

Except for P6u and the basal 1 ft of P9u at the No. 1 Algerita, all parasequences comprise a basal finer grained interval overlain by coarser grained rocks. Fenestral tidal-flat strata are not always laterally discontinuous. Finally, grainstone intervals are generally continuous along strike between the boreholes and outcrop measured section X (1,000 ft). Exceptions include certain grainstone intervals in P3u and P7u, which pinch out between sections X and Y (about 1,400 ft from the No. 1 Algerita).

OUTCROP GAMMA-RAY PROFILE ACQUISITION AND CORRELATION TO ALGERITA BOREHOLES

Outcrop Gamma-Ray Profile

To support outcrop-to-borehole correlations, an outcrop gamma-ray profile was generated with a portable gamma-ray spectrometer. Outcrop section Y was selected for this exercise because of its relative proximity to the No. 1 Algerita (1,400 ft) and its excellent exposures of P1u–P9u. Sample points were spaced about 1 ft apart vertically. Reproducibility of gamma-ray values (total counts, irrespective of isotopic source) was tested by taking two measurements at each sampling location (fig. 10). Individual measurements of thorium, potassium, and uranium were not taken. Figure 10a comprises the first of the two readings; figure 10b comprises the lower values, and figure 10c comprises the higher of the two values measured at each location. This test showed that a single measurement at each point was sufficient for correlation.

The correlation between the resulting gamma-ray profile and section Y is shown in figure 11. Although not quantitatively rigorous, the gamma-ray curve (fig. 11) shows some correspondence to lithology. In general, the higher gamma-ray values correspond to shalier rocks, particularly at the base of P1u, the upper part of P3u and base of P4u, the base of P7u, the base and upper part of P8u, the base of P9Au and P9Bu, and in the interval overlying P9u. Notable exceptions are the increasing values upward through P1u that correspond to coarser grained rocks and the relatively low value of the mudstone at the base of P5u.

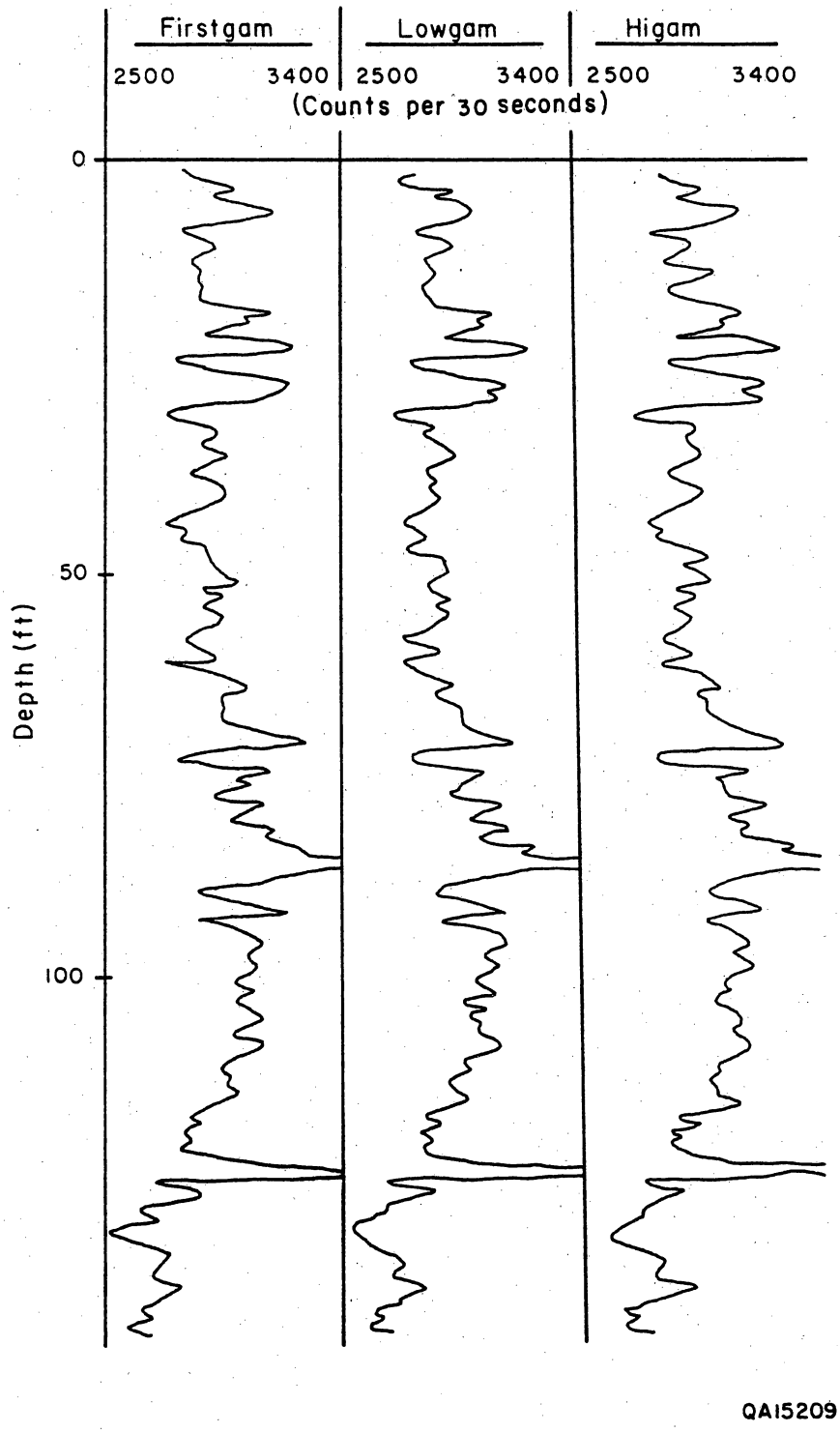

Figure 10. Outcrop gamma-ray profiles (raw data). Curves represent (a) first readings, (b) lower of two readings, and (c) higher of two readings. All curves are qualitatively similar and equally useful for correlations.

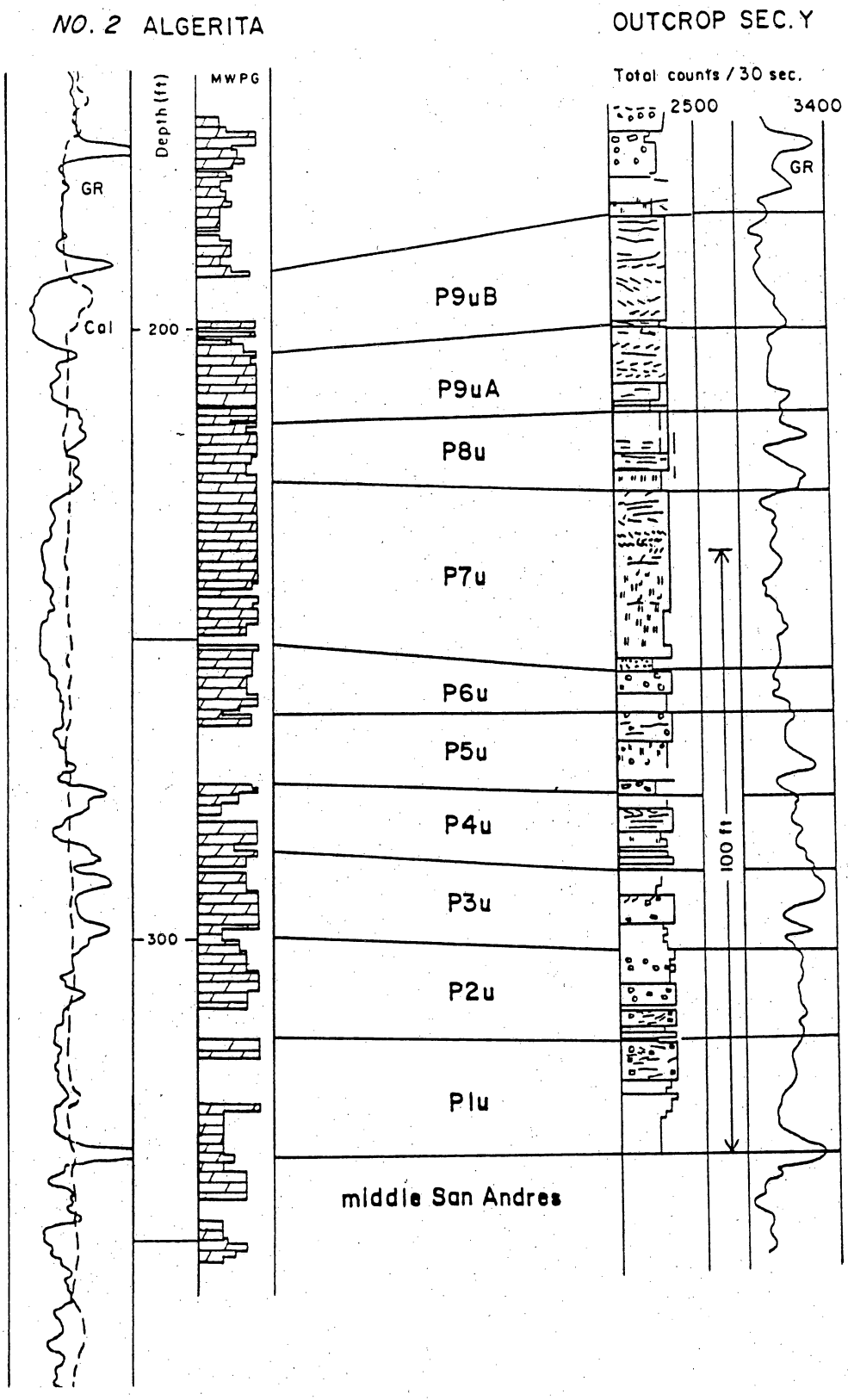

Figure 11. Correlations between outcrop gamma-ray profile, section Y, and gamma-ray log at No. 2 Algerita.

Correlation to Boreholes

The outcrop gamma-ray profile was correlated to the gamma-ray log at the No. 2 Algerita (fig. 11). Similarities between the outcrop profile and the borehole logs that lead to highest confidence in the correlation include the following: (1) the high value at the base of P1u; (2) relatively low values through P7u; (3) high values at the base and near the top of P8u; (4) the intermediate values associated with P9Au; (5) the high value at the base of P9Bu; and (6) the low values corresponding to the upper part of P9Bu.

The match between the outcrop profile and the borehole well logs is not perfect. This is to be expected because the distance between the outcrop and the borehole is 1,400 ft, and there is not even exact correspondence between the two borehole logs (the No. 2 and No. 3 Algerita, fig. 12), which are only 330 ft apart. Some of these differences reflect depositional and diagenetic heterogeneities between the different locations.

The LDT logs at the No. 2 and No. 3 Algerita resemble the "porosity log" prepared for No. 1 Algerita from core tests in only a general way. Most notable of these similarities is the high porosity of the Lovington Sandstone near the top of the core, the generally low porosities associated with the muddy lagoonal rocks in the upper 110 ft, the lower porosity in P2u, P3u, and P4u, the high porosity interval near the base of P7u, and the high porosity interval in P9u.

Correlations between the No. 2 and No. 3 Algerita are straightforward because the two gamma-ray logs are similar (fig. 12). It was possible with this limited three-dimensional control to produce fence diagrams and maps of the nine upper San Andres parasequences.

PARASEQUENCE DISTRIBUTION

The fence diagram (fig. 13) of the nine upper San Andres parasequences illustrates three-dimensional cross-sectional geometries and emphasizes the two porosity/permeability end

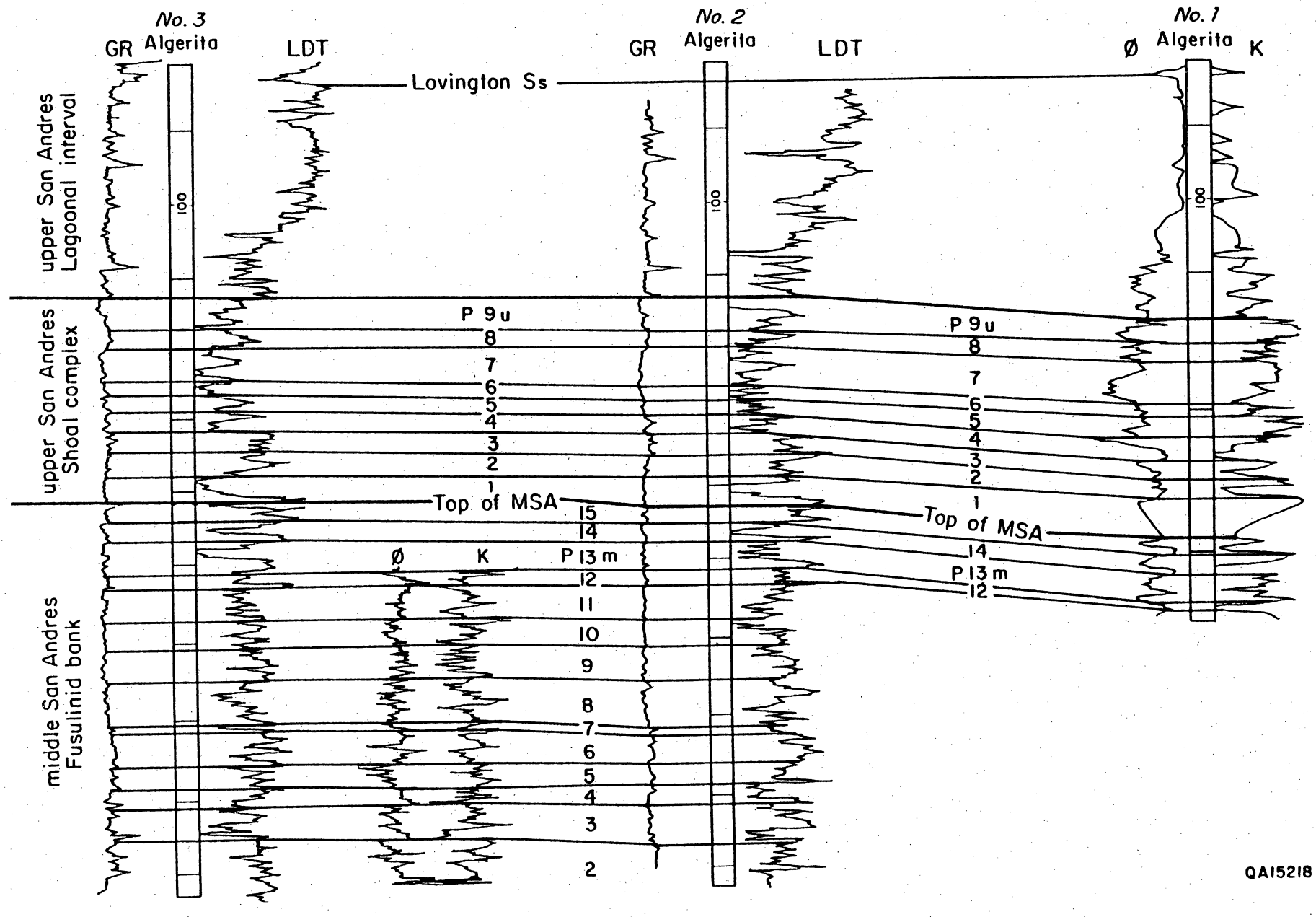

Figure 12. Parasequence correlations between borehole well logs at No. 2 and No. 3 Algerita and "porosity" log generated for No. 1 Algerita from irregularly spaced core tests. Results of core tests of middle San Andres strata correlated to those of No. 3 Algerita.

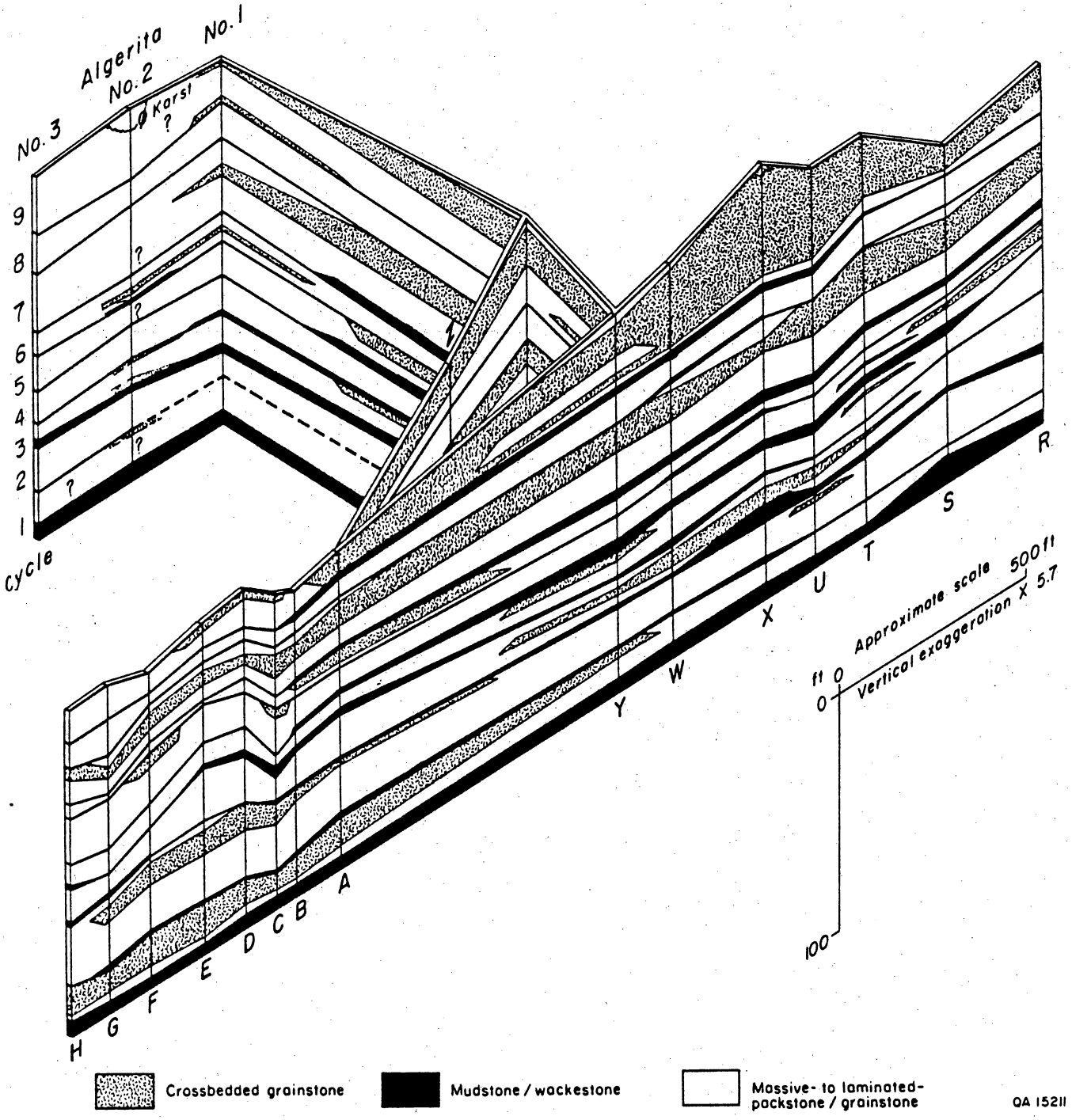

Figure 13. Fence diagram depicting three-dimensional parasequence thickness and distribution of basal mudstone/wackestone facies.

members among the several facies illustrated in the outcrop cross section (Kerans, this volume, pl. 2), namely, the tight basal mudstones/wackestones and relatively porous and permeable (on average) cross-laminated shoal-crest grainstones. Notable among the facies patterns in figure 13 is the extensiveness of the basal mudstone/wackestones and the limited lateral extent of shoal-crest grainstones. Interpretations of basal mudstones in parasequences 1 and 3 at the No. 3 Algerita (from which little upper San Andres core was recovered) are based on low porosity responses in LDT logs from the borehole. Other facies types show no reliable well-log signatures.

Parasequence isopach maps (fig. 14) are speculative. The best three-dimensional control is in the area bounded to the west by outcrop sections A–H and X–Z and to the east by the Algerita boreholes (fig. 1). Irregular contour intervals were used so that a maximum number of contour lines would pass through actual data points.

Most of the parasequence isopach maps show contour-pattern elongation parallel to interpreted depositional strike (fig. 2). Strike-elongate trends also are indicated in the net grainstone maps (fig. 15). If the strike-aligned geometries of San Andres parasequences and grainstone bodies shown in figures 14 and 15 are accurate, this may suggest deposition in an area dominated by onshore winds.

As mentioned before, net grainstone maps (fig. 15) show strike alignment of contours but grainstone thicks do not, in detail, correspond to thicks in the isopach maps. Grainstone distribution reflects higher energy conditions for their deposition than for deposition of the finer grained facies. Crossbedded grainstones at the tops of P5u and P6u probably indicate the final positions of high-energy shoal crests prior to sea-level fall and, as such, probably were topographic highs in the subtidal to intertidal environment. Net-grainstone thicks in P3u and P4u are not characterized by crossbedding and may be bioturbated inactive bars, carbonate sand deposits laterally adjacent to bars, or shelf sands unrelated to bars.

The strike-aligned projections shown on the net grainstone maps of P3u, P4u, P5u, and P6u superficially resemble features mapped on the Pleistocene Miami Oolite interpreted to be

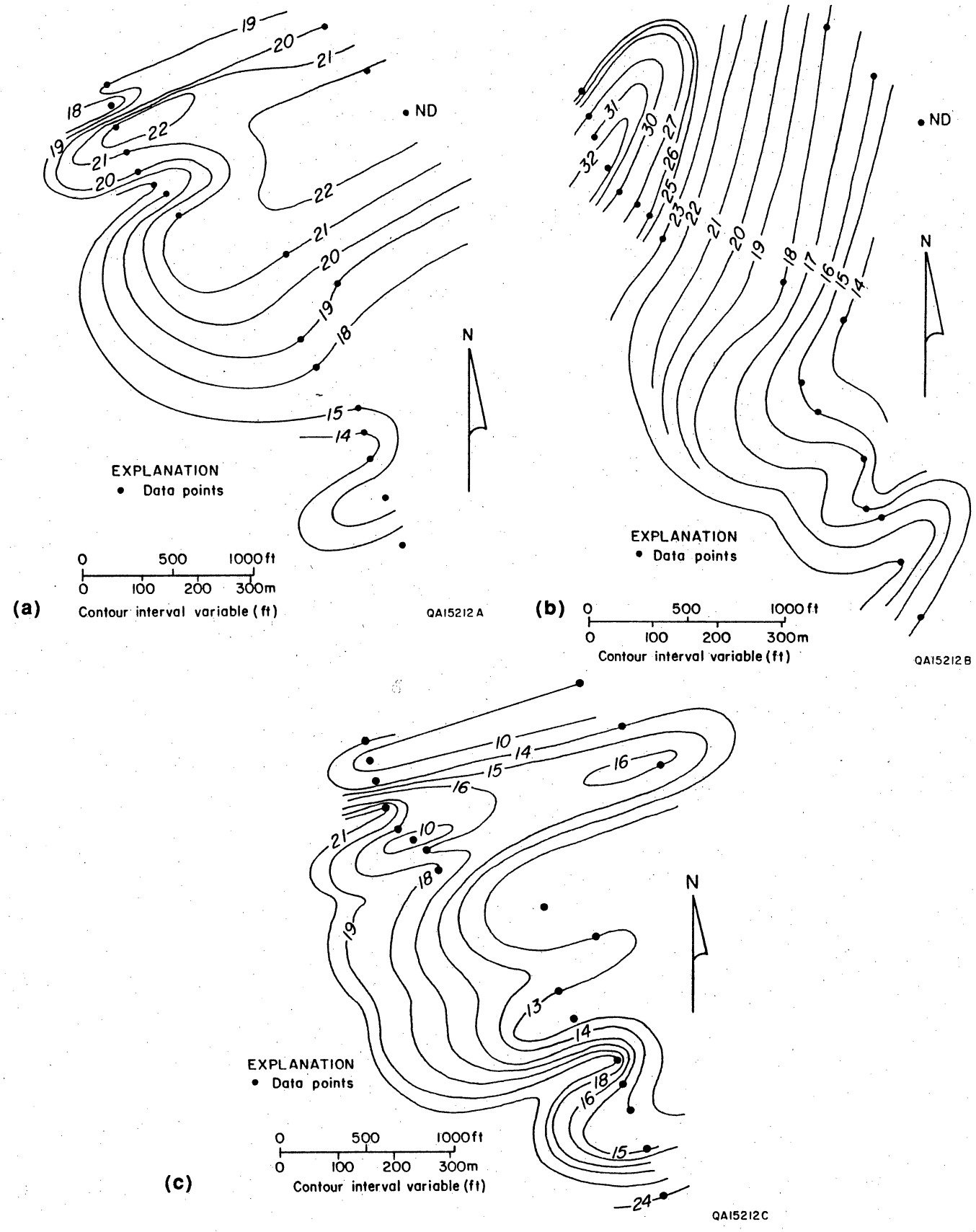

Figure 14. Isopach maps of upper San Andres parasequences 1–9: (a) P1u, (b) P2u, (c) P3u, (d) P4u, (e) P5u, (f) P6u, (g) P7u, (h) P8u, (i) P9u.

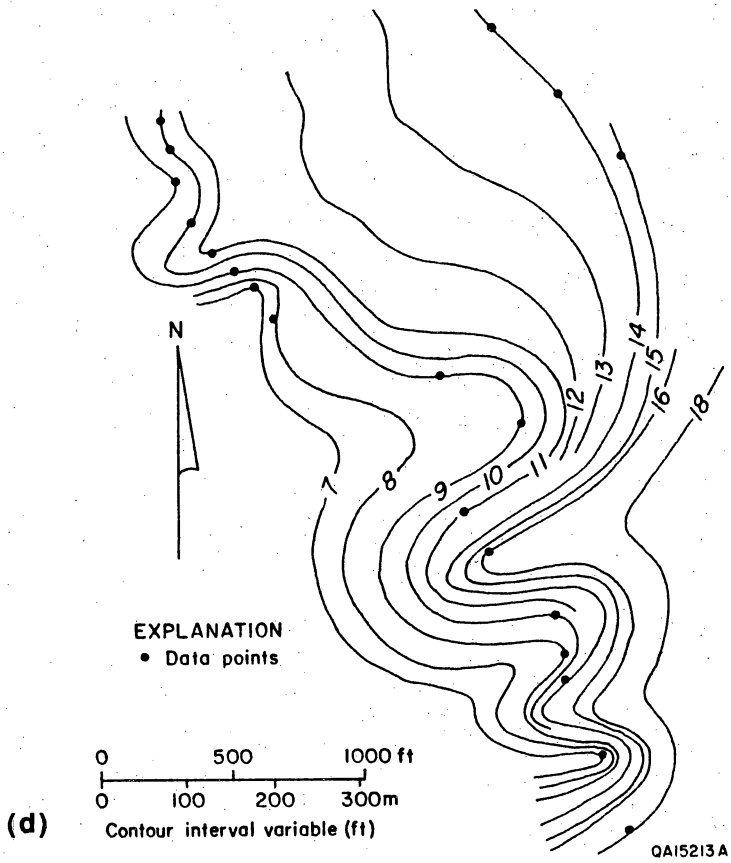
N
7
8
9
10
11
12
13
14
15
16
18
EXPLANATION
• Data points
0 500 1000 ft
0 100 200 300m
Contour interval variable (ft)
QA15213A

(d)

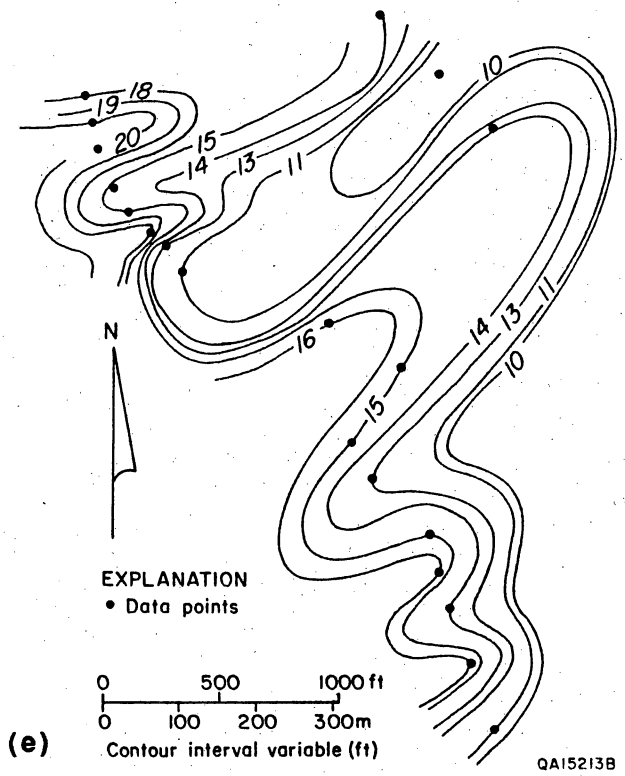
N
18
19
20
15
14
13
11
10
16
14
13
11
10
15
EXPLANATION
• Data points
0 500 1000 ft
0 100 200 300m
Contour interval variable (ft)
QA15213B

(e)

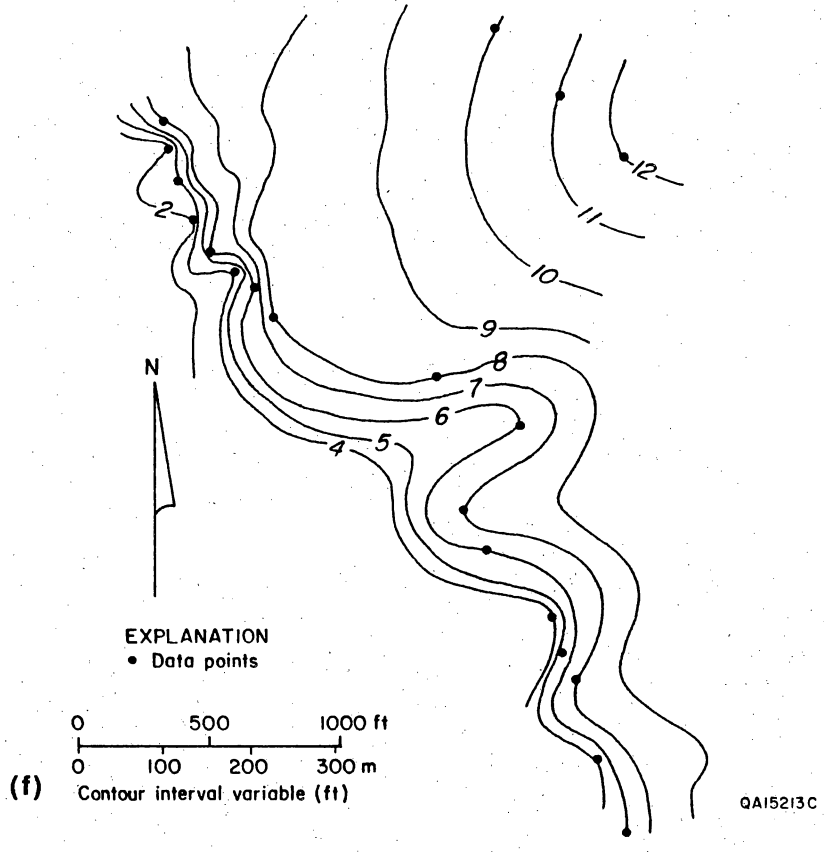
N
2
12
11
10
9
8
7
6
5
4
EXPLANATION
• Data points
0 500 1000 ft
0 100 200 300 m
Contour interval variable (ft)
QA15213C

(f)

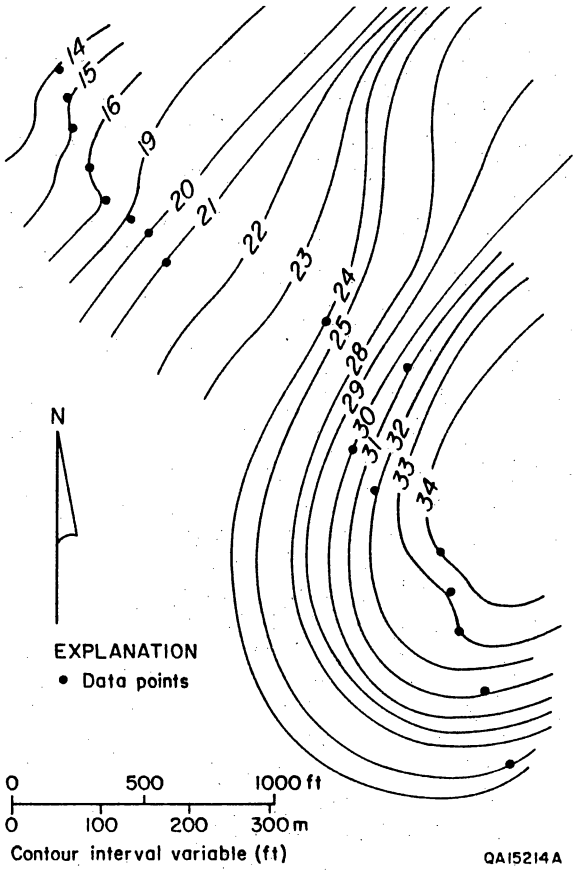
14
15
16
19
20
21
22
23
24
25
28
29
30
31
32
33
34
N
EXPLANATION
• Data points
0 500 1000 ft
0 100 200 300 m
Contour interval variable (ft)
QA15214A

(g)

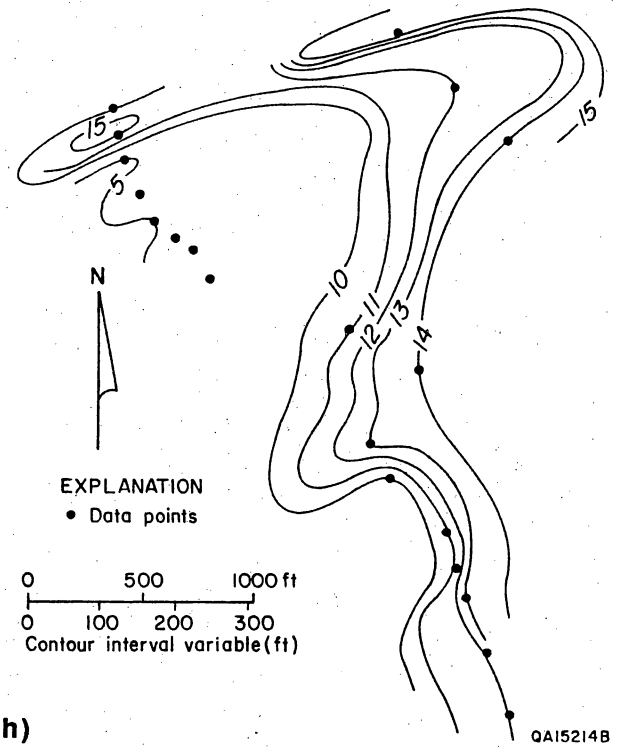
15
5
10
11
12
13
14
15
N
EXPLANATION
• Data points
0 500 1000 ft
0 100 200 300
Contour interval variable (ft)
QA15214B

(h)

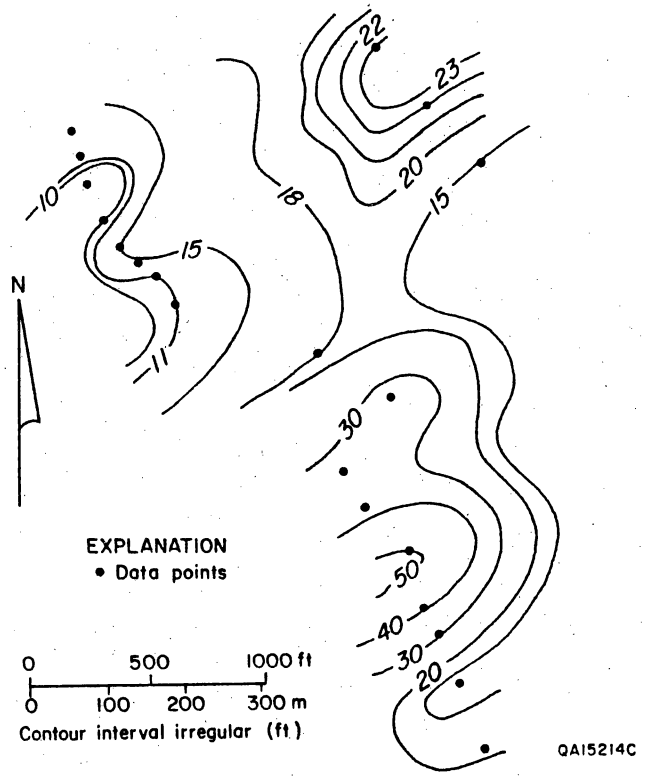
22
23
20
15
18
10
15
11
30
50
40
30
20
N
EXPLANATION
• Data points
0 500 1000 ft
0 100 200 300 m
Contour interval irregular (ft)
QA15214C

(i)

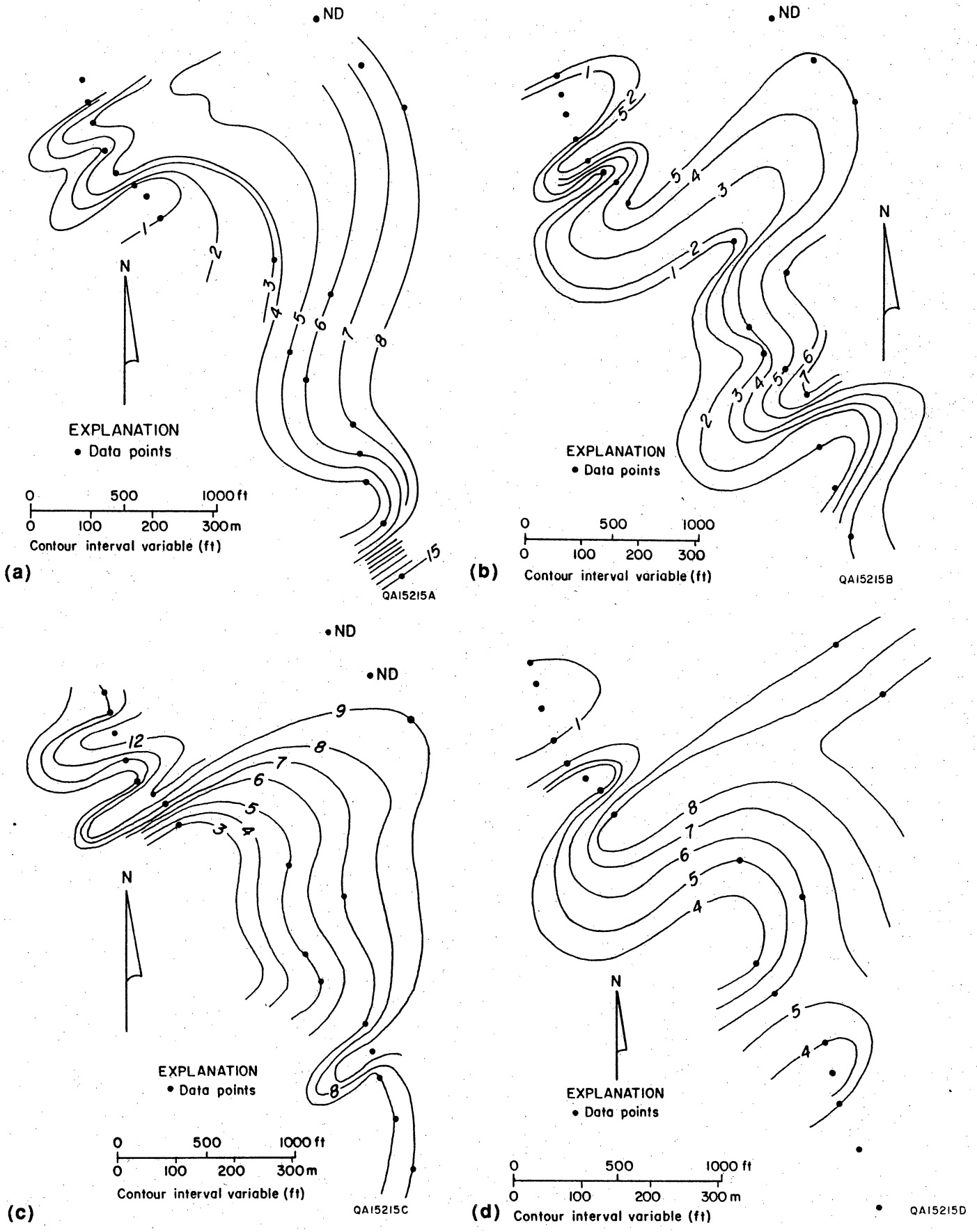

Figure 15. Net-grainstone maps for upper San Andres parasequences 3, 6, and 8: (a) P3u, (b) P4u, (c) P5u, (d) P6u, (e) P7u, and (f) P8u.

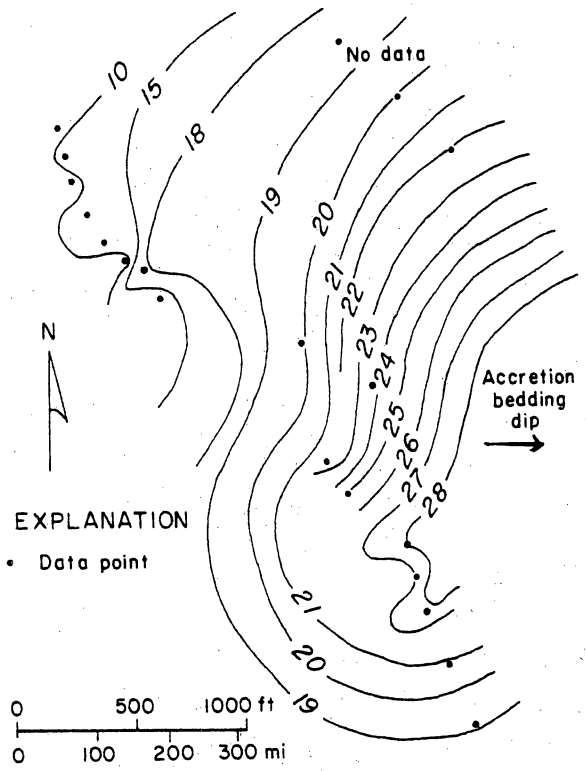

(e) Contour interval variable (ft) QA15198A

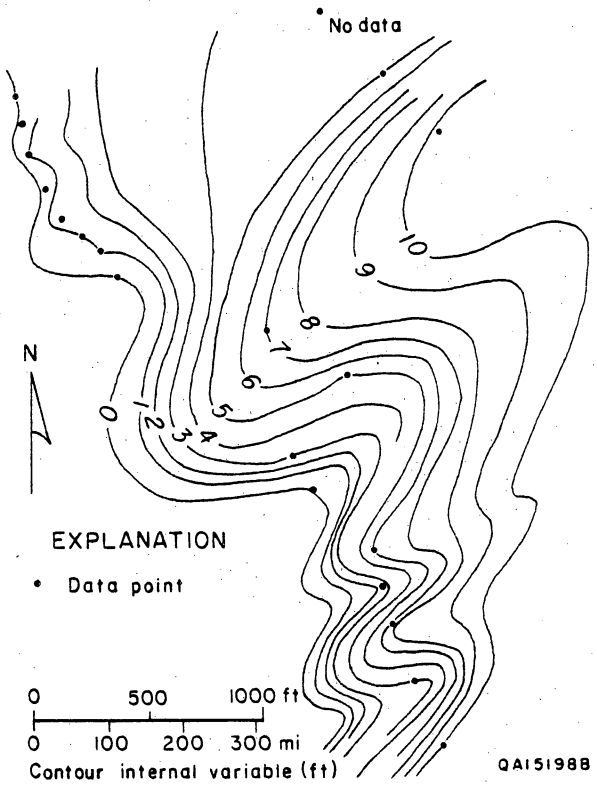

(f) Contour internal variable (ft) QA15198B

laterally accreted spits (Halley and others, 1977). Similarly, southerly strike-aligned accretion of carbonate sand bodies occurs on the south end of Isla Cancun, Yucatan Peninsula (Ward and Brady, 1973). Although insufficient evidence has been compiled to document these upper San Andres grainstone deposits as spits, strike-aligned wave or current distribution is likely. In an analogous reservoir (for example, Seminole field) the most important aspect is a potential strike elongation of producing intervals on the eastern (presumably windward) side of the field.

Isopach maps of P4u, P5u, and P6u show significant interrelationships. Thicks in P5u overlie thins in P4u; thicks in P6u overlie thins in P5u. These correspondences suggest that topographic lows present at the termination of parasequences were infilled during subsequent deposition. From the resulting parasequence stacking pattern it can be suggested that productive intervals of individual parasequences in an analogous reservoir setting may be offset along strike as well as dip.

PARASEQUENCE-SCALE VOLUMETRICS: PARASEQUENCE P9u

The prominent thickness variability in P9u is significant (figs. 13, 14, and 16, and Kerans, this volume, pl. 2). P9u is dominantly porous and permeable grainstone (figs. 4, 7, 8, and 9) and its potential fluid-storage capacity is largely controlled by its thickness. In a hypothetical reservoir setting, greater volumes of hydrocarbons would reside in the thicker parts of P9u. A 40-acre, 5-spot drilling pattern is superimposed on the isopach map (fig. 16) to demonstrate the difference in hypothetical productivity between two adjacent 40-acre areas. Area I is over the thicker part of P9u; Area II is over the thinner part. For simplicity, the following calculation of oil-in-place (OIP) assumes an average porosity of 10 percent, oil saturation (So) equal to 95 percent (approximate upper limit), and formation volume factor (Bo) equal to one.

Oil-in-place is calculated as follows:

$$\text{OIP (bbl)} = 7{,}758\ (\text{bbl/acre-ft}) \times \text{AREA (acre)} \times \text{AVG THICKNESS (ft)} \times \text{POROSITY} \times \text{So/Bo}$$

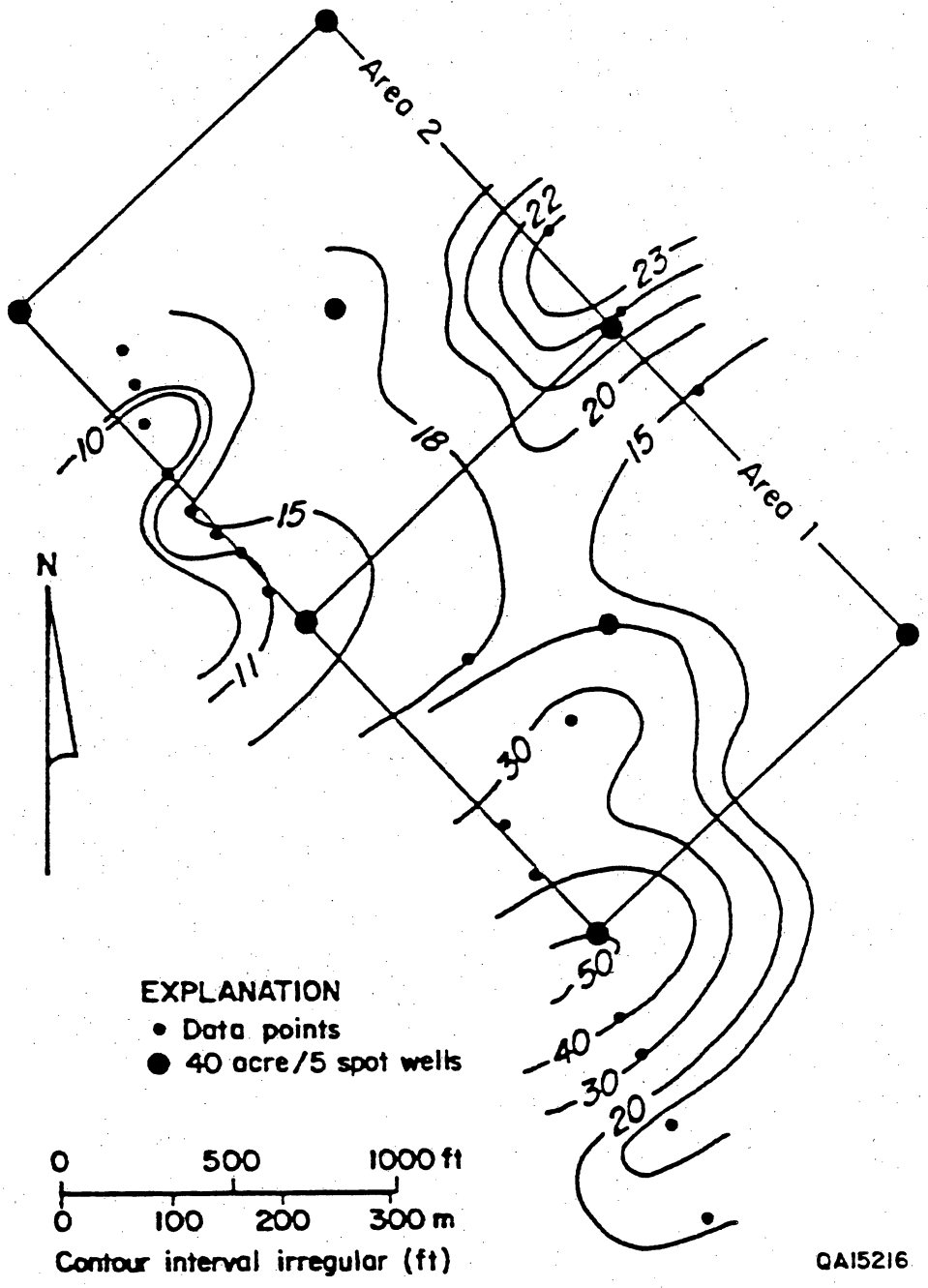

Figure 16. Isopach map of upper San Andres parasequence 9. Large dots represent corners and centers of two 40-acre, 5-spot development areas. Southern area is Zone I, northern area is Zone II (see text for discussion).

For Area I calculated OIP is 743 Mbbl; for Area II calculated OIP is 419 Mbbl. Production resulting from low recovery efficiencies characteristic of many carbonate reservoirs is also calculated. At 25 percent, recovery Area I produces 186 Mbbl; for Area II recovery is 105 Mbbl. At any saturation value assumed constant for both areas, Area I would contain and produce 1.8 times the volume of oil in Area II. P9u is an example of variability arising from rapid lateral changes of reservoir thickness.

RESULTS OF SAN ANDRES CORE TESTS

Porosity and permeability depth plots and cross plots of porosity versus permeability for the Algerita cores are presented in figures 17 and 18, respectively (see appendix for location of core-test data). Results from upper San Andres rocks (the No. 1 and No. 2 Algerita) are presented separately for comparison. Only middle San Andres rocks were sufficiently recovered for testing from the No. 3 Algerita. Middle San Andres rocks show somewhat better correlation between porosity and permeability than do upper San Andres rocks. Generally, permeabilities increase with increasing porosity, but the exceptions are abundant. It is impossible to predict permeability from porosity without first conducting a detailed rock-fabric analysis of sample points.

REGIONAL CROSS SECTION: OUTCROP TO SEMINOLE SAN ANDRES UNIT

The regional cross section illustrated in figure 19 is a summary of correlations between 42 gamma-ray/density, gamma-ray/neutron, and gamma-ray/sonic logs (see appendix) recorded in several reservoirs across the Northwest Shelf, and northern Central Platform Basin. Detailed well-to-well correlations are difficult across the Northwest Shelf, but the top of the San Andres Formation and the Leonardian "Glorieta" siliciclastic-bearing interval (below the San Andres) are widespread markers. Correlations are based primarily on maintaining relatively constant

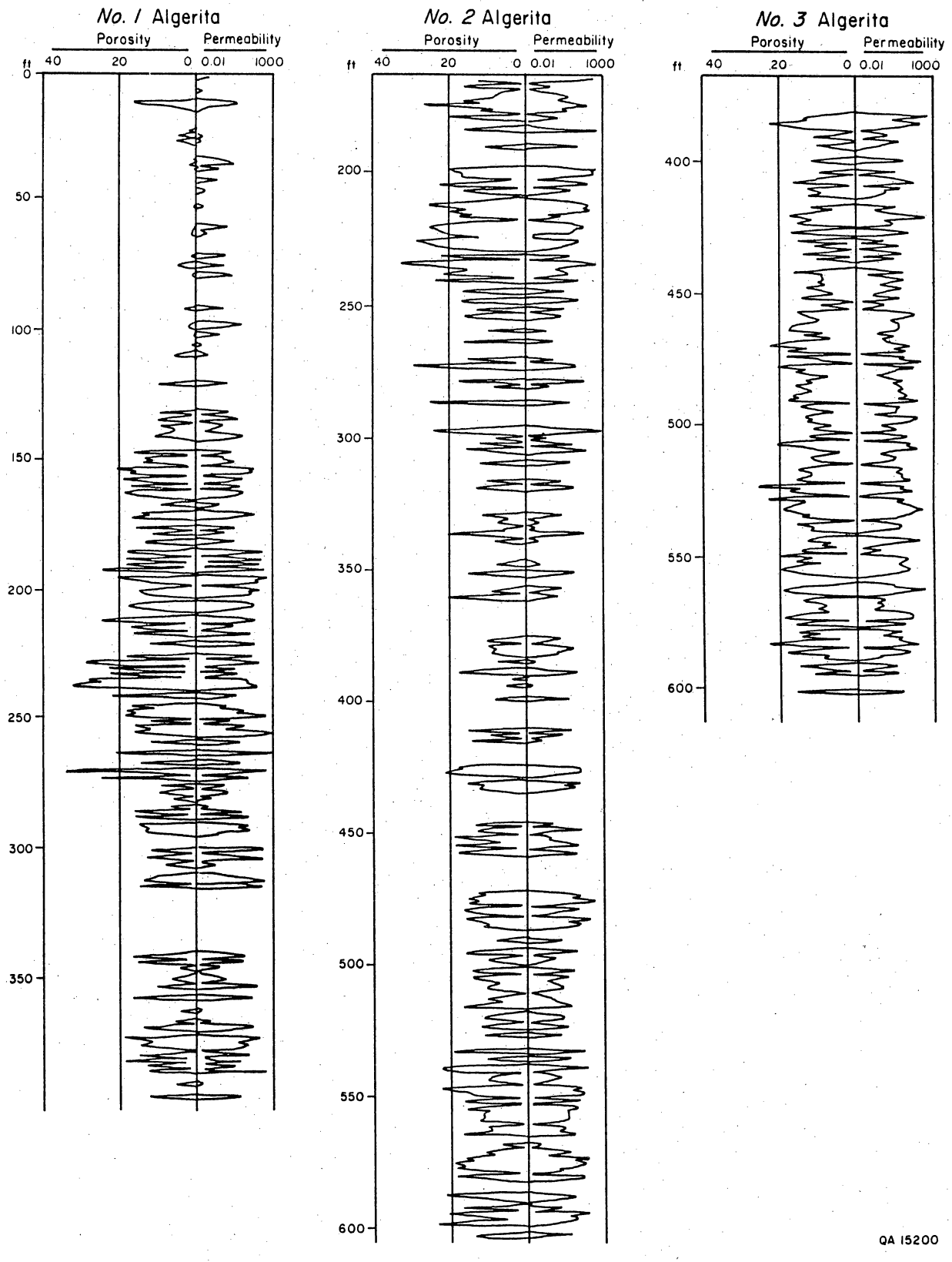

Figure 17. Depth plots of porosity and permeability from core tests for No. 1, No. 2, and No. 3 Algerita.

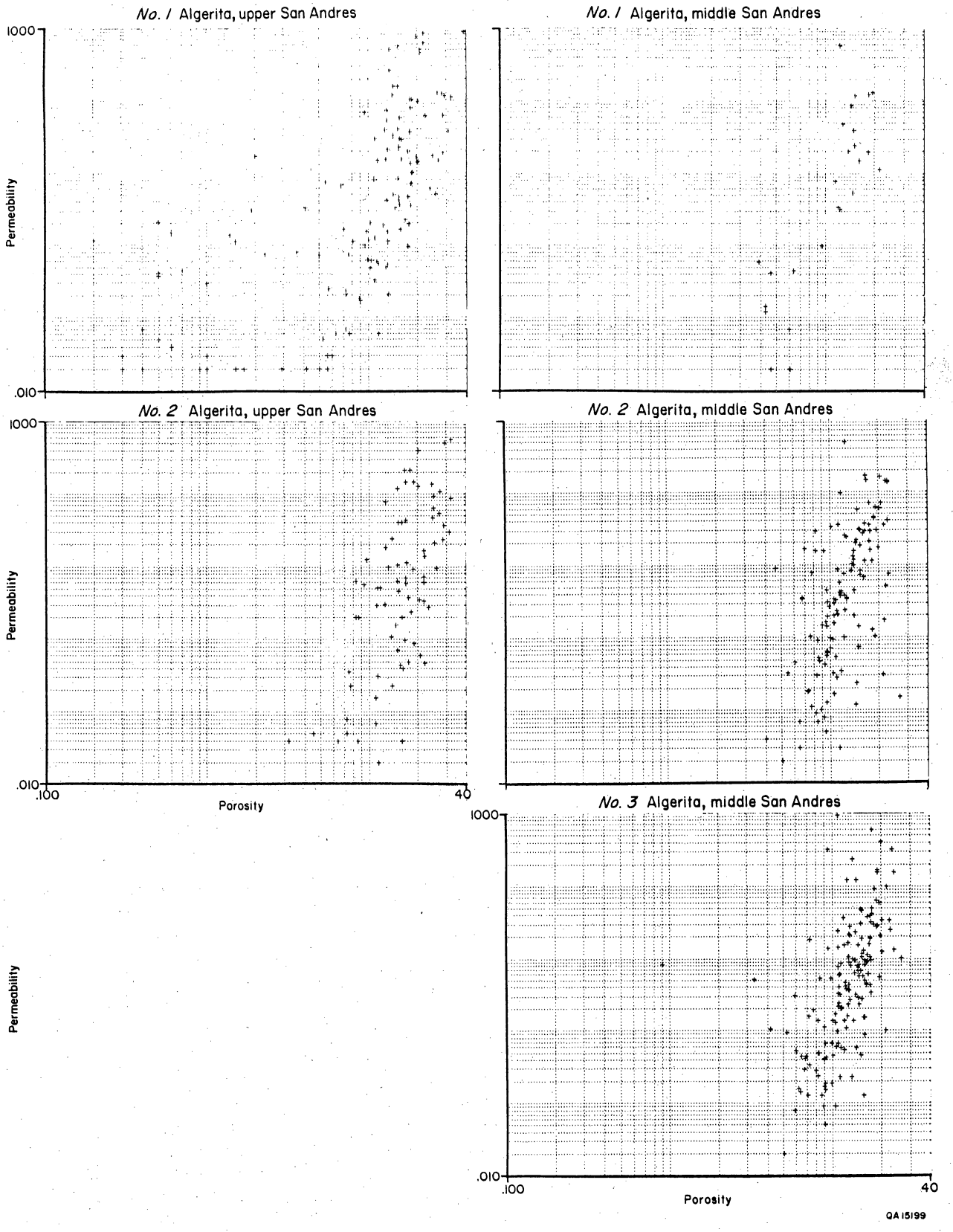

Figure 18. Cross plots of porosity and permeability for No. 1, No. 2, and No. 3 Algerita.

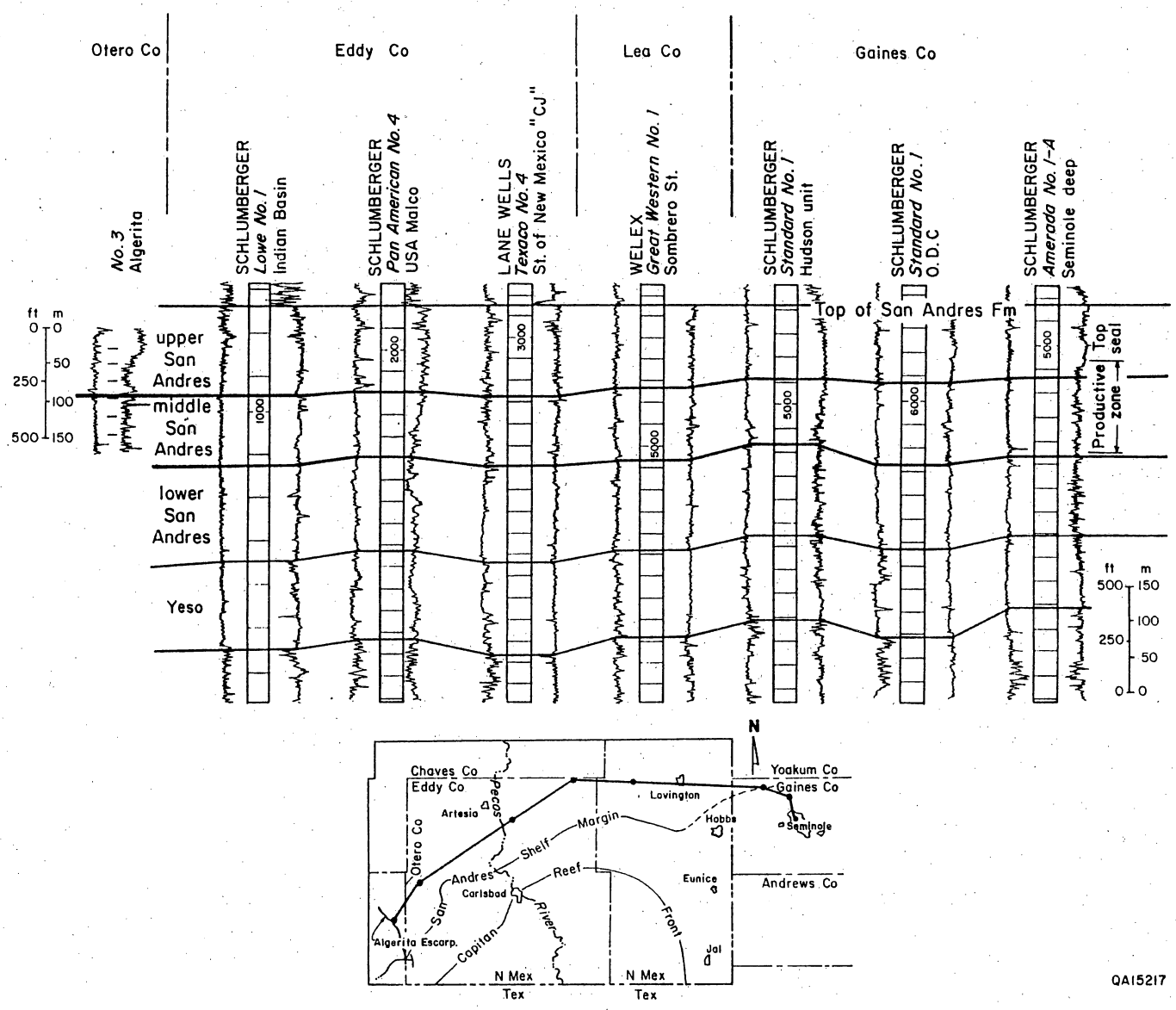

Figure 19. Correlation of No. 2 Algerita to San Andres Seminole Unit, Gaines County, Texas. Based on correlation of 45 gamma-ray/porosity logs. Most of Seminole San Andres production is from middle San Andres outcrop equivalents.

constant thicknesses of correlative intervals, coupled with identification of either gamma-ray log responses or porosity log responses similar to those observed in other wells along the section line. Difficulty rises from the limited penetration range of the Algerita boreholes that were spudded below the top and did not penetrate to the base of the San Andres Formation. The main correlation points are the Lovington Sandstone near the top of Algerita boreholes, which may correlate to a high gamma-ray response seen at 630 to 640 ft in Lowe/No. 1 Indian Basin well, Eddy County, New Mexico, and the porosity zone of P1u, which shows a high porosity response in the Algerita boreholes and that may correlate to a similar sonic porosity log response at 945 ft in the No. 1 Indian Basin well. The base of the San Andres Formation on the Algerita Escarpment is the siliciclastic-bearing interval above the Leonardian Yeso Formation (equivalent to the upper Clear Fork Formation on the Northwest Shelf) called the Glorieta Member of the San Andres Formation (Sarg and Lehman, 1986). Based on a San Andres thickness of 1,200 ft measured on the outcrop, the base of the San Andres is placed at the top of a relatively high gamma-ray and sonic porosity response at 1,700 ft in the Lowe/No. 1 Indian Basin well. Note that the Glorieta on the outcrop is not equivalent to the interval traditionally picked as the Glorieta in the subsurface (2,100 ft in the Lowe/No. 1 Indian Basin well). Correlation of siliciclastic markers across the San Simon Channel is problematic, probably because the siliciclastic supply across the Northwest Shelf to the Central Basin Platform was often blocked by the channel.

Although approximate, these correlations suggest that about 15 percent of the producing zone at Seminole field is from strata equivalent to upper San Andres rocks on Algerita Escarpment, whereas about 85 percent of the Seminole producing zone is in middle San Andres outcrop equivalents.

CONCLUSIONS

From correlations between outcrop and the exploratory boreholes, the following conclusions can be drawn that reflect applicability of the study area to studies of analogous reservoirs:

General

1. Pervasive fracturing of strata at the outcrop face results from proximity to major faults. Fractures are also present in core, limiting core recovery and quality.

2. Upper and middle San Andres upward-coarsening parasequences identified in outcrop can be identified in core. Lower porosity, finer grained strata that separate parasequences are laterally continuous along strike and dip. Grain-dominated intervals within parasequences are more continuous along strike than along dip where some, especially upper San Andres parasequences, become finer grained both updip and downdip.

3. Geophysical well log signatures are similar for correlative stratigraphic intervals over a minimum distance of 330 ft and probably at least 660 ft.

4. Sample permeability generally tends to increase as porosity increases; however, permeability of a given sample cannot be predicted solely from its porosity.

5. Productive intervals at the Seminole San Andres Unit, northern margin of Central Basin Platform, are mainly stratigraphically equivalent to the middle San Andres and lowermost upper San Andres interval as defined on the Algerita Escarpment.

Upper San Andres

6. Although thicker tidal-flat caps generally are more extensive than thinner caps, few parasequences have extensive tidal-flat caps; some intra-parasequence tidal caps also are

present. This suggests that caution must be exercised when using tidal-flat caps as stratigraphic datums for parasequence delineation in reservoir analysis, especially in facies tracts dominated by grainstone bars, with their associated local topography.

7. Exposure/onlap surfaces are only locally evident, giving rise to potential miscorrelation of parasequences.

8. Rapid lateral changes in parasequence thickness may result in considerable differences in productivity between adjacent development tracts as shown hypothetically for P9u.

9. Grainstone intervals, which include the highest average porosities and permeabilities within individual parasequences, extend at least from outcrop to boreholes, a distance of 1,400 ft along strike.

10. Parasequence thickness and net-grainstone trends suggest strike-related depositional processes; in analogous reservoirs the thickest parts of productive intervals within individual parasequences may have significant strike-elongate orientations.

11. Parasequence thickness generally reflects topography present on top of the immediately underlying parasequence; that is, topographic lows are filled by subsequent parasequence deposition; productive zones in an analogous reservoir may be vertically offset along strike as well as dip.

Middle San Andres

12. Parasequence thicknesses and lithologies are laterally consistent along strike and dip.

13. Development of fusulinid-moldic porosity is not systematic within individual parasequences.

REFERENCES

Ahr, W. M., 1973, The carbonate ramp: an alternative to the shelf model: Gulf Coast Association of Geological Societies Transactions, v. 23, p. 221–225.

Ball, M. M., 1967, Carbonate sand bodies of Florida and the Bahamas: Journal of Sedimentary Petrology, v. 37, p. 556–591.

Halley, R. B., Shinn, E. A., Hudson, J. H., and Lidz, B. H., 1977, Pleistocene barrier bar seaward of ooid shoal complex near Miami, Florida: American Association of Petroleum Geologists Bulletin, v. 61, p. 519–526.

Markello, J. R., and Read, J. F., 1982, Upper Cambrian intrashelf basin, Nolichucky Formation, southwest Virginia Appalachians: American Association of Petroleum Geologists Bulletin, v. 66, no. 7, p. 860–878.

Sarg, J. F., and Lehman, P. J., 1986, Lower-middle Guadalupian facies and stratigraphy, San Andres–Grayburg formations, Permian Basin, Guadalupe Mountains, New Mexico, *in* Moore, G. E., and Wilde, G. L., eds., Lower and Middle Guadalupian facies, stratigraphy, and reservoir geometries, San Andres–Grayburg Formations, Guadalupe Mountains, New Mexico and Texas: Society of Economic Paleontologists and Mineralogists, Permian Basin Section, Publication No. 86-25, p. 1–36.

Sheldon, V. P., 1954, Oil production from the Guadalupe series in Eddy County, New Mexico: New Mexico Geological Society, Fifth Field Conference Guidebook, p. 150–159.

Ward, W. C., and Brady, M. J., 1973, High-energy carbonates on the inner shelf, northeastern Yucatan Peninsula, Mexico: Gulf Coast Association of Geological Societies Transactions, v. 23, p. 226–238.

PETROGRAPHIC AND FACIES STUDY OF PARASEQUENCE 7, UPPER SAN ANDRES, OF THE LAWYER CANYON AREA, ALGERITA ESCARPMENT: DEVELOPMENT OF MOLDIC POROSITY

by Susan D. Hovorka

INTRODUCTION

In the upper San Andres dolomitized grainstones of the Lawyer Canyon area of the Algerita Escarpment, one stratigraphic unit, parasequence 7, exhibits extensive development of moldic pores formed by leaching of allochems. Petrographic examination was undertaken to describe the character of moldic and nonmoldic grainstones in this interval, to interpret the origins of fabric-related variability in permeability, and to relate the observed distribution of moldic porosity to a predictive model for the distribution of moldic porosity in grainstones in the upper San Andres. Presence of highly porous units of only moderate permeability is significant to flow models developed for the upper San Andres in this area and potentially in equivalent units in subsurface reservoirs.

METHODS

Petrographic analyses of thin sections from 123 1-inch core plugs at 1-ft vertical spacings from 7 measured sections along a 0.6-mi (1-km) transect along the Algerita Escarpment outcrop in the Lawyer Canyon area were the primary method of study. Porosity and permeability were measured for each plug by Rotary Engineers Laboratories, Midland Texas, using conventional core-plug analysis. Thin sections prepared from the ends of the plugs were examined petrographically and grain/pore relationships quantified by point-counting (table). Pore types in blue-epoxy-impregnated thin sections were separated according to the classification of Lucia (this report) into intergranular, intercrystalline, moldic, vugs, and fractures. Molds were separated from other vugs where origin by leaching of an allochem or anhydrite crystal was

Table. Petrographic data from parasequence 7, Lawyer Canyon area.

Section	Elevation (ft)	Plug porosity (%)	Permeability (md)	Total grains (%)	Grain size (μm)	Dolomite cement (%)	Dolomicrite (%)	Avg. crystal size (μm)	Calcite (%)	Other (%)	IG pores (%)	IC pores (%)	Moldic pores (%)	Frac. pores (%)	Other vug (%)	IC WP pores (%)	Fabric
A	90	19.6	5.04	44.7	150	30.7	0.3	15	13.0	0.0	4.0	0.0	0.3	0.0	7.0	0.0	G
A	91	14.6	1.13	23.3	170	33.3	24.3	15	11.3	0.0	3.3	0.0	0.3	0.0	3.7	0.3	GP
A	92	15.2	1.76	70.7	140	19.3	0.3	15	2.3	0.0	4.3	0.0	1.0	0.0	1.0	1.0	G(C)
A	93	13.2	0.08	67.0	150	24.7	0.0	15	2.3	0.0	3.7	0.0	1.3	0.0	0.7	0.3	G(C)
A	94	13.1	0.03	56.0	160	32.7	0.3	15	1.0	0.0	3.7	0.0	3.7	0.0	2.3	0.3	G(C)
A	95	15	0.33	50.3	150	36.7	0.0	20	3.0	0.0	2.7	0.0	6.3	0.0	1.0	0.0	G
A	96	13.9	4.31	44.0	150	42.0	0.0	20	4.7	0.0	0.3	0.0	4.3	0.0	4.7	0.0	G
A	97	16.8	0.26	54.7	140	36.0	0.0	15	0.7	0.0	2.3	0.0	1.3	0.0	5.0	0.0	G(C)
A	98	11.2	7.13	53.3	140	38.0	0.0	20	0.3	0.0	1.3	0.0	2.7	0.0	4.3	0.0	G(C)
A	99	19.9	33.97	57.7	150	23.0	0.3	20	7.0	0.3	1.3	0.0	3.3	0.0	7.0	0.0	G
A	100	14.9	5.04	40.3	200	35.7	0.0	25	15.3	0.0	3.0	0.0	2.7	0.0	2.7	0.3	G
A	101	23.9	146.4	2.0	120	28.3	6.0	20	44.3	0.0	0.0	2.7	1.3	0.0	15.3	0.0	GP?
A	102	18.5	2.73	31.3	100	42.7	0.0	30	17.0	0.3	2.7	0.0	5.0	0.0	1.0	0.0	G
A	103	17.4	0.77	38.7	200	44.0	0.0	20	8.7	0.0	1.7	0.0	5.0	0.0	1.7	0.3	G
A	104	20.4	4.41	34.7	150	39.3	2.0	30	14.3	0.3	2.0	0.0	3.0	0.0	3.3	1.0	G(C)
A	105	16.2	0.38	38.0	150	43.7	0.0	20	5.3	0.0	1.7	0.0	7.0	0.0	4.0	0.3	G(C)
A	106	12.3	0.16	46.3	250	40.0	0.0	30	2.7	0.3	6.0	0.0	3.0	0.0	1.3	0.3	G(C)
A	107	16.5	0.8	42.3	150	44.3	0.0	20	4.7	0.3	2.3	0.0	5.3	0.0	0.0	0.7	G(C)
A	108	12.9	0.74	47.7	325	27.7	14.0	15	4.7	0.3	3.3	0.0	1.3	0.0	0.0	1.0	G(C)
A	109	13.1	0.29	54.7	250	29.0	1.0	30	2.3	0.0	6.3	0.0	5.7	0.0	0.0	1.0	G
H	92	14.5	7.92	67.3	200	21.3	3.0	20	3.3	0.0	4.3	0.0	0.7	0.0	0.0	0.0	GP
H	93	15.8	27.47	64.3	200	14.3	2.7	15	7.3	0.0	8.7	0.0	0.3	0.3	2.0	0.0	GP
H	94	16.5	9.22	39.3	150	34.7	8.7	15	9.0	0.3	5.7	1.0	1.0	0.0	0.3	0.0	GP
H	95	17.1	3.37	43.0	130	23.7	0.0	20	21.7	0.0	9.3	0.0	2.0	0.0	0.3	0.0	G
H	96	19.4	7.25	43.7	120	25.7	0.0	15	21.7	0.0	5.7	0.0	2.0	0.0	0.7	0.7	G
H	97	21.8	17.38	54.3	130	19.3	0.0	20	14.3	0.0	9.3	0.0	2.0	0.0	0.0	0.7	G
H	98	11.2	22.23	59.0	150	21.7	0.0	20	5.3	0.0	7.7	0.0	1.0	0.0	5.0	0.3	G
H	99	13.1	79.64	66.0	150	24.0	0.0	20	1.3	0.0	5.7	0.0	0.3	0.0	2.7	0.0	G
H	100	19.4	227.3	62.3	400	4.7	0.0	20	10.0	0.0	9.3	0.0	1.3	0.0	12.0	0.3	G
H	101	15.4	91.57	74.3	150	4.0	0.0	20	6.3	0.0	10.0	0.0	0.7	0.7	2.7	1.3	G
H	102	18.1	52.54	78.3	140	2.3	0.3	15	8.7	0.0	7.7	0.0	1.7	0.0	1.0	0.0	G
H	103	8.5	0.51	81.0	140	8.7	0.0	15	0.7	0.0	8.7	0.0	0.0	0.0	0.3	0.7	G
H	104	10.2	0.48	67.7	200	8.0	13.7	20	1.0	0.0	6.0	0.0	1.0	0.0	2.3	0.3	GP(C)
H	105	9.1	4.51	76.0	300	8.3	0.7	15	1.7	0.0	11.7	0.0	1.7	0.0	0.0	0.0	G
H	106	9.6	0.04	72.0	150	9.3	12.7	15	0.0	0.3	4.3	0.0	1.3	0.0	0.0	0.0	G

Table. (cont.)

Section	Elevation (ft)	Plug porosity (%)	Permeability (md)	Total grains (%)	Grain size (µm)	Dolomite cement (%)	Dolomicrite (%)	Avg. crystal size (µm)	Calcite (%)	Other (%)	IG pores (%)	IC pores (%)	Moldic pores (%)	Frac. pores (%)	Other vug (%)	IC WP pores (%)	Fabric
X	77	18.7	17.78														
X	78	6.6	0.02														
X	79	7.2	0.04	0.7	100	0.0	90.0	10	6.3	0.0	0.0	0.7	1.7	0.0	0.7	0.0	M
X	80	17.6	18.59	35.3	400	19.7	28.7	20	8.7	0.3	1.0	0.0	0.7	0.0	5.0	0.7	P
X	81	22.8	10.69	11.3	250	1.7	74.3	15	6.3	0.0	0.0	0.7	3.3	0.0	2.3	0.0	W?
X	82	18	2.4	40.3	200	30.0	4.3	25	6.0	0.0	1.7	0.0	3.7	0.0	14.0	0.0	GP
X	83	16.5	1.26	50.0	130	29.3	13.7	20	2.3	0.0	1.0	0.0	1.3	0.0	2.3	0.0	P?
X	84	13.5	1.22	49.7	200	35.3	6.0	20	1.7	0.0	5.7	0.0	0.7	0.0	1.0	0.0	GP(C)
X	85	16.3	0.81	53.3	250	35.0	1.0	25	2.0	0.0	3.7	0.0	0.7	0.0	4.3	0.0	G(C)
X	86	18.2	2.82	54.7	200	35.0	0.0	25	0.7	0.0	3.7	0.0	2.3	0.0	3.7	0.0	G(C)
X	87	23.3	3.32	37.0	150	29.7	1.7	20	0.3	0.0	7.0	0.0	11.3	0.0	12.7	0.3	G
X	88	24.2	21.49	23.7	150	44.3	1.3	15	4.3	0.0	0.7	0.0	10.0	0.0	15.0	0.7	GP(C)
X	89	27.3	5.76	23.7	150	56.3	2.3	20	4.3	0.0	3.3	0.0	10.0	0.0	0.0	0.0	GP
X	90	30.1	32.51	11.7	140	53.7	0.3	15	4.7	0.0	5.3	0.0	23.3	0.0	0.3	0.7	G
X	90	0	0	14.3	130	47.3	0.0	15	4.0	0.0	6.7	0.0	27.7	0.0	0.0	0.0	G
X	91	25.9	1.7	17.0	140	50.7	0.0	20	7.7	0.0	4.0	0.0	20.7	0.0	0.0	0.0	G
X	92	23.8	3.24	11.7	140	65.7	0.0	20	5.7	0.3	0.7	0.0	16.0	0.0	0.0	0.0	G
X	93	26.7	1.85	14.7	130	65.0	0.0	30	6.0	0.0	1.0	0.0	13.3	0.0	0.0	0.0	G
X	94	26.8	1.29	11.0	130	61.3	0.0	20	8.3	0.0	2.3	0.0	17.0	0.0	0.0	0.0	G
X	95	34.4	55.66	36.3	160	48.3	0.0	20	5.0	0.0	4.3	0.0	4.7	0.0	0.7	0.7	G
X	96	22	0.05	14.3	150	60.3	0.0	30	3.0	0.0	0.7	0.0	21.0	0.0	0.3	0.3	G
X	97	26.8	9.54	36.3	150	39.3	0.0	20	2.3	0.0	5.0	0.0	13.0	0.0	3.0	1.0	G
X	98	22.6	3.42	38.7	160	47.0	0.0	20	0.3	0.0	4.7	0.0	7.0	0.0	1.7	0.7	G
X	99	26.1	1.11	23.0	150	44.3	0.0	20	2.0	0.0	1.7	0.0	26.7	0.0	1.0	1.3	G
X	100	25.4	813	42.0	200	31.3	6.0	15	1.3	0.0	6.3	0.3	5.3	0.0	7.3	0.0	GP
X	101	27.6	113	48.3	160	26.7	0.0	20	1.0	0.0	1.0	0.0	9.3	0.0	13.7	0.0	G
X	102	25.1	3.39	40.0	250	36.7	0.3	20	1.0	0.0	3.7	0.0	18.3	0.0	0.0	0.0	G

Table. (cont.)

Section	Elevation (ft)	Plug porosity (%)	Permeability (md)	Total grains (%)	Grain size (μm)	Dolomite cement (%)	Dolomicrite (%)	Avg. crystal size (μm)	Calcite (%)	Other (%)	IG pores (%)	IC pores (%)	Moldic pores (%)	Frac. pores (%)	Other vug (%)	IC WP pores (%)	Fabric
Z	78	17.6	0.47	39.7	170	28.7	10.3	20	0.3	0.0	6.0	0.0	4.0	0.0	11.0	0.0	GP
Z	79	20.1	1.96	47.0	150	32.0	3.0	20	0.0	0.0	8.0	0.0	7.7	0.0	2.3	0.0	GP
Z	80	15.8	2.45	50.7	150	25.0	5.0	30	0.3	0.0	6.7	0.0	11.3	0.0	1.0	0.0	GP
Z	81	17	1.89	64.3	350	12.0	1.7	20	0.3	0.0	9.0	0.0	5.7	0.0	7.0	0.0	G?
Z	82	17.1	1.86	38.7	250	19.3	22.0	20	3.7	0.0	2.7	1.0	9.7	0.0	3.0	0.0	GP
Z	83	19.5	0.83	27.3	150	47.0	6.3	20	2.0	0.0	2.0	1.0	6.7	0.0	7.7	0.0	GP
Z	84	24.9	2.23	13.3	120	58.0	2.0	20	0.0	0.0	4.0	0.7	20.3	0.0	1.7	0.0	G
Z	85	21.8	0.1	13.7	130	59.7	0.0	30	4.3	0.0	2.7	1.0	17.7	0.0	1.0	0.0	G
Z	86	24.3	12.39	9.7	140	55.7	2.3	30	10.3	0.0	1.3	1.7	17.3	0.0	1.7	0.0	GP
Z	87																BRECCIA
Z	88	18.9	11.63	9.3	100	58.7	0.0	25	15.3	0.0	0.0	0.0	16.3	0.0	0.0	0.3	G
Z	89	25.7	3.88	12.3	100	60.0	0.0	30	7.3	0.0	1.3	0.0	19.0	0.0	0.0	0.0	G
Z	90	23.8	0.39	10.3	110	62.3	0.0	30	0.0	0.0	1.7	0.0	20.7	0.0	5.0	0.0	G
Z	91	20.2	0.06	20.7	160	59.0	0.0	20	0.0	0.0	1.0	0.0	17.7	0.0	1.7	0.0	G
Z	92	24	0.13	19.0	120	63.3	0.0	30	0.0	0.0	0.7	0.0	15.3	0.0	1.7	0.0	G
Z	93	24.1	2.24	29.0	150	50.0	0.0	30	0.0	0.0	1.0	0.0	17.3	0.0	2.7	0.0	G
Z	94	16.6	0.37	37.0	150	46.3	0.0	30	0.0	0.0	1.7	0.0	14.7	0.0	0.3	0.0	G
Z	95	22.6	14.72	46.0	200	23.7	1.7	20	0.7	0.3	9.0	0.3	15.3	0.0	3.0	0.0	GP
Z	96	20.1	15.97	44.3	300	13.7	11.0	20	21.7	0.0	5.0	0.0	3.7	0.0	0.7	0.0	GP
Z	97	11.8	0.02	52.3	200	17.7	21.0	30	0.0	0.0	3.0	0.0	6.0	0.0	0.0	0.0	GP
Z	98	16.4	579	37.3	300	23.7	25.0	20	0.0	0.0	4.0	0.0	9.7	0.0	0.3	0.0	GP
Z	99	8.4	0.17	58.0	250	19.0	19.7	25	0.0	0.0	2.3	0.0	1.0	0.0	0.0	0.0	GP
Z	100	15.6	1.28	0.0	300	0.0	88.0	10	0.0	0.3	0.0	4.0	5.3	0.0	2.3	0.0	W
Z	101	18.4	4.64	47.3	80	18.0	20.3	10	0.0	0.0	3.7	1.3	6.3	0.0	2.3	0.7	GP
R	93	17.8	3.7	51.0	100	2.0	22.0	30	14.7	0.0	4.7	1.3	4.3	0.0	0.0	0.0	GP
R	95	15.1	3.13	3.0	200	1.7	65.7	30	15.0	0.3	0.0	5.0	8.3	0.0	1.0	0.0	W
R	98	17.1	2.14	37.0	100	46.7	0.7	40	9.7	0.0	0.7	0.0	4.7	0.0	0.0	0.7	G
R	100	17.2	3.17														
R	102	19.6	51.94	14.3	100	30.3	12.3	15	22.0	0.0	3.0	6.3	8.7	0.3	2.7	0.0	GP
R	106	17.7	2.31	23.0	130	55.0	0.0	25	13.0	0.0	1.3	1.3	6.0	0.0	0.3	0.0	
R	104	16.5	10.84														
R	108	21.2	17.11	29.7	150	40.0	6.0	35	11.7	0.0	0.7	4.0	6.3	0.0	1.7	0.0	GP
Q	1	6.4	0.53	11.3	120	0.0	84.3	20	0.0	0.0	0.0	0.0	0.0	0.0	4.3	0.0	W
Q	4	8.6	0.32	72.0	150	22.0	0.0	30	0.0	0.0	5.7	0.0	0.0	0.0	0.0	0.3	G
Q	7	18.4	2.55	26.3		40.7	0.0	30	22.3	0.0	0.7	0.0	10.0	0.0	0.0	0.0	G
Q	7(a)			47.3	200	33.0	0.0	20	11.0	0.0	2.7	0.0	6.0	0.0	0.0	0.0	G
Q	10	23.2	17.16	58.7	110	20.0	1.3	20	13.7	0.0	0.7	0.0	5.0	0.0	0.3	0.3	GP
Q	13	19.6	8.7	59.3	250	10.7	6.7	17	16.7	0.0	4.3	0.0	1.3	0.0	0.0	1.0	GP
Q	13 (a)			53.0	250	28.7	0.0	15	11.3	0.0	1.7	0.3	4.7	0.0	0.0	0.7	G
Q	16	20.4	5.84														
Q	19	20.3	7.55	49.7	275	32.3	0.0	40	9.3	0.0	2.7	0.3	5.7	0.0	0.0	0.0	G
Q	22	20.3	0.67	51.3	200	27.0	0.0	15	12.3	0.0	1.7	0.0	6.0	0.0	0.7	1.0	G
Q	25	14.5	2.28	54.3	200	30.7	0.0	15	3.3	0.0	2.3	0.0	9.3	0.0	0.0	0.0	G

Table. (cont.)

Section	Elevation (ft)	Plug porosity (%)	Permeability (md)	Total grains (%)	Grain size (μm)	Dolomite cement (%)	Dolomicrite (%)	Avg. crystal size (μm)	Calcite (%)	Other (%)	IG pores (%)	IC pores (%)	Moldic pores (%)	Frac. pores (%)	Other vug (%)	IC WP pores (%)	Fabric
O	0	7.4	0.02	0.3	100	0.0	97.7	15	0.3	0.0	0.0	0.7	0.0	0.0	1.0	0.0	M
O	3	7.3	0.05	0.0		0.0	94.7	10	1.0	0.0	0.0	4.3	0.0	0.0	0.0	0.0	M
O	6	16.6	0.36	47.7	200	42.3	0.7	20	6.0	0.0	1.3	0.3	0.7	0.0	1.0	0.0	GP
O	9	20.2	10.82	29.0	100	0.0	28.7	15	21.0	0.0	4.7	0.0	4.0	0.0	12.7	0.0	GP
O	12	29.9	173														P
O	15	13.6	1571	57.3	150	32.3	0.0	0	0.3	0.0	2.3	0.0	0.3	0.0	7.3	0.0	G
O	18	12.3	43.03	67.3	150	23.0	0.0	0	2.0	0.0	1.7	0.0	0.0	0.0	6.0	0.0	G(C)
O	21	12.9	5.93	74.7		7.3	0.0	15	10.7	0.0	4.7	0.0	0.0	0.0	2.7	0.0	G(C)
O	24	22	67.28	79.7	140	2.3	0.0	20	7.0	0.0	9.0	0.0	1.0	0.0	0.3	0.7	G
O	27	10.6	4.99	77.7	200	3.3	2.0	15	5.3	0.0	6.3	0.0	0.3	0.0	4.3	0.7	G

EXPLANATION

Section: Measured sections at Lawyer Canyon study area, Algerita Escarpment.

Elevation: Height in feet above base upper San Andres cycle 1, except sections O and Q, where height is measured from base cycle 7.

Porosity and permeability: Measured by standard analysis on 1-inch plugs.

Total grains : Preserved grains measured by point counting 300 points on thin section.

Grain size: Estimated average grain size in thin section.

Dolomite cement : Intergranular dolomite spar and microspar interpreted as cement and measured by point counting 300 points on thin section.

Dolomicrite: Dolomite micrite and microspar interpreted as originating as carbonate mud and measured by point counting 300 points on thin section.

Crystal size: Estimated average dolomite crystal size in thin section.

Calcite: Measured by point counting 300 points on thin section.

Other: Other minerals measured by point counting 300 points on thin section.

IG pores: Intergranular pores in grainstone or grain-dominated packstone measured by point counting 300 points on thin section.

IC pores: Intercrystalline pores typically in mudstone or wackestone measured by point counting 300 points on thin section.

Moldic pores: Vugs formed by leached carbonate allochems measured by point counting 300 points on thin section.

Fracture pores: Open fractures measured by point counting 300 points on thin section.

Other vug: Vugs larger than average grain size and not identified as a leached grain; may be vugs formed by leached anhydrite.

IC WP pores: Intercrystalline pores within particles.

Fabric: M = mudstone; W = wackestone; P = packstone; GP = grain-dominated packstone; G = grainstone; (C) = compressed grains.

interpreted. Nonmoldic vugs are generally larger than the allochems. In samples where dolomitization has partly obscured the definition of allochems, intercrystalline pores were separated from intergranular pores on the basis of size as well as the geometry of and the relationship to preserved and inferred grains. Additional petrographic variables collected were grain type and size, average dolomite crystal size, and late diagenetic modification of grain/pore relationships such as calcite cement, leached anhydrite, and leaching and other alteration caused by outcrop weathering.

GEOMETRY OF PARASEQUENCE 7

Parasequence 7 is a depositional unit composed of a thin transgressive basal mudstone overlain by burrowed grainstones and crossbedded grainstones (fig. 1). This parasequence thickens from 15 ft (5 m) in the updip northern part of the transect to 33 ft (11 m) in the more seaward southern part. The thin northern part of the transect lacks a continuous basal mudstone. Thickening toward the south is accompanied by development of thick crossbed sets interpreted as a channel-fill or spillover lobe (Kerans, this report). A thin fenestral bed caps the parasequence in the southern part of the transect. Most of the grainstone is fine grained and well sorted. Fusulinids occur scattered throughout the grainstones and as lag concentrations defining crossbedding.

PETROGRAPHY

Grain Type

Parasequence 7 is dominantly composed of well-sorted 150-μm spherical grains. Where the grains are preserved, they are dominantly structureless micrite peloids (fig. 2a). A few grains have micrite coats. Other grains identified include fusulinids, small mollusks and mollusk fragments, echinoderm plates, and ooids. Local concentrations of coarser grains are

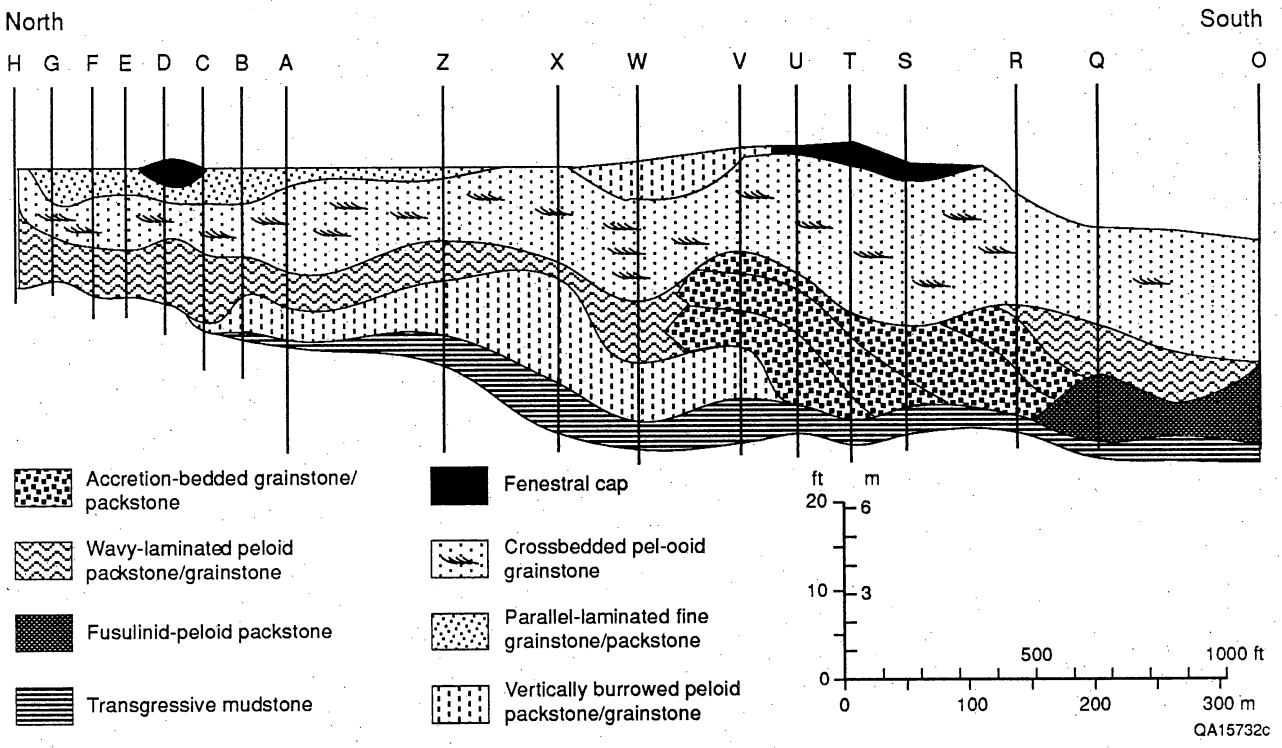

Figure 1. Cross section along the Algerita Escarpment, including sections O and Q, which extend the parasequence 7 study south of the Lawyer Canyon hydrologic modeling area.

Figure 2. (a) Typical parasequence 7 grainstone with abundant preserved grains, normal fine-grained intergranular dolomite cement, and some moldic pores. Sample O 18, transmitted plane light. (b) Variable grain preservation: some grains are now 5- to 15-μm dolomite, others are 20- to 40-μm dolomite. Sample A93, transmitted plane light. (c) Abundant moldic porosity and associated abundant intergranular cement. Sample X90, crossed nicols. (d) Distinctive deformed and overcompacted peloid grainstones are diagenetically formed low-permeability rocks. Note that the isopachous cement rims most grains, even where they are compressed against one another. Photomicrograph X85, transmitted plane light.

characterized by unidentified fragments of poorly preserved green algae (micritic grains with a regular or irregular pattern of dolomite spar-filled tubes or pores, variable replacement by coarser dolomite spar, and typical irregular grain shapes). Brachiopod valves, mollusks, and bryozoans are rare.

Grain Preservation

All allochems in parasequence 7 are now composed of fine-grained dolomite, with crystal size between 10 and 40 μm (fig. 2b). Grain preservation is variable, from excellent to poor, depending on (1) stabilization or leaching of grains and (2) the contrast between the crystal size in grains and the crystal size in interparticle cement or micrite.

Development of molds is a prominent diagenetic process in parasequence 7 and a key element in understanding porosity and permeability trends. Peloids 150 μm in diameter are the grain type most likely to be leached, as indicated by comparison of grain size and shape of molds to preserved grains (fig. 2c and d). Mollusk fragments, recognizable by their elongated grain shape and fractured rectangular ends, are moldic in all thin sections, but the great variability in the abundance of molds is caused by development of molds of spherical grains. No correlation between the abundance of mollusk fragments with moldic porosity was found. All grain types locally show some leaching. Even echinoderm plates are locally partly leached. Fusulinids are variably leached or preserved as fine-grained dolomite, but are not abundant enough in most thin sections to define a dominant grain size on scatter plots (fig. 2d).

Distribution of Moldic Porosity

Moldic porosity is extensively developed in the middle of the study area, whereas only minor amounts of moldic porosity exist in the northern and southern parts of the study area (fig. 3). The amount of moldic porosity in sections Z, X, R, and Q is 10 to 30 percent of the

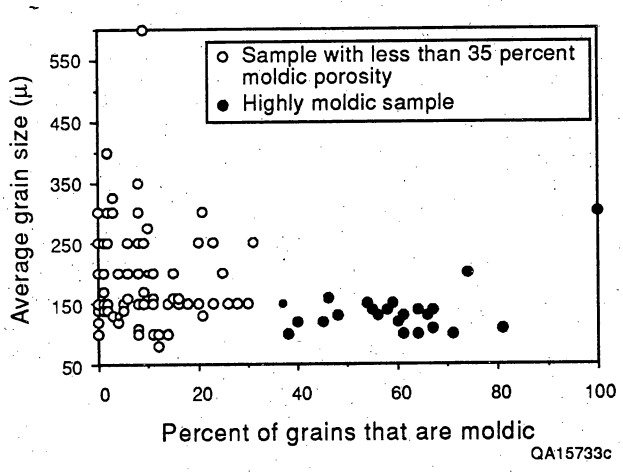

Figure 3. The dominant grain in most samples from parasequence 7 is 150-μm peloids. Percentage of original grains that are now molds exhibit a modal grain size in this range.

bulk volume, removing 20 to 80 percent of the grains. At the updip and more seaward parts of the cross section (sections H, A, and Q), moldic pores are less than 10 percent of the bulk volume, removing less than 10 percent of the grains. No consistent trend in the amount of moldic porosity from base to top is recognized, and no direct relationship can be identified between facies and the distribution of moldic pores (compare figure 1 with figure 3).

Grain Deformation and Cementation

Two types of dolomite cement are recognized in parasequence 7. A first generation of isopachous rim cement is the pervasive dolomite cement type, recognized in all grainstones. Variable amounts of fine-grained (10 to 20 μm) equant intergranular dolomite cement postdate the rim cement in areas with normal preserved grainstone fabrics or molds. These two generations of cement cannot be consistently separated, and therefore were described but not separated during point-counting. Syntaxial overgrowths did not develop on echinoderms. Micrite rims or other features limiting overgrowths are not identified.

Systematic variations in the amount of dolomite cement in grainstones are observed. A relationship is observed between abundant molds, underpacking, and abundant dolomite cement (fig. 4). In intervals with the most abundant molds, only 40 to 60 percent of the bulk volume of the rock is composed of grains and grain molds. The remaining volume is 0 to 60 percent dolomite spar (cement plus possible coarsely recrystallized grains and micrite), intergranular pores, and variable amounts of late diagenetic phases (large vugs and calcite). The increased cement is petrographically identified as equant intergranular dolomite spar precipitated after the rim cement. Increased cement in areas with abundant molds corresponds to decreased intergranular porosity (fig. 5).

Deformation of grains is common in peloid grainstones. The deformation is distinctive in that concentric banding within ooids and coated grains indicates that the deformation has occurred evenly through the grain instead of being localized on the grain margins, and that the

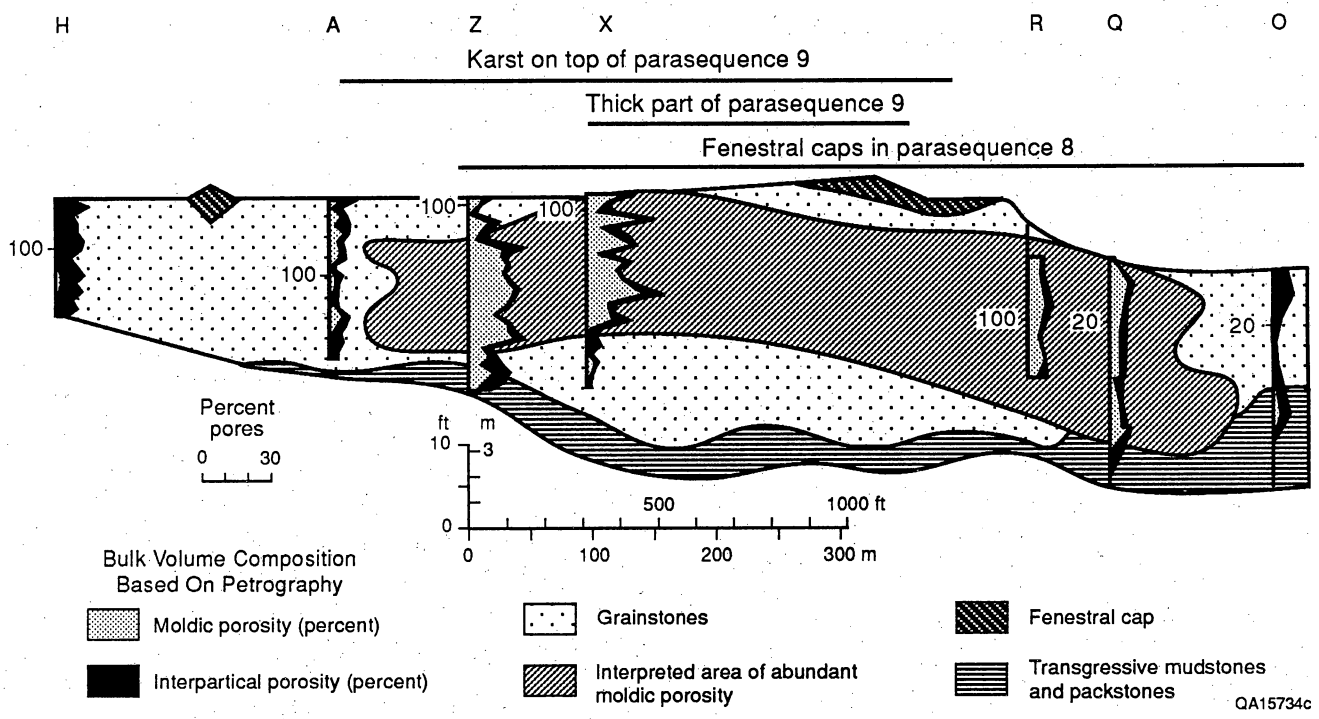

Figure 4. The geographic control of the distribution of total moldic porosity in parasequence 7 is apparent in the cross section along the Algerita Escarpment.

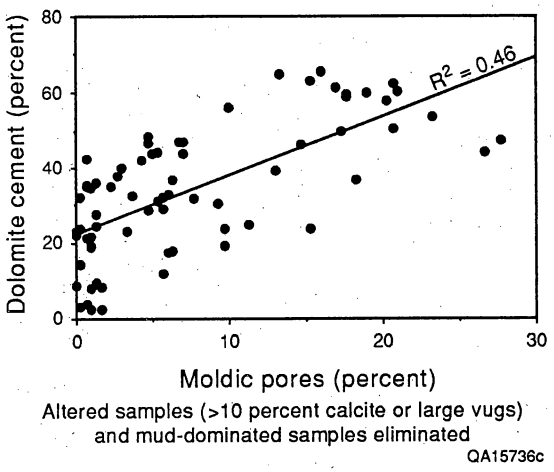

Figure 5. The percent dolomite cement (rim cement and intergranular cement not separated) increases directly with the percent molds. Wide scatter of data reflects other variables that contribute to percent cement, such as compaction, amount of calcite and leached void space, and amount of rim cement.

10- to 15-μm rim cement is not thinned or removed in areas where grains have indented each other (fig. 6). The result is closely packed grains having little or no intergranular porosity, with each grain conforming to the shape of its surrounding grains but separated from them by a 10- to 15-μm rim of dolomite cement. Grains are typically flattened to a third of their presumed original spherical shapes and can be flattened to 10-μm-thick wisps. On a macroscopic scale, deformed layers are gradationally interbedded with nondeformed layers, supporting the assumption that the deformed grains and preserved spherical grains were initially similar. Micritic, possibly algal, grains are most susceptible to deformation; skeletal grains such as mollusks are not deformed, and peloids and ooids exhibit an intermediate amount of deformation. Molds of round grains are not flattened, although some molds of elongated mollusk fragments may be partly collapsed. In highly moldic rocks, neither molds nor preserved grains are deformed. Deformation of possibly similar origin is recognized in fusulinid skeletons. Fusulinids can be deformed from their original round cross sections by a factor of 1/3 to 1/8 with increasing amounts of destruction of original chambered fabric.

Large Vugs, Leaching, and Calcite Cement

Several other variables probably have a locally important influence on porosity/permeability relationships; however, these variables are difficult to quantitatively separate from each other and from previously described pore/grain/compaction/cement relationships. Some samples with large vugs also have higher than average permeability, although the rest of the rock fabric is similar to other samples, suggesting that some large vugs may function as touching vugs (Lucia, 1983). Upper San Andres rocks of the Algerita Escarpment probably were anhydrite cemented in the same way as equivalent rocks are in the subsurface (for example, Chuber and Pusey, 1985; Bebout and others, 1987; Ruppel and Cander, 1988) and anhydrite has been leached in the shallow-burial or near-surface environment. Evidence of the former presence of anhydrite in the Lawyer Canyon outcrops is rare preserved molds of anhydrite

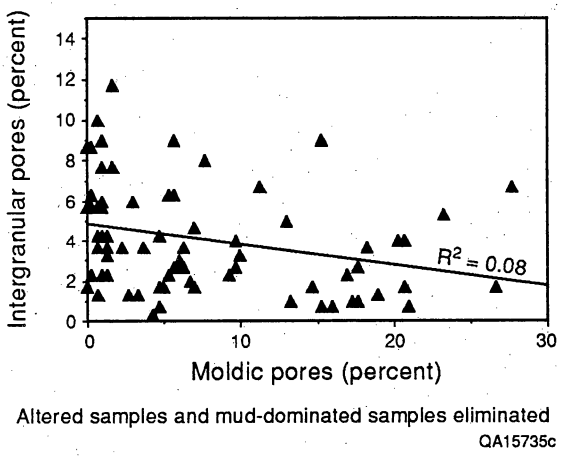

Figure 6. Correspondingly, the percent intergranular pore space (based on point count), has a general inverse relationship to percent of molds. Large scatter reflects other factors contributing to development of intergranular pore space, such as compaction and amount of leached void space and calcite.

laths and locally preserved anhydrite in silicified nodules. Molds and vugs larger than the average grain size have distributions similar to those of the various forms of anhydrite nodules in the subsurface. By analogy with subsurface samples, poikilotopic anhydrite cement probably filled intergranular and moldic pores and replaced variable amounts of grains and cement. However, diagnostic petrographic evidence for the former presence of this kind of anhydrite has not been recognized in outcrop samples.

Variable amounts of coarse sparry calcite fill all pore types including intergranular pores, leached molds, and molds after anhydrite. Large amounts of calcite are not characteristic of dolomitized San Andres shelf grainstones in the subsurface. Because the calcite fills molds of leached anhydrite, calcite is interpreted as a late diagenetic phase precipitated when anhydrite and gypsum were leached in the shallow subsurface. Calcite is partly analogous to anhydrite cement in the subsurface in that it is a diagenetic phase that variably reduces porosity. However, calcite does not consistently replace anhydrite in the same locations or in the same volume, as demonstrated by molds of anhydrite nodules and laths that are variably open, partly or completely filled with calcite. Fine-grained, inclusion-rich (brown in transmitted light) calcite travertine or caliche with several types of complex fabrics is the final cement generation.

Karstic vugs created by carbonate dissolution during Permian and modern surficial weathering are recognized in core and outcrop but are difficult to distinguish from leached anhydrite on a thin-section scale.

ANALYSIS OF POROSITY/PERMEABILITY RELATIONSHIPS RELATED TO PETROGRAPHIC OBSERVATIONS

Porosity/Permeability Relationships

The control by original depositional fabric (mudstone-wackestone-packstone-grainstone) on porosity and permeability is obscured San Andres cycle 7 because of the variations

introduced by diagenetic overprints (fig. 7). Only in the case of mudstones and mud-rich wackestones are fabric-controlled low porosity and permeability preserved. Several types of diagenetic controls on porosity/permeability relationships can be identified:

(1) Grainstones with abundant moldic porosity (greater than 10 percent bulk volume) plot with an offset porosity/permeability relationship compared with nonmoldic grainstones in which much of the porosity is intergranular (fig. 8). This offset demonstrates that, as expected (Lucia and Conti, 1987), moldic porosity functions as separate-vug porosity and is not as effective in transmitting fluids as intergranular porosity.

(2) An increase in the volume percent of intergranular dolomite cement is observed in samples with abundant molds (fig. 4), causing a corresponding decrease in the percentage of intergranular porosity and therefore a decrease in permeability. Development of moldic porosity is therefore an important diagenetically controlled cause of heterogeneities in the permeability of grain-rich rocks of parasequence 7.

(3) Compaction and grain deformation result in decreased porosity and permeability. This distinctive compaction is generally associated with restricted-shelf or hypersaline grainstones rather than with open-marine intervals (Bebout and others, 1982; Bein and Land, 1982; Fracasso and Hovorka, 1986); however, its origin remains undetermined.

(4) Subsurface fabrics are overprinted by fabrics interpreted as related to shallow-subsurface alteration or to outcrop weathering. This includes development of large vugs by leaching of anhydrite and carbonate and precipitation of variable amounts of calcite spar and travertine cement.

Interpretation of Diagenetic Fabrics

Several observations concerning the distribution of abundant molds and comparison of petrographic relationships between those areas with abundant molds and those with few molds are useful for development of a predictive model.

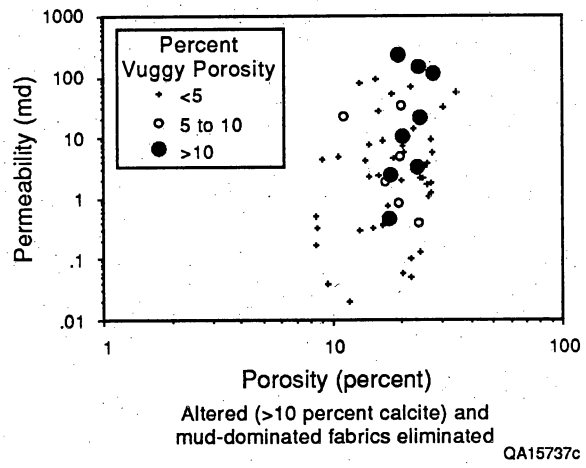

Figure 7. No clear-cut relationship between porosity/permeability trends and rock fabric is apparent, reflecting the significance of diagenetic overprints.

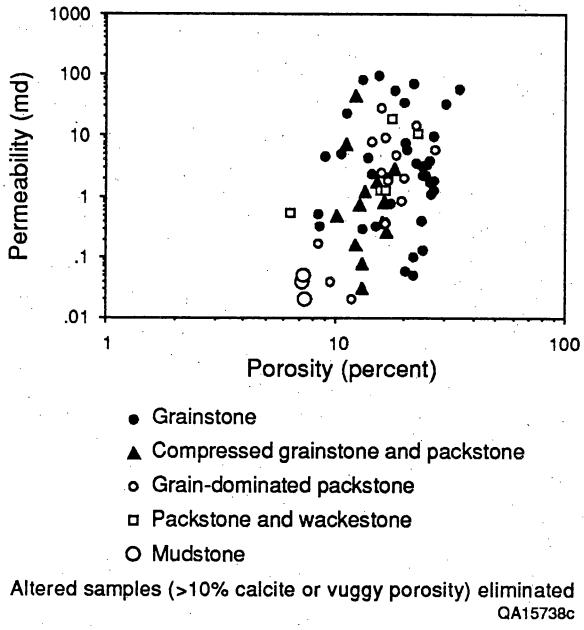

Figure 8. Porosity/permeability trends show separate trends for samples with abundant molds and those with few molds. Percent molds is volume percent, on the basis of point counting; porosity and permeability data are from plug analysis. Molds are identifiable leached grains, distinct from larger vugs of a variety of origins.

Most grainstones in parasequence 7 have an early generation of 10-μm dolomite rimming grains (fig. 9a). This early generation is similar in thickness and abundance in deformed grainstones (fig. 9d) to the first cement generation in moldic grainstones (fig. 9b) and therefore is presumed to have formed during the same diagenetic event. The thickness and distribution of the 10-μm rim cement are not affected by the deformation of the grains and therefore cement precipitation is interpreted as predating compaction.

The grains with abundant moldic porosity have the most open intergranular packing, reflected in the abundance of intergranular cement (fig. 9b). The good correspondence between molds, abundant intergranular dolomite cement, and loose packing suggest a genetic relationship. Abundant cement could have been locally derived from dissolution of metastable aragonite and high-magnesium-calcite grains. Local derivation of intergranular cement might indicate dissolution and precipitation in a hydrologic system that was sluggish or partly closed, similar to the hydrology observed beneath modern ooid sand islands in the Bahamas (Budd, 1988; Vacher and others, 1990). The abundance of intergranular cement in highly moldic rocks compared with that of sparsely moldic rocks indicates cementation before compaction and dates formation of molds to the shallow-burial environment.

Porosity of wet, well-sorted sand is experimentally determined as about 45 percent and varies only slightly with sorting and grain size (Beard and Weyl, 1975). High cement volumes (more than 45 percent) (fig. 4) may be partly the result of point-counting errors caused by the inability to identify some grains or areas of original carbonate mud matrix in dolomitized and cemented grainstones. However, inspection of spacing between preserved grains in moldic rocks (fig. 2d) supports the observation based on point-counting that moldic rocks are characterized by abundant intergranular cement. Abundant intergranular cement might indicate introduction of displacive cement such as that found in caliche (Walls and others, 1975); however, other features diagnostic of vadose diagenesis or caliche formation have not been recognized.

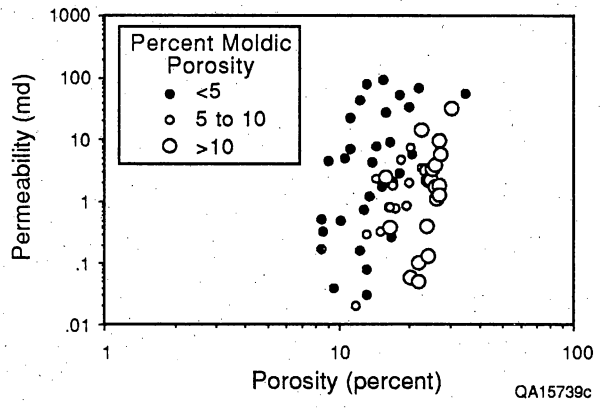

Figure 9. Three endmember fabrics formed after (a) precipitation of initial 10-μm cement rims; (b) most grains were leached and abundant intergranular cement precipitated; (c) minor intergranular cement precipitated around preserved grains, allowing some compaction but preserving most of the intergranular porosity; and (d) compaction of grains, resulting in internal deformation and loss of most intergranular pore space.

Grains of several different initial mineralogies were dissolved, indicating pore water was significantly undersaturated with respect to aragonite and high-magnesium calcite (Walter, 1985). This undersaturated water could have been formed under a variety of conditions, including sea-level drop, exposure, and influx of meteoric water or locally increased P_{CO_2}. Absence of syntaxial rims on echinoderms with no apparent micrite rims may indicate precipitation of cement as a mineral other than calcite.

The zone dominated by moldic porosity is found in the thickest parts of parasequence 7 (fig. 3). The thick part of parasequence 7 has a thin fenestral cap, documenting an episode of exposure terminating deposition of that parasequence. Parasequence 8 contains fenestral beds overlying the area of moldic porosity. The thick southern part of parasequence 9 is coincident with the thickest part of parasequence 7 and has karst pits at the top infilled with sediments of the overlying cycles, documenting sea-level drop and prolonged exposure. Evidence of the exposure of bar crests suggests the possibility of development of fresh-water lenses. Coincidence between the distribution of abundant moldic pores with bar crests and the distribution of exposure surfaces capping parasequences 7, 8, and 9 suggests that moldic porosity may have originated in the fresh-water lens associated with one or more of these exposure events.

Combining these observations, the following diagenetic history is proposed: (1) Precipitation of early 10-μm rim cements (mineralogy not determined) occurred in all parts of the study area prior to emergence. (2) The thickest parts of parasequence 7 were locally exposed during formation of fenestral caps or during the event of exposure and karstification of the top of parasequence 9. (3) An undersaturated phreatic lens developed causing dissolution of grains and precipitation of intergranular cement. Analogous moldic porosity and early intergranular cement are observed in fresh-water lenses beneath modern ooid sand islands in the Bahamas (Budd, 1988; Vacher and others, 1990). Aragonite and high-magnesium calcite allochems dissolve and equant calcite cement precipitates in the fresh-water lens in the very shallow burial environment.

CONCLUSIONS

(1) Abundant moldic pores in upper San Andres parasequence 7 of the Lawyer Canyon area cause a decrease in permeability for a given porosity on a porosity/permeability cross plot. This diagenetic effect is considered in flow models of the Lawyer Canyon area (Kasap, this report) and should be considered in modeling analogous areas in the subsurface.

(2) Correspondence between moldic pores and abundant intergranular cement, abundance of intergranular cement indicating precipitation prior to compaction, and localization of moldic pores in and beneath the thick and subaerially exposed parts of parasequences 7, 8, and 9 are interpreted as evidence that moldic porosity formed early, possibly related to a fresh-water lens beneath an exposed bar crest. If geometry of grainstone bars is mapped on an individual parasequence scale, areas of thick grainstones with low-permeability caps, potentially topographic high points of grainstone bars with fenestral caps indicating local exposure, can be identified. Exposed bar crests are areas of potential development of fresh-water lenses. The fresh-water lens may cause development of abundant moldic porosity and corresponding precipitation of abundant cement. Association of moldic porosity with facies therefore can be used as a predictive model for distribution of areas of anomalously low permeability/porosity ratios in reservoirs.

REFERENCES

Beard, D. C., and Weyl, P. K., 1973, Influence of texture on porosity and permeability of unconsolidated sand: American Association of Petroleum Geologists Bulletin, v. 57, p. 349–369.

Bebout, D. G., Budd, D. A., and Schatzinger, R. A., 1981, Depositional and diagenetic history of the Sligo and Hosston Formations (Lower Cretaceous) in South Texas: The University of Texas at Austin, Bureau of Economic Geology Report of Investigations No. 109, 69 p.

Bebout, D. G., Lucia, F. J., Hocott, C. R., Fogg, G. E., and Vander Stoep, G. W., 1987, Characterization of the Grayburg reservoir, University Lands Dune field, Crane County, Texas: The University of Texas at Austin, Bureau of Economic Geology Report of Investigations No. 168, 98 p.

Bein, Amos, and Land, L. S., 1982, Carbonate sedimentation and diagenesis associated with Mg-Ca-chloride brines: the Permian San Andres Formation in the Texas Panhandle: Journal of Sedimentary Petrology, v. 53, p. 243–260.

Budd, D. A., 1988, Aragonite-to-calcite transformations during fresh-water diagenesis of carbonates: insights from pore-water chemistry: Geological Society of America Bulletin, v. 100, p. 1260–1270.

Chuber, Stewart, and Pusey, W. C., 1985, Productive Permian carbonate cycles, San Andres Formation, Reeves field, West Texas, *in* Roehl, P. O., and Choquette, P. W., eds., Carbonate petroleum reservoirs: New York, Springer-Verlag, p. 292–307.

Fracasso, M. A., and Hovorka, S. D., 1986, Cyclicity in the middle Permian San Andres Formation, Palo Duro Basin, Texas Panhandle: The University of Texas at Austin, Bureau of Economic Geology Report of Investigations No. 156, 48 p.

Lucia, F. J., 1983, Petrophysical parameters estimated from visual descriptions of carbonate rocks: a field classification of carbonate pore space: Journal of Petroleum Technology, v. 35, no. 3, p. 629–637.

Lucia, F. J., and Conti, R. D., 1987, Rock fabric, permeability, and log relationships in an upward-shoaling vuggy carbonate sequence: The University of Texas at Austin, Bureau of Economic Geology Geological Circular 87-5, 22 p.

Ruppel, S. C., and Cander, H. S., 1988, Effects of facies and diagenesis on reservoir heterogeneity: Emma San Andres field, West Texas: The University of Texas at Austin, Bureau of Economic Geology Report of Investigations No. 178, 67 p.

Vacher, H. L., Bengtsson, T. O., and Plummer, N. L., 1990, Hydrology of meteoric diagenesis: residence time of meteoric ground water in island fresh-water lenses with application to aragonite-calcite stabilization rate in Bermuda: Geological Society of America Bulletin, v. 102, p. 223–232.

Walls, R. A., Harris, W. B., and Nunan, W. E., 1975, Calcareous crusts (caliche) profiles and early subaerial exposure of Carboniferous carbonate, northeastern Kentucky: Sedimentology, v. 22, p. 417–440.

Walter, L. M., 1985, Relative reactivity of skeletal carbonate during dissolution: implications for diagenesis, *in* Schneidermann, Nahum, and Harris, P. M., eds., Carbonate cements: Society of Economic Paleontologists and Mineralogists Special Publication No. 36, p. 3–16.

GEOLOGICAL ENGINEERING ASPECTS OF THE SAN ANDRES RESERVOIR IN THE LAWYER CANYON, ALGERITA ESCARPMENT, OUTCROP AND SEMINOLE, SUBSURFACE FIELD

by F. Jerry Lucia

INTRODUCTION

The goal of reservoir description is to describe the spatial distribution of petrophysical parameters such as porosity, permeability, and saturation. Geologic concepts of sedimentation, diagenesis, and tectonics provide the basis for constructing a three-dimensional reservoir framework. Engineering measurements from wireline logs, core analysis, production history, pressure analysis, and tracer tests provide quantitative measurements of the petrophysical parameters in the vicinity of the wellbore. Rock-fabric studies relate rock texture to pore-size distribution and are the key element necessary to convert geologic descriptions into engineering measurements for input into computer simulators.

Classification of Carbonate Porosity by Rock-Fabric Method

Pore space in carbonate rocks can be divided into interparticle and vuggy pores on the basis of the particulate nature of carbonate rocks. The pore size and distribution of interparticle porosity is controlled by particle size, sorting, and volume of interparticle porosity. Two classes of particle size and sorting are recognized: (1) mud-dominated, where the interparticle space is filled with lime mud, and (2) grain-dominated, where the interparticle space is partially filled or free of lime mud (fig. 1). To relate this to Dunham's classification, the packstone category must be split into grain-dominated packstones and mud-dominated packstones.

Dolomitization may increase the particle size and thus the interparticle pore size. Mud-dominated fabrics with dolomite crystal sizes larger than 20 microns (μm) are grouped into two classes: medium crystal size (20 to 100 μm) and large crystal size (>100 μm) (fig. 2). Dolomite crystal size has little effect on the pore size of grainstone fabrics. However, the pore size of

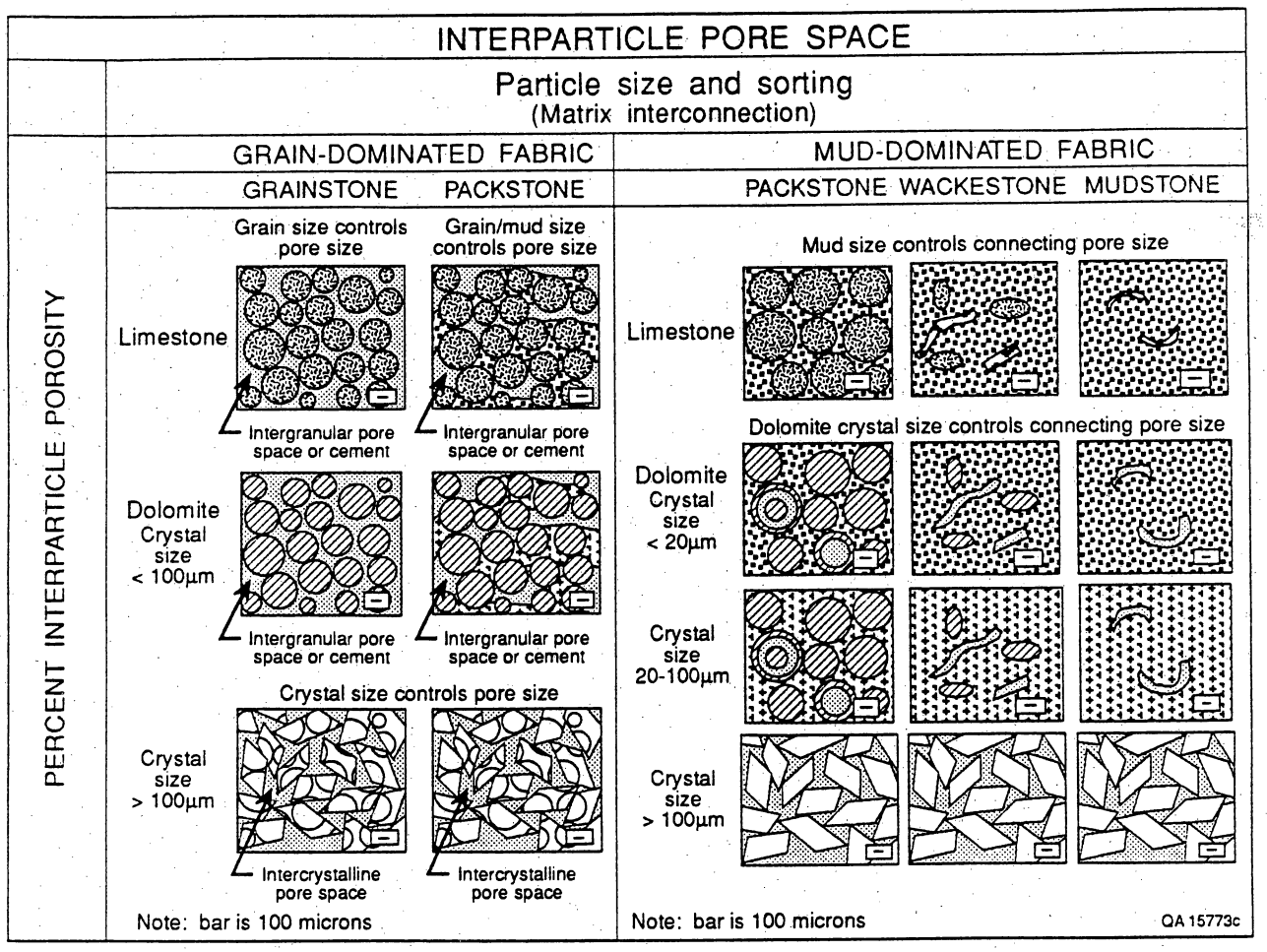

Figure 1. Classification of interparticle pore space.

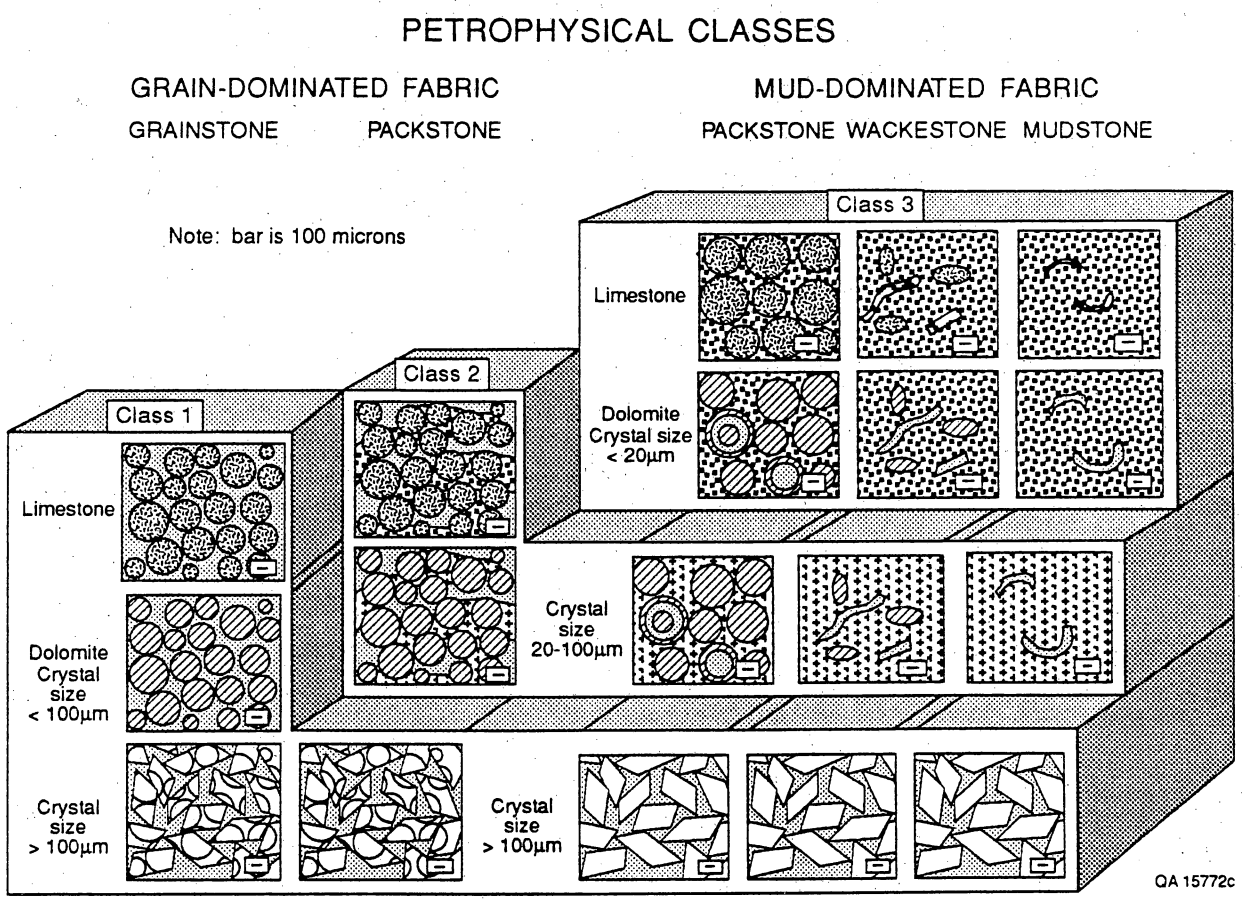

Figure 2. Petrophysical/rock-fabric classes.

grain-dominated packstones will increase when replaced by dolomite crystals greater than 100 μm in diameter.

Three petrophysical classes are recognized (fig. 2). The most favorable petrophysical characteristics are in a class composed of grainstones, dolograinstones with any size of dolomite crystals, and mud-dominated dolomites with large crystal sizes (>100 μm). The least favorable petrophysical characteristics are in a class composed of mud-dominated limestones and dolomites with fine crystal sizes (<20 μm). A class with intermediate petrophysical characteristics is composed of grain-dominated packstones, both limestones and dolomites with crystal sizes less than 100 μm, and medium crystal mud-dominated dolomites.

The three petrophysical classes can be expressed in permeability as shown in figure 3. Generic porosity-permeability transforms for the three classes are given as follows:

Grainstones and dolograinstones	$\text{LOG } k = 9.82 + 8.65 \text{ LOG } \phi$	(1)
Grain-dominated packstones and medium crystalline mud-dominated fabrics	$\text{LOG } k = 6.31 + 6.38 \text{ LOG } \phi$	(2)
Mud-dominated and fine crystalline dolomud-dominated fabrics	$\text{LOG } k = 4.02 + 4.82 \text{ LOG } \phi$	(3)

The three petrophysical classes can also be expressed in saturation as shown in figure 4. The relationships between particle size and sorting, interparticle porosity, and water saturation were derived using mercury capillary pressure curves from samples of the same petrophysical class. The equations expressing the relationships are given as follows:

Grainstones and dolograinstones	$S_w = .022192 \times H^{-0.316} \times \phi^{-1.745}$	(4)
Grain-dominated packstones and medium crystal dolomud-dominated fabrics	$S_w = 0.14038 \times H^{-0.407} \times \phi^{-1.440}$	(5)

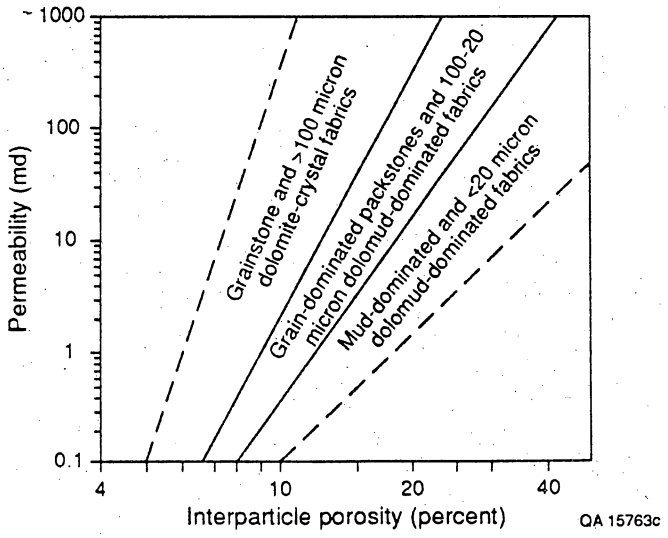

Figure 3. Porosity-permeability relationships of various rock-fabric fields in nonvuggy carbonate rocks.

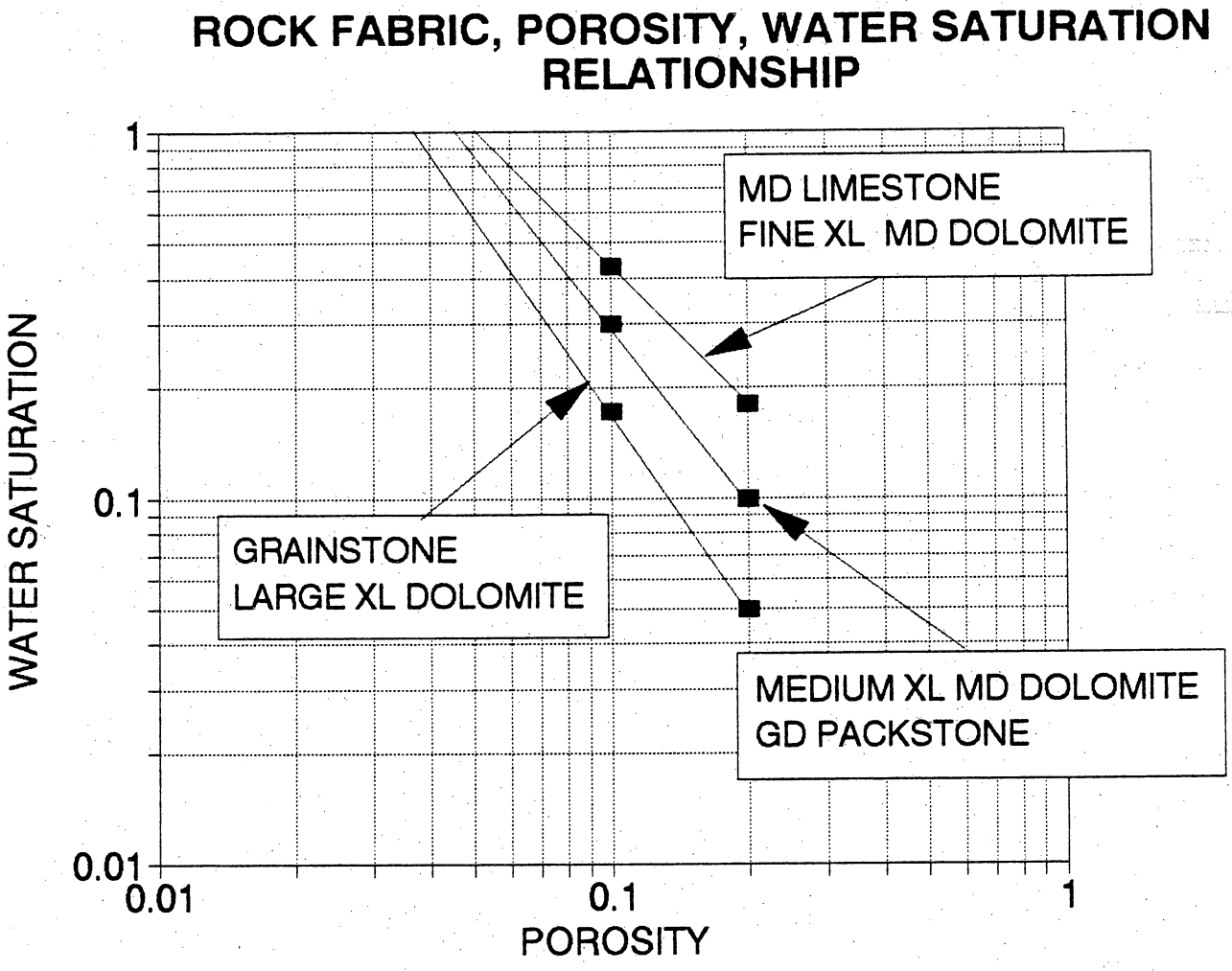

Figure 4. Rock-fabric, porosity, and water saturation relationships from capillary pressure curves.

Mud-dominated and fine crystal dolomud-dominated fabrics	$S_w = 0.6110 \times H^{-0.505} \times \phi^{-1.210}$	(6)

Vuggy pore space is divided into separate vugs and touching vugs on the basis of the type of interconnection (fig. 5). Separate vugs are connected only through interparticle pore space, and some examples include moldic pores, composite moldic pores, intrafossil pores, microporosity in grainstones, and shelter pores in mud-dominated carbonates. Touching vugs form a connecting pore network on the interwell scale. Cavernous, fracture, and breccia porosity are examples.

Separate-vug pore space reduces permeability from what would be expected if the porosity were all interparticle. However, permeability is higher than would be expected from interparticle porosity in a touching-vug pore system. With the exception of intraparticle microporosity, a vuggy pore type that is normally filled with water, vuggy pore space is large enough that it is thought to be filled with hydrocarbon.

Geologic descriptions can be quantified in engineering terms if they characterize rock fabrics. Three petrophysical/rock-fabric fields are recognized that define unique transforms between (1) permeability and interparticle porosity and (2) water saturation, interparticle porosity, and reservoir height. This approach has been used in the study of the San Andres outcrop and Seminole (San Andres) reservoir, as described next.

APPLICATION OF PETROPHYSICAL/ROCK-FABRIC APPROACH TO LAWYER CANYON (UPPER SAN ANDRES) OUTCROP

Rock samples from the upper San Andres outcrop at Lawyer Canyon are composed of dolomite, sparry calcite, and minor amounts of replacement quartz and authigenic clay. The crystal size of the dolomite averages about 15 μm, except for the grainstones in the upper part of parasequence 9, where the dolomite crystal size averages about 100 μm.

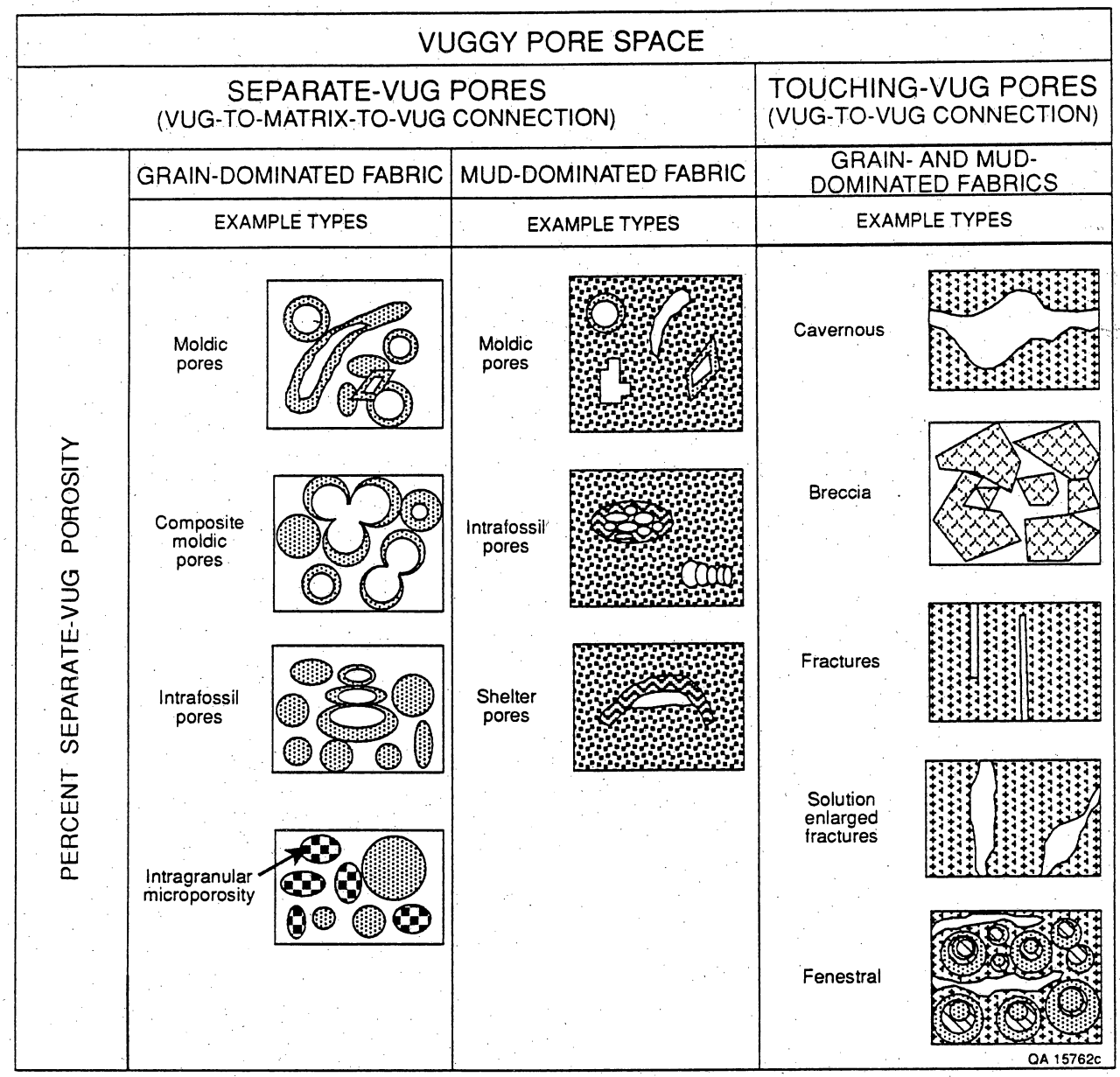

Figure 5. Classification of vuggy porosity.

Outcrop Effects

Features that affect petrophysical properties, which can be directly related to uplift and exposure of the San Andres outcrop, are fracturing, cave development, travertine precipitation, and the dissolution of gypsum and anhydrite to form vugs and breccias. Every effort was made to avoid these features when taking samples for petrophysical analysis. Some samples, however, contain a gravity-oriented fibrous calcite cement similar to travertine, which is believed to be a product of uplift and subaerial exposure. Samples with travertine were discarded from the data set.

One of the major concerns at the onset of the study was the comparison of outcrop and subsurface petrophysical data, because calcium sulfate typically is a major porosity occluder in San Andres reservoirs but is absent in the outcrop study area. The one-time presence of anhydrite is indicated by anhydrite inclusions in diagenetic quartz crystals.

Sparry calcite was present in many samples and is believed to be a byproduct of sulfate dissolution. Calcite replacement of anhydrite in the Tansill Formation of the Guadalupe Mountains was suggested by Lucia (1961), and Back and others (1983) concluded that calcite in the Mississippian of the Black Hills area of South Dakota and Wyoming is related to dissolution of gypsum and dolomite. Whereas the shape of most of the sparry calcite found in upper San Andres samples from the Algerita Escarpment does not indicate a sulfate precursor, a few sparry calcite blebs have straight sides and rectangular reentrants suggesting they are pseudomorphic after poikilotopic anhydrite crystals (fig. 6).

Although as much as 40 percent sparry calcite is present in one sample, there is no relationship between calcite volume and porosity (fig. 7). This situation is similar to the relationship between poikilotopic anhydrite and porosity in San Andres reservoirs. Therefore, although the sparry calcite may not be replacing sulfate on a one-to-one basis, it is affecting the

Figure 6. Plane-polarized photomicrographs of outcrop samples: (a) Sparry calcite bleb with straight sides and rectangular reentrants interpreted to be pseudomorphic after replacement anhydrite. Width of photomicrograph is 3.4 mm. (b) Dolomitized grainstone with intergranular pore space and dolomite crystals 100 μm in diameter. Sample is from parasequence 9. Core-analysis porosity = 18.8 percent; permeability = 410 md. Width of photomicrograph is 0.8 mm. (c) Dolomitized grainstone from parasequence 7 illustrating separate-vug (moldic) pore space. Core-analysis porosity = 20.1 percent; permeability = 1.8 md. Width of photomicrograph is 3.4 mm. (d) Enlarged area of figure 6c, illustrating the presence of intergranular pore space as well as separate-vug pore space. Width of photomicrograph is 0.8 mm.

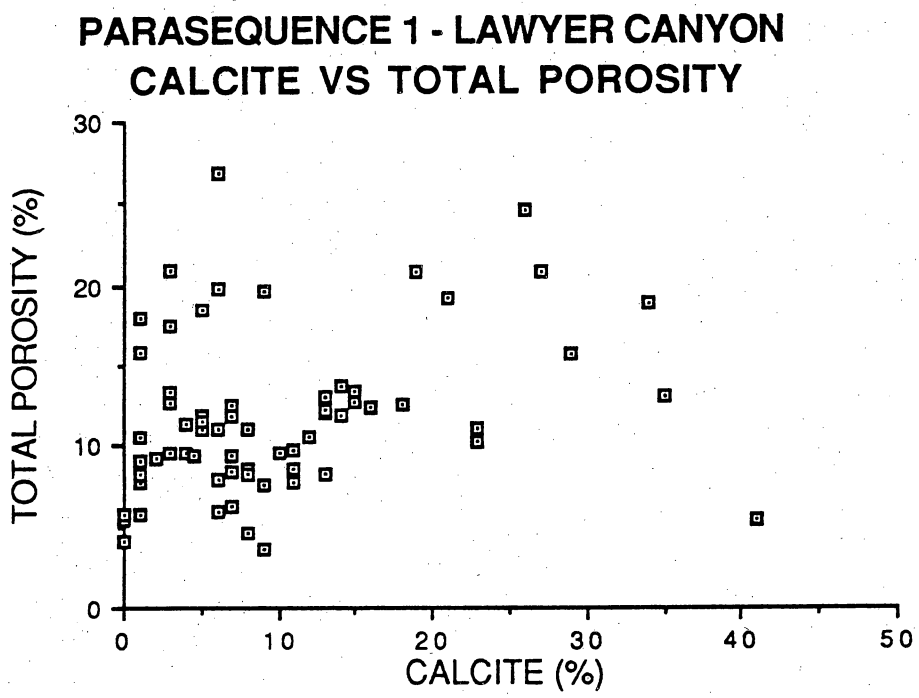

Figure 7. Cross plot of percent calcite versus percent porosity in samples from parasequence 1, showing no relationship between these two elements.

petrophysical properties of the samples in a manner comparable to that caused by anhydrite in San Andres reservoirs.

Rock Fabrics

Five productive rock fabrics are recognized: grainstones, grain-dominated packstones, and mud-dominated packstones, wackestones, and mudstones (fig. 8). The average porosity and geometric average permeability of these rock fabrics are given in table 1. The information is based on analysis of core plugs taken from the outcrop. In addition, two nonproductive fabrics are present but not included in table 1: mudstones and wackestones that are tight and dense, and fenestral fabrics that are assumed to be tight and dense.

Table 1. Average porosity and geometric average permeability of five productive rock fabrics.

Productive rock fabrics	Porosity (percent)	Permeability (geometric average, md)
Nonvuggy		
Grainstones	11.7%	10.7 md
Grain-dominated packstones	12.9%	1.9 md
Mud-dominated fine dolomite	10.5%	0.3 md
Vuggy		
Highly moldic grainstones	23.0	2.5 md
Moldic grainstones	15.9	2.2 md

The data in table 1 show that the average porosity of the nonvuggy productive fabrics does not vary significantly but the average permeability varies by an order of magnitude between each rock-fabric class. The porosity in the vuggy grainstone fabrics is high but the

Figure 8. Plane-polarized photomicrographs of outcrops samples illustrating classes of rock fabrics: (a) Dolomitized grainstone from parasequence 1, illustrating intergranular porosity. Core-analysis porosity = 12.3 percent; permeability = 71 md. Width of photomicrograph is 3.4 mm. (b) Dolomitized grain-dominated packstone from the lower part of parasequence 9, illustrating areas with intergranular pore space and areas of intergranular dolomitized mud. Core-analysis porosity = 11.3 percent; permeability = 0.68 md. Width of photomicrograph is 0.8 mm. (c) Dolomitized mud-dominated packstone from parasequence 9, illustrating intergranular dolomitized mud. Core-analysis porosity = 13.9 percent; permeability = 2.1 md. Width of photomicrograph is 3.4 mm. (d) Dolomitized wackestone from parasequence 1, illustrating sparry calcite after anhydrite replacing fossil material. Core-analysis porosity = 8.5 percent; permeability = 0.5 md. Width of photomicrograph is 3.4 mm.

permeability is lower than would be expected for a nonvuggy grainstone. The dolomite crystal size of all fabrics is about 15 μm, but the dolomite crystal size in the grainstone fabric of parasequence 9 is 100 μm. Despite this larger crystal size, figure 9 shows that grainstones in parasequence 9 group with dolomitized grainstones of fine crystal size from parasequences 1, 2, and 3, indicating that the dolomite crystal size is of little importance in describing the flow characteristics of grainstones. The porosity-permeability transform for the grainstone fabrics is given as follows:

$$\text{LOG } k = 9.3600 + 8.33 \text{ LOG } \phi. \qquad (7)$$

Types of separate-vug porosity observed are moldic, intrafossil, and intraparticle microporosity. Grainstones in parasequence 1 contain small amounts of microporosity within the grains, and permeability is reduced in the presence of this microporosity (fig. 10). Parasequence 7 contains as much as 30 percent moldic porosity. In the highly moldic fabrics (moldic porosity greater than 10 percent) the porosity averages 22 percent and the permeability varies from 0.5 to 20 md with decreasing amounts of moldic porosity (fig. 11). The moldic grainstone of parasequence 7 has an average porosity of 15 percent, and, again, the permeability increases as the separate-vug porosity decreases (fig. 12).

Rock-Fabric Flow Model

A flow model was developed by integrating the rock-fabric descriptions, parasequence framework, and average permeabilities (fig 13). Thin, dense, and tight mudstone beds form discontinuous flow barriers at the bases of the parasequences. Fenestral caps found at the top of some parasequences are considered to be dense and tight by analogy with those found in San Andres reservoirs.

Nonvuggy grainstones with permeabilities typically ranging from 10 to 100 md are found in parasequences 1, 2, 3, and 9. Grain-dominated packstones with permeabilities ranging from

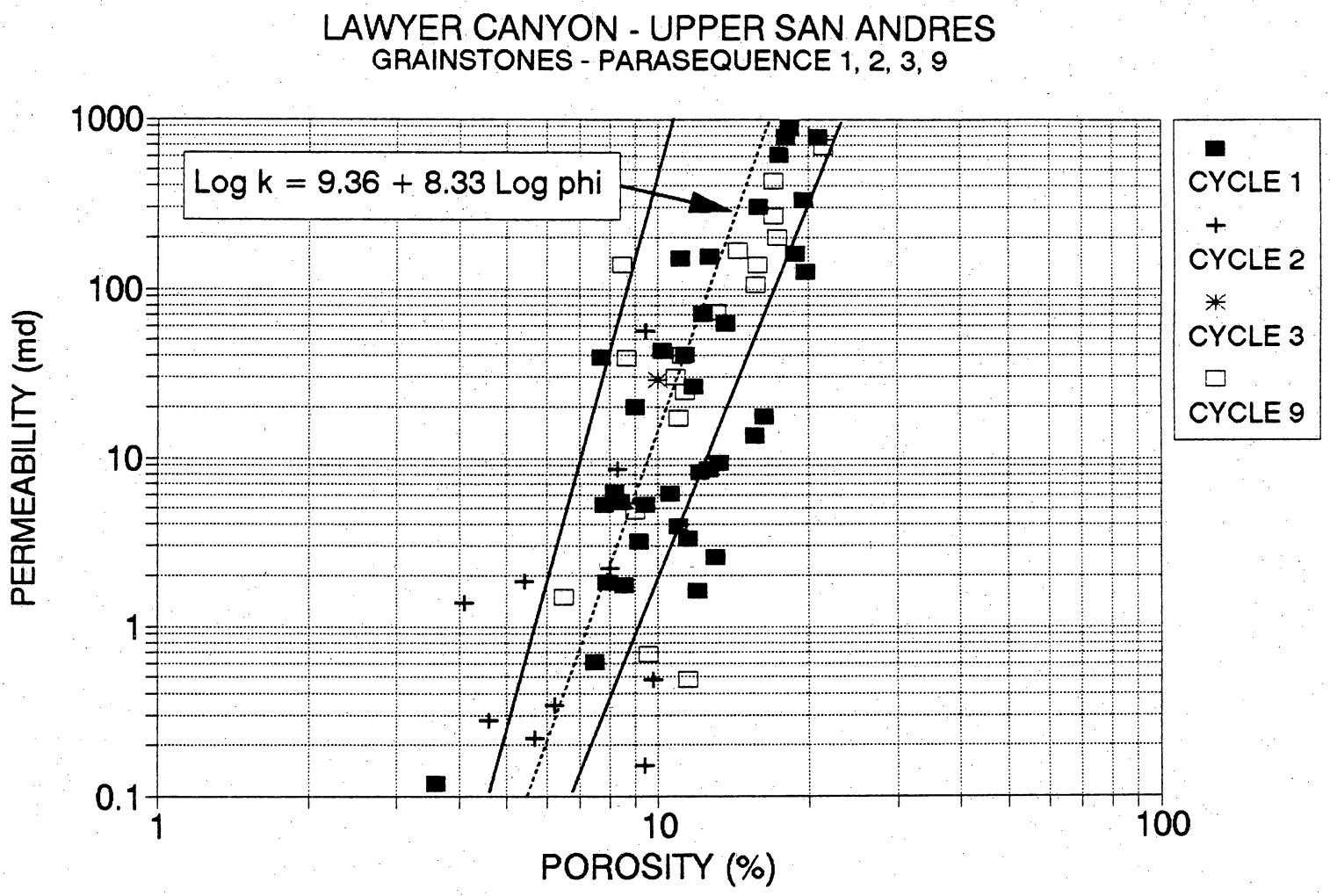

Figure 9. Porosity-permeability cross plot for grainstones of parasequences 1, 2, 3, and 9, compared with the grainstone petrophysical field.

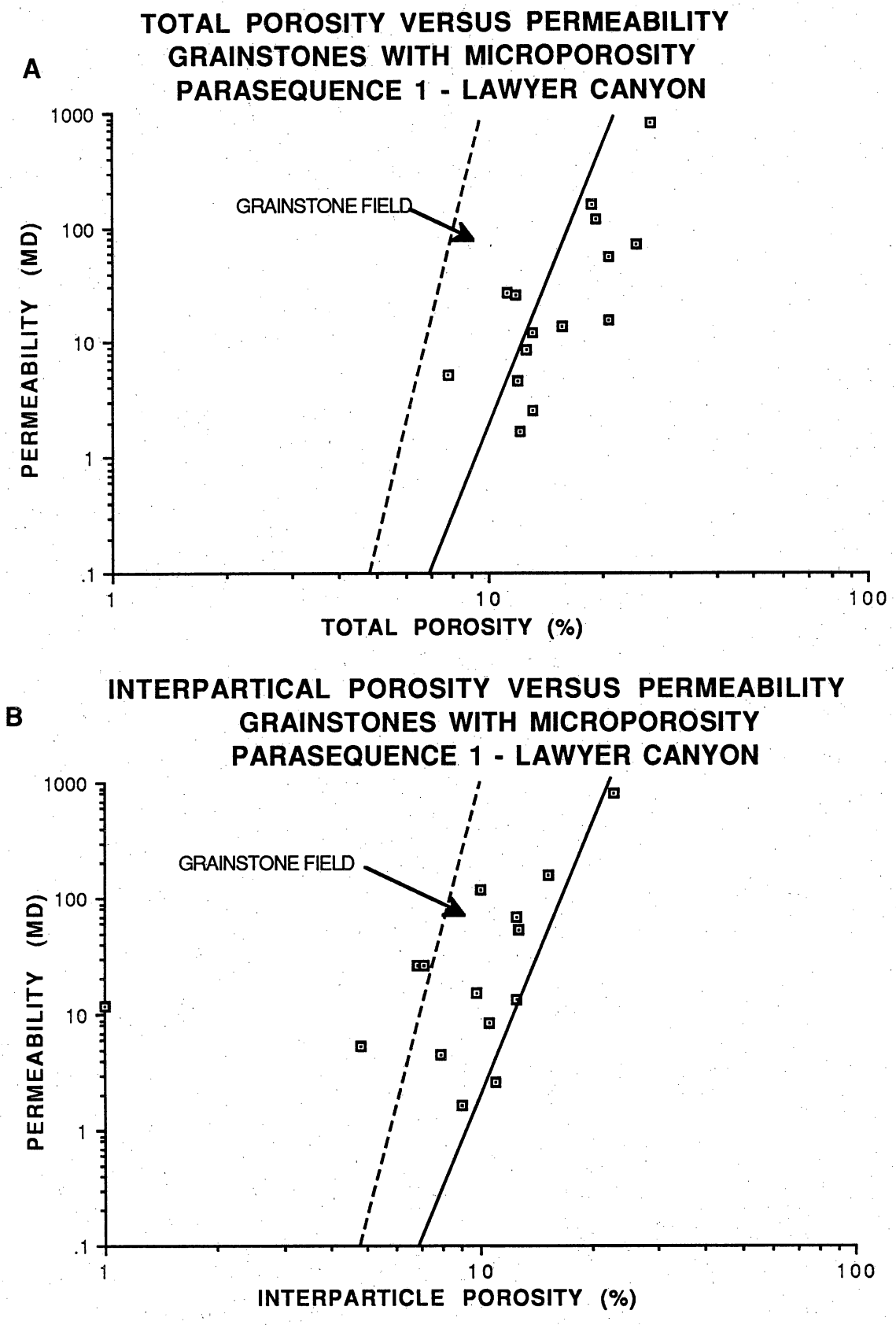

Figure 10. Effect of intragranular microporosity on permeability. (a) Porosity-permeability cross plot for parasequence 1 grainstones including intragranular microporosity in total porosity illustrating that the data points fall to the right of the grainstone petrophysical field. (b) Porosity-permeability cross plot for parasequence 1 grainstones using only interparticle porosity (total porosity less intragranular microporosity), illustrating that the data points fall within the grainstone petrophysical field.

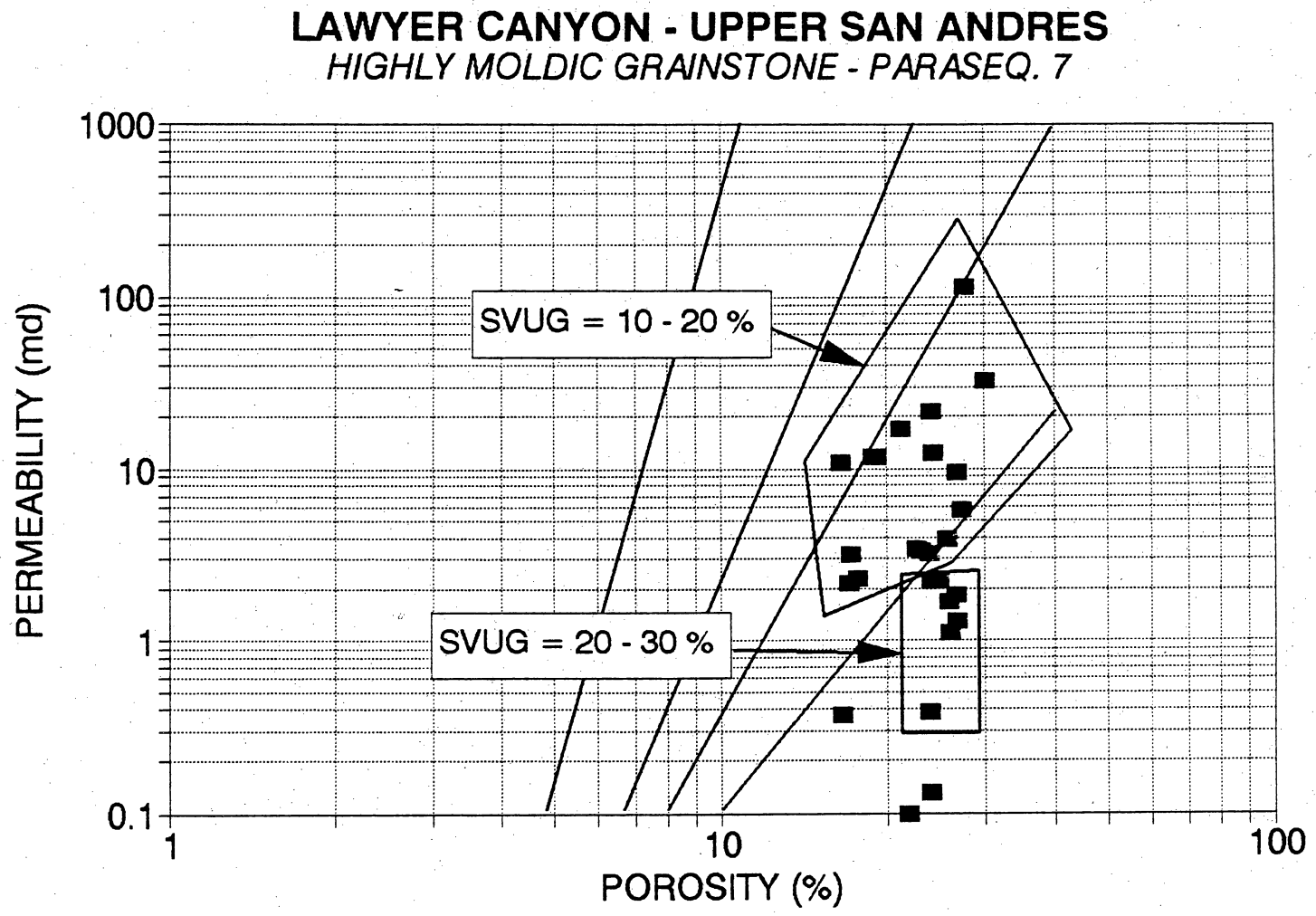

Figure 11. Porosity-permeability cross plot for the highly moldic grainstone facies of parasequence 7, illustrating that permeability is a function of separate-vug porosity. The three petrophysical fields are presented to illustrate that the data points fall well to the right of the grainstone field. Note that the porosity range does not vary with permeability.

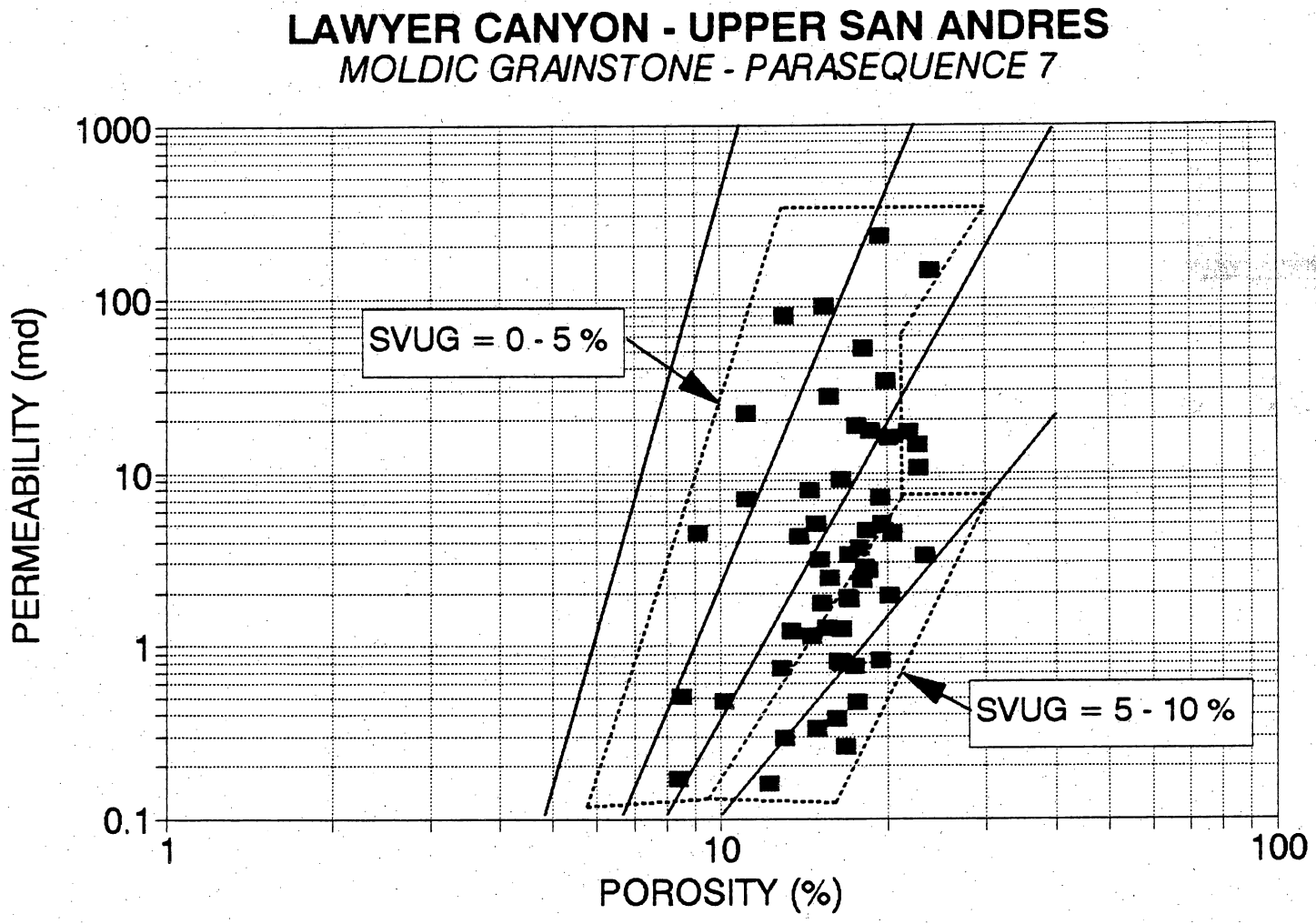

Figure 12. Porosity-permeability cross plot for the moldic grainstone facies of parasequence 7, illustrating that permeability is a function of separate-vug porosity. The three petrophysical fields are presented to illustrate that the data points with the least volume of separate vugs plot closest to the grainstone field.

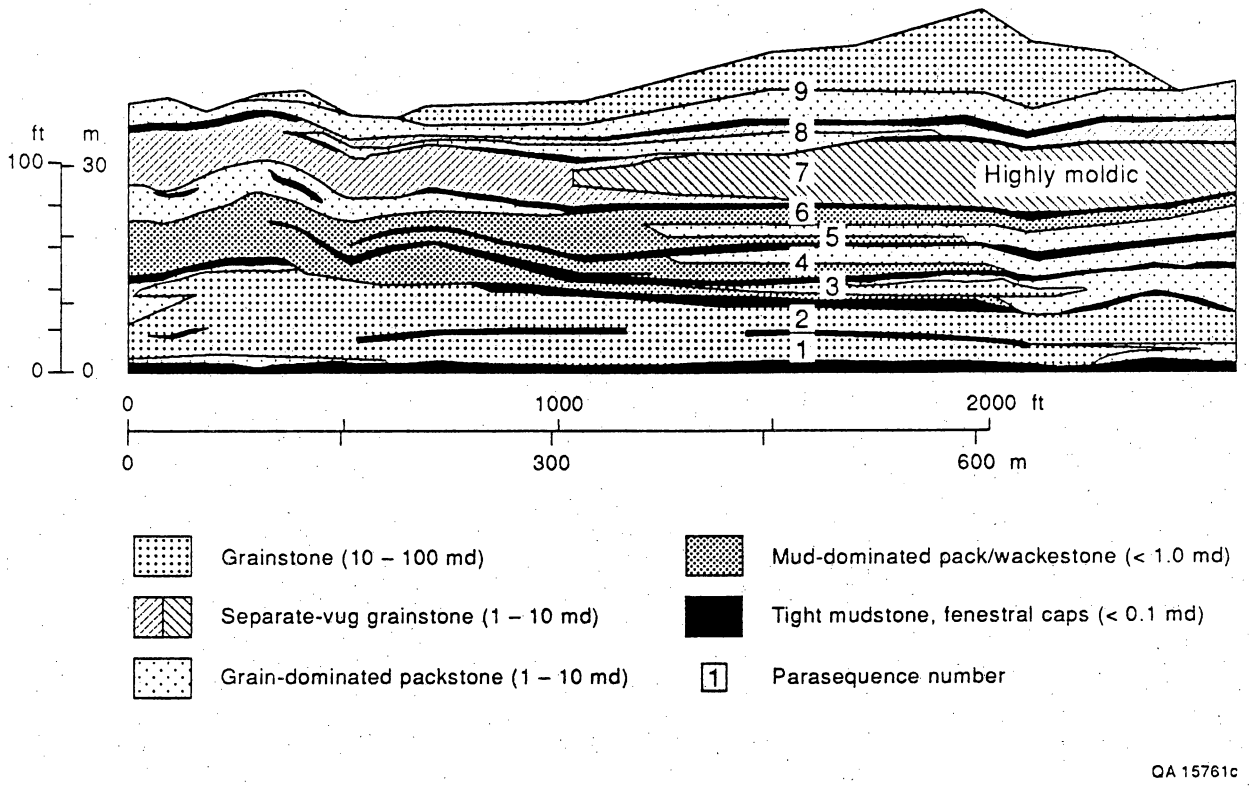

Figure 13. Rock-fabric flow units of the upper San Andres parasequence window, Lawyer Canyon, Algerita Escarpment, Guadalupe Mountains, New Mexico.

1 to 10 md and mud-dominated packstones and wackestones with permeabilities ranging from 0.1 to 1 md dominate parasequences 3 through 6 and 8. Separate-vug porosity is concentrated in parasequence 7, and the permeability ranges from 1 to 10 md.

Parasequence 1 is an ideal upward-shoaling sequence from tight, mud-dominated fabrics through slightly permeable grain-dominated packstone to permeable grainstones (fig. 14). The grainstone flow unit is continuous across most of the model but changes to grain-dominated packstone and mud-dominated fabrics at the southern end of the model (fig. 13). Grainstone flow units in parasequences 2 and 9 are very continuous, whereas the grainstone in parasequence 3 is isolated within packstones and wackestones (fig. 14). The rock fabrics in parasequences 3 through 6 change laterally from mud-dominated to grain-dominated across the model resulting in a lateral change in average permeability of about one order of magnitude.

In parasequence 7, the highly moldic fabric (>10 percent separate vugs) changes laterally to the moldic fabric with no change in average permeability, although the average porosity changes from 22 percent in the highly moldic to 15 percent in the moldic.

SEMINOLE RESERVOIR, UPPER INTERVAL

The Seminole (San Andres) reservoir is located on the northern edge of the Central Basin Platform in the Permian Basin. A two-section area in the northern sector of the reservoir was selected for a detailed reservoir study because of the excellent core control available (fig. 15). Only the detailed study of the upper interval of the productive zone has been completed. All 11 cores have been described and 1 core has been analyzed in detail using thin sections. Quantitative relationships between wireline-log response, rock fabrics, pore types, saturation, and permeability have been developed and used to define a rock-fabric flow model.

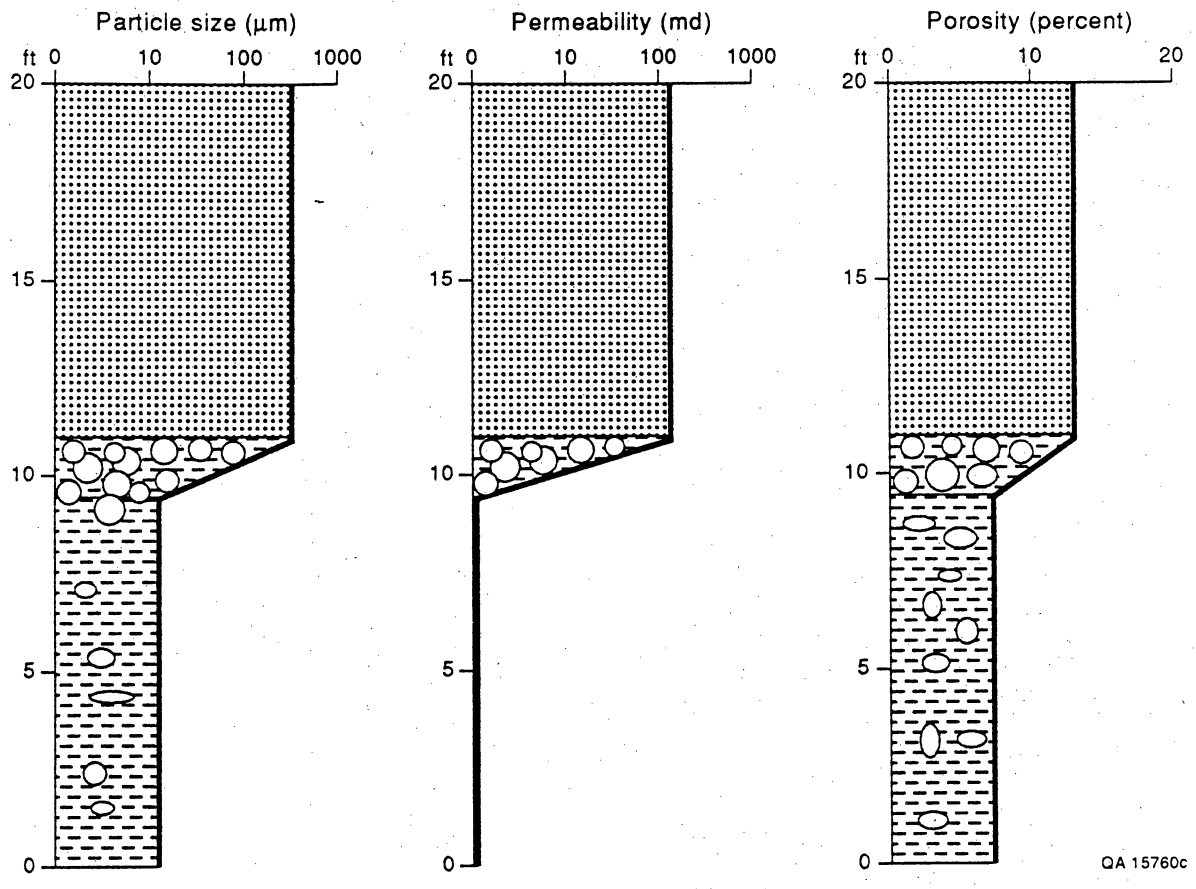

Figure 14. Vertical sequence of particle size, permeability, and porosity in parasequence 1.

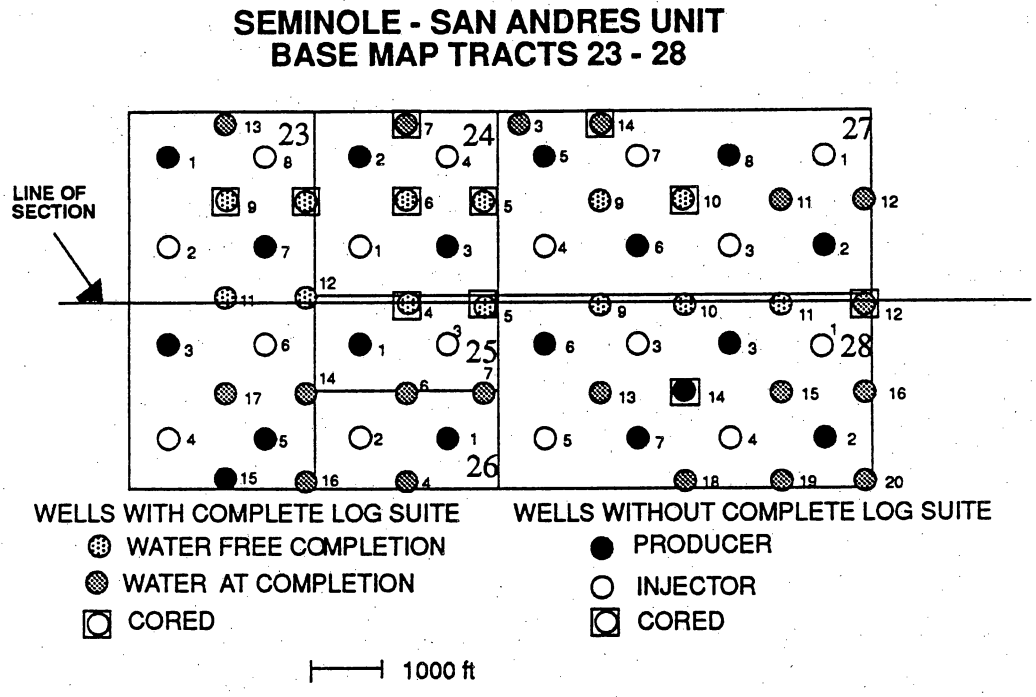

Figure 15. Index map of the two-section study area in Seminole field, Gaines County, Texas.

Core Description

The core from well 2505 was chosen for detailed thin-section analysis. Thin sections were prepared from each foot of core; 150 thin sections were prepared from the upper interval of the San Andres reservoir. Percentages of minerals, grains, mud, cement, interparticle pores, and separate vugs were determined by the point-count method. Average crystal and grain sizes were estimated using an ocular micrometer.

A detailed investigation into the accuracy and variability of porosity, permeability, and fabric elements was conducted on 12 whole-core samples. Three core plugs were taken from each of 12 whole-core analysis samples: 1 sample of grainstone, 4 samples of grain-dominated packstone, and 7 samples of wackestone. Porosity and permeability were measured on each plug, and thin sections were prepared from plug ends; porosity and fabric elements were measured by the point-count method.

Rock Fabrics

Three basic dolomite rock fabrics are present in the upper productive interval of the Seminole (San Andres) reservoir: fine crystalline grainstones, grain-dominated packstones, and mud-dominated wackestones (fig. 16). The dolomite crystal size is generally 10 to 20 μm in diameter but increases slightly to 25 μm at the base of the upper interval. This increase in dolomite crystal size defines a fourth rock fabric, a mud-dominated dolomite with medium crystal size.

Particle Size and Sorting

A depth plot of particle size and sorting is shown in figure 17. Grainstones are composed of grains averaging about 250 μm in diameter. Grain-dominated packstones are composed of a

Figure 16. Plane polarized photomicrographs of samples from the upper productive interval, Seminole (San Andres) reservoir, illustrating classes of rock fabrics. Width of photomicrographs is 3.4 mm. (a) Dolomitized grainstone from parasequence 9, illustrating intergranular porosity. Depth is 5,110 ft. (b) Dolomitized grain-dominated packstone from parasequence 6, illustrating areas with intergranular pore space and areas of intergranular dolomitized mud. Depth is 5,139 ft. (c) Dolomitized grain-dominated packstone from parasequence 1, illustrating poor sorting and intergranular dolomitized mud. Depth is 5,080 ft. (d) Dolomitized wackestone from parasequence 5. Depth is 5,133 ft.

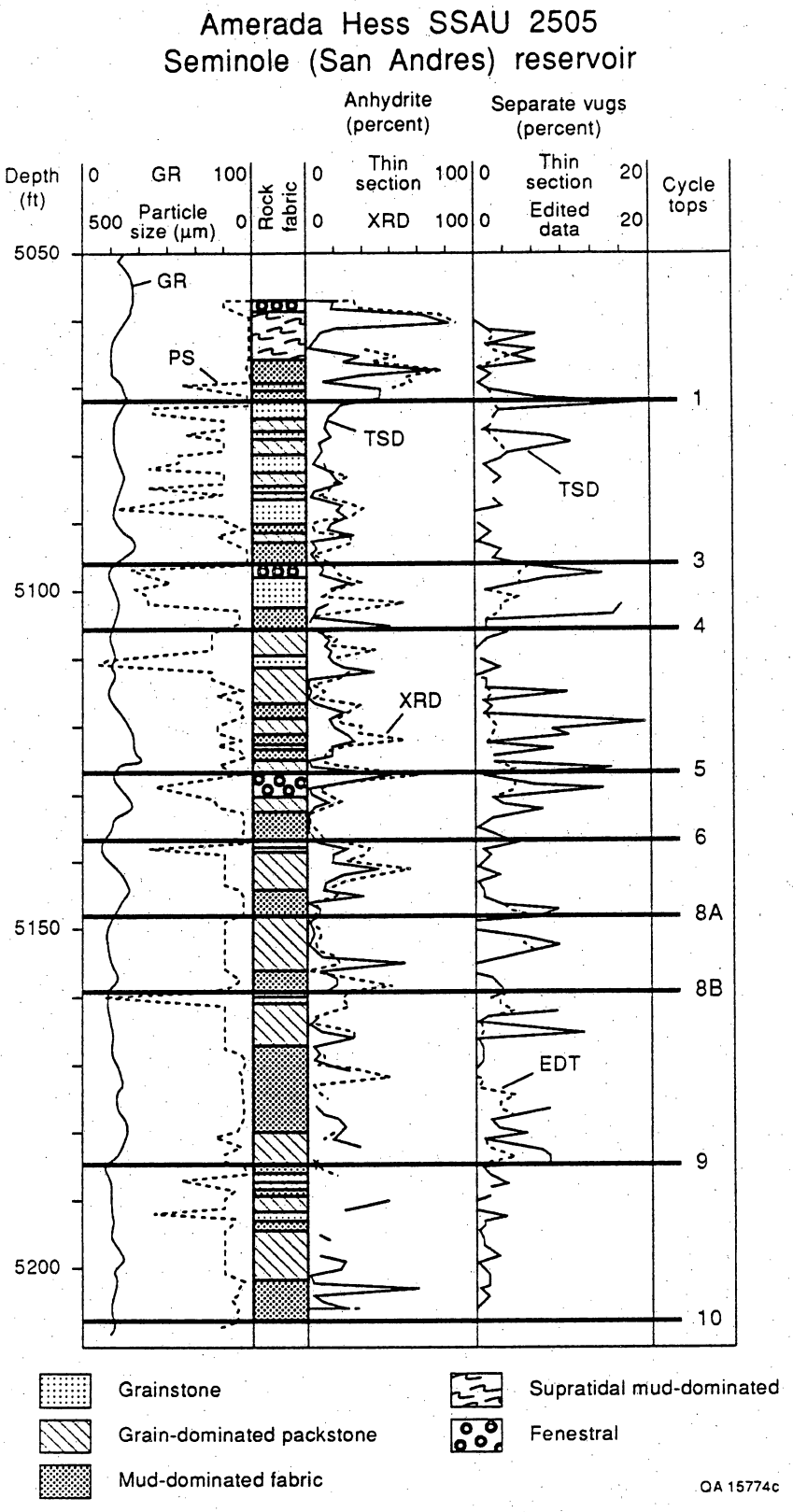

Figure 17. Depth plot from upper productive interval of well 2505, illustrating gamma-ray log, particle size, rock fabric, anhydrite volume, separate-vug porosity, and parasequences.

mixture of 250-μm grains, intergranular dolomitized mud, and intergranular pore space and cement. Grain-dominated packstones are represented in figure 17 as having a particle size of 100 μm. Mud-dominated fabrics have particle sizes equal to the dolomite crystal size, 10 to 25 μm.

Particle size increases upward within each cycle, representing upward-shoaling conditions. Grain-dominated packstones, however, dominate the upper parts of the cycles, with grainstones increasing in importance in the upper cycles.

Anhydrite

All four rock fabrics contain poikilotopic and pore-filling anhydrite in varying amounts. The volume of anhydrite in the thin sections was measured by the point-count method (TSD). Samples from the same foot were crushed and the volume of anhydrite determined by XRD. Sample density was every foot over most of the cored interval. The XRD results show higher amounts of anhydrite than do the TSD results. The average anhydrite from XRD is 23 percent, whereas the average value from TSD is 13 percent.

The TSD and XRD values were averaged and a depth plot was made (fig. 17). Where only one value was present it was used and where no value was present a value was interpolated. To correlate with wireline logs, 3-ft running averages were made of the depth plot (fig. 17). Anhydrite volumes range from 5 to 45 percent in the upper productive interval. However, a plot of whole-core porosity versus percentage of anhydrite in the thin section (fig. 18) shows no correlation. This suggests that anhydrite is predominantly replacement rather than pore filling.

The volume of poikilotopic anhydrite varies significantly within a whole-core sample. Commonly, the amount of anhydrite varies by a factor of 2 and occasionally by a factor of 10 (fig. 19). The values from the original thin sections and from the XRD fall mostly within the range of values from the three plugs.

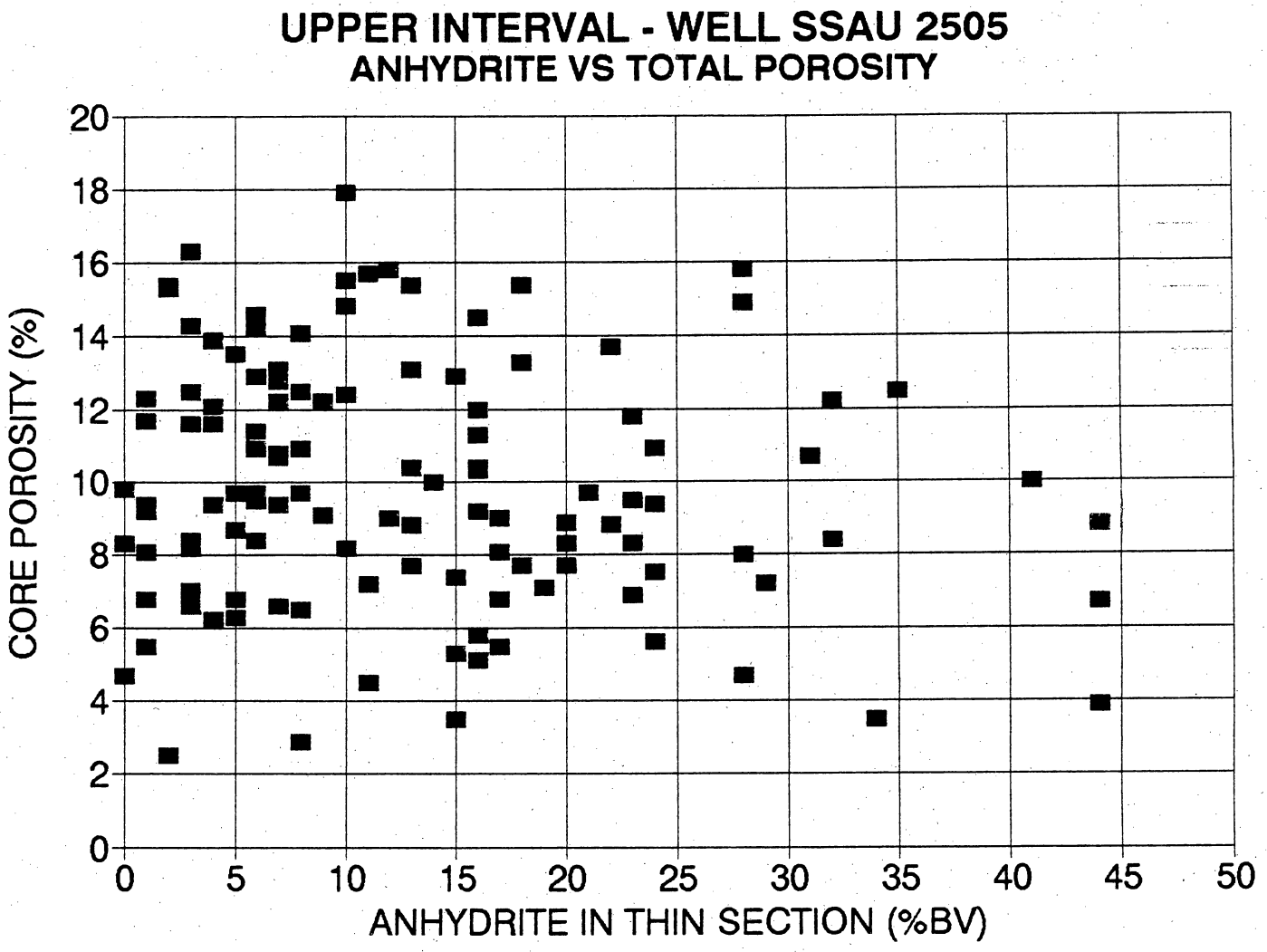

Figure 18. Plot of percent anhydrite versus percent porosity, showing that porosity is not a function of anhydrite volume.

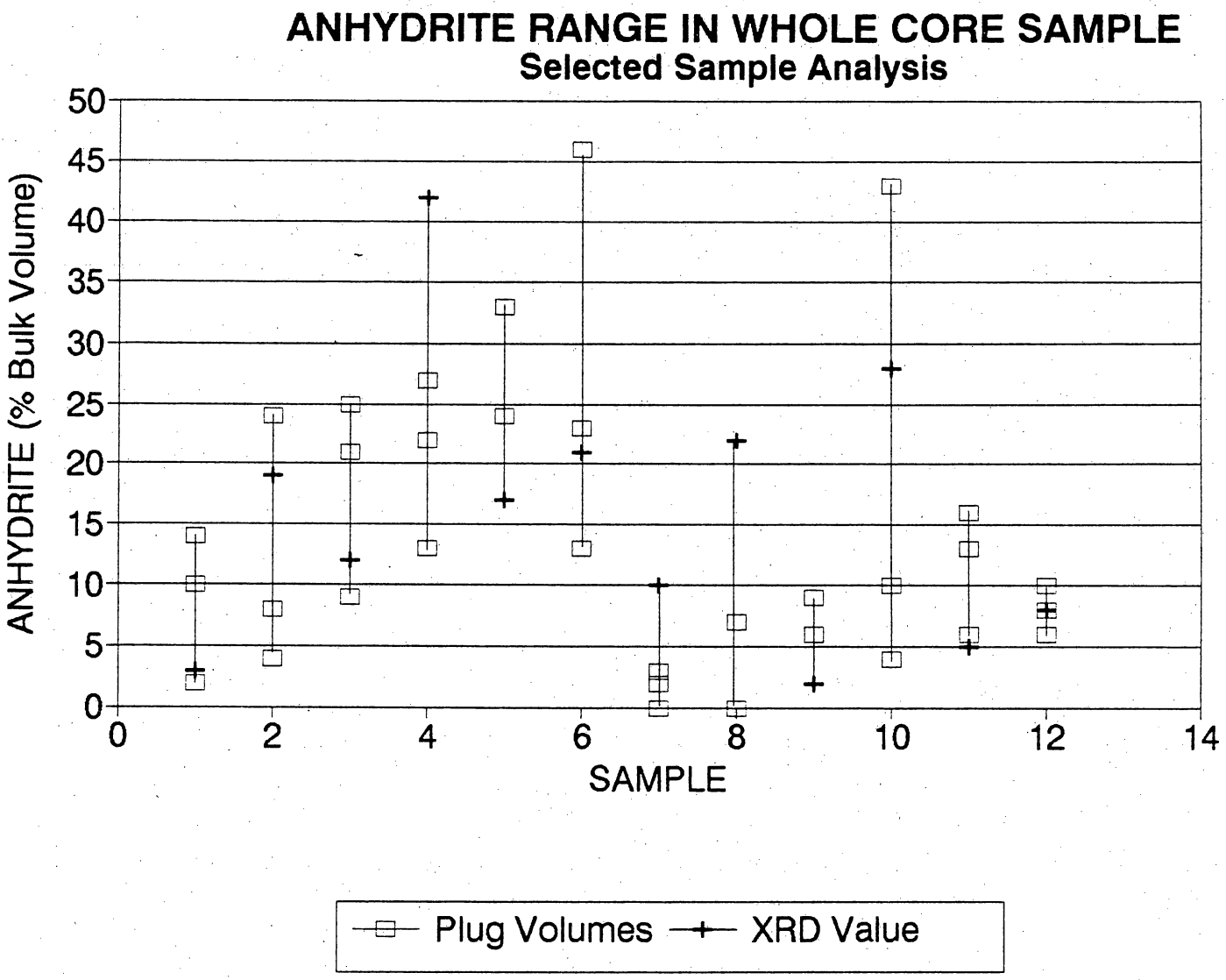

Figure 19. Graphic display showing the range of anhydrite in selected whole-core samples. Values are from plugs about 1 inch apart and the XRD sample of a small area.

Porosity

The relationship between point-count porosity from thin sections and Boyle's-law porosity from whole-core samples is shown in figure 20. In general, point-count porosity is expected to be lower than core-analysis porosity because very small pores are not visible in thin section. However, many of the data points show thin-section porosity higher than core-analysis porosity. This anomalous relationship was investigated by measuring porosity and permeability of 3 plug samples from each of 12 whole-core samples and point-counting thin sections made from the samples. Porosity and permeability were measured before and after sample cleaning.

The results show that porosity in the cleaned plugs is several units higher than in the uncleaned plugs and that the porosity of the cleaned plugs is as much as 4 porosity percent higher than porosity from whole-core analysis (fig. 21). Plug porosity values from one whole-core sample typically vary by 2 or 3 porosity percent. Thin-section porosity varies but is always less than plug porosity.

Adding 4 porosity percent to the whole-core porosity values results in most thin-section porosity values being lower than the corrected core-analysis porosity (fig. 20). Thin sections that have more porosity than the corrected core porosity also tend to have the highest separate-vug porosity. Core examination shows high separate-vug porosity values to be concentrated in beds that are a few inches thick, suggesting that thin sections with high separate-vug porosity are not representative of the core. Indeed, a statistical analysis of the frequency of separate-vug porosity shows a modal value of 2 percent and that 90 percent of the samples have a separate-vug porosity of less than 10 percent (fig. 22). The reservoir can be characterized as having a few thin beds with greater than 10 percent separate-vug porosity dispersed within beds containing separate-vug porosity of 0 to 9 percent with a mode of 2 percent.

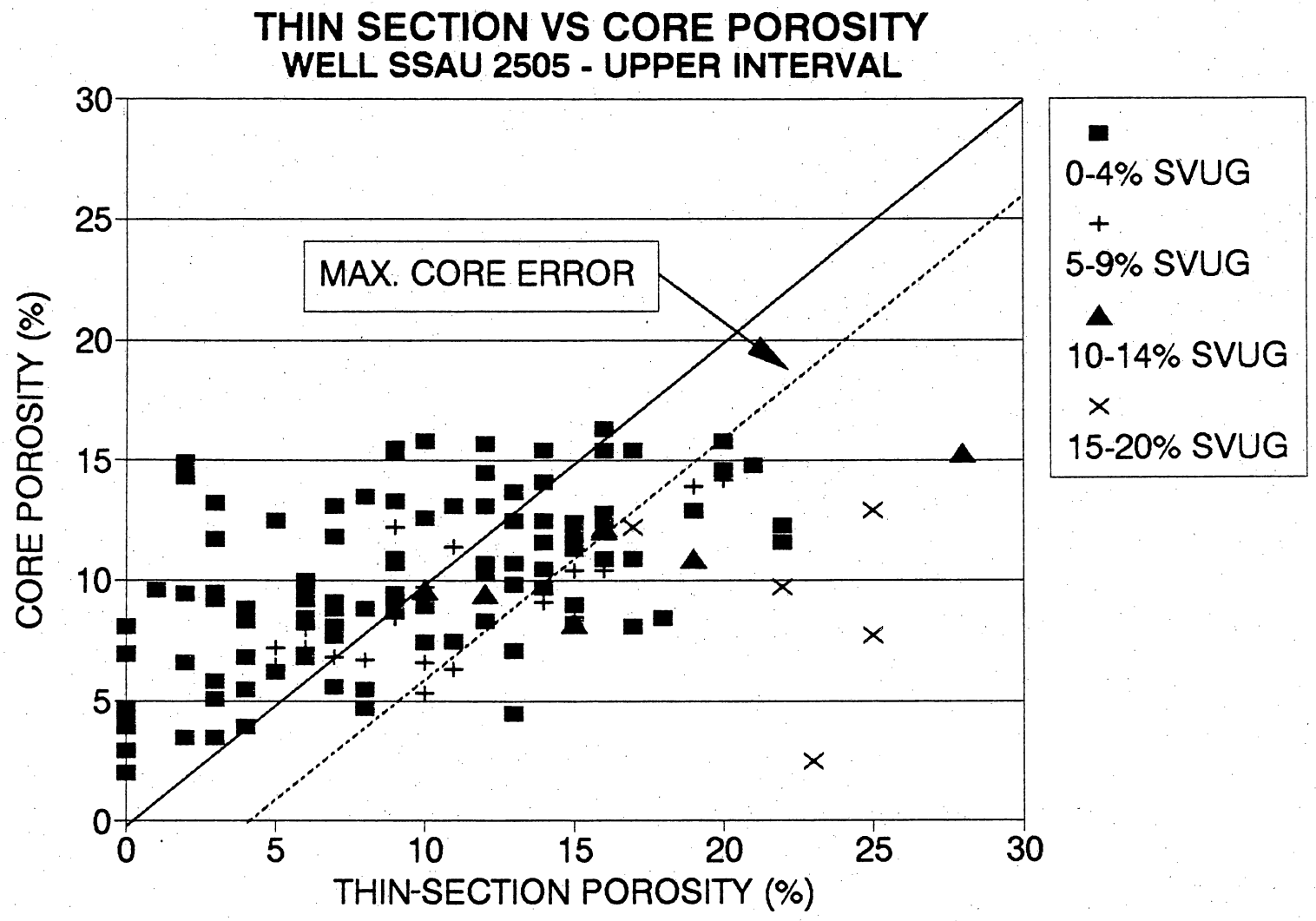

Figure 20. Plot of thin-section porosity versus whole-core porosity showing that thin-section porosity is larger than core-analysis porosity in many samples. The amount of separate-vug porosity is labeled, showing that many samples with high thin-section porosity also have high values of separate-vug porosity. The dashed line assumes that core-porosity values are too low by 4 porosity percent, the maximum porosity error measured (fig. 21).

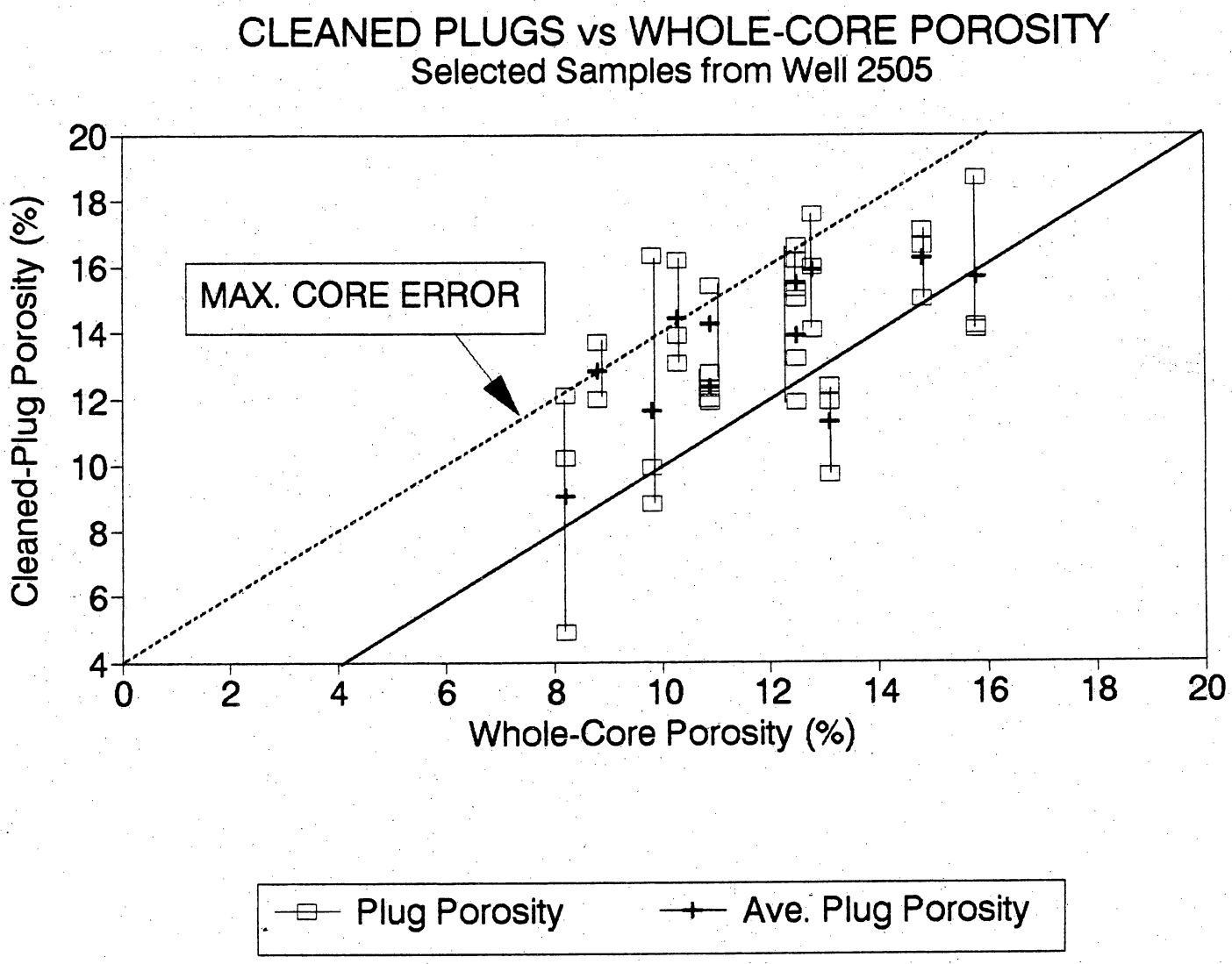

Figure 21. Plot of whole-core porosity values versus porosity from plug samples taken from the whole-core samples and cleaned. Whole-core porosity is too low by 0 to 4 porosity percent.

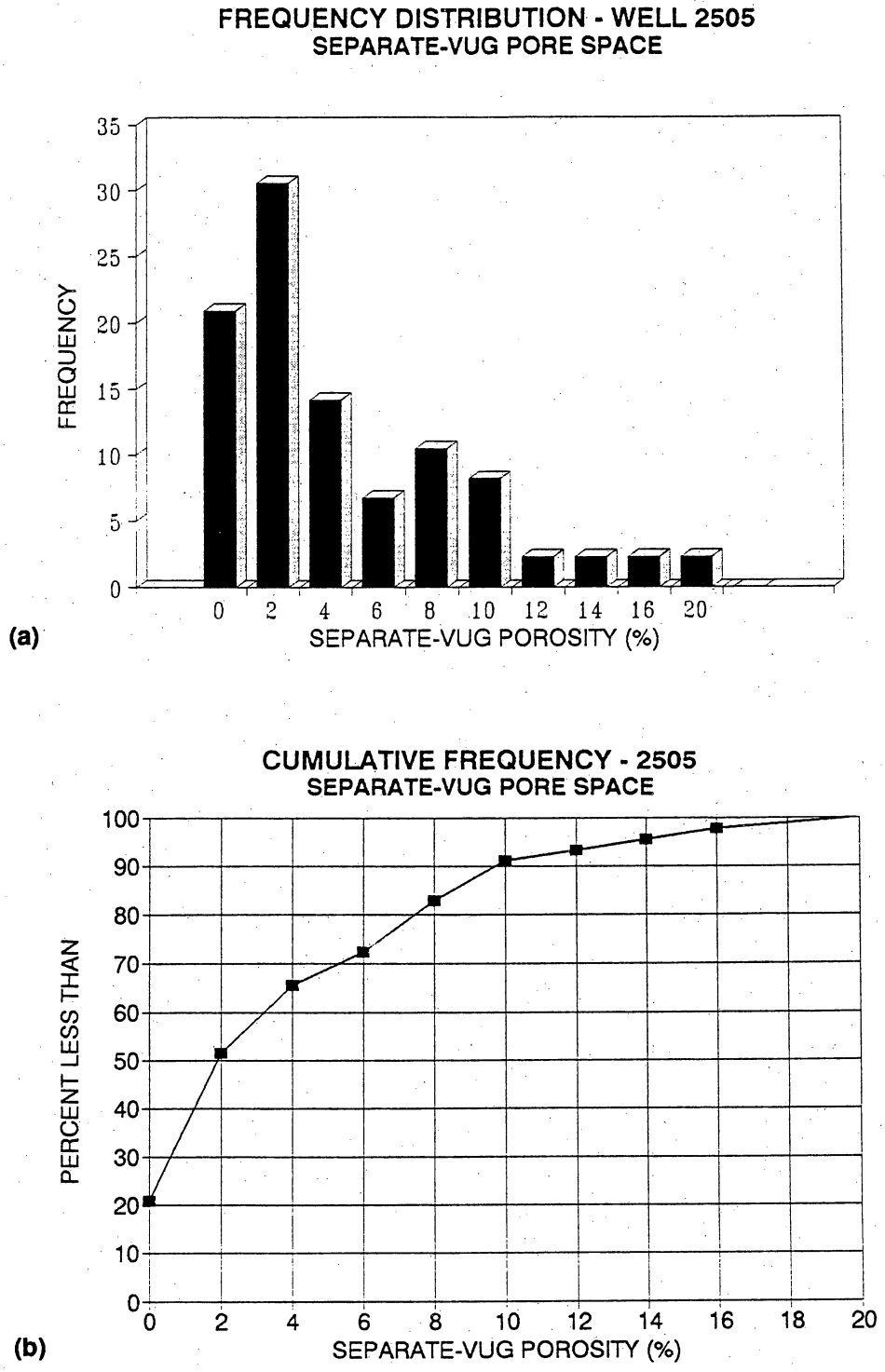

Figure 22. Separate-vug porosity statistics: (a) frequency distribution of separate-vug porosity and (b) cumulative frequency distribution of separate-vug porosity.

A depth plot of separate-vug porosity was made by deleting separate-vug porosities of 10 percent or more from the thin-section data and then calculating a 3-ft running average on the resulting data. The results, shown in figure 17, show no intervals of consistently high vuggy porosity.

Permeability

The difference in permeability values between whole-core, averaged uncleaned-plug, and averaged cleaned-plug samples is not significant, probably because residual oil is present in the small pores, pores which do not effectively contribute to permeability. A significant range is present, however, between the three plug measurements (fig. 23).

Mechanical field permeameter (MFP) measurements were made on the slabbed faces of the 12 whole-core samples at a density of about 1 measurement per square inch (fig. 24). The average MFP values are similar to the whole-core permeability values, but the standard deviation is about the same as the average permeability shown in table 2. The range in permeability found with the MFP is similar to the range found between the three core plugs.

Table 2. Mechanical field permeameter (MFP) measurements on slabbed core surfaces.

Depth (ft)	MFP Average permeability (md)	MFP Standard deviation (md)	Whole-core permeability	Rock-fabric classification
5106	14.15	13.7	7.5	Grain-dominated packstone
5107	56.1	26.4	55.0	Grain-dominated packstone
5108	52.1	28.6	39.0	Grain-dominated packstone
5109	4.8	4.0	5.7	Grain-dominated packstone
5110	14.0	23.7	23.0	Grainstone
5143	0.9	1.1	1.7	Wackestone
5144	3.8	2.8	3.8	Wackestone
5145	1.8	3.0	2.3	Wackestone
5146	0.9	.07	0.2	Wackestone
5166	1.8	2.2	1.2	Wackestone
5167	5.1	6.1	1.3	Wackestone
5168	2.1	1.6	2.2	Wackestone

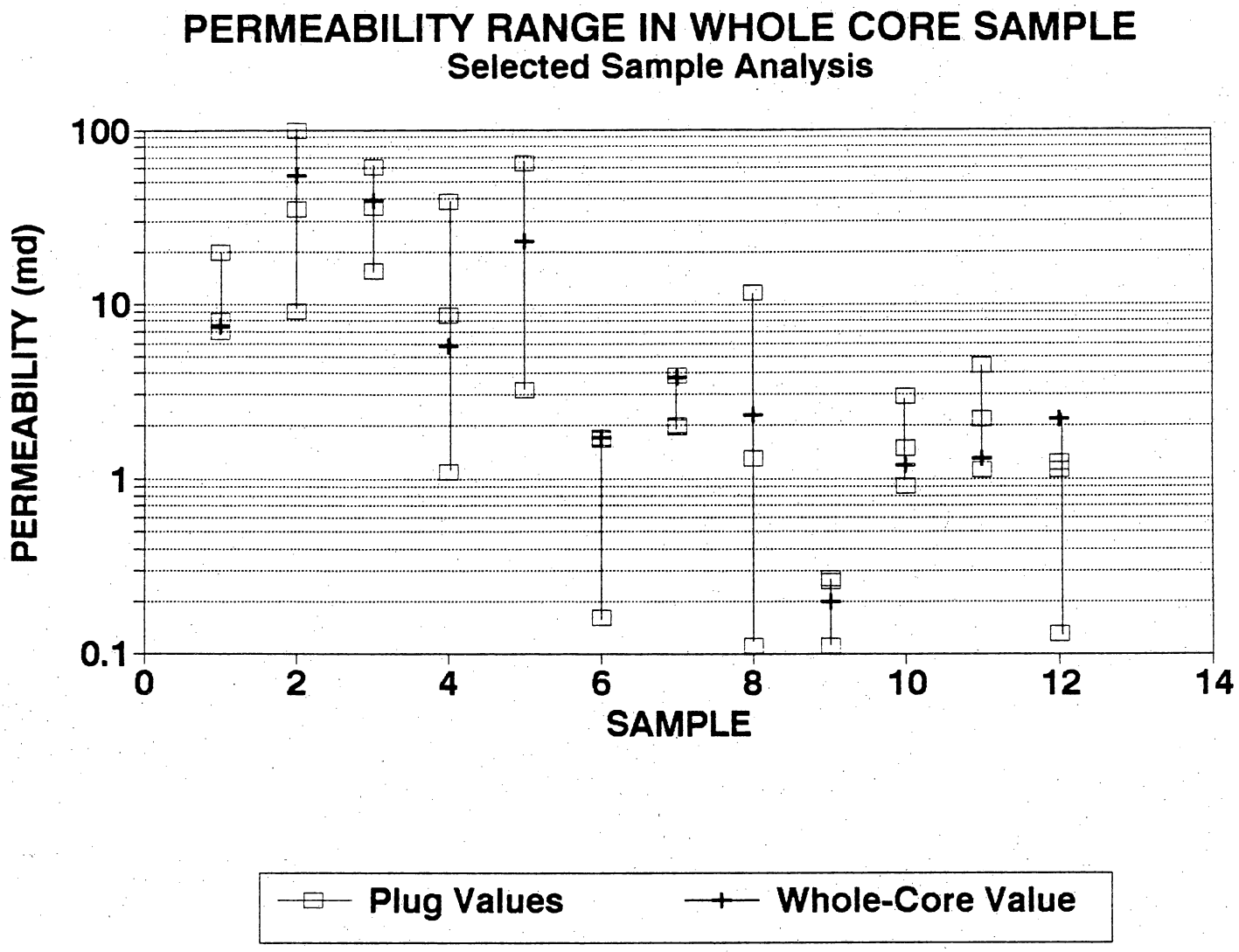

Figure 23. Graphic display showing the range of permeability in selected whole-core samples. Values from plugs about 1 inch apart are compared with original whole-core values.

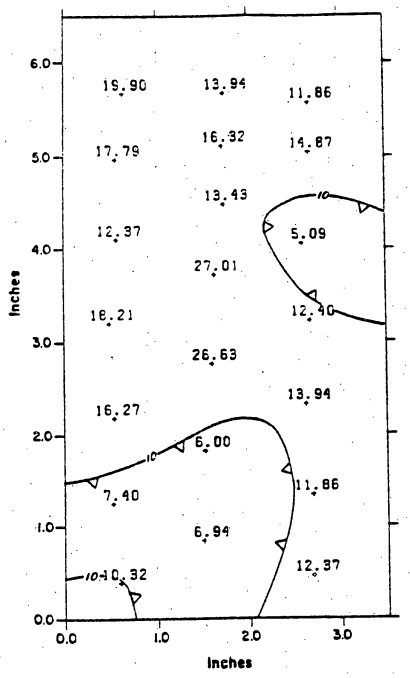

Depth 5106 ft
Grain-Dominated Packstone

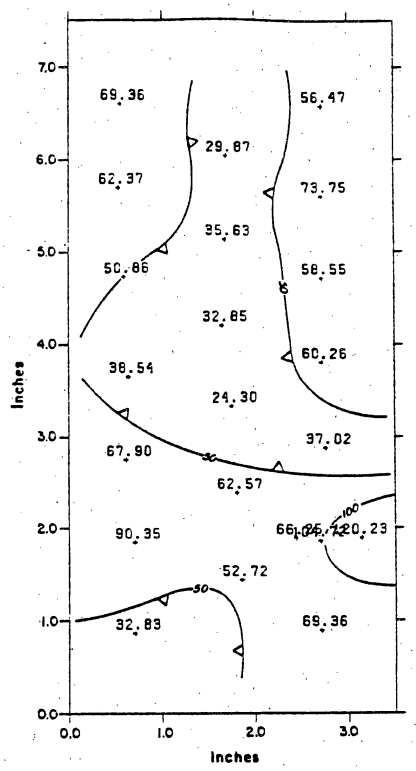

Depth 5107 ft
Grain-Dominated Packstone

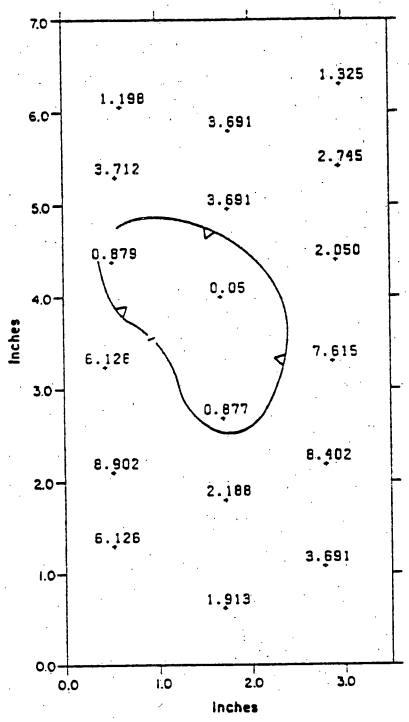

Depth 5144 ft
Wackestone

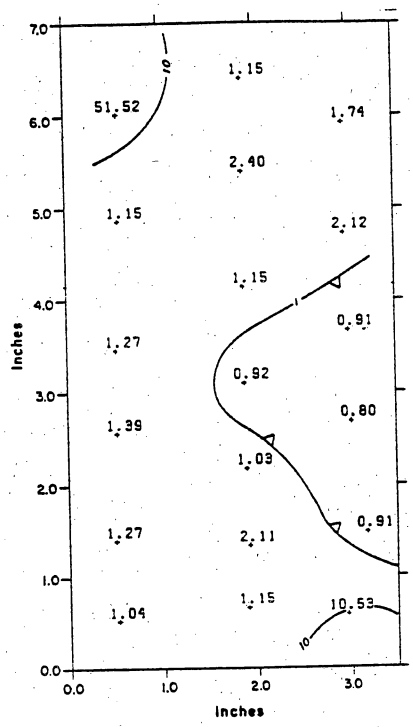

Depth 5166 ft
Wackestone

Figure 24. Examples of permeability distribution based on mechanical field permeameter measurements spaced 1 inch apart on the face of core slabs from samples used for whole-core analysis. Values are in millidarcys.

Rock-Fabric, Porosity, and Permeability Transforms

Cross plots of porosity and permeability of specific rock fabrics, using the original whole-core values, show permeability values too high for corresponding porosity values. Cross plots based on data from the plug samples, however, show transforms that are in agreement with the petrophysical/rock-fabric classes defined in this report and in Lucia (1983) (fig. 25). Porosity-permeability transforms are based on interparticle porosity, not total porosity. The transform for the grain-dominated packstones falls in the middle field (fig. 25a), as expected. The transform for mud-dominated wackestones (fig. 25b) falls at the upper limit of the fine-dolomite field because the crystal size is about 20 μm, the upper crystal-size limit for dolomite fabrics in this field.

Log Analysis

The core description and the analysis of the accuracy and variability of porosity, permeability, and fabric elements were used to calibrate wireline log response. Numerical relationships were developed to calculate porosity, separate-vug porosity, rock fabrics, and permeability using CNL, density, acoustic, and Laterologs. The Terra Science log-analysis program was used in this analysis.

Calculation of Porosity and Lithology

Lithology was calculated from the wireline logs assuming a composition of anhydrite, dolomite, and porosity. Minor amounts of calcite and quartz identified by XRD were ignored. The amount of anhydrite in the well was established by thin-section analysis and by XRD, as described above, and plotted versus depth. A 3-ft running average of the anhydrite data was calculated and compared with log calculations.

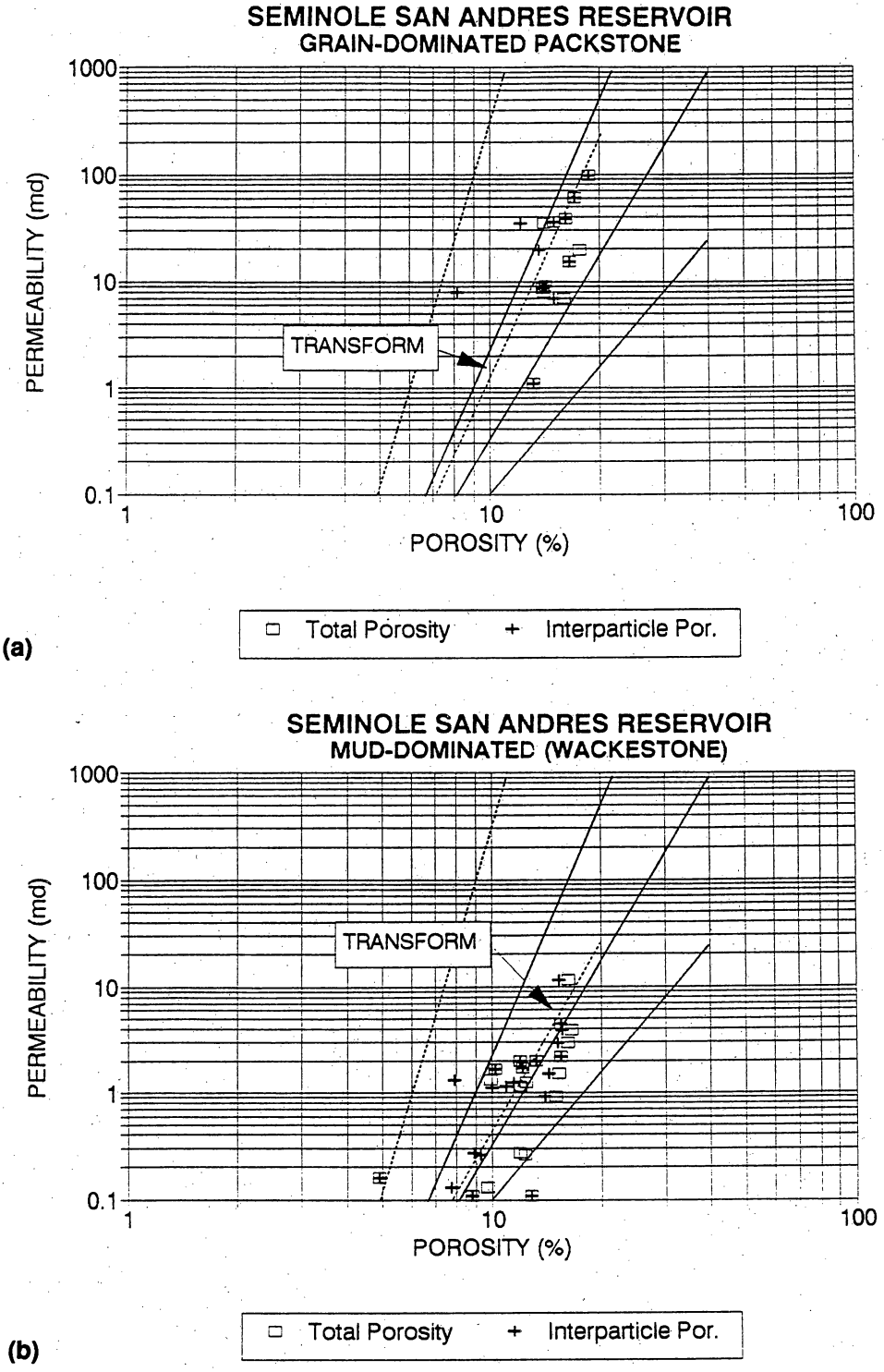

Figure 25. Porosity, permeability, and rock-fabric transforms from plug samples, Seminole (San Andres) reservoir: (a) Cross plot of data from plug samples of grain-dominated packstone showing both total porosity and interparticle porosity (total porosity less separate-vug porosity). The three petrophysical/rock-fabric fields are also shown. The porosity-permeability transform is based on interparticle porosity data and the middle petrophysical/rock-fabric field. (b) Cross plot of data from plug samples of mud-dominated wackestone with 20-μm dolomite crystals showing both total porosity and interparticle porosity (total porosity less separate-vug porosity). The three petrophysical/rock-fabric fields are also shown. The porosity-permeability transform is based on interparticle porosity data and the middle petrophysical/rock-fabric field.

Only when all three porosity logs were included in the log calculations were reasonable anhydrite volumes calculated (fig. 26). The combination of density and CNL logs resulted in wide swings from 0 to 100 percent anhydrite. Combining density and acoustic logs resulted in low anhydrite values, whereas using the CNL-acoustic combination resulted in high anhydrite values.

To obtain a reasonable fit between log and core anhydrite volumes and to correctly calculate porosity, the fluid transit time was reduced from the standard 189 μsec/ft to 150 μsec/ft. Using 189 μsec/ft resulted in low porosity values (fig. 27).

Comparison of CNL limestone porosity values with porosity values from the plug samples suggests that true porosity is 4 porosity percent lower than CNL limestone porosity. Therefore, the neutron porosity parameter was reduced from 7.5 to 4. Using a value of 7.5 resulted in high anhydrite values.

Table 3 presents the matrix values that gave the best fit between log analysis and anhydrite and corrected porosity values from core analysis.

Table 3. Matrix values used for porosity log calculations.

	Matrix Values		
Log	Dolomite	Anhydrite	Porosity
Acoustic (μsec/ft)	43.5	50.0	150
CNL (P.U.)	4	–0.2	100
Density (g/cc)	2.87	2.95	1.00

Calculation of Separate-Vug Porosity

Interparticle porosity is calculated by subtracting separate-vug porosity from total porosity. In cores, the volume of separate vugs can be determined visually. In uncored intervals, the acoustic log can be used to estimate separate-vug porosity.

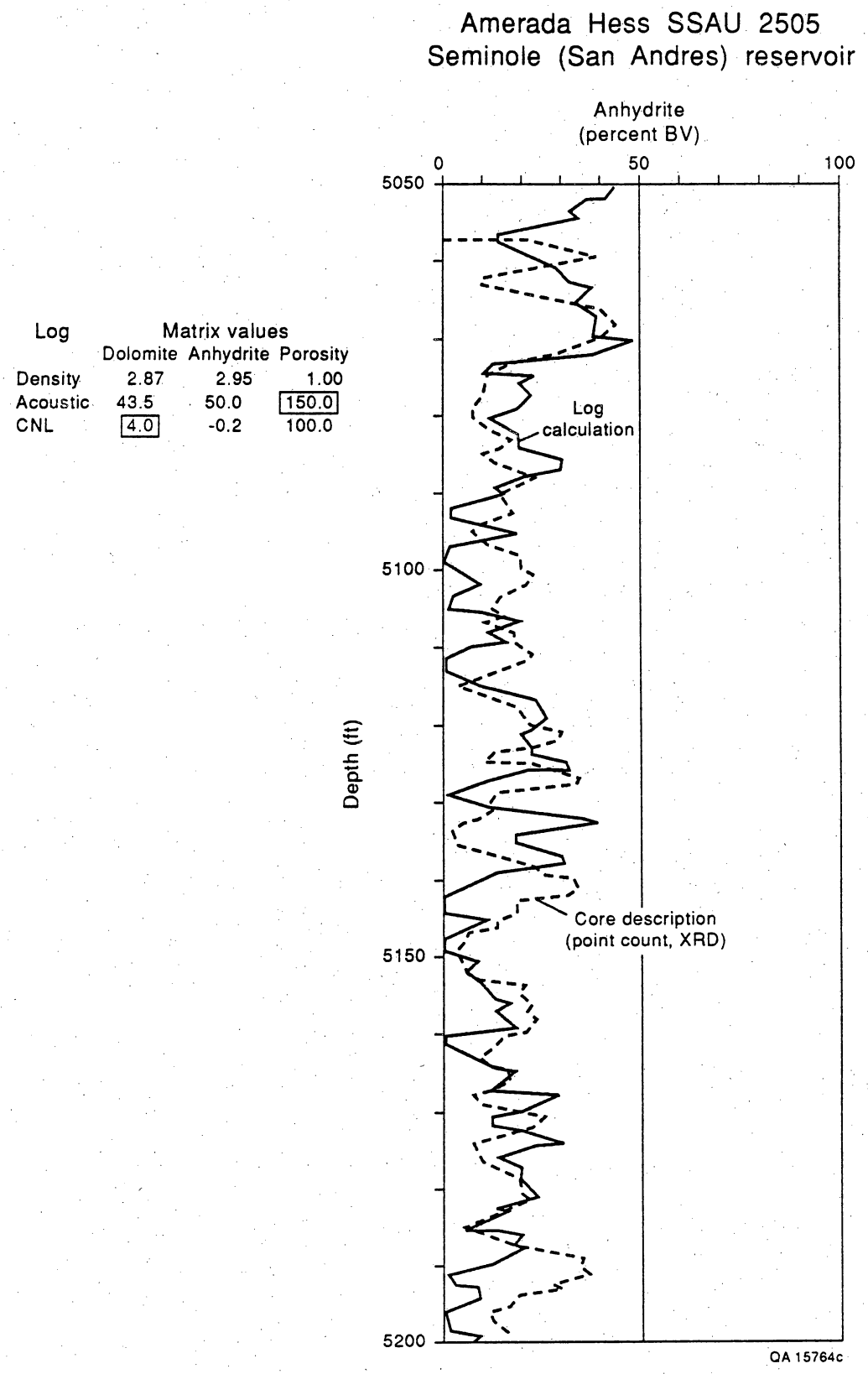

Figure 26. Comparison of log-calculated anhydrite volumes and anhydrite volumes from core description in well Amerada No. 2505, Seminole field.

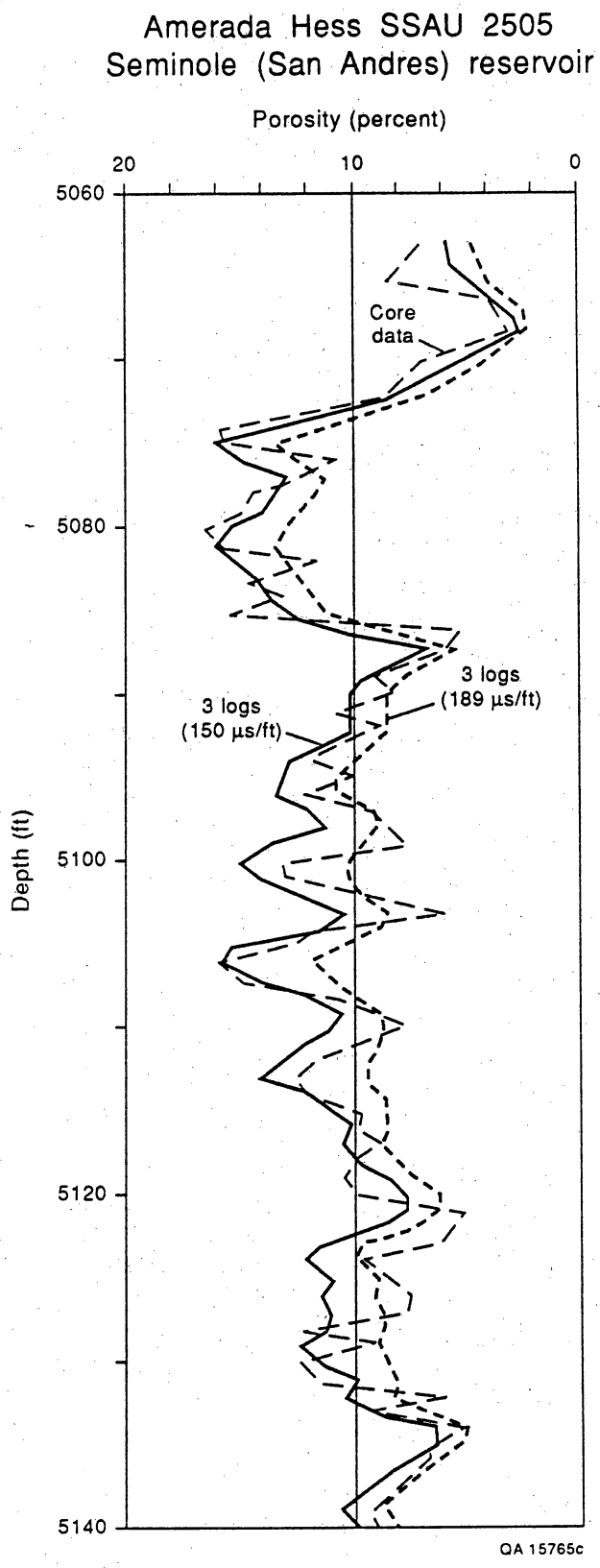

Figure 27. Comparison of porosity calculated from three porosity logs using 150 µsec/ft and 189 µsec/ft with core-analysis porosity values in well Amerada No. 2502, Seminole field.

To calibrate wireline log response with separate-vug porosity in the Seminole field, a 3-ft running average of the separate-vug porosity from thin-section analysis was calculated. A Z-plot of acoustic transit time, total porosity calculated from porosity logs, and separate-vug porosity from core description shows a systematic relationship (fig. 28).

The slope of the line relating transit time to porosity in figure 28 indicates a fluid transit time of about 150 μsec/ft. Because no fluid has a travel time of 150 μsec/ft, the faster travel time is probably related to the presence of separate-vug porosity. Acoustic waves respond to separate-vug porosity as if it were a solid mineral and not pore space. If no separate-vug porosity were present, or if separate-vug porosity were constant and did not vary with porosity, the slope of the line would indicate a fluid transit time of 189 μsec/ft. Assuming this to be true, parallel lines with slopes equal to a fluid velocity of 189 μsec/ft can be drawn representing various separate-vug values. The intercept of these lines with the transit-time axis can be plotted against values of separate-vug porosity (fig. 29). A line connecting these points describes the semilog relationship between separate-vug porosity, total porosity, and interval transit time given in equation (8). This relationship applies to anhydritic dolomites only. A relationship for vuggy limestones developed by Lucia and Conti (1987) has a similar slope but a different intercept:

$$\phi_{sv} = (2.766 \times 10^4)\ (10^{[-0.1526\ (\Delta t - 141.5\phi)]}) \qquad (8)$$

where

ϕ = total porosity (fraction)

ϕ_{sv} = separate-vug porosity (fraction)

Δt = interval transit time (μsec/ft)

Using equation (8), separate-vug porosity is calculated from acoustic log values and calculated total porosity. In figure 30, the calculated separate-vug porosity and the 3-ft averages of the thin-section separate-vug values are compared in a depth plot. Whereas the calculated values are in the correct range, the two profiles do not match well. This may be due to the

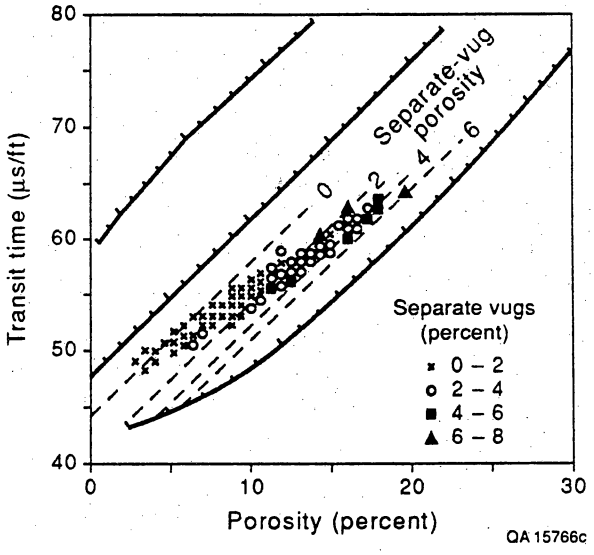

Figure 28. Relationship between transit time, total porosity, and separate-vug porosity in well Amerada No. 2505, Seminole field.

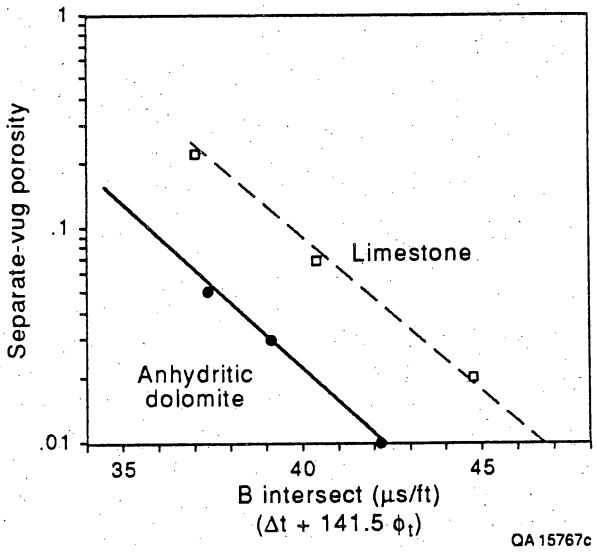

Figure 29. Transforms for separate-vug porosity, transit time, and total porosity for dolomite and limestone. The dolomite transform is developed from well Amerada No. 2505, Seminole field (fig. 28), and the limestone transform is from Lucia and Conti (1987).

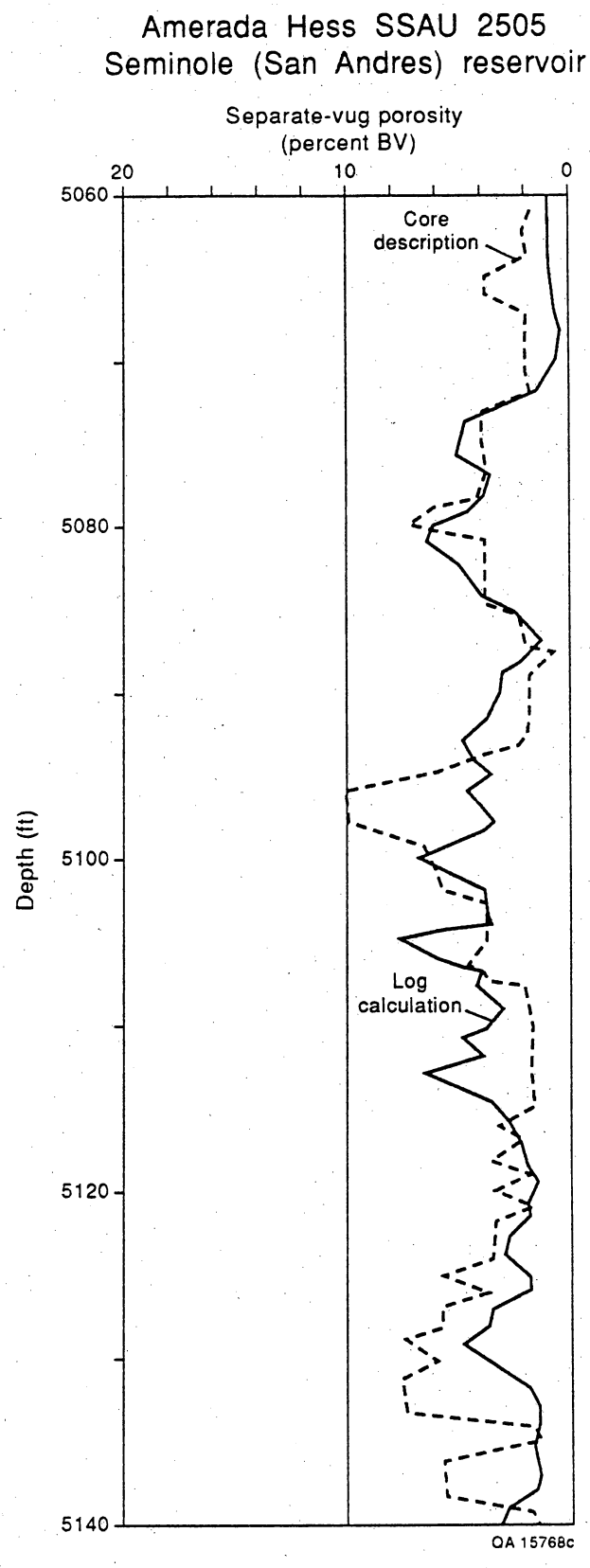

Figure 30. Comparison of separate-vug porosity calculated from logs with separate-vug porosity from core description in well Amerada No. 2505, Seminole field.

difficulty in obtaining a reasonable value for separate-vug porosity from core descriptions or because of the inadequacy of the wireline logs in reflecting separate-vug porosity.

Calculation of Rock Fabric

Particle size and interparticle porosity control pore size and pore-size distribution. Water saturation can be calculated from wireline logs and is controlled by pore size and height above the free water table. In the Seminole field, cross plots of the log of porosity versus the log of water saturation can be used to determine particle size and rock fabric. Water saturation was calculated using the Archie equation. Water resistivity was determined to be 0.2 ohmm, the saturation exponent n was assumed to be 2, and the lithology exponent m was calculated from the following relationship between separate-vug porosity and m:

$$m = 2.14\left(\frac{\phi_{sv}}{\phi}\right) + 1.76 \qquad (9)$$

Figure 31 shows that mud-dominated and grain-dominated fabrics are clearly grouped into separate porosity/saturation fields. The data were obtained by averaging porosity and water saturation values for the mud-dominated and grain-dominated intervals of parasequences 1 through 8. The mud-dominated interval of parasequence 9 is a medium-crystal dolomite and is petrophysically similar to the grain-dominated fabrics.

A line interpolated between the points of figure 31 was used to separate mud-dominated from grain-dominated fabrics. In addition, a line separating grain-dominated packstones from grainstones was added on the basis of the presence of a few grainstone intervals. These lines, which divide the porosity-saturation graph into three petrophysical/rock-fabric fields, are shown on figure 32 and the equations are presented as follows:

The boundary between mud-dominated (<20 μm) and grain-dominated fabrics is given as

$$Sw = (3.05 \times 10^{-2}) \times (\phi^{-0.9813}). \qquad (10)$$

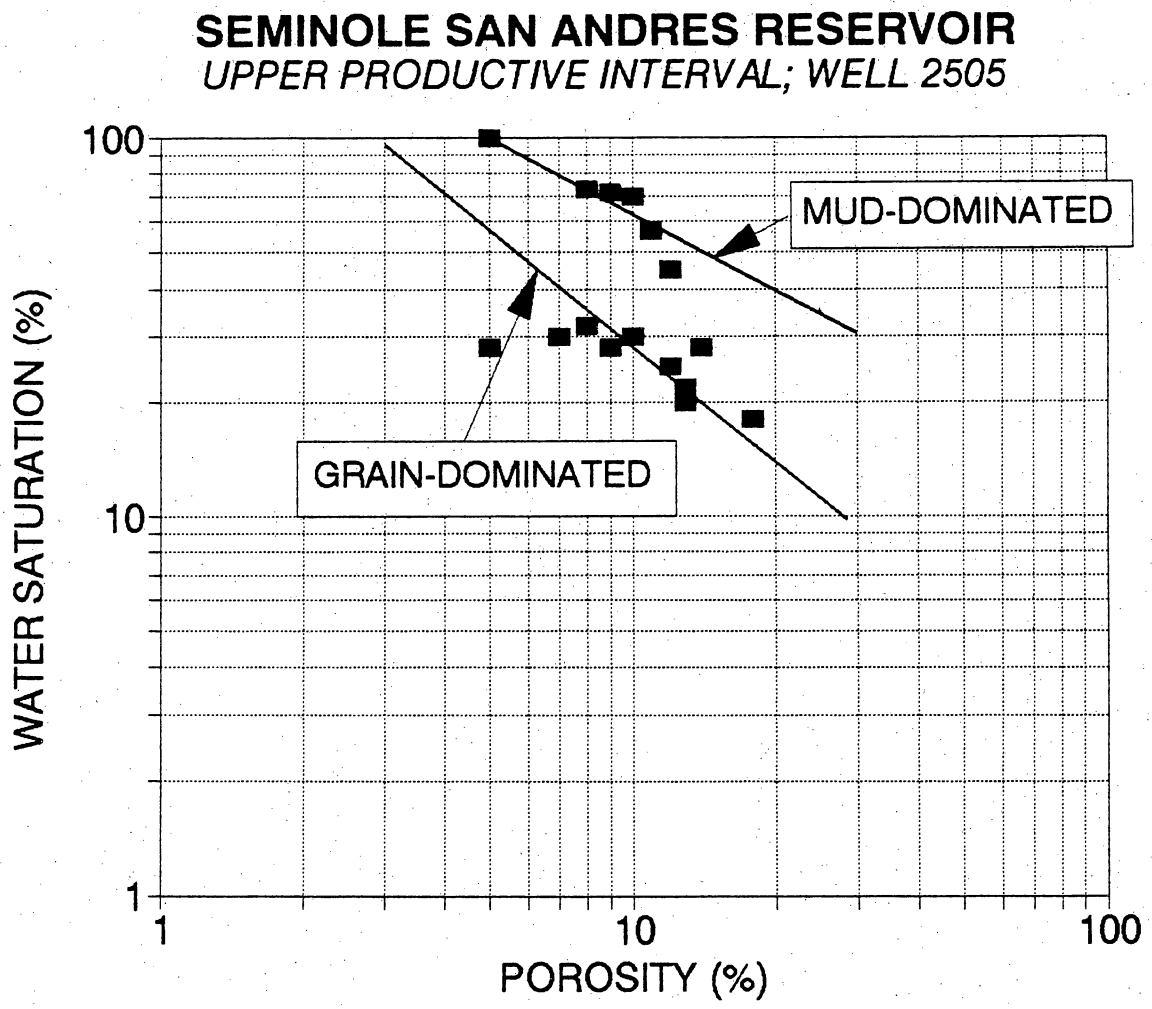

Figure 31. Porosity, water-saturation, rock-fabric cross plot for the upper productive interval in well Amerada No. 2505, Seminole field, using averaged data from each parasequence.

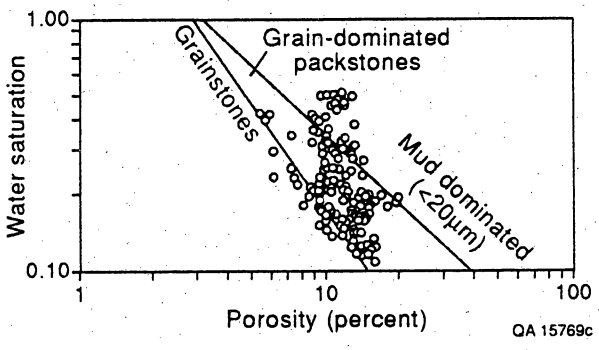

Figure 32. Porosity, water-saturation, rock-fabric cross plot for the upper productive interval in well Amerada No. 2505, Seminole field, showing 1-ft data points.

The boundary between (1) grainstones and (2) grain-dominated packstone and medium-crystalline mud-dominated fabrics is given as

$$Sw = (6.522 \times 10^{-3}) \times (\phi^{-1.401}). \quad (11)$$

Porosity, Permeability, and Rock-Fabric Transforms

Porosity, permeability, and rock-fabric transforms were prepared using core permeability values and log-calculated porosity values. Log-calculated porosity values were used because the core porosity values are too low. Total porosity was converted to interparticle porosity by subtracting separate-vug porosity calculated from logs. The rock fabrics used to group the porosity and permeability data were determined from log analysis and checked by core descriptions. Figure 32 shows the data points used in the porosity-permeability plots shown in figure 33. The resulting transforms are presented as follows:

Mud-dominated (<20 μm) fabrics—

$$k(md) = (1.2303 \times 10^{6}) \times (\phi - \phi_{sv})^{5.90}. \quad (12)$$

Grain-dominated packstones and medium crystal mud-dominated dolomites—

$$k(md) = (6.6069 \times 10^{9}) \times (\phi - \phi_{sv})^{8.85}. \quad (13)$$

Grainstone fabrics—

$$k(md) = (7.9432 \times 10^{9}) \times (\phi - \phi_{sv})^{8.75}. \quad (14)$$

The transforms are similar to those determined from the core plugs (fig. 25) but are shifted slightly to the left. This suggests that either the log-calculated porosity values are still slightly low by 1 to 2 porosity percent, or the separate-vug porosity is too high by 1 to 2 porosity percent.

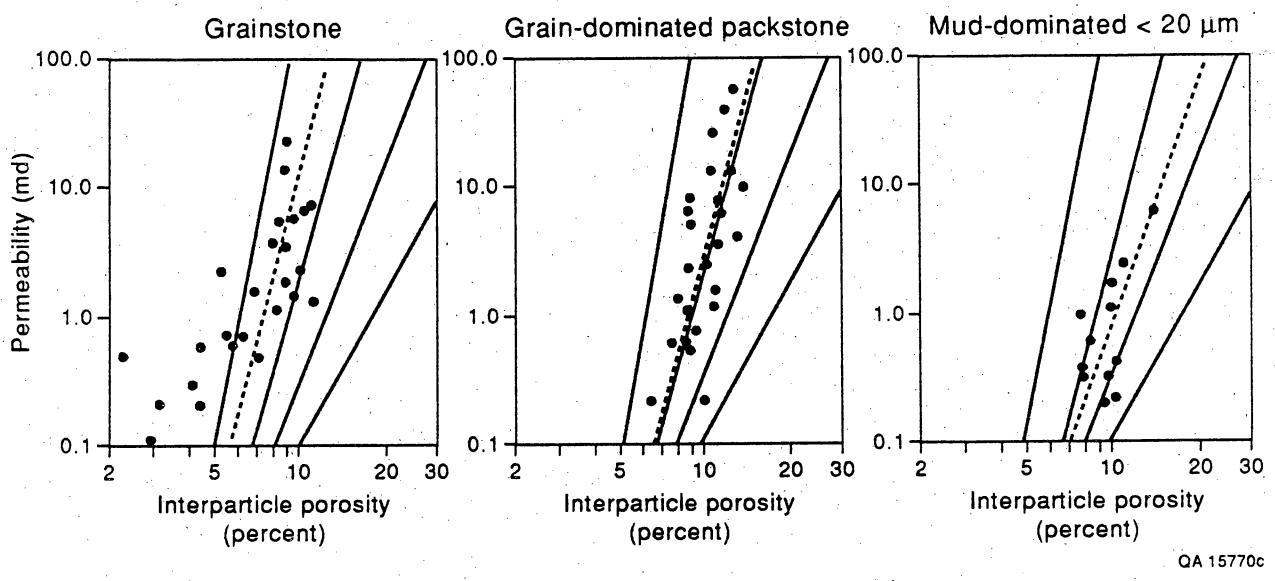

Figure 33. Porosity, permeability, and rock-fabric transforms from log calculations. The rock fabric is from porosity/water-saturation relationships shown in figure 32, interparticle porosity is from log calculations, and permeability is from core analysis. The transforms are based on the data points and on the geometry of the petrophysical/rock-fabric fields.

Permeability is calculated from wireline logs by (1) calculating total porosity from three porosity logs, (2) calculating separate-vug porosity from acoustic logs and total porosity, (3) calculating interparticle porosity by subtracting separate-vug porosity from total porosity, (4) calculating water saturation by the Archie method using separate-vug porosity to estimate the Archie m factor, (5) determining the rock fabric from saturation/porosity relationships, (6) selecting the proper rock-fabric transform, and (7) using interparticle porosity to calculate permeability.

The rock-fabric method of calculating permeability was tested in well 2309 located about 0.75 mi west of the control well Amerada No. 2505 (fig. 15). The results are shown in figure 34. The depth plots compare well except in four intervals where the calculated permeability is significantly higher than the core permeability. However, the total footage that does not compare well is 18 ft: 11 percent of the 160 ft tested. The causes of the poor comparison in the four intervals are being investigated.

Rock-Fabric Flow Model

The quantitative rock-fabric flow model of the two-section study area is illustrated in figure 35. The parasequence framework is based on core descriptions and log correlations. The rock fabrics are from wireline log calculations checked by core descriptions. The permeability profiles are calculated from logs calibrated by core analysis and core descriptions.

Flow-unit boundaries have not yet been determined so no permeability averaging has been done. However, it is clear that, in general, grain-dominated intervals have the highest permeabilities and mud-dominated intervals have the lowest permeabilities. Mud-dominated intervals with less than 0.1 md are probably flow barriers. Some grainstones also have less than 0.1 md permeability and are probably flow barriers. The model shows that the flow barriers are discontinuous.

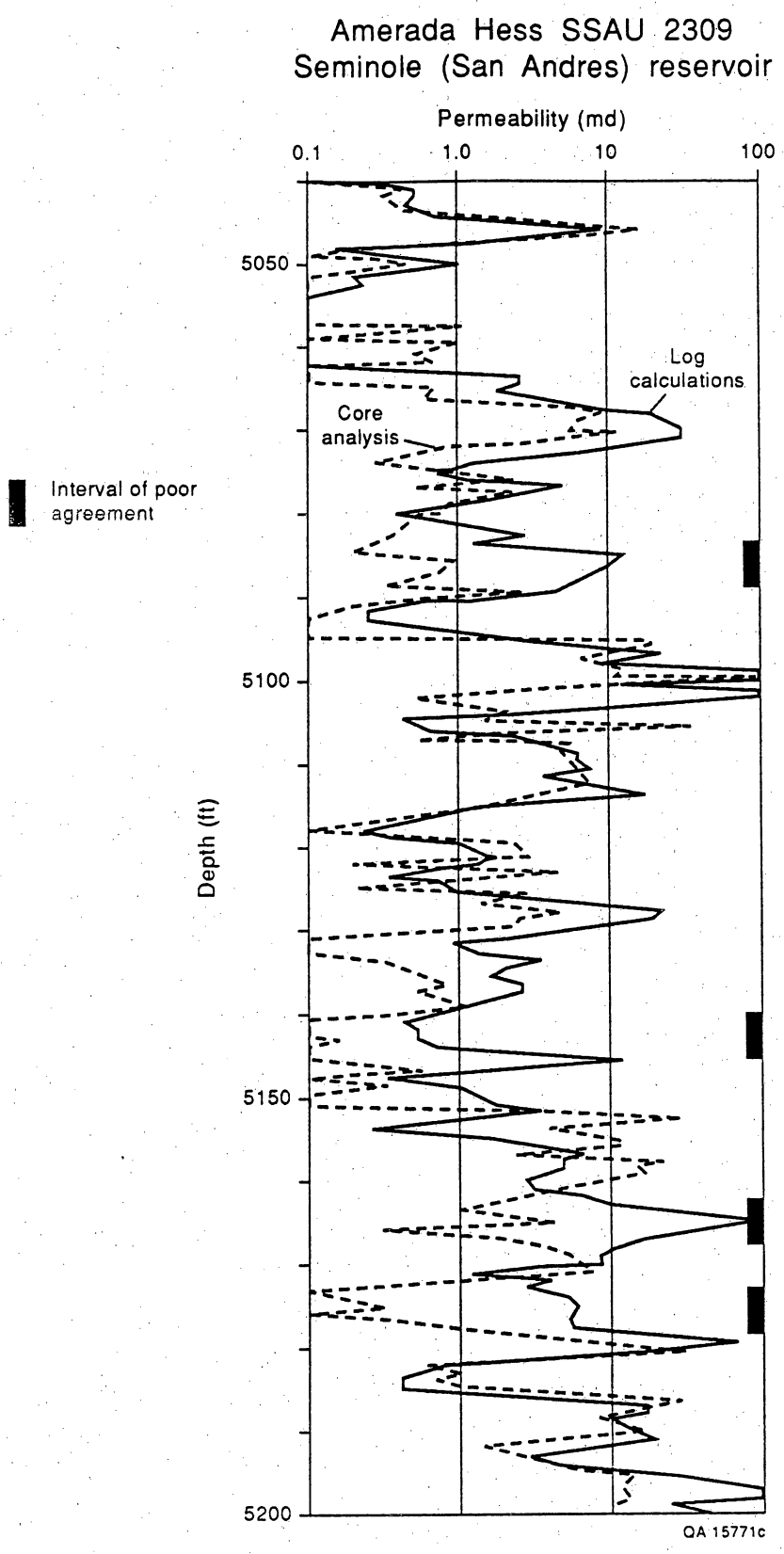

Figure 34. Comparison of permeability calculated from logs and permeability determined from core analysis in well Amerada No. 2505, Seminole field. The four intervals where the difference in the two permeability values is greater than an order of magnitude are shown.

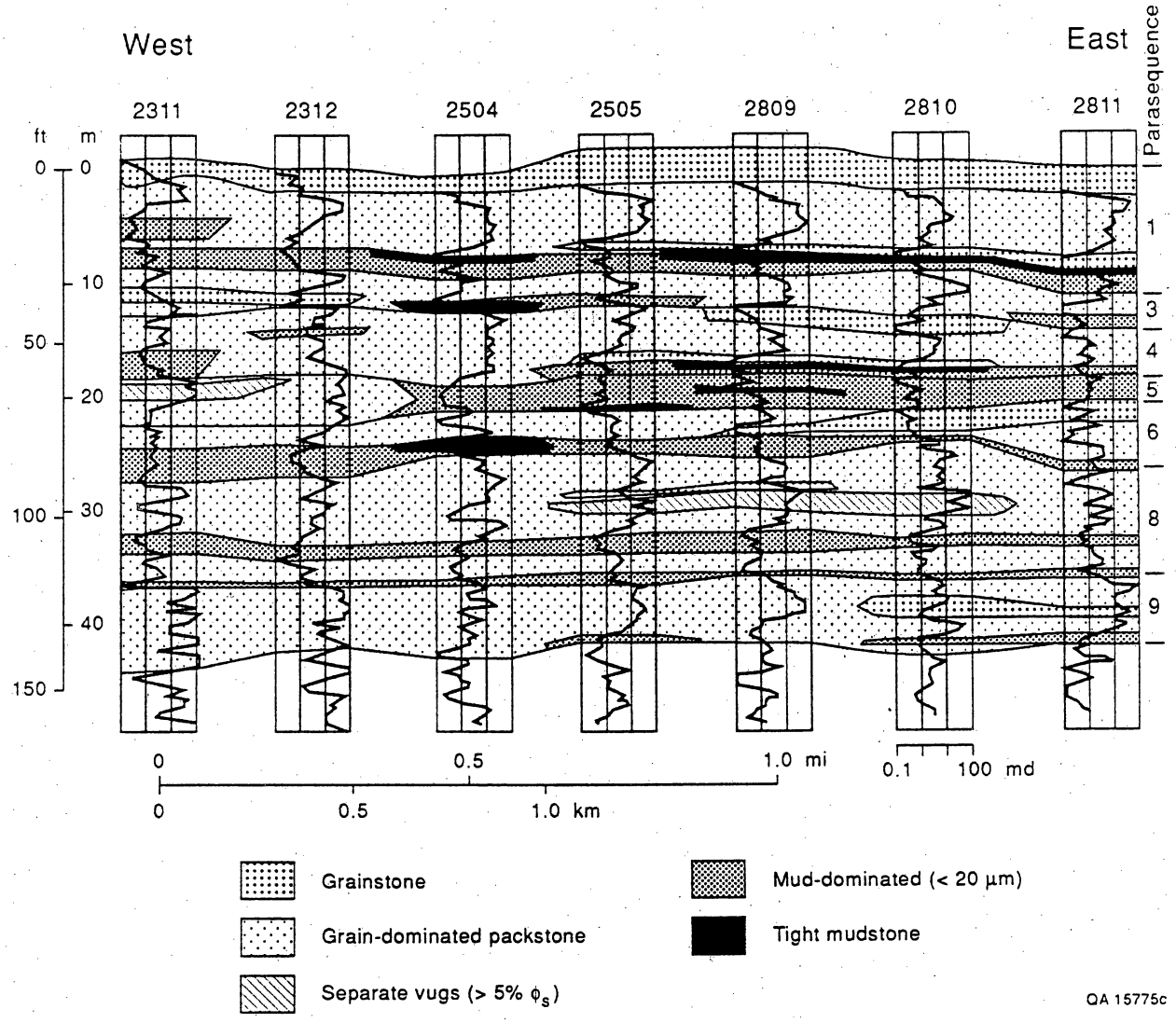

Figure 35. Cross section illustrating the rock-fabric flow model of the upper productive interval in the two-section study area of the Seminole (San Andres) field. Rock fabric and permeability of each well are from log calculations. Correlations are based on stratigraphic framework. See figure 15 for location of cross section.

CONCLUSIONS

One of the most significant problems in describing the petrophysical characteristics of a carbonate reservoir is scale averaging. Considerable effort, as described elsewhere in this report, has been expended examining this problem on the outcrop. The results show that within a rock-fabric type, permeability is highly variable on all scales. Detailed study of selected whole-core samples from the Seminole field shows that in one core sample, permeability varies by as much as a factor of 10, total porosity and separate-vug porosity by several porosity units, and anhydrite commonly by a factor of 2 or more. Particle size and sorting, however, are relatively constant for a whole-core sample. These observations are consistent with outcrop results.

Because particle size and sorting are relatively constant on the scale of feet, this rock-fabric element is used to group petrophysical information. Three petrophysical/rock-fabric groups or classes can be defined that apply to both outcrop and subsurface data. These are (1) dolomitized grainstones, (2) dolomitized grain-dominated packstones and medium-crystal mud-dominated dolomites, and (3) mud-dominated dolomites with <20-μm dolomite crystal size. Each class can be characterized by a porosity/permeability transform and a porosity/saturation/reservoir-height transform.

Mapping the distribution of rock fabrics found within each parasequence provides the key element needed to quantify the geologic framework in petrophysical terms. A rock-fabric reservoir model for the Lawyer Canyon study area was constructed using this approach together with analyses of relationships between rock fabrics, porosity, permeability, and water saturation established from outcrop and subsurface data. The resulting numerical geologic reservoir model is suitable for input into reservoir simulators.

In the subsurface, wireline logs are the principle source of geologic and petrophysical information. The established relationships between rock fabric, porosity, permeability, and saturation provide the basis for distinguishing between the three petrophysical/rock-fabric

classes using water-saturation/porosity cross plots. Once the class has been determined, rock-fabric specific porosity/permeability transforms can be used to calculate permeability from wireline calculations of porosity.

Rock-fabric studies have shown that permeability is a function of interparticle porosity, not total porosity as measured by wireline logs. Interparticle porosity is defined as total porosity less separate-vug porosity. The new method for calculating separate-vug porosity developed as part of this study, and using interval travel time and total porosity, provides a more accurate measure of interparticle porosity needed to estimate permeability from rock-fabric specific porosity/permeability transforms.

The parasequence framework of the upper productive interval of the two-section study area was quantified in petrophysical terms using the wireline-log calculations developed during this study. The results are consistent with core descriptions, and the resulting rock-fabric reservoir flow model shows many similarities to the model described from the upper San Andres at Lawyer Canyon.

REFERENCES

Back, W., Hanshaw, B. B., Plummer, L. N., Rahn, P. H., Rightmire, C. T., and Rubin, M., 1983, Process and rate of dedolomitization: mass transfer and ^{14}C dating in a regional carbonate aquifer: Geological Society of American Bulletin, v. 94, no. 12, p. 1415–1429.

Lucia, F. J., 1961, Dedolomitization in the Tansill (Permian) Formation: Geological Society of America Bulletin, v. 72, no. 7, p. 1107–1109.

———— 1983, Petrophysical parameters estimated from visual descriptions of carbonate rocks: a field classification of carbonate pore space: Journal of Petroleum Technology, v. 35, no. 3, p. 629–637.

Lucia, F. J., and Conti, R. D., 1987, Rock fabric, permeability, and log relationships in an upward-shoaling, vuggy carbonate sequence: The University of Texas at Austin, Bureau of Economic Geology Geological Circular 87-5, 22 p.

INVESTIGATION OF SPATIAL PERMEABILITY DISTRIBUTION IN THE SAN ANDRES OUTCROP, ALGERITA ESCARPMENT, NEW MEXICO: GEOSTATISTICAL ANALYSIS OF RESERVOIR FLOW CHARACTERISTICS

by
Rainer K. Senger and Graham E. Fogg

assisted by
Malcolm Ferris and Andrew Czebieniak

INTRODUCTION

The investigation of spatial permeability distribution in carbonate-ramp deposits of the upper San Andres Formation that crop out along the Algerita Escarpment, New Mexico, is a research element of the geologic and petrophysical studies conducted at the Bureau of Economic Geology's Reservoir Characterization Research Laboratory (RCRL). The primary goal of the investigation is to develop an integrated strategy involving geological, petrophysical, geostatistical, and reservoir simulation studies on continuous outcrop that can be used to better predict flow characteristics in subsurface reservoirs.

To characterize the complex heterogeneity associated with depositional and diagenetic processes at the interwell scale, detailed permeability data were collected from the outcrop at Lawyer Canyon, Algerita Escarpment, New Mexico. Geologic mapping revealed a series of upward-shallowing parasequences (10 to 40 ft thick and several thousand feet long) representing the geologic framework of the reservoir model (Kerans and Nance, this volume). Parasequence boundaries are typically marked by tight mudstone/wackestone beds that display variable degrees of lateral continuity ranging from several hundred ft to more than 2,500 ft and are potentially important as flow barriers (fig. 1). Within these parasequences, distinct variability of facies and petrophysical characteristics is present at scales well below those of interwell spacing (660 to 1,330 ft). Pore types and permeability-porosity relationships can also be specific to individual parasequences (Hovorka, this volume; Lucia, this volume).

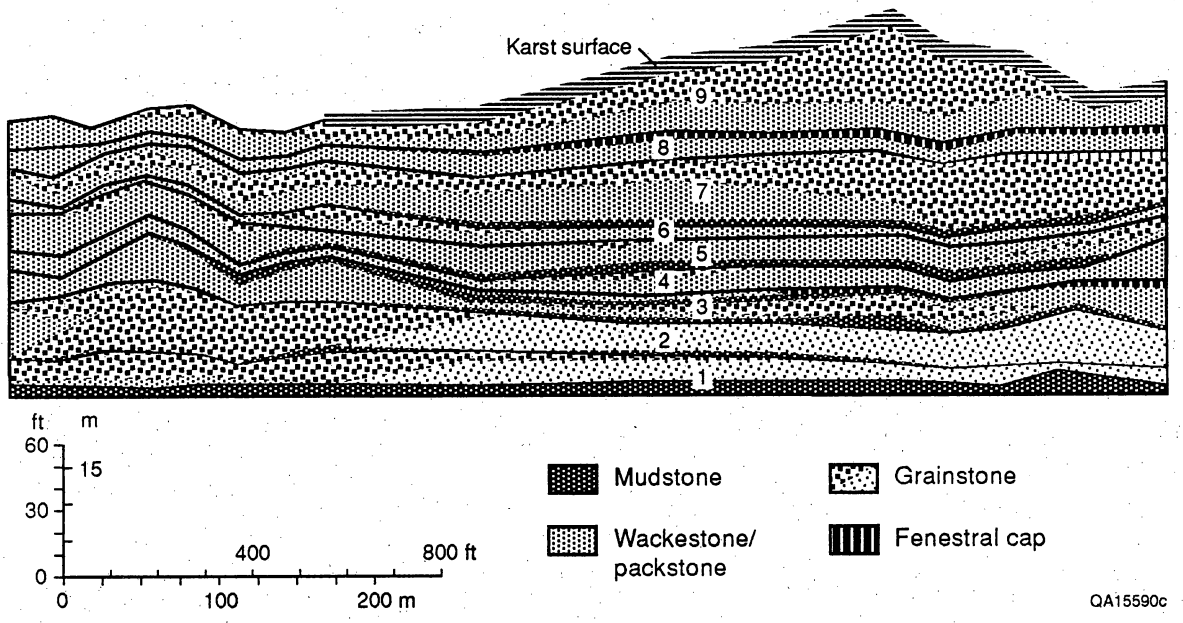

Figure 1. Generalized geologic framework of detailed upper San Andres parasequence window, Lawyer Canyon study area.

In this part of the study, standard statistics are used to relate permeability to facies and rock fabric characteristics. In addition, geostatistical analysis is applied to evaluate spatial permeability characteristics. Stochastic modeling is then used to generate a series of "realistic" permeability distributions on the basis of the underlying permeability structure and uncertainty of measurement data. Numerical waterflood simulations of selected permeability realizations were designed to characterize interwell heterogeneity and to represent heterogeneity by appropriate average properties that can be used in reservoir-scale flow models.

METHODOLOGY

Permeability Measurements

Permeability was measured using a mechanical field permeameter (MFP), which measures gas flow rates and pressure drop by pressing an injection tip against the rock surface. These data are used to calculate permeability values on the basis of a modified form of Darcy's law that incorporates effects of gas slippage at high velocity (Goggin and others, 1988). In addition, permeability and porosity were determined on the basis of conventional Hassler sleeve methods, using 1-inch-diameter core plugs taken from the outcrop. Core and MFP permeability compared reasonably well for permeabilities greater than about 1 md, which is approximately the detection limit of MFP measurements (Goggin and others, 1988).

The distribution of permeability measurements taken from the upper San Andres at Lawyer Canyon is shown in figure 2. Sampling focused on parasequence 1, represented by grainstones forming bar-crest and bar-flank facies overlying wackestones and mudstones of a flooded-shelf facies, and on parasequence 7, represented by low-moldic and highly moldic grainstones (fig. 1). Permeability distributions were measured at scales ranging from detailed grids of 1-inch spacing to 1-ft spacing and vertical transects that were spaced laterally between 5 and 100 ft and contained permeability measurements at 1-ft vertical intervals. (With the exception of permeability measurements from the 1-inch and 1-ft grids in parasequence 1, for

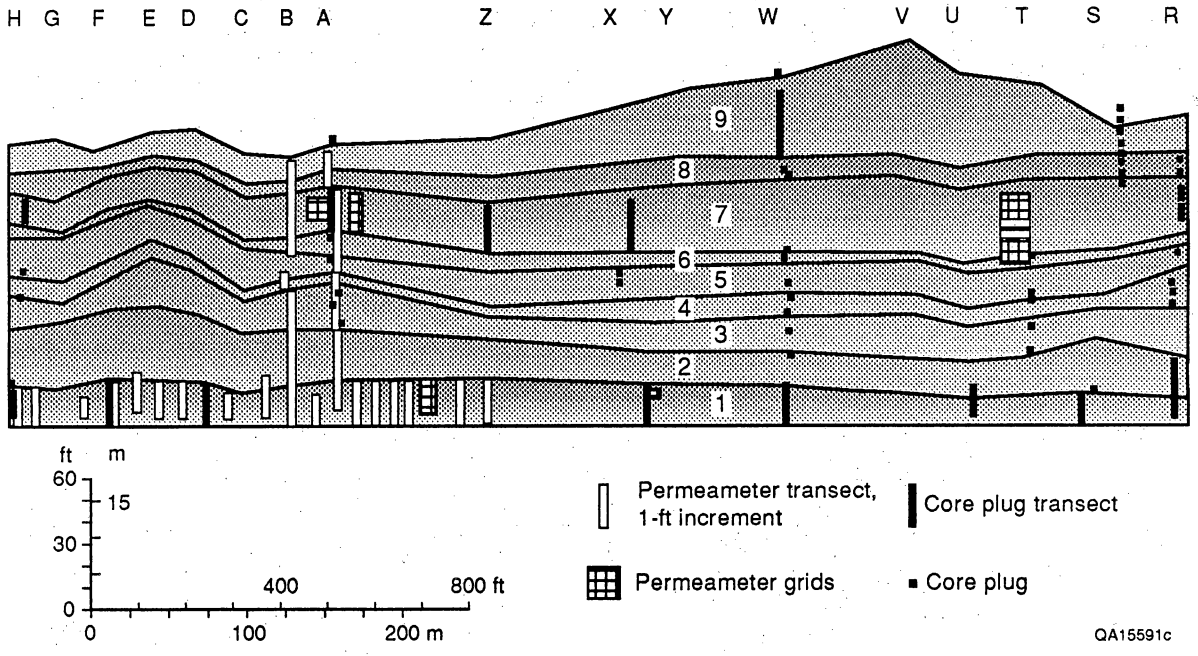

Figure 2. Location of sampling grids and transects of MFP measurements and core plugs.

both MFP and core-plug data, as well as the respective coordinates, facies, and fabric designations, see the appendix.) Although a number of core and MFP permeabilities show the same spatial coordinates, MFP measurements are not from the core plug but from an area within approximately 1 ft of the core plug.

The total number of MFP measurements taken at the Lawyer Canyon parasequence window was 1,584. Removing the outer weathering surface of the rock by chipping an area of about 1 square inch gave the best representation of permeability (Ferris, in preparation). Preparing the sampling surface with a grinder produced overall lower permeabilities than did chipped surfaces because fines plugged the pore space (Kittridge and others, 1990). Within each chipped area, typically, several measurements were made and averaged. Depending on measurement discrepancies, as many as six different MFP readings were taken at various locations within the chipped area (appendix).

Geostatistics

Variography, a geostatistical technique for analyzing spatial variability of a property, such as permeability, is used to help quantify the spatial permeability pattern at different scales. For further details, refer to Journel and Huijbregts (1978) and Fogg and Lucia (1990). The variogram describes variability as a function of distance between measurements. Generally, two measurements in close proximity can be expected to have similar permeability values. The average variance of measurement pairs within certain distance intervals typically show increasing variability (q) with increasing interval range (fig. 3). Beyond a certain distance (range), q may no longer increase. The variance that corresponds to the range is the sill, which reflects the variability where spatial correlation no longer exists; it typically corresponds to the ensemble variance of the entire data set. Small-scale heterogeneity or measurement errors can cause a variogram to originate at a high variance referred to as a nugget, representing local random variability.

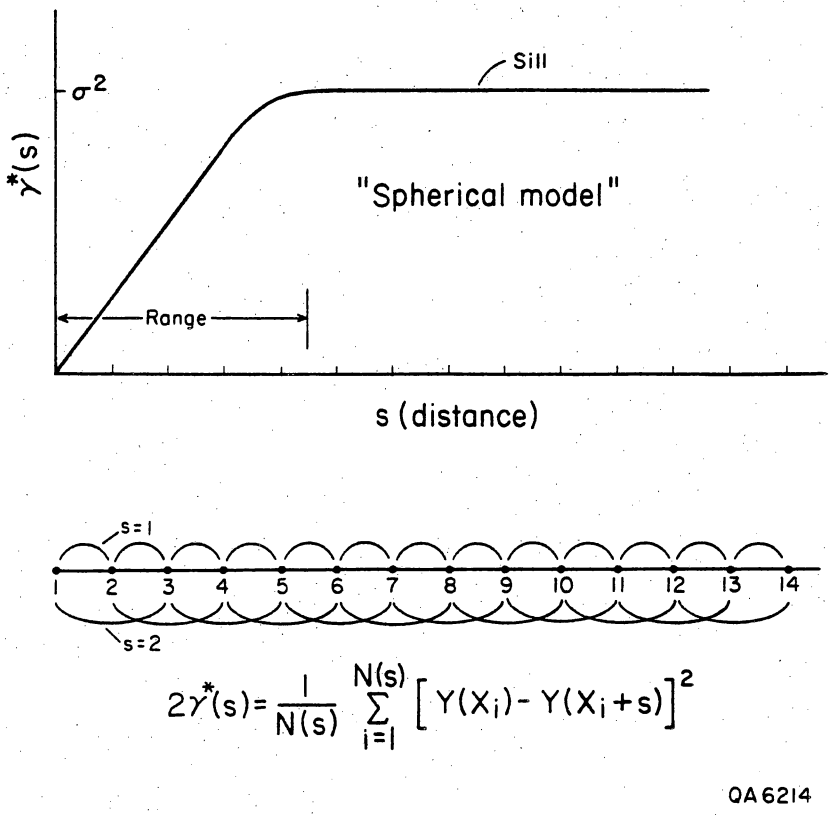

Figure 3. Schematic example of calculation of the experimental variogram.

Spatial permeability characteristics can be described by the nugget, the correlation range, the sill, and the variogram model. The latter is obtained by fitting a certain type of mathematical function to the experimental variogram. In this study the computer program GAMUK (Knudsen and Kim, 1978) was used to compute the experimental variogram.

Application of the variogram to kriging or conditional simulation usually requires an assumption of stationarity, which requires that the mean and variogram are the same over the area of interest.

Kriging is a technique of estimating properties at points or blocks distributed over the area of interest by taking a weighted average of sample measurements surrounding a regularly spaced grid point or block. Kriging incorporates the spatial correlation structure contained in the variogram model. The kriging program is based on the program UKRIG, developed by Knudsen and Kim (1978). The point-kriged permeability values were contoured with the CPS-1 contouring package (Radian Corporation, 1989).

Conditional simulation uses the underlying permeability structure obtained from kriging and adds the stochastic component associated with the uncertainty of the limited permeability data. Conditional simulation is performed with the program SIMPAN (Fogg, 1989). A large number of permeability realizations are screened for maximum and minimum continuity of permeable zones using the program MCSTAT (Fogg, 1989). These end member representations of "realistic" permeabilities, conditioned on the same permeability data, are then used in waterflood simulations to evaluate reservoir flow characteristics. The reservoir simulator ECLIPSE (ECL Petroleum Technologies, 1990) was used for two-phase waterflood simulations.

CHARACTERIZATION OF PERMEABILITY DATA

For the evaluation of permeability characteristics with respect to facies and fabrics, only those data were taken that follow the geologic measured sections for which spatial coordinates, facies, and fabric designations are available (appendix). The histogram of permeabilities using

both core and MFP measurements (fig. 4) shows a roughly lognormal distribution. Core permeabilities show a much wider range toward lower permeabilities than MFP measurements owing to the 1-md detection limit of the MFP data. Within relatively permeable facies (that is, the bar-crest facies within parasequence 1), core and MFP measurements have statistically similar populations, with similar geometric means of 1.33 and 1.34 md, respectively. Statistical comparison of the two populations via a t-test indicated that the null hypothesis cannot be rejected at the 80-percent confidence level (t-statistics = –0.1318; p-value = 0.8953).

Several of the mapped parasequences indicate significantly different hydraulic properties, as shown by the statistical comparison of mean permeabilities within each parasequence (fig. 5). Mean permeabilities in parasequences 1, 2, 7, and 9 are significantly higher than those in parasequences 3, 4, 5, 6, and 8. The latter sequences consist mostly of packstone and wackestone, whereas parasequence 1, 2, 7, and 9 consist predominantly of grainstones. The somewhat lower permeabilities in parasequence 7 are caused by moldic pore-type characteristics, as compared with intergranular porosity in the other cycles (Hovorka, this volume; Lucia, this volume). The dominant rock fabrics exhibit significant differences in mean permeability (fig. 6), with mudstone having the lowest permeability and grainstones having the highest permeabilities. Most of the mapped facies are also characterized by significantly different mean permeabilities (fig. 7). Generally, shelf facies exhibit significantly lower mean permeabilities than bar facies, with the bar-crest and bar-accretion-set facies having the highest mean permeability of log k = 1.1 md. The facies characteristic (fig. 7) is consistent with the rock fabric characteristic (fig. 6) because the bar facies consist mostly of high-permeability grainstones and the shelf facies consist mostly of low-permeability mud-dominated fabrics. However, within individual facies, permeability varies by as much as five orders of magnitude. Characterization of spatial permeability patterns within individual facies is therefore crucial for predicting flow behavior in these ramp-crest grainstone bar complexes. If permeability within facies is spatially uncorrelated (that is, random), then effective permeability of that facies can be estimated by taking the geometric average of the local permeabilities (Warren and Price,

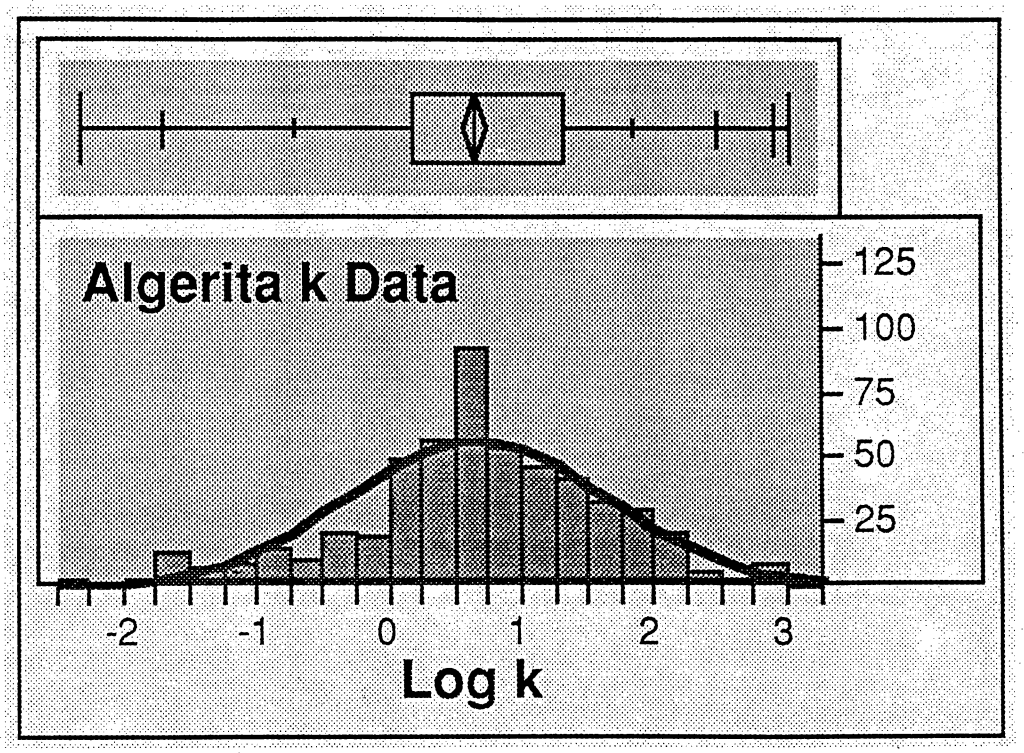

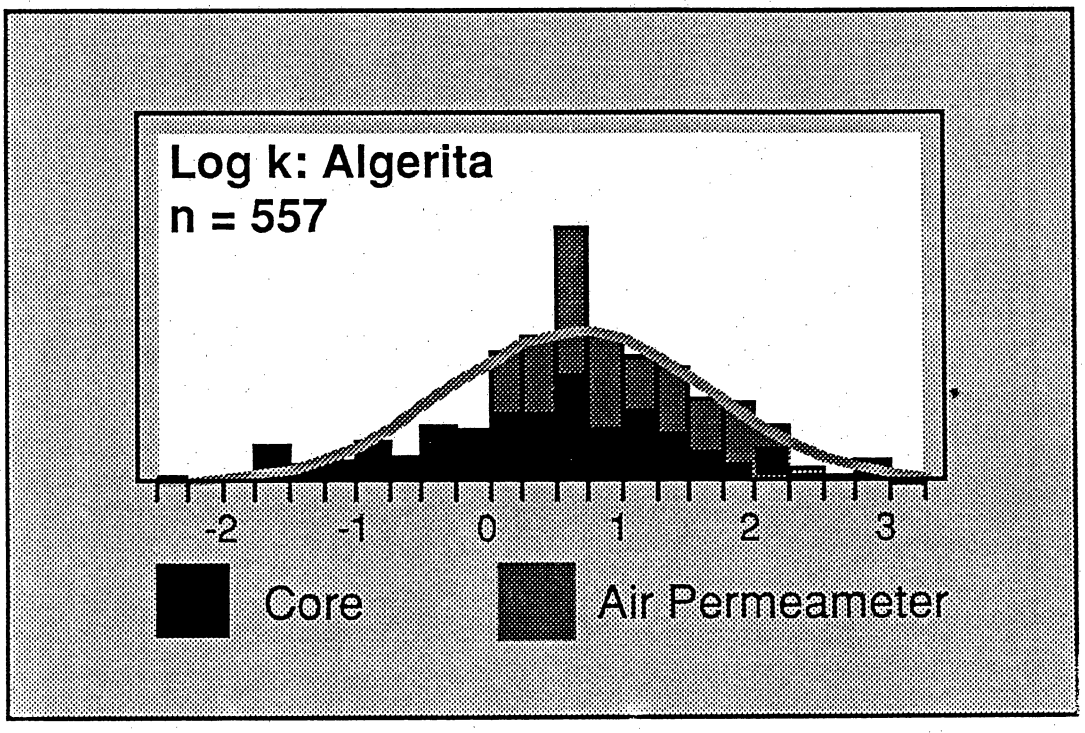

Figure 4. Histogram of permeabilities along the geologically measured sections.

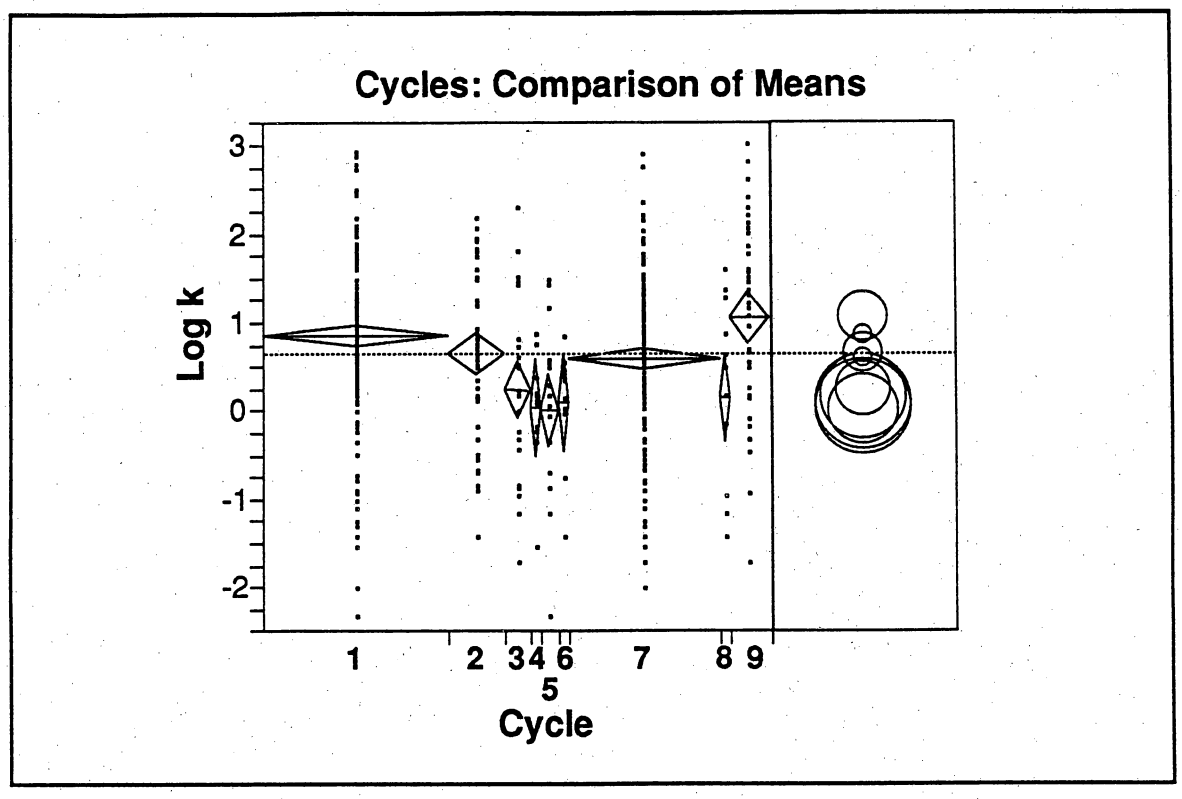

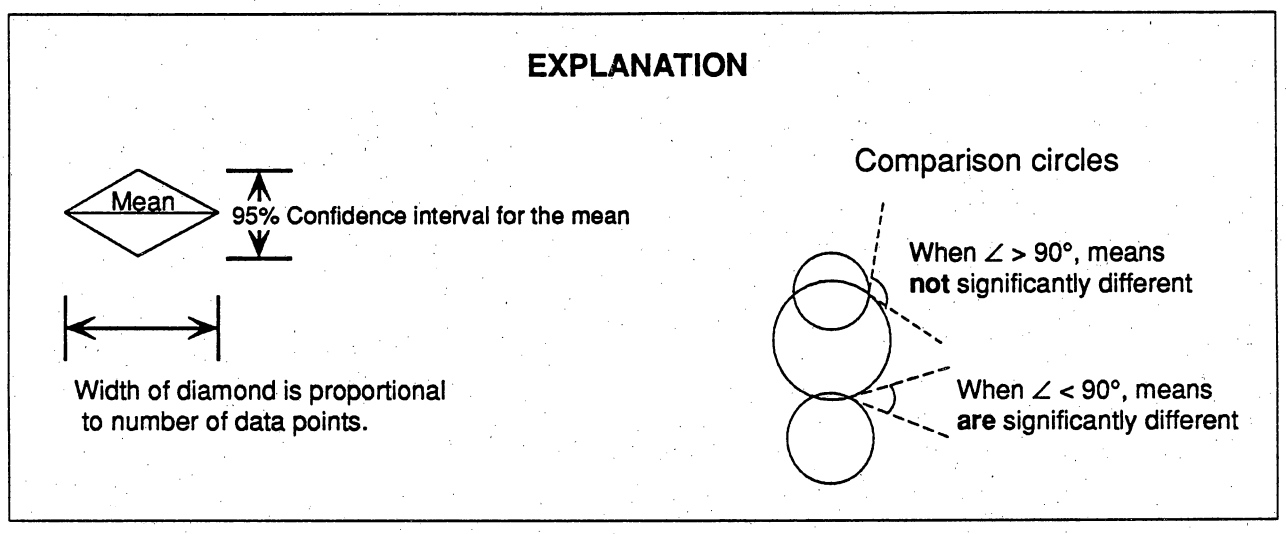

Figure 5. Statistical comparison of means of permeability for the different parasequences. Comparison circles correspond to the 95-percent confidence intervals for the means.

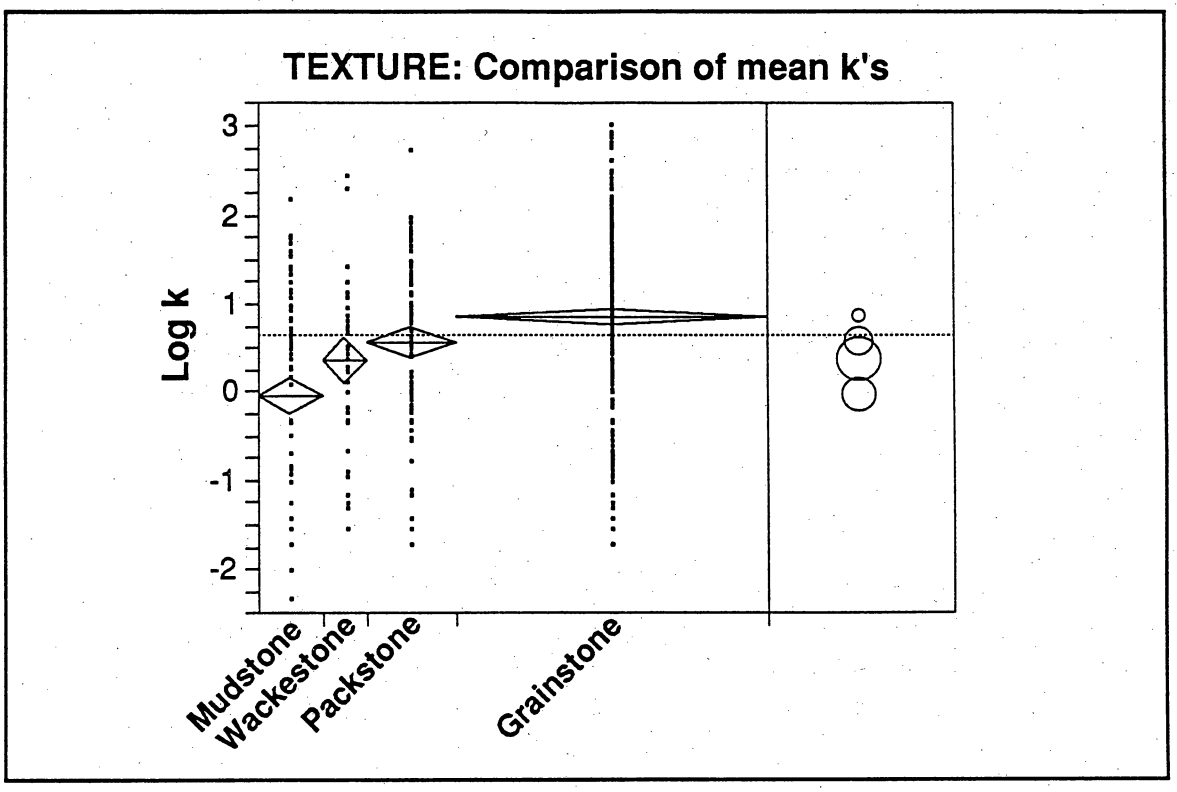

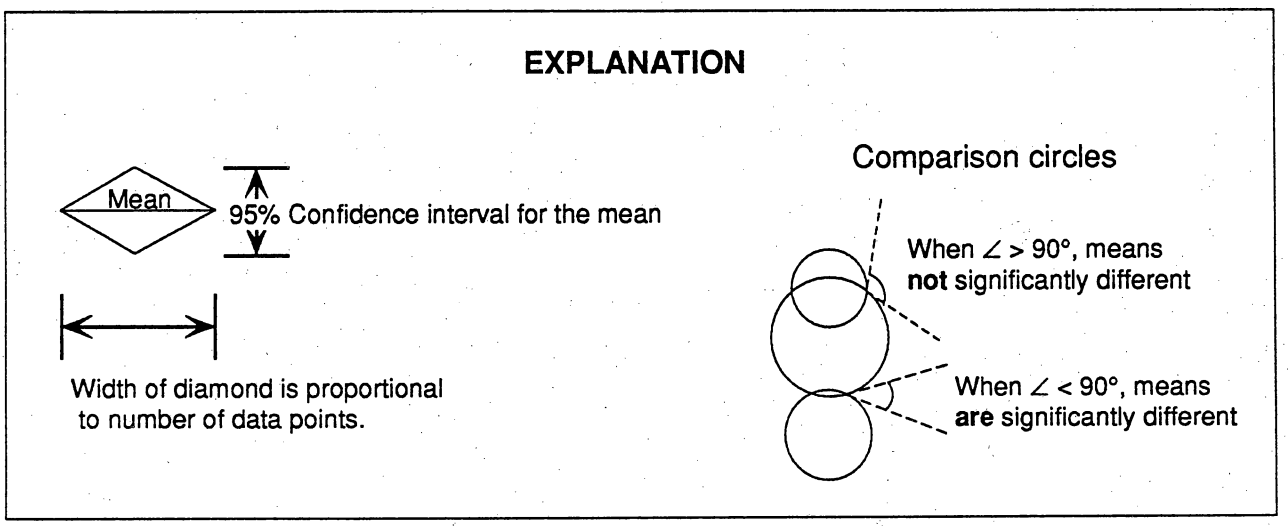

Figure 6. Statistical comparison of means of permeability for different textures.

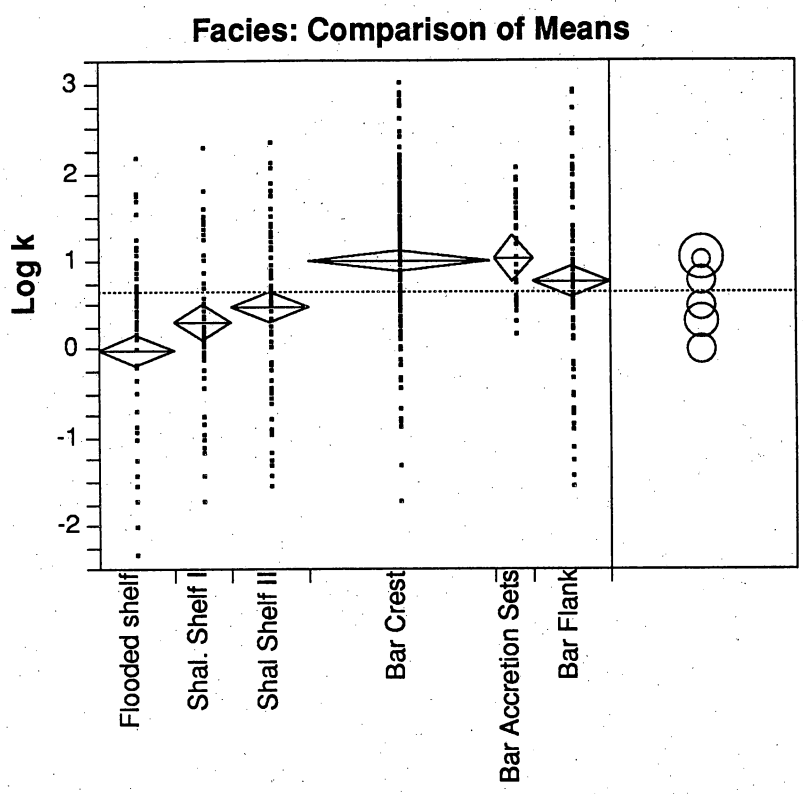

Mean Estimates

Facies	N	Mean	Std Error
Flooded shelf	82	-0.01	0.10
Shallow shelf I	48	0.25	0.13
Shallow shelf II	73	0.51	0.11
Bar crest	158	1.07	0.07
Bar top	6	0.10	0.37
Tidal flat	2	0.37	0.65
Bar accretion sets	18	1.11	0.22
Bar flank	82	0.76	0.10
Shallow shelf I (moldic)	16	0.45	0.23
Shallow shelf II (moldic)	9	0.26	0.30
Bar crest (moldic)	39	0.73	0.15
Bar accretion sets (moldic)	24	0.98	0.19

Figure 7. Statistical comparison of means of permeability for different facies. Standard error values refer to the estimated means.

1961). If permeability within facies exhibits significant spatial correlation, then effective permeability of that facies must be estimated by taking some other type of average.

Spatial Permeability Patterns and Variography

Spatial patterns in permeability were characterized and mapped in three steps. First, the data were contoured with an inverse-distance-squared algorithm to depict any trends or anisotropies in the data. Second, variograms were computed for different lag spacings and directions that were consistent with the data spacings and inverse-distance maps. Third, variogram models were fit to the variograms and were used to create point-kriged maps of spatial permeability patterns.

Standard contouring (inverse-distance-squared) of the detailed permeability transects spaced between 25 and 100 ft in parasequence 1 (fig. 2), using the CPS-1 contouring package, shows extreme heterogeneity (fig. 8) within the bar and open-shelf grainstone and packstone facies, which are referred to as the grainstone facies in parasequence 1. Permeability is controlled by total porosity with separate-vug porosity (intragranular microporosity) having a second-order effect (Lucia, this volume). To evaluate heterogeneity at different spacings, permeability measurements were taken on local grids at different scales, which include the following: (a) A 5-ft grid consisting of eight vertical transects spaced 5 ft apart and sampled every foot (fig. 9). The 5-ft grid is located between sections A and Z in parasequence 1 (fig. 2). (b) A 1-ft grid consisting of 21 vertical transects and 14 horizontal transects, sampled every foot or half foot (fig. 10). The 1-ft grid is located within the 5-ft grid (fig. 9). (c) A 1-inch grid consisting of four 25-inch vertical transects and two 46-inch horizontal transects (fig. 11). The 1-inch grid is located within the 0.5-ft spaced measurement points of the 1-ft grid (fig. 10). Each transect contains one measurement per inch. The upper horizontal transect followed a "porous" zone as identified in the outcrop, whereas the lower transect followed a "tight" zone. Additional detailed sampling grids are located near transect Y in parasequence 1 and near

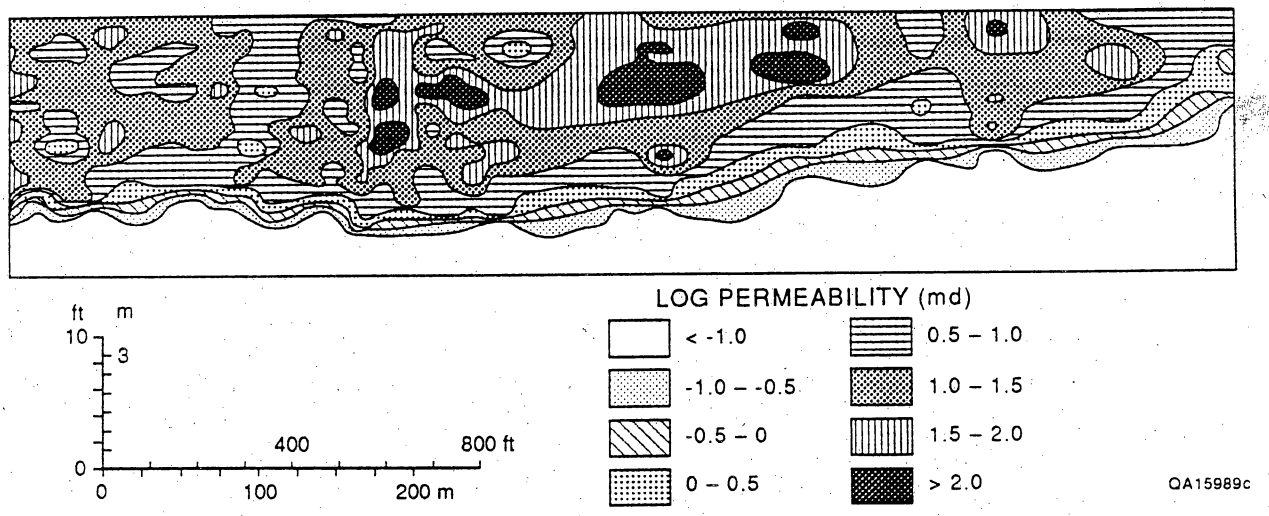

Figure 8. Permeability distribution for normalized parasequence 1 based on inverse-distance squared contouring algorithm using CPS-1.

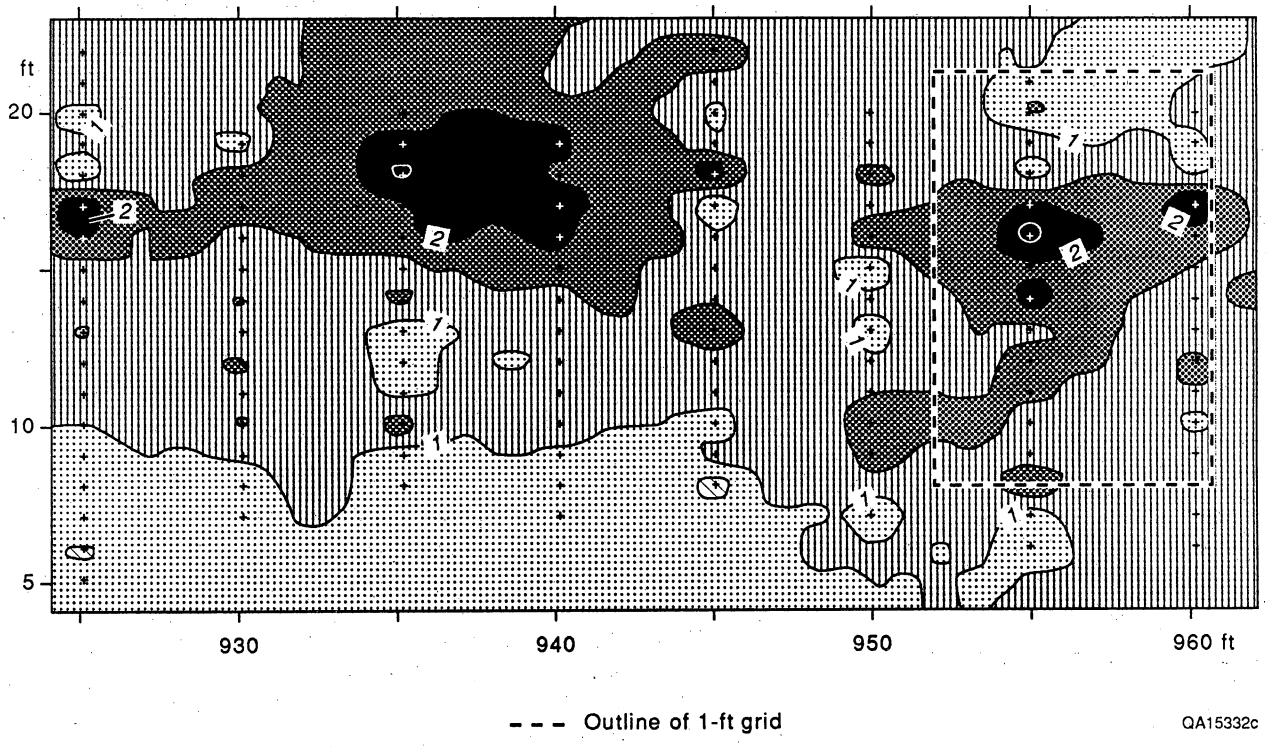

Figure 9. Five-foot sampling grid, located between sections A and Z in parasequence 1; permeability contours are kriged on the basis of variogram analysis.

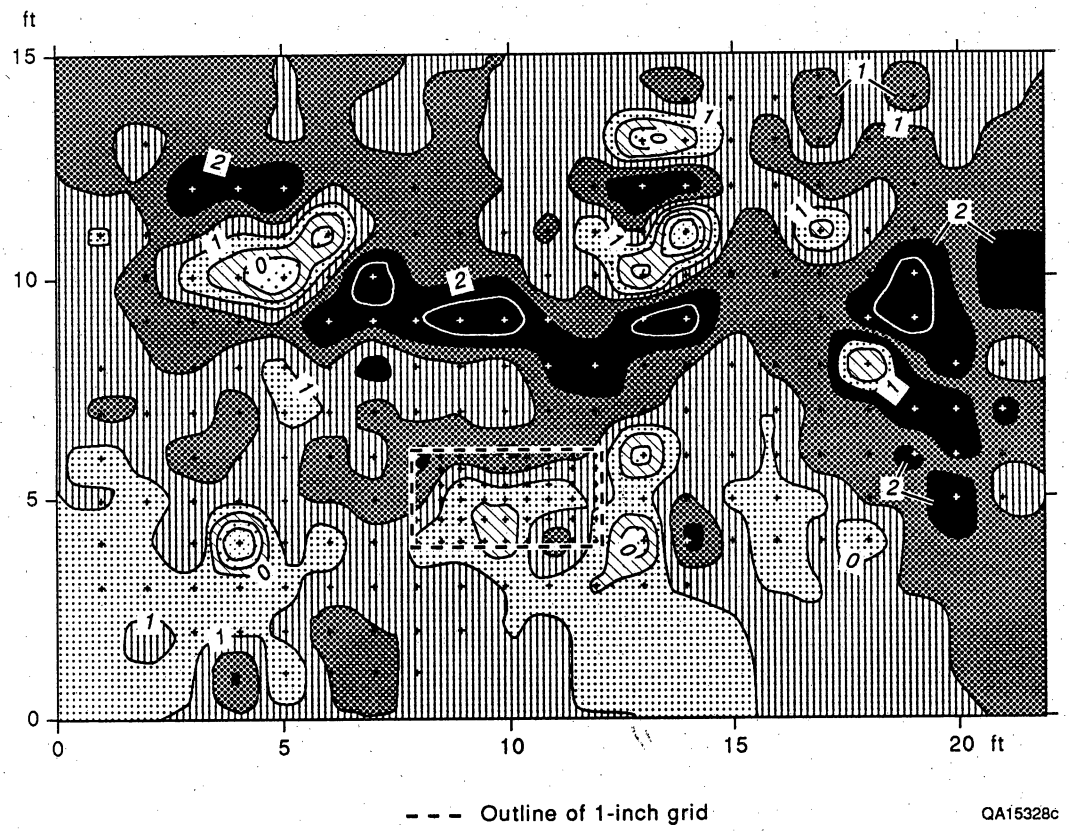

Figure 10. One-foot sampling grid in parasequence 1 with kriged permeability contours.

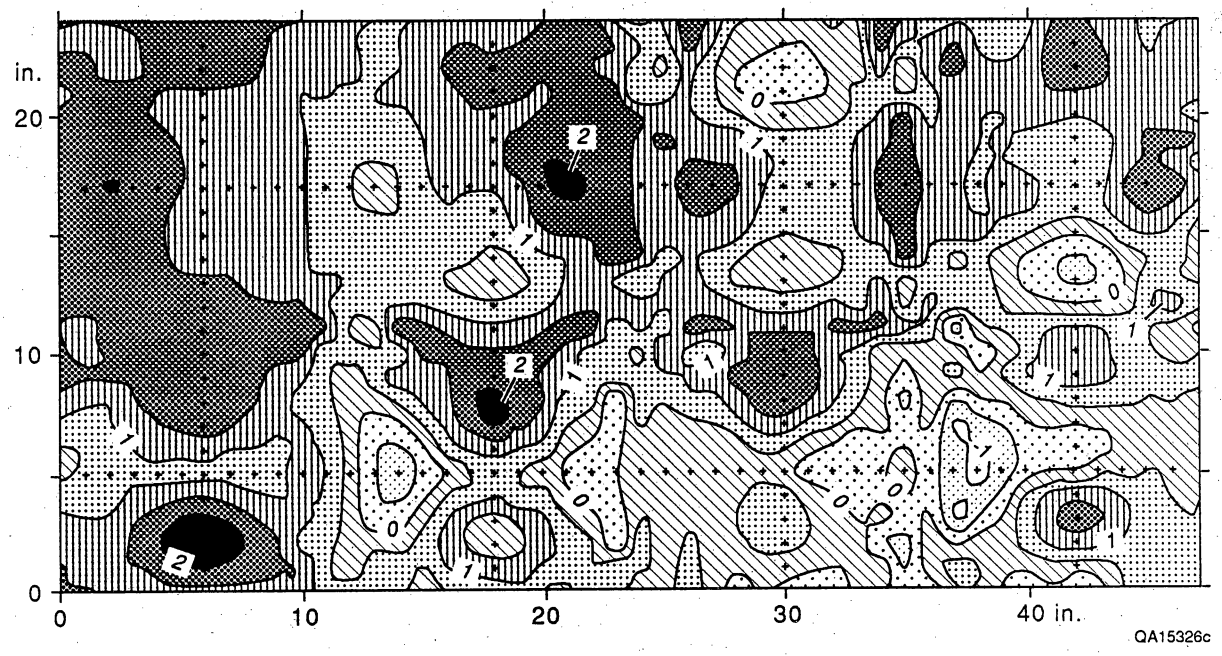

Figure 11. One-inch sampling grid in parasequence 1 with kriged permeability contours.

transects A and T in parasequence 7 (fig. 2). The sampling grid near transect T in parasequence 7 consists of four 30-ft vertical transects that were sampled every 0.5 ft and two 45-ft horizontal transects that were sampled every foot (fig. 12).

Variograms for the horizontal and vertical transects of the 1-inch grid in parasequence 1 (fig. 13a, b) exhibit different characteristics. The vertical variogram suggests a 2-inch range with a nugget of approximately 0.4 md^2 and the data scatter around a sill of about 0.4 md^2. Mean and variance for the vertical transects (1.30 md and 0.92 md^2, respectively) are higher than those for the horizontal transects (0.90 md and 0.82 md^2, respectively). The horizontal variogram suggests a hole effect, which can be fitted with a Bessel-function model. The horizontal variogram indicates a nugget of about 0.4 md^2, but shows a sill of 0.2 md^2, which is lower than that of the vertical variogram. The Bessel-function model may also be applicable to the vertical variogram in representing the wide scatter around the sill (fig. 13a). The difference between the horizontal and vertical variograms indicates anisotropy in hydraulic properties at this scale. The nugget, sill, and range from the variogram model are then used to krige the permeability data on 1-inch, regularly spaced grid points. However, the difference in sill between the horizontal and vertical variogram could not be taken into account in the contoured, point-kriged permeability distribution (fig. 11). The effect of potentially different variogram models in horizontal and vertical directions on kriged permeability pattern needs further study.

The vertical variogram of the 1-ft grid scatters around the sample variance with no correlation structure (fig. 14a), whereas the horizontal variogram vaguely suggests a small correlation length of about 1 ft (fig. 14b). For practical purposes, both variograms exhibit a pure nugget effect, indicating no spatial correlation. The mean and variance (log k) of the 241 permeability measurements of the 1-ft grid are 1.30 md and 0.59 md^2, respectively. Note that the variance of the 1-ft grid is lower than the variance of the 1-inch grid. The kriged permeability distribution of the 1-ft grid (fig. 12) shows larger areas of relatively high permeability than does the 1-inch grid (fig. 11), which is expressed in the higher mean permeability for the 1-ft grid (fig. 14).

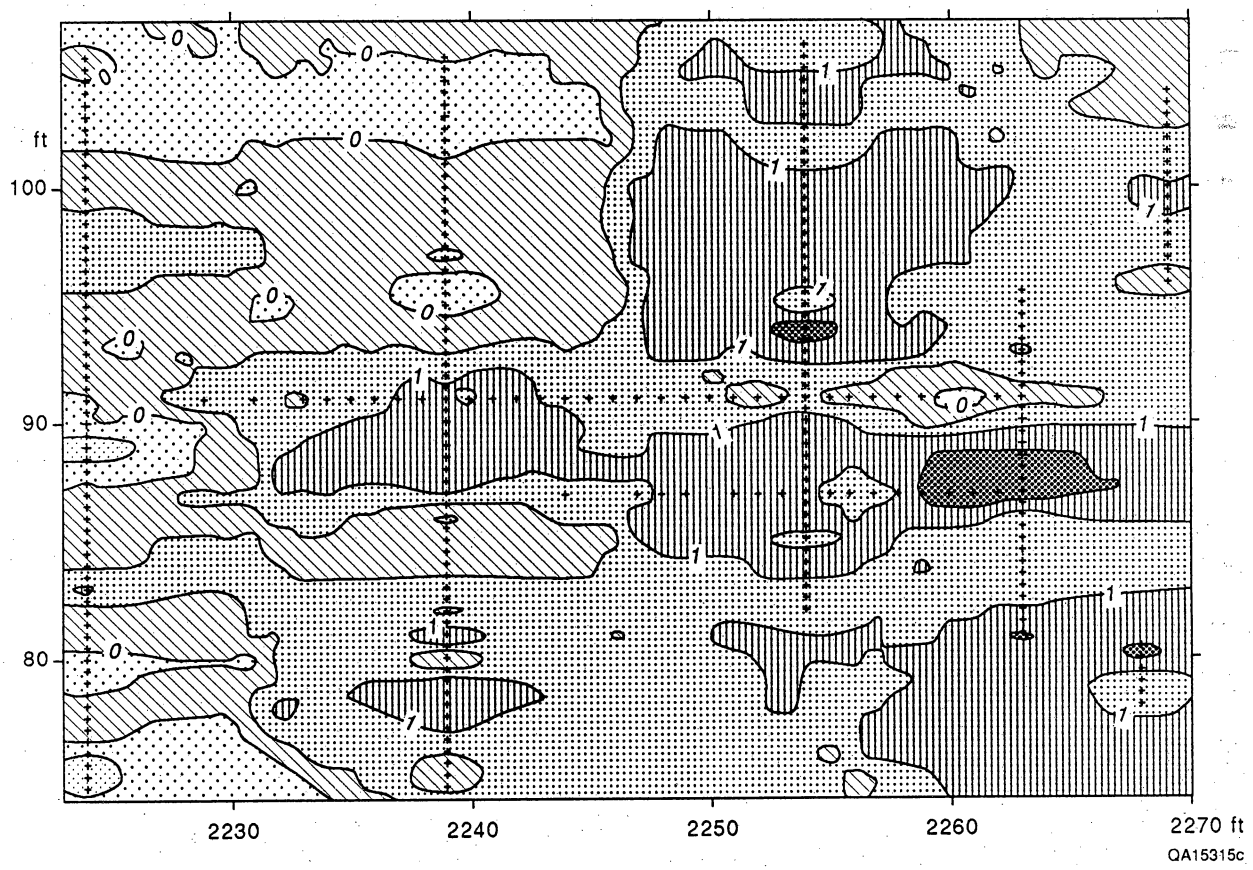

Figure 12. One-foot sampling grid located near section T in parasequence 7 with kriged permeability contours.

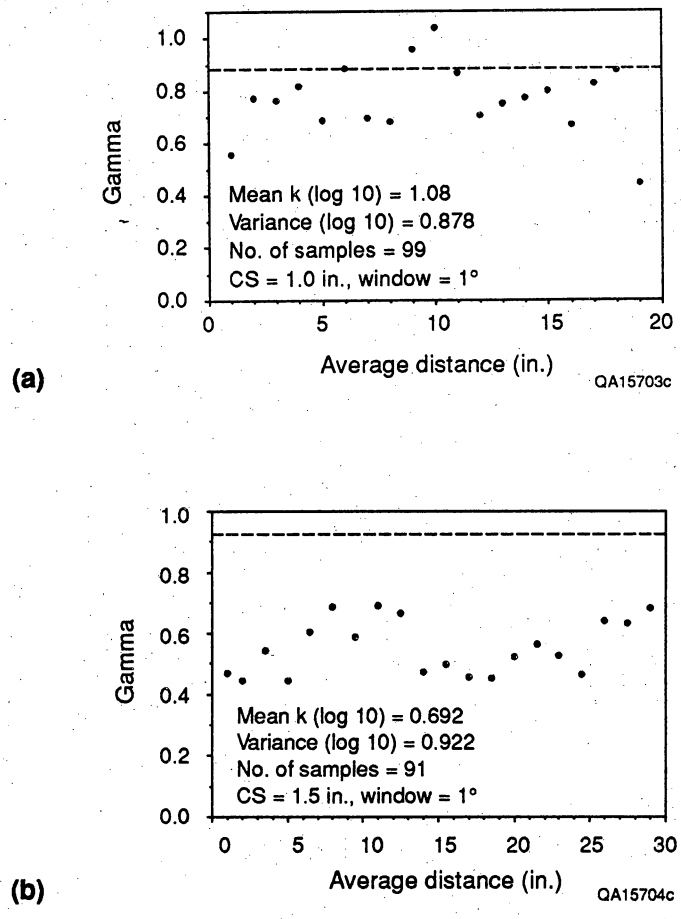

Figure 13. Sample variograms for permeability data from the 1-inch sampling grid: (a) vertical direction and (b) horizontal direction.

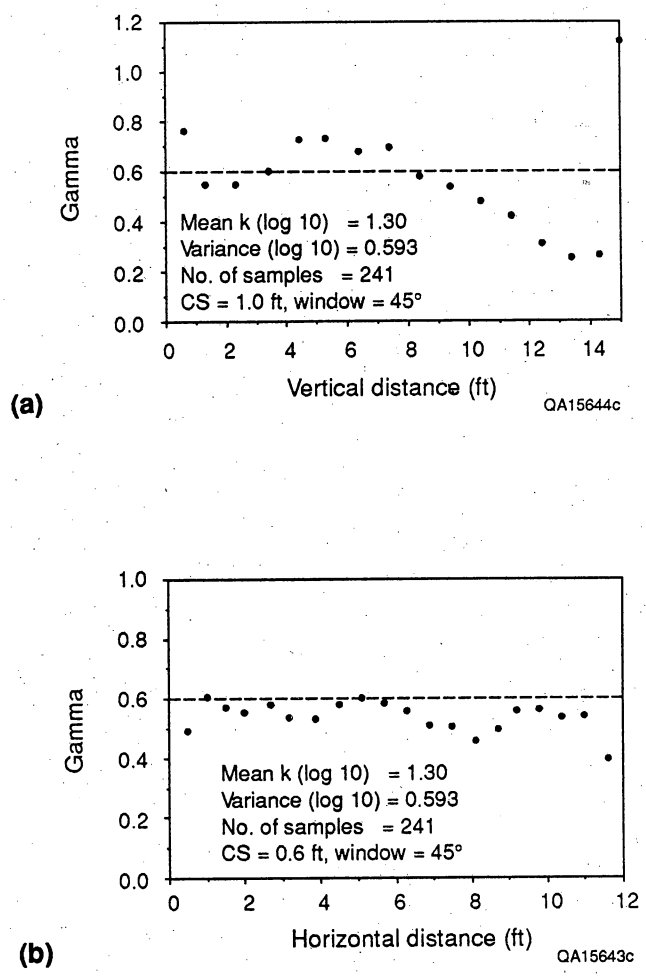

Figure 14. Sample variograms for permeability data from the 1-ft sampling grid: (a) vertical direction and (b) horizontal direction.

The vertical variogram of the 5-ft grid suggests a correlation range of about 2 ft, again with a nugget equal to half the variance, which is 0.46 md^2 (fig. 15). The point-kriged permeability map for the 5-ft grid shows a more uniform permeability pattern (fig. 9) than does the 1-ft grid (fig. 10) or the 1-inch grid (fig. 11). The difference in mean and variance of permeability between the different sampling grids may reflect nonstationarity of permeability.

The vertical variogram, using all the vertical transects of the grainstone facies in parasequence 1 suggests a range of about 3 ft (fig. 16a). The horizontal variogram suggests a short-range correlation of about 30 ft with a large nugget (fig. 16b). Increasing the variogram interval to 50 ft, the resulting horizontal variogram shows nested structures representing long-range correlation (fig. 16c). The long-range permeability correlation is depicted in the permeability contour map of parasequence 1 (fig. 8).

The other detailed sampling grids are located near transects A and T in parasequence 7 (fig. 2). This parasequence is characterized by vuggy porosity (Lucia, this volume); vugs are disconnected and hence strongly affect permeability but only weakly affect porosity. Variograms for the vertical and horizontal transects at Section T indicate anisotropic permeability behavior with a vertical correlation range of about 3 ft and a horizontal range of roughly 13 ft (fig. 17a, b, respectively). Mean permeabilities are lower than average permeabilities in parasequence 1; however, similar to parasequence 1, the nugget is of the same magnitude as the sill. The point-kriged permeability map for section T (fig. 12) shows generally lower permeability than the sampling grids in parasequence 1 (figs. 9 through 11). Along the vertical transects, the permeability correlation is indicated by relatively uniform permeability segments that average about 3 ft in thickness.

Conditional Simulation

Even though kriging can incorporate permeability correlation structures, it tends to average permeability over larger areas, ignoring small-scale heterogeneity. On the basis of the

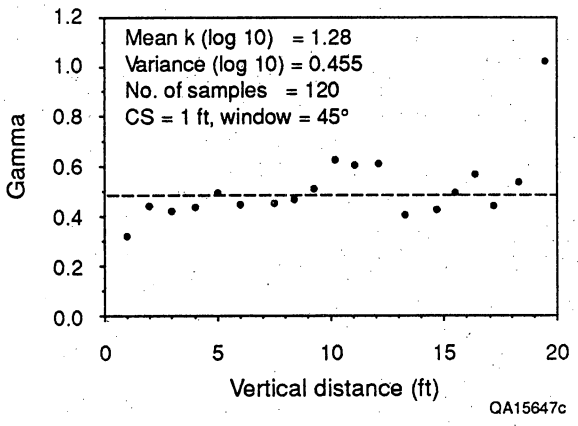

Figure 15. Sample variogram (vertical) for permeability data from the 5-ft grid.

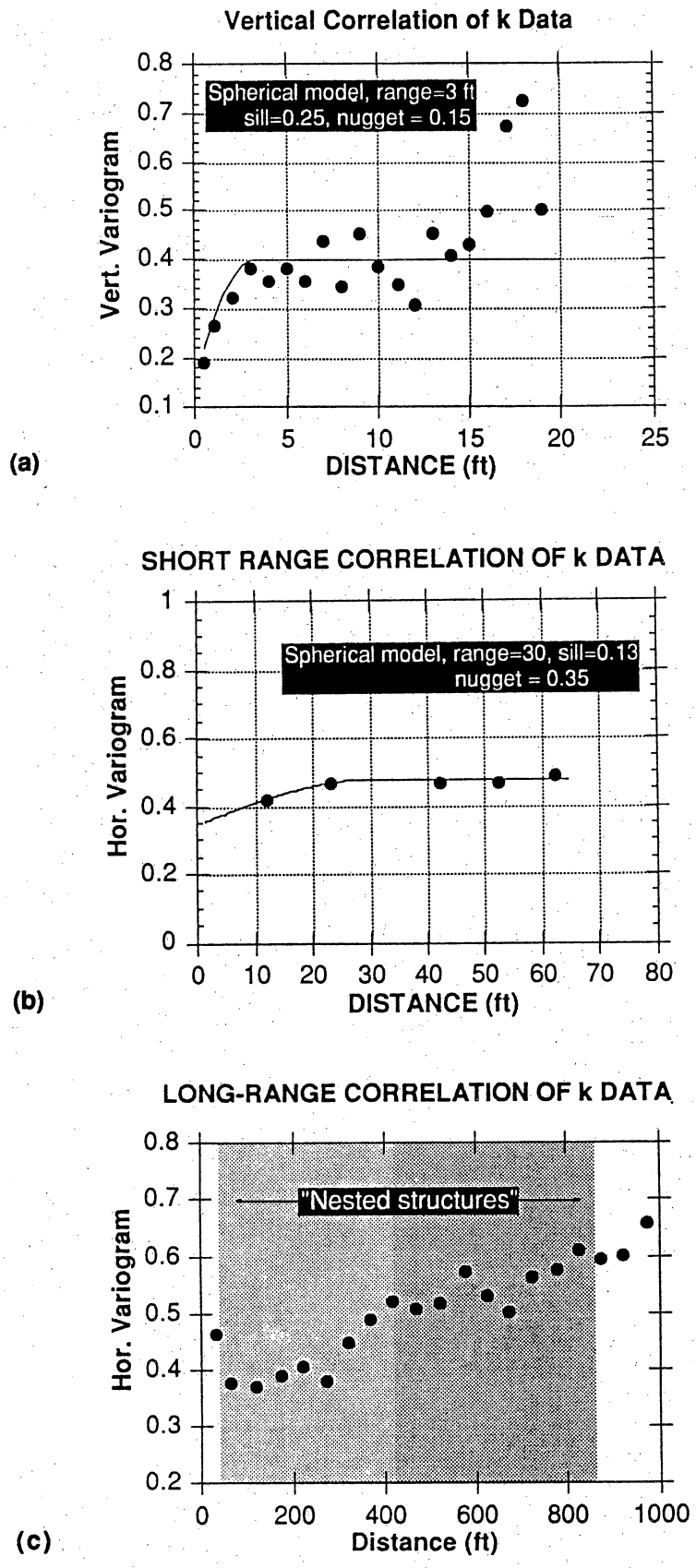

Figure 16. Sample variograms for the entire permeability transects from the grainstone facies in parasequence 1: (a) vertical variogram, (b) short-range horizontal variogram, based on the 5-ft grid, and (c) long-range horizontal variogram, based on all transects spaced about 50 ft apart.

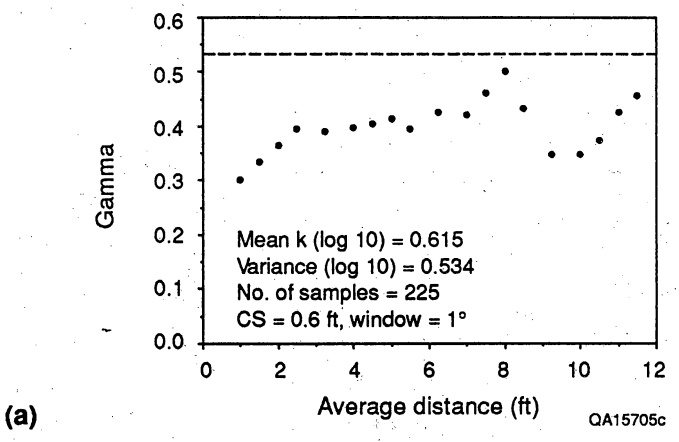

(a)

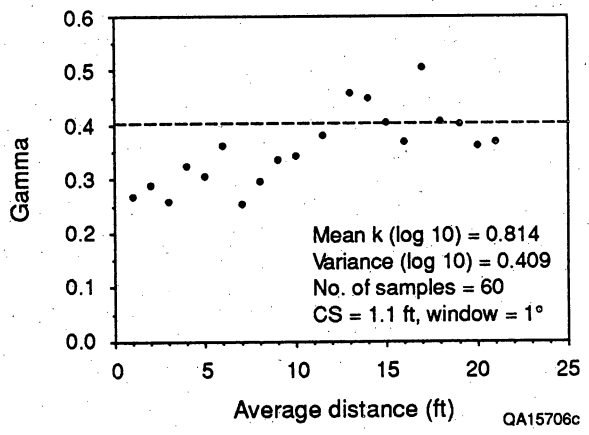

(b)

Figure 17. Sample variograms for permeability data from the 1-ft sampling grid in parasequence 7, section T: (a) vertical variogram and (b) horizontal variogram.

short-range permeability correlation of permeability data (fig. 16a, b), a series of permeability realizations were produced for the grainstone facies in parasequence 1. The model extends laterally from 0 to 1,050 ft and is 17 ft thick with block sizes of 5 ft by 1 ft. The simulations are conditioned to the permeabilities measured along the vertical transects that are spaced approximately 50 ft apart (fig. 2) and incorporate the correlation structure from the variograms.

Two permeability realizations were selected for flow simulations, representing maximum and minimum lateral continuity of domains having permeability values greater than 50 md. Comparison of the two permeability realizations (fig. 18a, b) does not show a noticeable difference. The ranges of 3 ft (vertical) and 30 ft (horizontal) (fig. 16a, b) are not immediately apparent in these realizations (fig. 18); the permeability patterns appear spatially uncorrelated because of the relatively large nugget, which is of the same magnitude as the sill. These conditional simulated realizations, however, preserve the spatial variability exhibited in the variograms, whereas the kriged permeability maps average out much of this variability.

In figure 19, the two realizations are represented by a binary permeability distribution based on a cutoff value of 50 md. Both show a higher density of relatively permeable blocks at the right side of the model (fig. 19a, b) because they both honor the data, which exhibit higher permeabilities in that area. Note that although realization 7 exhibits greater lateral continuity for permeabilities above 50 md, realization 11 has somewhat higher mean permeability (fig. 18a, b).

Results of Waterflood Simulations of Parasequence 1

Waterflooding of the hypothetical two-dimensional reservoir is simulated by injecting water along the right boundary and producing along the left boundary. Injection and production were controlled by prescribed pressure conditions of 2,450 psi and 750 psi, respectively.

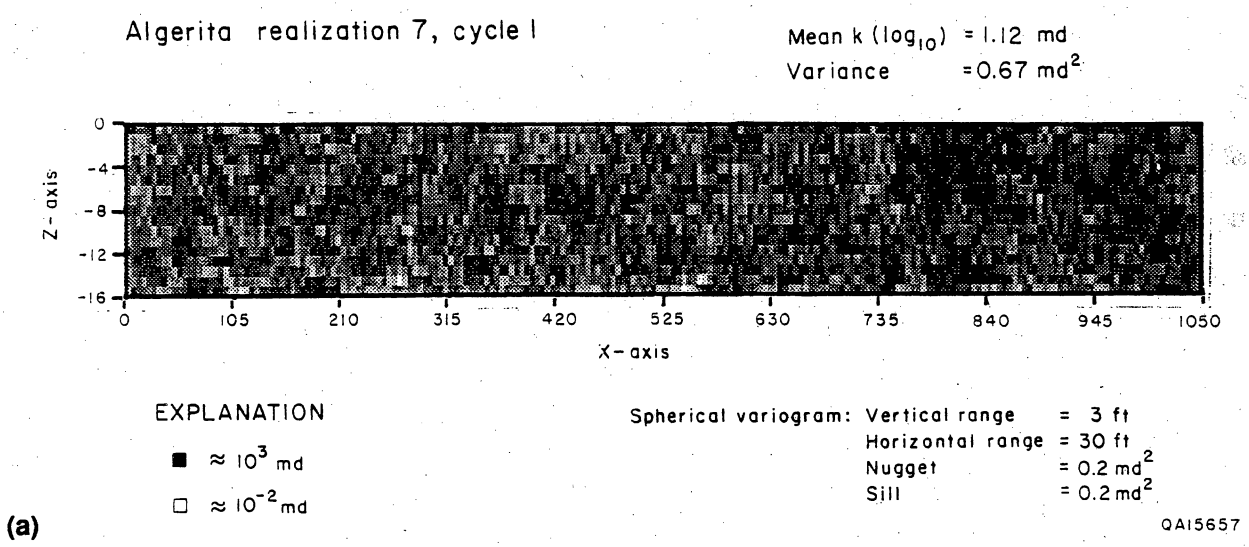

(a)

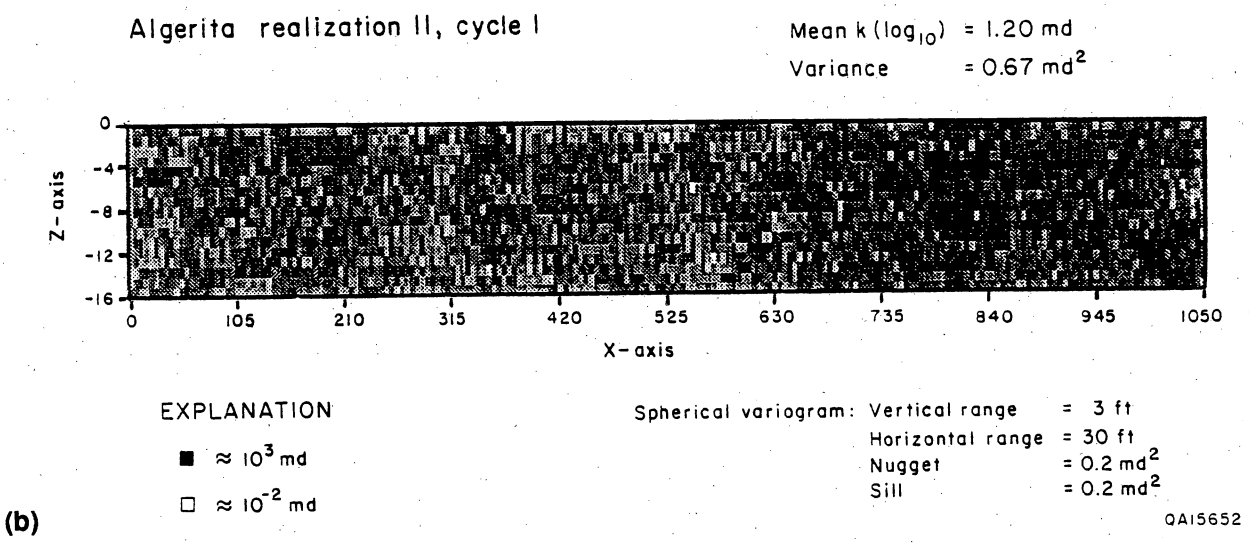

(b)

Figure 18. Stochastic permeability distributions of (a) realization 7, representing higher lateral continuity, and (b) realization 11, representing lower lateral continuity but slightly higher average permeability.

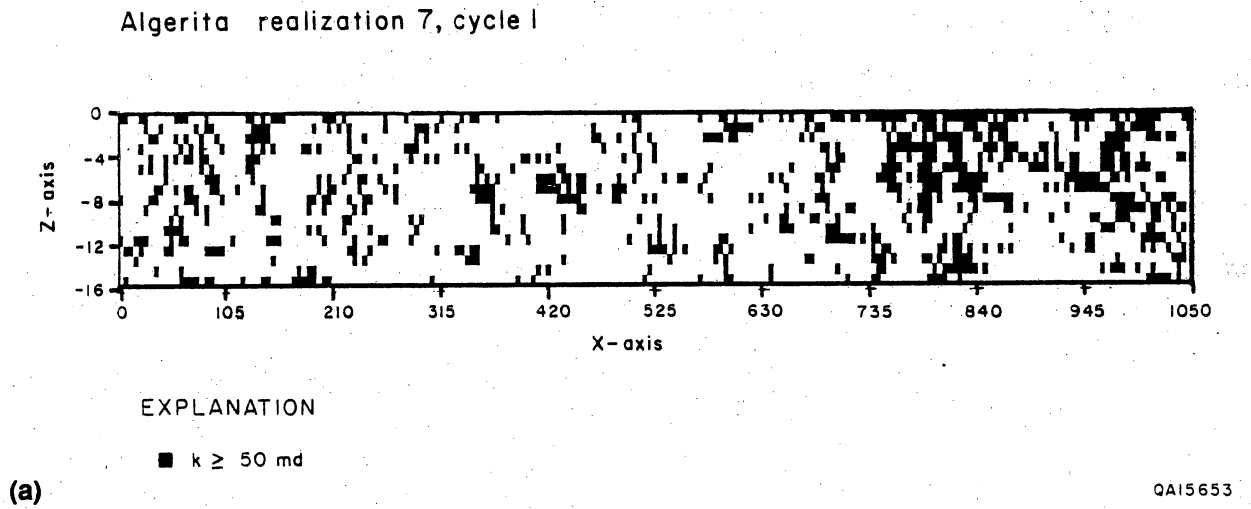

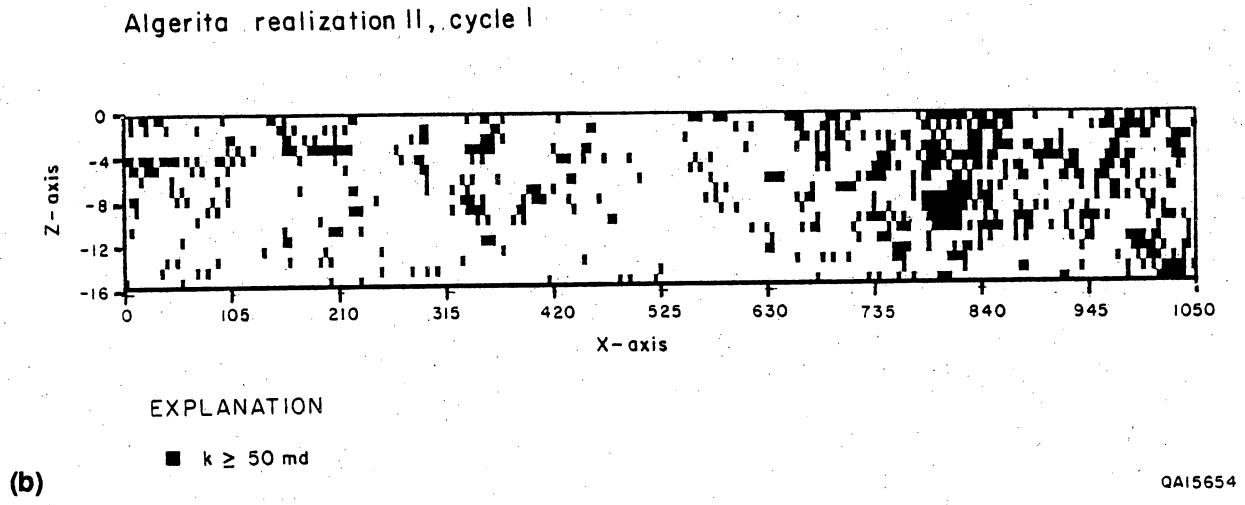

Figure 19. Binary permeability distribution of (a) realization 7 and (b) realization 11. Using a cutoff value of 50 md, block permeabilities above the cutoff were set to 125 md and permeabilities below the cutoff were set to 1.23 md.

Porosity-permeability relationships established on the basis of core-plug analyses for grainstones in parasequence 1 were used to calculate porosity distributions from the stochastic permeability realizations (fig. 18). The following empirical porosity-permeability relation is based on a linear transform representing intergranular pore characteristics (Lucia, this volume):

$$k = (5.01\times10^{-8})\,\phi^{8.33}, \qquad (1)$$

where k is intrinsic permeability (md) and ϕ is porosity (fraction). Similarly, an empirical relationship between water saturation, porosity, and capillary pressure, established for intergranular grainstones (Lucia, this volume), was used to calculate capillary pressure as a function of water saturation for average porosity of the grainstone facies in parasequence 1:

$$S_w = 68.581\ h^{-0.316}\,\phi^{-1.745}, \qquad (2)$$

where h represents capillary pressure as the height of the reservoir above the water-oil contact. Initial water saturation was assumed to be uniform at 25 percent and residual water saturation was set at 19 percent. The computed capillary pressure function is based on a weighted average porosity of 13.4 percent of the three different facies in parasequence 1 (excluding the flooded-shelf facies); it reflects only the change in capillary pressure with saturation during water flooding and not the variation in capillary pressure with varying porosity.

The relative-permeability functions for oil and water were determined from the following equation (Honarpour and others, 1982):

$$k_{rw} = k^{o}_{rw}\left(\frac{S_w - S_{wr}}{1 - S_{or} - S_{wr}}\right)^{N_w}, \text{ and} \qquad (3a)$$

$$k_{ro} = k^{o}_{ro}\left(\frac{1 - S_w - S_{wr}}{1 - S_{or} - S_{wr}}\right)^{N_w}, \qquad (3b)$$

where the residual water saturation S_{wr} is assumed to be 0.10, and the residual oil saturation S_{or} is 0.25. The exponents N_w and N_o were derived from fitting relative-permeability data obtained from grainstone fabric of two Dune field cores. Both exponents were approximately 3 and were determined from the slope of the regression line representing the log of relative-permeability versus the log of the normalized saturations in equations (3a) and (3b). Similarly, the relative-permeability endpoints k^o_{rw} and k^o_{ro} were derived from the intercepts of the log-log plots of the measured relative-permeability data versus saturation, which were 0.266 and 0.484, respectively.

Five numerical simulation runs were performed assuming uniform initial water saturation of 0.10 and residual oil saturation of 0.25, as well as the relative permeability curves according to equations (3a) and (3b). The simulations include: (a) simulation 1 incorporated the conditional permeability realization 7 (fig. 18a); (b) simulation 2 incorporated the conditional permeability realization 11 (fig. 18b); (c) simulation 3 represented permeability realization 7 and incorporated a capillary pressure relation; (d) simulation 4 represented the binary permeability distribution of realization 7 (fig. 19a) and incorporated a capillary pressure relation; and (e) simulation 5 incorporated the facies-averaged permeability distribution (fig. 20). In theory, when permeability is spatially uncorrelated, the effective permeability can be represented by the geometric mean of the local permeabilities. Although the variogram analyses shows short-range permeability correlation (fig. 16), the stochastic permeability distributions appear spatially uncorrelated because of a relatively high nugget (fig. 16). To evaluate whether the lack of correlation is sufficient to justify scale-averaging by taking the geometric mean, geometric mean permeabilities for the bar crest (k = 16.8 md), bar flank (k = 9.3 md), and shallow shelf (k = 3.4 md) were assigned to the three facies represented in the facies-averaged flow model (fig. 20).

Computed water saturations for the five simulations after water injection for 730 days are shown in figures 21 through 25. Note that simulations 3 and 4 (figs. 23 and 24), which incorporate capillary pressure relation, show a much smoother saturation distribution than

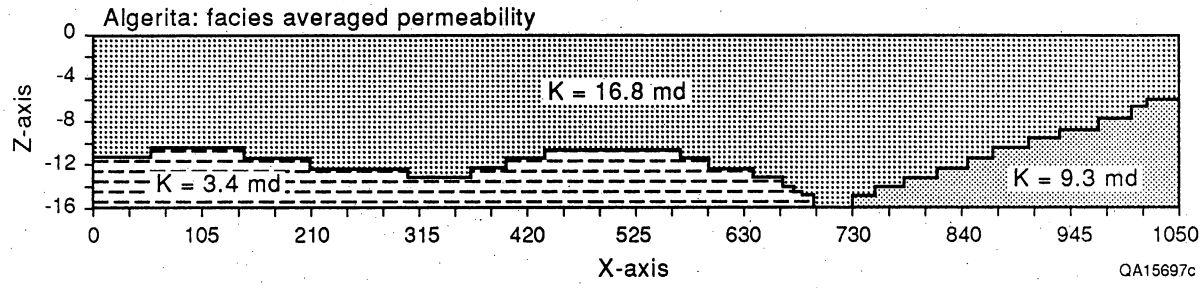

Figure 20. Facies-averaged permeability distribution, represented by geometric mean permeability for the bar-crest, bar-flank, and shallow-shelf facies.

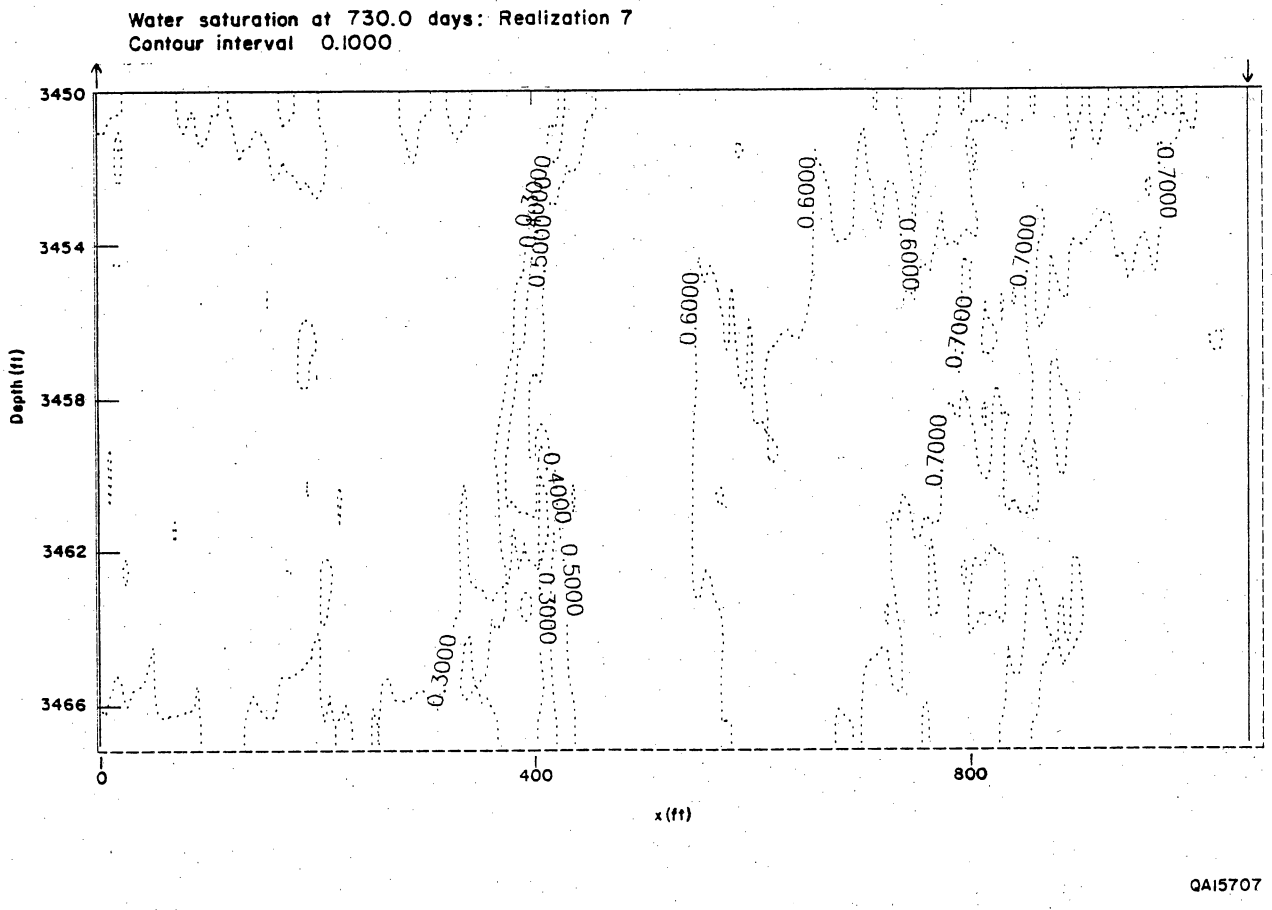

Figure 21. Computed water saturations for simulation 1, incorporating the permeability of realization 7 (without capillary pressure) after injecting water for 730 days.

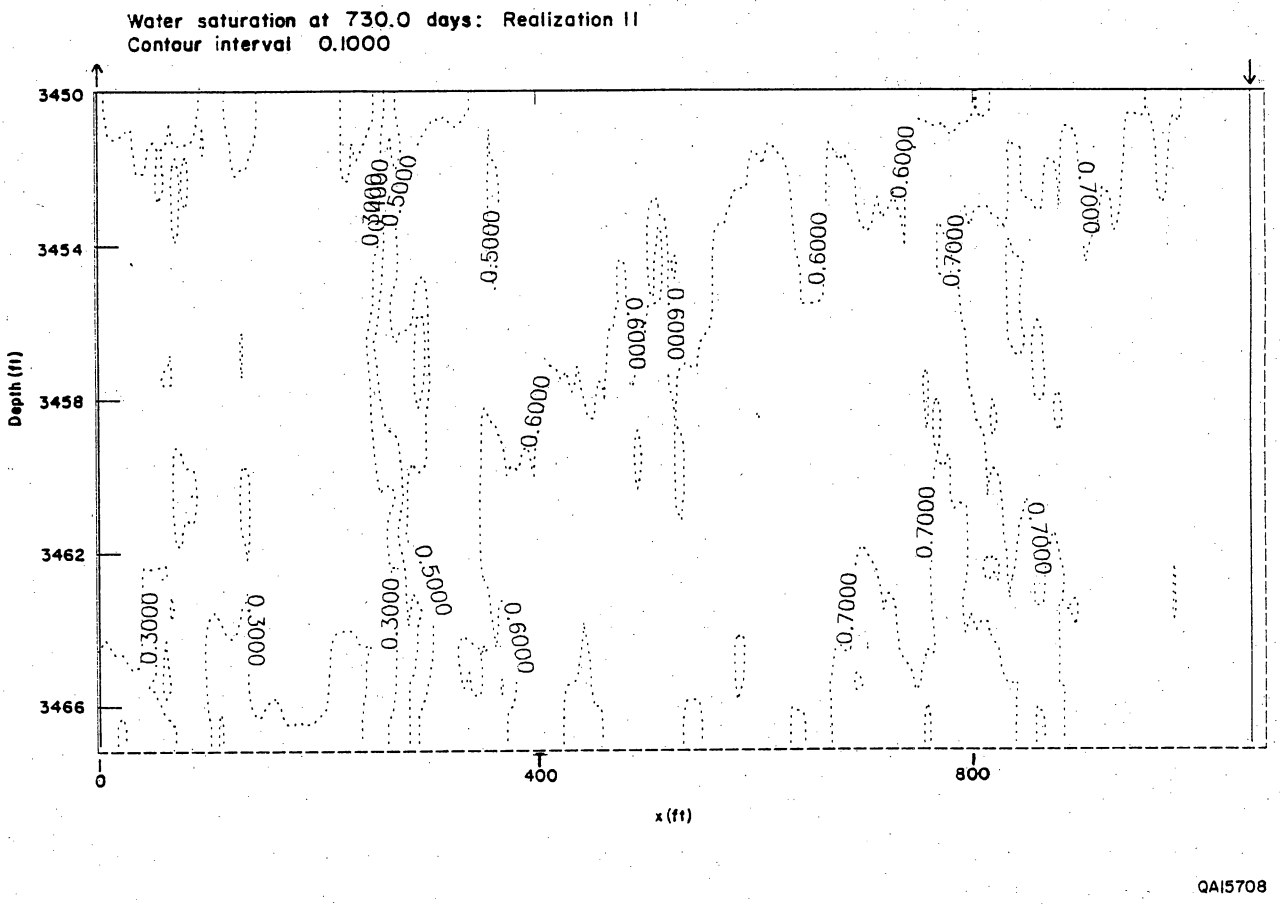

Figure 22. Computed water saturations for simulation 2, incorporating the permeability of realization 11 (without capillary pressure) after injecting water for 730 days.

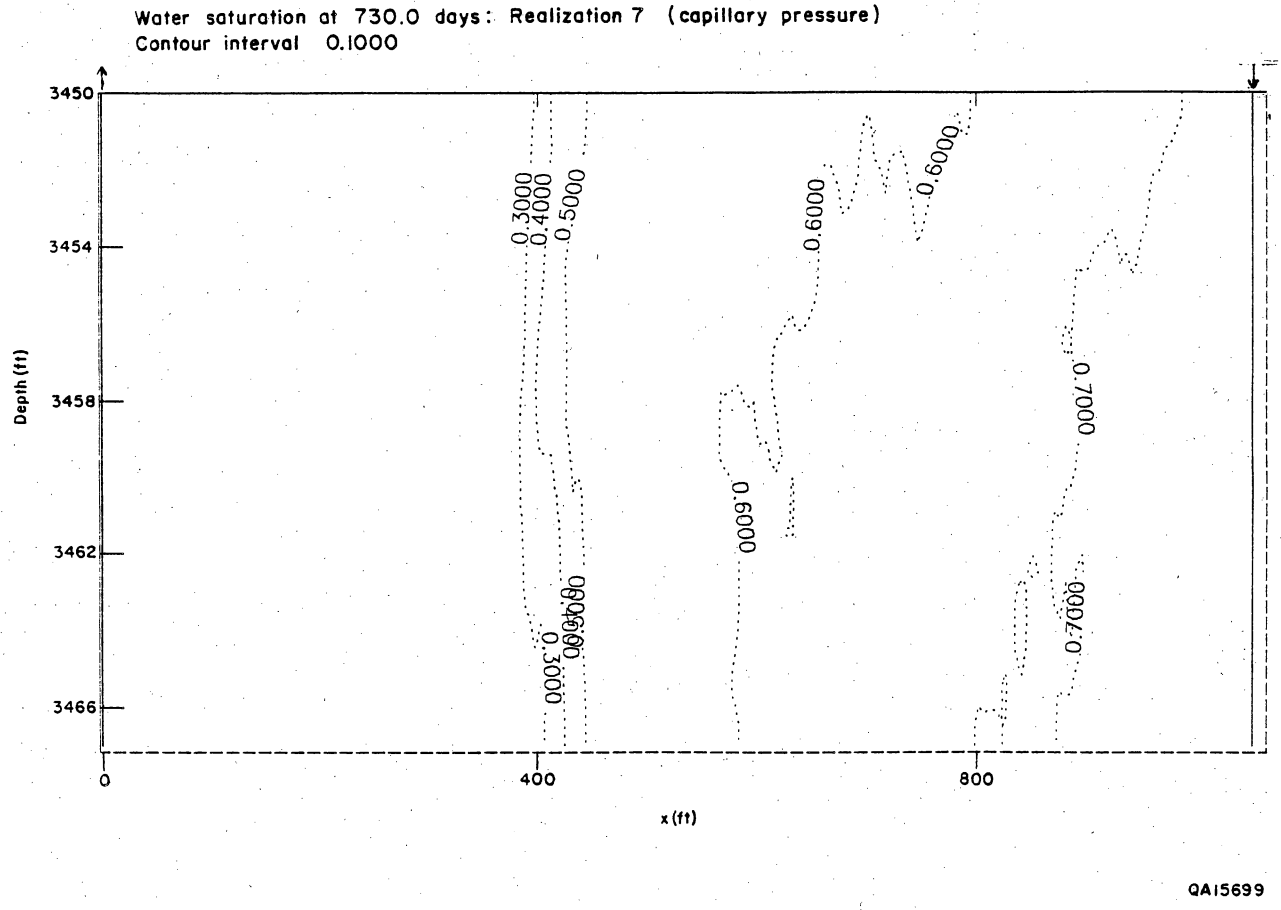

Figure 23. Computed water saturations for simulation 3, incorporating the permeability of realization 7 (with capillary pressure) after injecting water for 730 days.

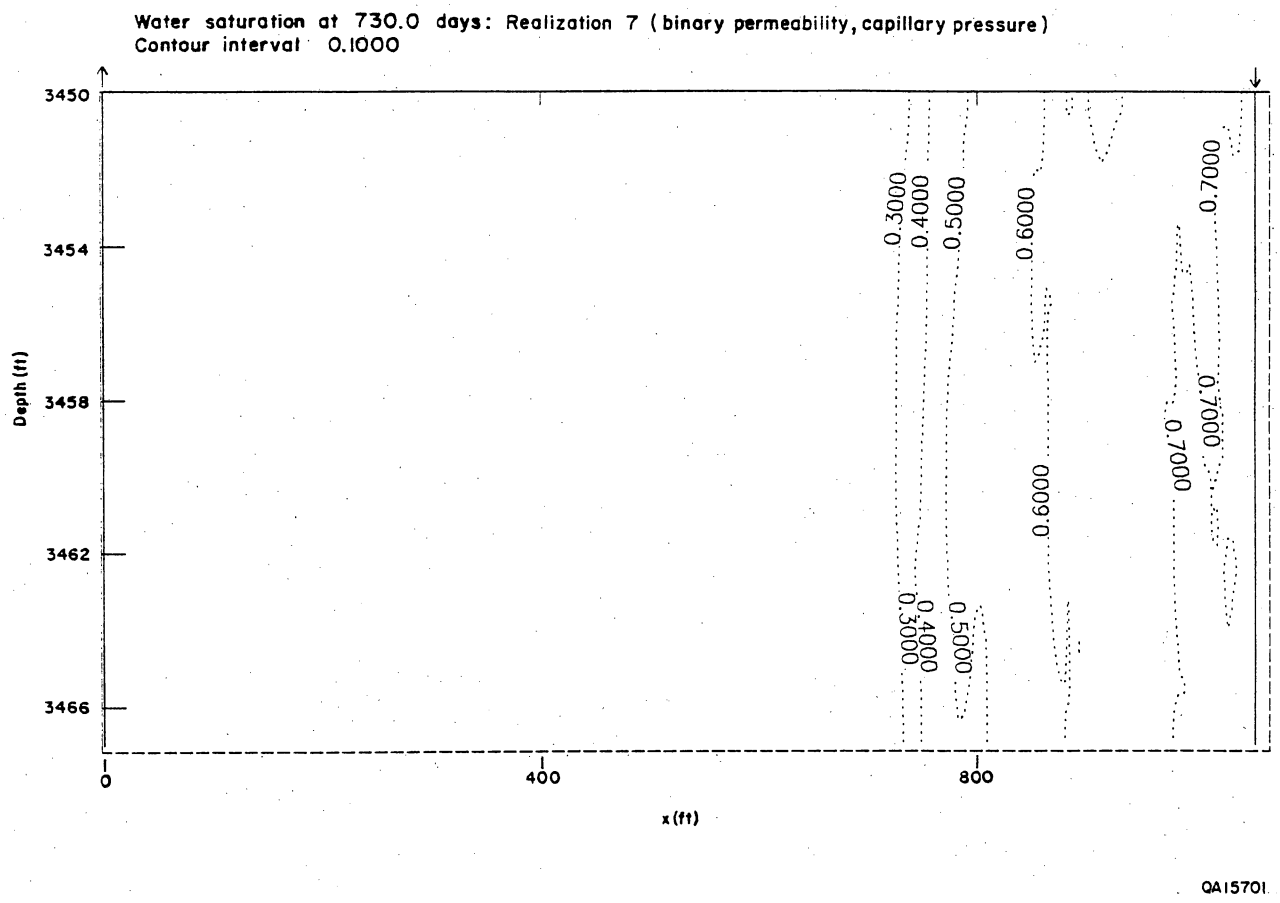

Figure 24. Computed water saturations for simulation 4, incorporating the binary permeability distribution of realization 7 (with capillary pressure) after injecting water for 730 days.

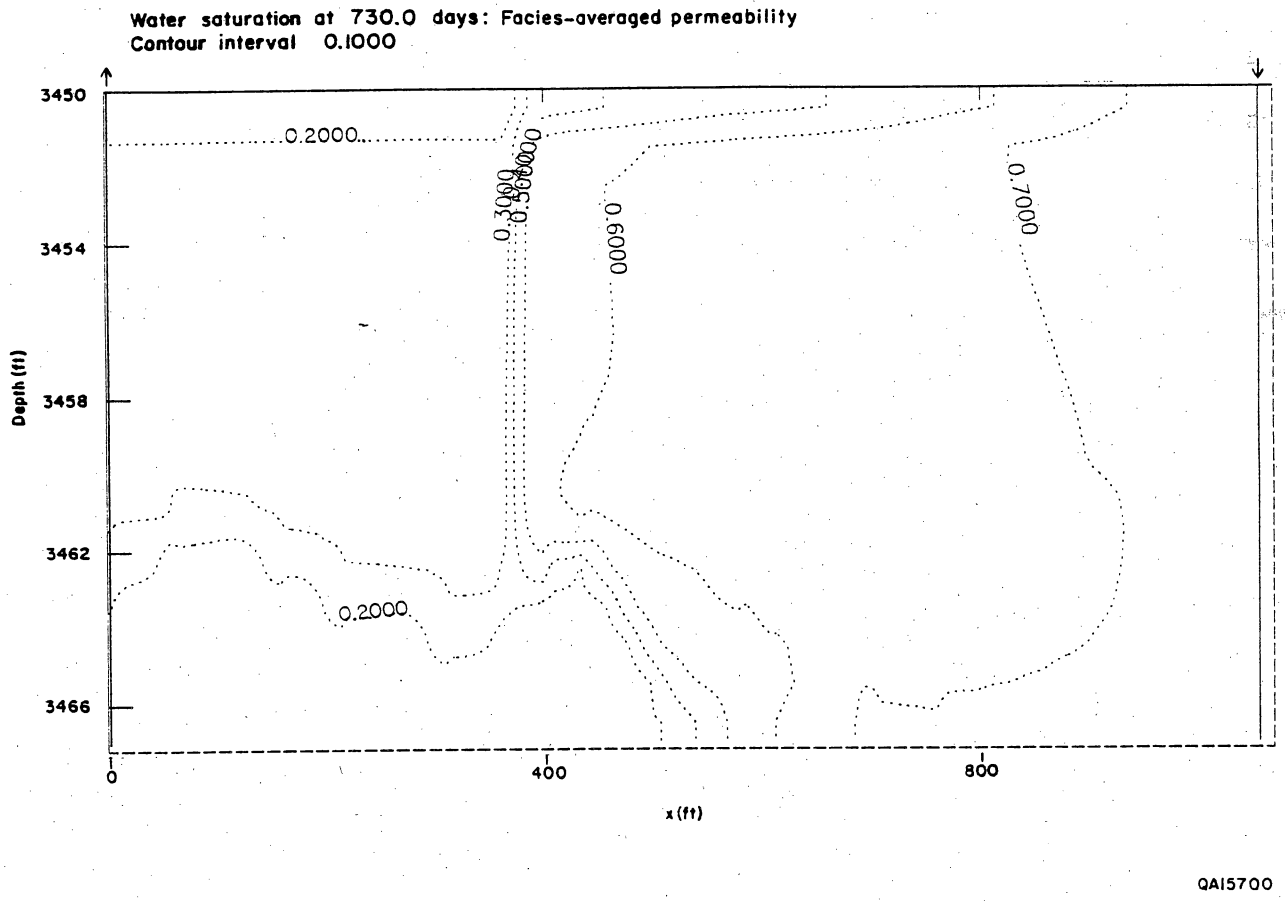

Figure 25. Computed water saturation for simulation 5, incorporating the facies-averaged permeability distribution (without capillary pressure) after injecting water for 730 days.

simulations 1 and 2 (figs. 21 and 22), which do not incorporate capillary pressure. All simulations, however, indicate relatively sharp, vertical displacement fronts.

The production characteristics of the different simulations are shown in figures 25 through 27. The difference in oil production rate between the simulations result mainly from the differences in average permeabilities. Realization 11, having slightly higher average permeability than realization 7, shows the highest initial production rate (fig. 26). Although realization 7 has slightly higher continuity than realization 11, the styles of heterogeneity are essentially identical in the two realizations. Simulation 4, incorporating the binary permeability distribution of realization 7 (fig. 19) indicates a much lower production rate (fig. 23) because of the overall lower average permeability.

Plotting production characteristics against injected pore volumes (figs. 26, 27, and 28) does not indicate noticeable differences between the different simulations. Incorporating a single capillary pressure function, representative of average porosity, has negligible impact on production characteristics, as shown in simulations 1 and 3 (figs. 21 and 23). Note that the effect of capillary pressure variation as a function of varying porosity is not taken into account in these simulations. More importantly, however, results from the facies-averaged simulation coincide with results from the stochastic permeability realizations. This indicates that the short-range permeability correlation does not significantly affect reservoir behavior. Thus, for practical purposes, the observed heterogeneity within individual facies can be represented with geometric mean permeability. The finite-element reservoir model for the entire parasequence window study area (Kasap, this volume), incorporating the geometry of individual facies (fig. 1), uses geometric average permeabilities for the different facies.

SUMMARY

To characterize the complex heterogeneity associated with depositional and diagenetic processes on the interwell scale, geologic and petrophysical data were collected from outcrops

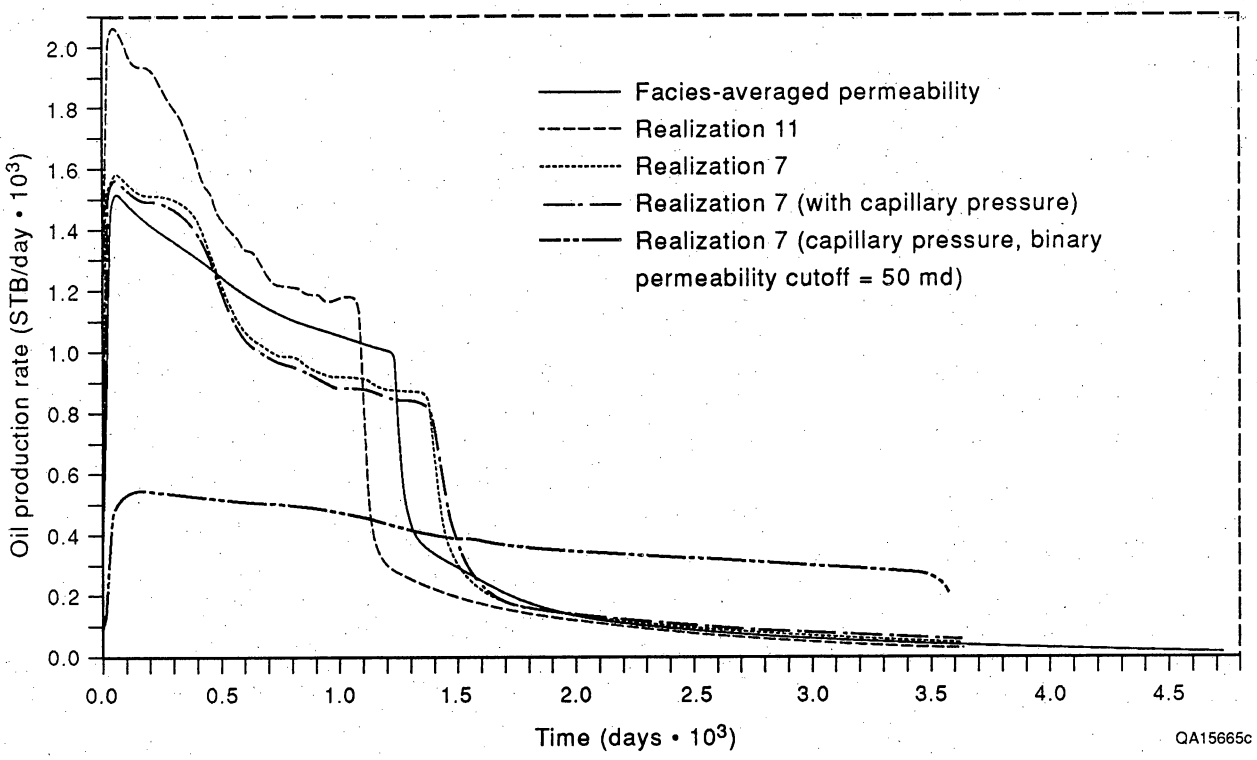

Figure 26. Oil production rate versus time for the different simulations.

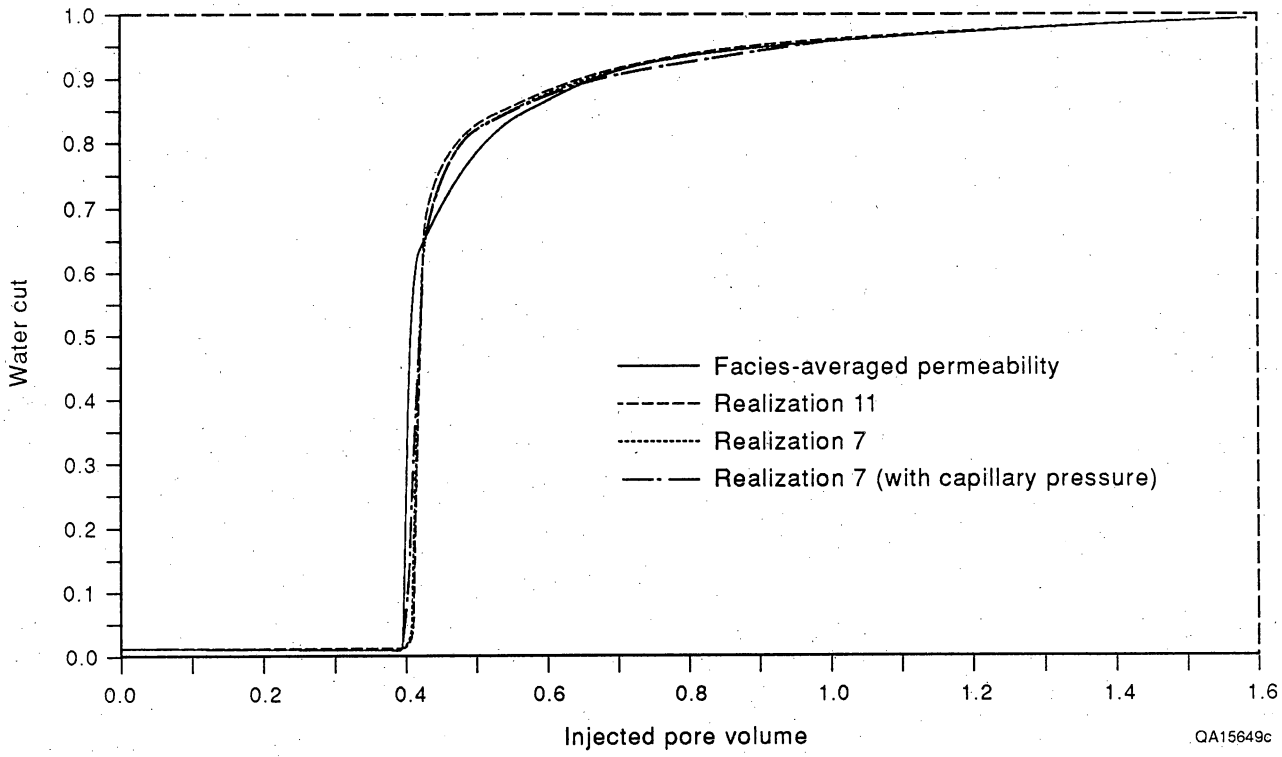

Figure 27. Water-oil ratio versus injected pore volumes for the different simulations.

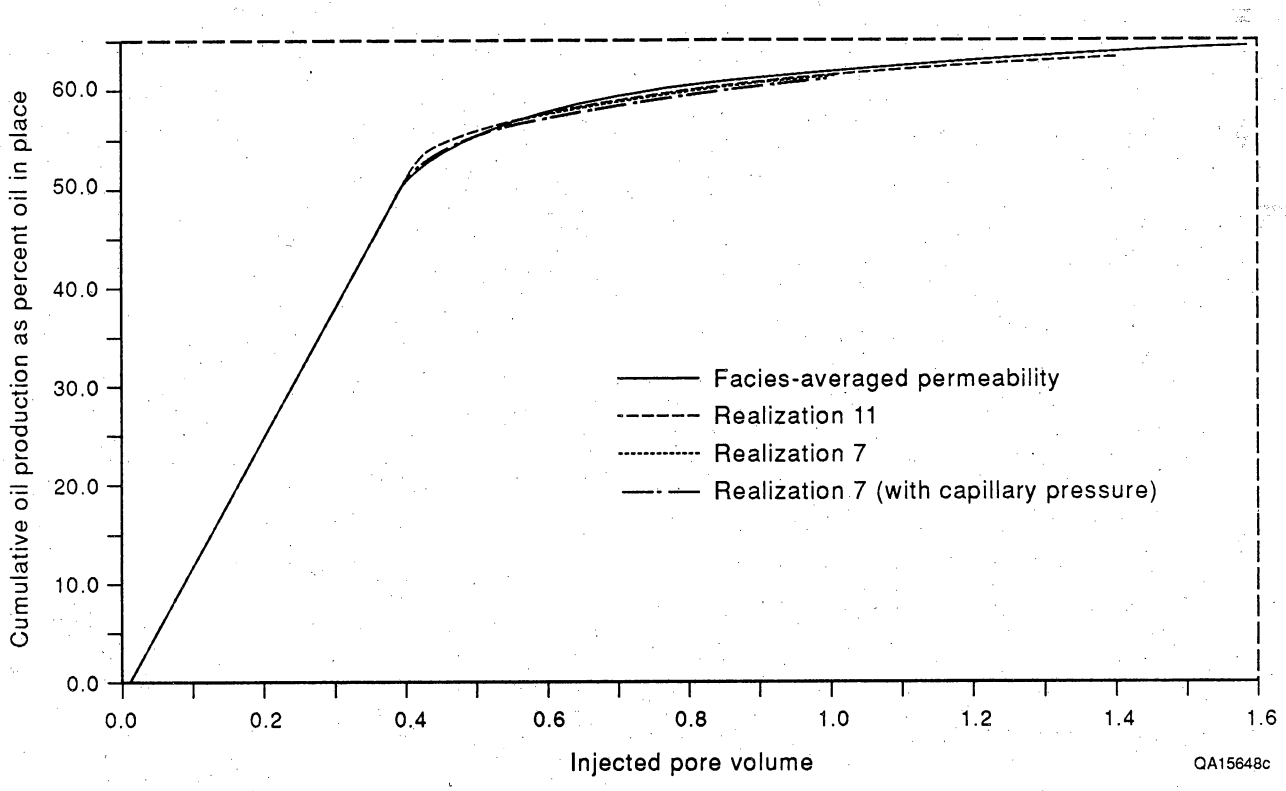

Figure 28. Cumulative oil production as percentage of original oil in place for the different simulations.

of the Algerita Escarpment, New Mexico. Detailed geologic mapping revealed a series of upward-shallowing parasequences (10 to 40 ft thick and several thousand feet long) representing the stratigraphic framework of the reservoir simulation model. Detailed permeability measurements using both mini-air permeameter and core plugs were taken and shown on scales with grids ranging from 1 inch to 1 ft and vertical transects that are spaced horizontally between 5 and 100 ft and sampled every foot. Geostatistical analysis of permeability measurements indicates small-scale permeability correlation and nested structures in the long-range permeability correlation. In both cases, however, approximately half of the permeability variability (variance) is due to locally random heterogeneity (nugget effect). Conditional simulation of permeability within individual facies indicates apparent randomness owing to the large nugget effect. Waterflood simulations indicate that the observed permeability heterogeneity within facies can be represented by a geometric mean. Mean permeabilities of most facies and rock fabrics differ significantly at the 95 percent confidence level and can be used to represent large-scale heterogeneity in reservoir-scale flow simulators.

REFERENCES

ECL Petroleum Technologies, 1990, ECLIPSE reference manual.

Ferris, M. A., in preparation, Permeability distribution on the upper San Andres Formation outcrop, Guadalupe Mountains, New Mexico: The University of Texas at Austin, Master's thesis.

Fogg, G. E., 1989, Stochastic analysis of aquifer interconnectedness: Wilcox Group, Trawick area, East Texas: The University of Texas at Austin, Bureau of Economic Geology Report of Investigations No. 189, 68 p.

Fogg, G. E., and Lucia, F. J., 1990, Reservoir modeling of restricted platform carbonates: geologic/geostatistical characterization of interwell-scale reservoir heterogeneity, Dune field, Crane County, Texas: The University of Texas at Austin, Bureau of Economic Geology Report of Investigations No. 190, 66 p.

Goggin, D. J., Thrasher, R. L., and Lake, L. W., 1988, A theoretical and experimental analysis of minipermeameter response including gas slippage and high velocity flow effects: In Situ, v. 12, no. 1/2, p. 79–116.

Honarpour, Mehdi, Koederitz, Leonard, and Harvey, A. H., 1982, Relative permeability of petroleum reservoirs: CRC Press, Inc., Boca Raton, Florida, 143 p.

Journel, A. G., and Huijbregts, Ch. J., 1978, Mining geostatistics: New York, Academic Press, 600 p.

Kittridge, M. G., 1988, Analysis of areal permeability variations—San Andres Formation (Guadalupian): Algerita Escarpment, Otero County, New Mexico: The University of Texas at Austin, Master's thesis, 360 p.

Kittridge, M. G., Lake, L. W., Lucia, F. J., and Fogg, G. E., 1990, Outcrop/subsurface comparisons of heterogeneity in the San Andres Formation: Society of Petroleum Engineers Formation Evaluation, September, p. 233–240.

Knudsen, H. P., and Kim, Y. C., 1978, A short course on geostatistical ore reserve estimation: University of Arizona, Department of Mining and Geological Engineering, 224 p.

Radian Corporation, 1989, CPS-1 user's guide.

Warren, J. E., and Price, H. S., 1961, Flow in heterogeneous porous media: Society of Petroleum Engineers Journal, September, p. 153–169.

FINITE ELEMENT SIMULATION OF WATERFLOODING IN A SAN ANDRES OUTCROP

by Ekrem Kasap

INTRODUCTION

Flow simulations are the final phase of a reservoir characterization study aimed at maximizing the recovery of oil in heterogeneous reservoirs. The objectives of our flow simulations were (1) to quantify the effects of realistic reservoir heterogeneity on recovery efficiency (generate recovery curves), (2) to investigate the trapping of mobile oil on the basis of improved descriptions of flow field, and (3) to develop pseudovertical sweep efficiency functions (Kasap, 1990) to overcome computational limitations in large-scale simulations, while still taking into account the effects of heterogeneity.

Heterogeneity is the one factor that controls almost everything about sweep efficiency. For example, based on current production practices, the amount of remaining recoverable oil trapped in the highly heterogeneous San Andres and Grayburg reservoirs may be as much as 13 billion barrels, an indication of poor recovery efficiency.

One approach to examining the effects of heterogeneity on the sweep characteristics of a reservoir is to study outcrop analogs. Two advantages of an outcrop study are (1) the heterogeneity of the flow field is exposed in two or sometimes three dimensions; therefore, mapping of facies boundaries can be deterministic, and (2) a large number of petrophysical data can be collected for a reasonable cost (using core plugs and Mechanical Field Permeameter [MFP] measurements).

This study was an analysis of the San Andres reservoirs of the Permian Basin, West Texas, and focused on quantifying the effects of facies architecture on recovery efficiency and fluid flow characteristics (such as crossflow and trapping). An outcrop of

the upper San Andres Formation in the Algerita Escarpment, Guadalupe Mountains, is the analogous formation. This outcrop was characterized and mapped in detail and extensive petrophysical measurements were made. These studies are described in the sections in this volume by Kerans, Lucia, and Senger and were the basis for our fluid flow simulations.

Waterflooding simulation runs were carried out using a two-dimensional finite element simulator. The finite element method makes it possible to generate a grid scheme that will fit facies boundaries so that the reservoir heterogeneity does not have to be averaged. Although we included gravitational forces in the formulations, we assumed that both displacing and displaced fluids, as well as the rock, are incompressible and that capillary forces are negligible.

Petrophysical Variables

Petrophysical variables are the secondary dependent variables that appear in differential equations describing fluid flow through permeable media. For a simulation of two-phase flow of incompressible fluids, porosity, absolute permeability, relative permeability, initial saturations, and densities are needed as known functions of rock or fluid types. The data for these petrophysical variables were obtained using methods discussed by Lucia and Senger in this volume.

Permeability, Porosity, and Initial and Residual Saturations

The permeability distribution in the outcrop shows a randomness and simulation runs show that using the geometric average permeability for a rock-fabric type gives satisfactory results. Therefore, an average permeability (geometric) and an average porosity (arithmetic) were calculated from the measurements on core plug samples for

each rock-fabric type. Initial saturations, on the other hand, were obtained from initial-saturation/porosity/reservoir-height relationships (Lucia, this volume). These initial saturations are mainly controlled by pore-throat sizes and capillary pressures and can be related to permeabilities. The rock properties used in the flow simulations are given in table 1. Properties of the displacing and displaced fluids (water and oil here) are in table 2.

Relative Permeability Curves

Although some relative permeability data are available for the subsurface San Andres Formation, those data are not correlated with rock fabrics. Therefore, in the flow simulations we used exponential functions to calculate relative permeabilities as a function of normalized saturations and exponent parameters (Lake, 1989). Normalized saturation S_j^n is defined as

$$S_j^n = \frac{S_j - S_{jr}}{1 - S_{wr} - S_{or}} ,$$

where j refers to water or oil.

The relative permeability functions are given as

$$k_{rw} = k_{rw}^o \, (S_w^n)^{ew} \qquad (1a)$$

for water and

$$k_{ro} = k_{ro}^o \, (S_o^n)^{eo} \qquad (1b)$$

for oil. In (1a) and (1b), k_{ro}^o and k_{rw}^o are end-point relative permeabilities for oil and water, respectively. End-point relative permeability is defined as the relative permeability of a phase during which the saturations of all other phases are at residual saturations. The initial water saturation was assigned as a function of rock fabric (see

Table 1. Rock-fabric flow units, location, simulator codes, porosity, permeability, initial and residual water saturation, and residual oil saturations

Flow Units	Rock fabric	Input file codes	Parasequence locations	Porosity (arithmetic) (average)	Permeability (geometric) (average) (md)	S_{wr} and S_{wi}	$1-S_{or}$
1	Mudstone—fenestral	1	1,2,3,4 5,6,7,8,9	0.04	0.01	0.9	1.0
2	Wackestone	2,27, 29,7	3,4,5,6 also 7,8	0.105	0.3	0.5	0.6
3	Grainstone—moldic	68	8	0.145	0.7	0.12	0.6
4	Grain-dominated packstone	35,8,6	3,4,5,6 also 1,2	0.129	1.8	0.3	0.65
5	Grainstone—moldic	87,93 96,97	7 North	0.159	2.2	0.1	0.6
6	Grainstone—highly moldic	37,47, 67,77	7 South	0.23	2.5	0.1	0.6
7	Grain-dominated packstone	61	1,2	0.085	4.5	0.26	0.65
8	Grain-dominated packstone	69	9	0.118	5.3	0.16	0.65
9	Grainstone—bar flank	5	1,2	0.095	9.5	0.23	0.65
10	Grainstone—bar crest	3	1,2,3	0.11	21.3	0.19	0.75
11	Grainstone—large dol xls	39	9	0.135	44.	0.15	0.75

Table 2. Reservoir and flow parameters.

Reservoir	
Length	= 2,700 ft
Average height	= 141.5 ft
Width	= 0.0328 ft
No. of elements	= 4,643
No. of nodes	= 4,639
Av. element size	= 5 × 25 ft
Average porosity	= 0.12
Average permeability	= 5.66 md
Average S_{wi}	= 0.256
Pore volumes	= 1,487.534714 ft^3 (assuming width)
Av. residual oil sat.	= 0.3391
Long. dispersivity	= 13 ft
Flow	
Injection rate	= 0.104143 ft^3/day
Water density	= 62.4 lb/ft^3
Oil density	= 56.16 lb/ft^3
Water viscosity	= 0.3 cp
Oil viscosity	= 1.5 cp
k_{ro} at S_{rw}	= 0.9
k_{rw} at S_{ro}	= 0.3
Dimensionless groups	
Gravity number	= 0.01875
End-point mobility ratio	= 1.6667
Aspect ratio	= 19.8

table 1 and Lucia, this volume). Residual oil saturation was estimated on the basis of preliminary data suggesting a relationship between rock fabric and residual oil. In (1a) and (1b), ew and eo are the exponent parameters defining the shape of the relative permeability curves for the water and oil phases, respectively; ew = 1 and eo = 2 were used in our numerical simulation runs. Figure 1 shows an example of relative-permeability curves generated by using equations (1a) and (1b) for the bar-crest grainstones in parasequences 1, 2, and 3.

Dispersion

Because waterflooding is an immiscible displacement process, no molecular diffusion occurs between the two phases. A form of dispersionlike behavior is, however, caused by the capillary-pressure function. Since capillary pressure is not included in this analysis, the numerical simulations are entirely free from any physically derived dispersive effects.

As is true of many high-order numerical schemes, the absence of dispersion leads to clearly nonphysical results. If we had been using finite element simulation, for example, the absence of dispersion could have led to oscillations and instabilities in calculated saturations. To eliminate this possibility, we added a small amount of artificial dispersion to the simulator input. The amount of dispersion added was not so great as to affect any of the results, but it was large enough to eliminate numerical problems. If we had been simulating a miscible displacement, the dispersion could have been estimated from the procedure of Arya and others (1988) or from pseudocapillary pressure curves as discussed in Lake (1989). Neither option was used here; the dispersion was input simply to eliminate numerical errors.

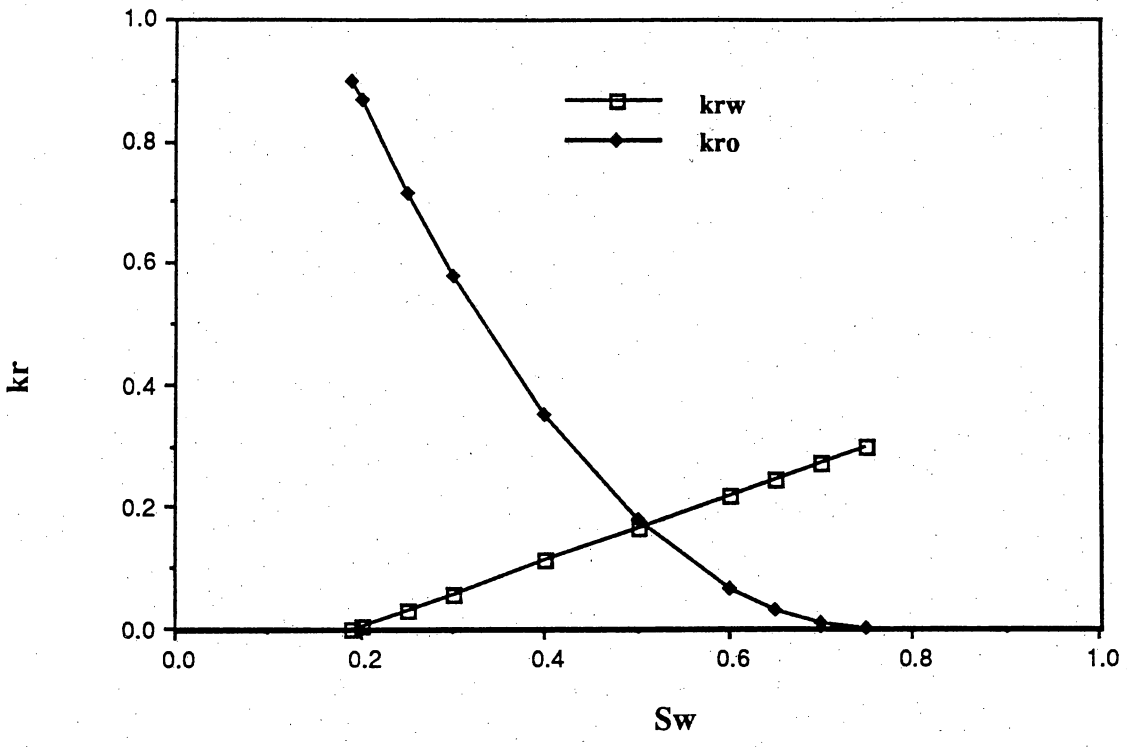

Figure 1. Relative-permeability curves used for bar-crest grain-dominated fabrics in parasequences 1, 2, and 3. The curves are generated from an exponential model. Exponents are 1 and 2 for water and oil curves, respectively.

Boundary Conditions

The flow field was flooded from left to right using vertical wells, which were exposed to the entire section. Except where noted, the wells are vertical lines located at the end of the flooded section. The total injection rate was specified at a value typical of a Permian Basin waterflood, and a constant bottom-hole pressure was specified at the production well. Lateral boundaries were assumed to be impermeable.

Results

Distribution of Injected Fluid (As a Boundary Condition)

Although it is assumed that the total injection rate is unchanged throughout the displacement process, the amount of injected fluid that an individual facies is receiving will be a function of absolute permeability, relative permeability, and the thickness of the facies at the wellbore. Any heterogeneity at the injection well or any density difference between the fluids will cause an uneven distribution of the injected fluid.

The injected fluid is initially allocated to the reservoir at the injection well according to (1) the distribution of permeabilities exposed in the well (the units with the larger permeability/feet taking more fluid) and (2) the pressure differences between wells. The pressure in the well must be corrected for the static gravity head of a fluid column. After the initial injection, the allocation depends on the mobilities of the fluid residing in the injection elements, a quantity that changes with time and injection rate. After sweep-out of the reservoir, the allocation is again made according to the distribution of the permeabilities.

Boundary Conditions

The flow field was flooded from left to right using vertical wells, which were exposed to the entire section. Except where noted, the wells are vertical lines located at the end of the flooded section. The total injection rate was specified at a value typical of a Permian Basin waterflood, and a constant bottom-hole pressure was specified at the production well. Lateral boundaries were assumed to be impermeable.

Results

Distribution of Injected Fluid (As a Boundary Condition)

Although it is assumed that the total injection rate is unchanged throughout the displacement process, the amount of injected fluid that an individual facies is receiving will be a function of absolute permeability, relative permeability, and the thickness of the facies at the wellbore. Any heterogeneity at the injection well or any density difference between the fluids will cause an uneven distribution of the injected fluid.

The injected fluid is initially allocated to the reservoir at the injection well according to (1) the distribution of permeabilities exposed in the well (the units with the larger permeability/feet taking more fluid) and (2) the pressure differences between wells. The pressure in the well must be corrected for the static gravity head of a fluid column. After the initial injection, the allocation depends on the mobilities of the fluid residing in the injection elements, a quantity that changes with time and injection rate. After sweep-out of the reservoir, the allocation is again made according to the distribution of the permeabilities.

Figure 2 shows the injected fluid distribution as a percentage of the total injection rate at the well for the cross section of San Andres outcrop. The figure indicates that the largest part of the fluid is injected into parasequences 1 and 2, while negligible amounts of fluid are injected into parasequences 3, 4, and 8.

Sweep Efficiency

San Andres reservoirs are typically very heterogeneous, displaying permeabilities that vary by several orders of magnitude. A pilot simulation study was designed that focused on parasequence 1 in order to investigate the effects of small-scale heterogeneity. About 1,000 permeability measurements were taken using the mechanical field permeameter (MFP). These data were supported by porosity and permeability measurements on core plugs from the outcrop.

A map of permeability in parasequence 1 shows great variation in permeability values in the upper part of the parasequence referred to as the grainstone facies (fig. 3a). In the lower part, a mud-dominated facies, the variation is not detectable because the permeability values are less than 0.1 md, which is below the measuring capability of the MFP.

We used the finite element simulator to investigate the effects of these highly varied permeability values on sweep efficiency in this parasequence. (See Kasap [1990] for details on the simulator.) In these investigations the injection well was put on the left side, the right side, or in the center of the flow field. The single-phase mobility of the displacing fluid was identical to that of the displaced fluid, and the gravitational force was disregarded. This was done to isolate the effects of permeability heterogeneity on flow paths.

Figure 3b shows that regardless of the displacement direction, only the upper part of the parasequence (grain-dominated fabric) was swept, whereas the lower part (mud-

Figure 2 shows the injected fluid distribution as a percentage of the total injection rate at the well for the cross section of San Andres outcrop. The figure indicates that the largest part of the fluid is injected into parasequences 1 and 2, while negligible amounts of fluid are injected into parasequences 3, 4, and 8.

Sweep Efficiency

San Andres reservoirs are typically very heterogeneous, displaying permeabilities that vary by several orders of magnitude. A pilot simulation study was designed that focused on parasequence 1 in order to investigate the effects of small-scale heterogeneity. About 1,000 permeability measurements were taken using the mechanical field permeameter (MFP). These data were supported by porosity and permeability measurements on core plugs from the outcrop.

A map of permeability in parasequence 1 shows great variation in permeability values in the upper part of the parasequence referred to as the grainstone facies (fig. 3a). In the lower part, a mud-dominated facies, the variation is not detectable because the permeability values are less than 0.1 md, which is below the measuring capability of the MFP.

We used the finite element simulator to investigate the effects of these highly varied permeability values on sweep efficiency in this parasequence. (See Kasap [1990] for details on the simulator.) In these investigations the injection well was put on the left side, the right side, or in the center of the flow field. The single-phase mobility of the displacing fluid was identical to that of the displaced fluid, and the gravitational force was disregarded. This was done to isolate the effects of permeability heterogeneity on flow paths.

Figure 3b shows that regardless of the displacement direction, only the upper part of the parasequence (grain-dominated fabric) was swept, whereas the lower part (mud-

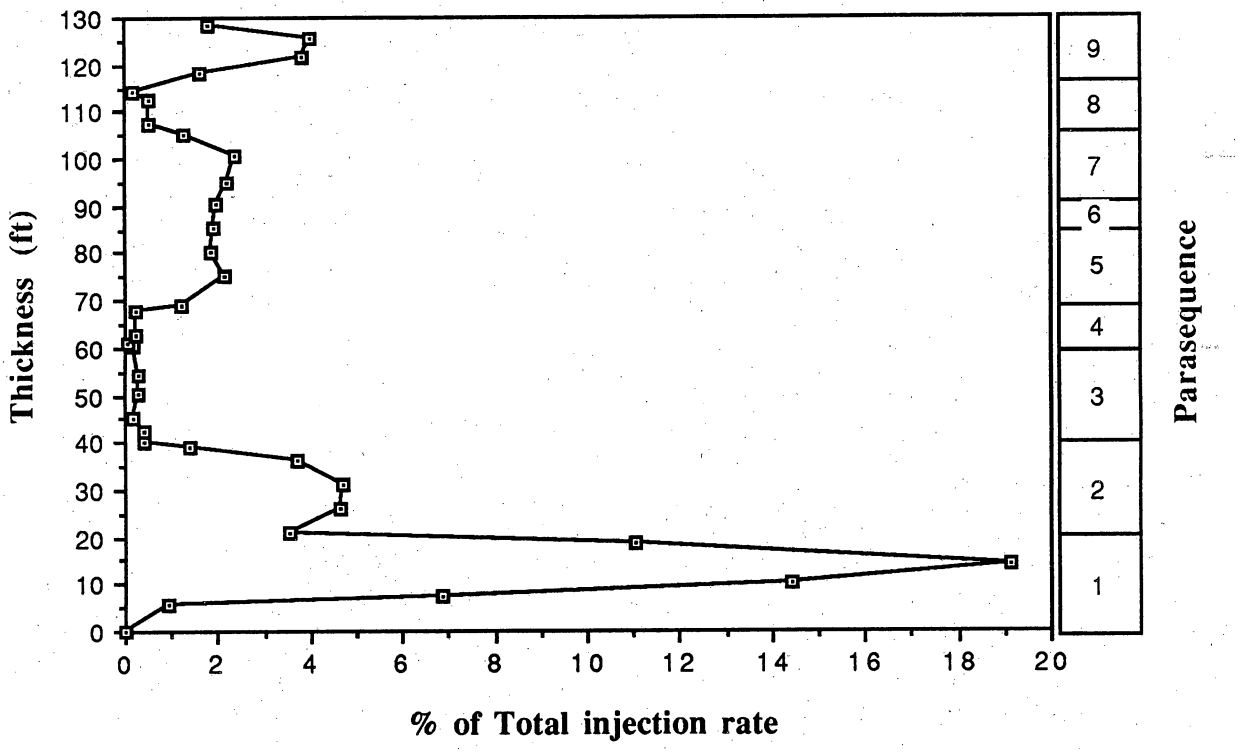

Figure 2. Injectivity profile compared with parasequence stratigraphy. The rates are given as a percent of the total flow rate.

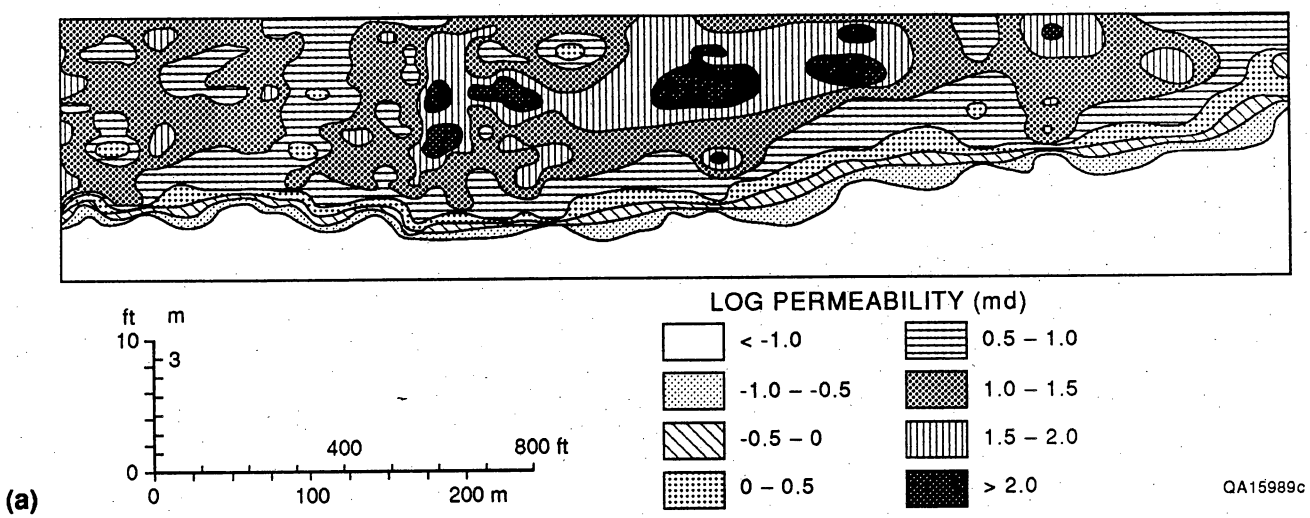

(a)

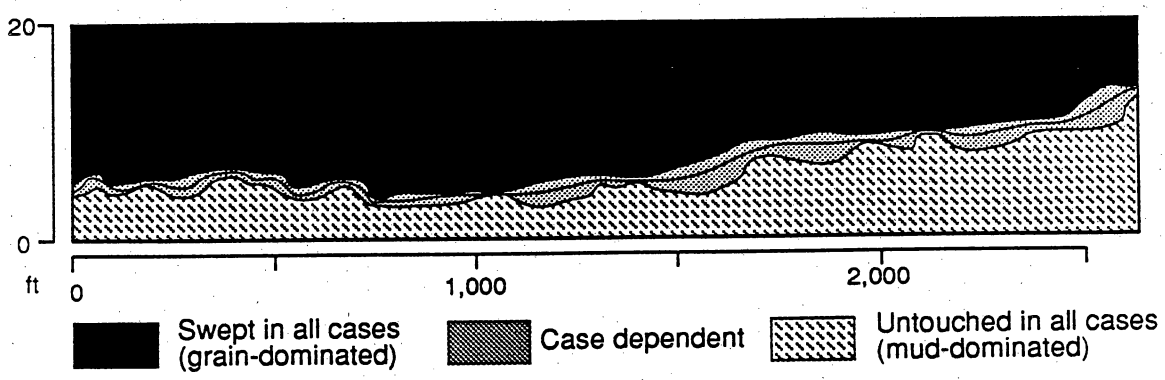

(b)

Figure 3. Relationship between facies boundaries and swept regions in parasequence 1. (a) Permeability map. (b) Swept, grain-dominated facies (shaded area) and untouched, mud-dominated facies (unshaded area) from finite element simulations.

dominated fabric) remained untouched. From these results we conclude that, whereas heterogeneity affects sweep efficiency greatly, the direction of the sweep is unimportant as long as the rock fabric remains constant.

Two-Dimensional Waterflooding Simulation in the Upper San Andres

A numerical simulation of the waterflooding process in the whole outcrop cross section was run by using the finite element simulator. A detailed sequence-stratigraphic framework defining the geologic setting was available from previous work (Kerans, this report). On the basis of the results of the pilot simulation runs in parasequence 1, average porosity, permeability, and initial and residual saturations were used for each rock-fabric type described from the outcrop (table 1).

A finite element grid scheme was generated using parasequence boundaries and numerical restrictions. Figure 4 shows 4,643 elements containing 4,639 node points on a flow field measuring 2,700 ft in length and a maximum of about 160 ft in thickness. Figure 5 shows the contours of initial water saturations assigned to each facies as given in table 1. In general, low-permeability rock types contain high initial water saturations. Because parasequences 3, 4, and 8 consist of low-permeability rock types, these parasequences have higher initial water saturations. The simulator was run until the volume of injected water was equal to that of movable oil. Pertinent data used in this simulation run are shown in table 2, and general nomenclature in table 3.

Figures 6 through 8 show the distribution (shaded area) of the increase in water saturation from the initial saturation at three time intervals. Figure 9, on the other hand, shows the final (injected plus initial) water saturations greater than 0.4.

Figure 8 indicates that parasequences 3 through 6 and 8 do not receive much of the injected water, although they have higher initial water saturation. Discontinuous mudstone and fenestral beds basically define the flow paths by preventing crossflow

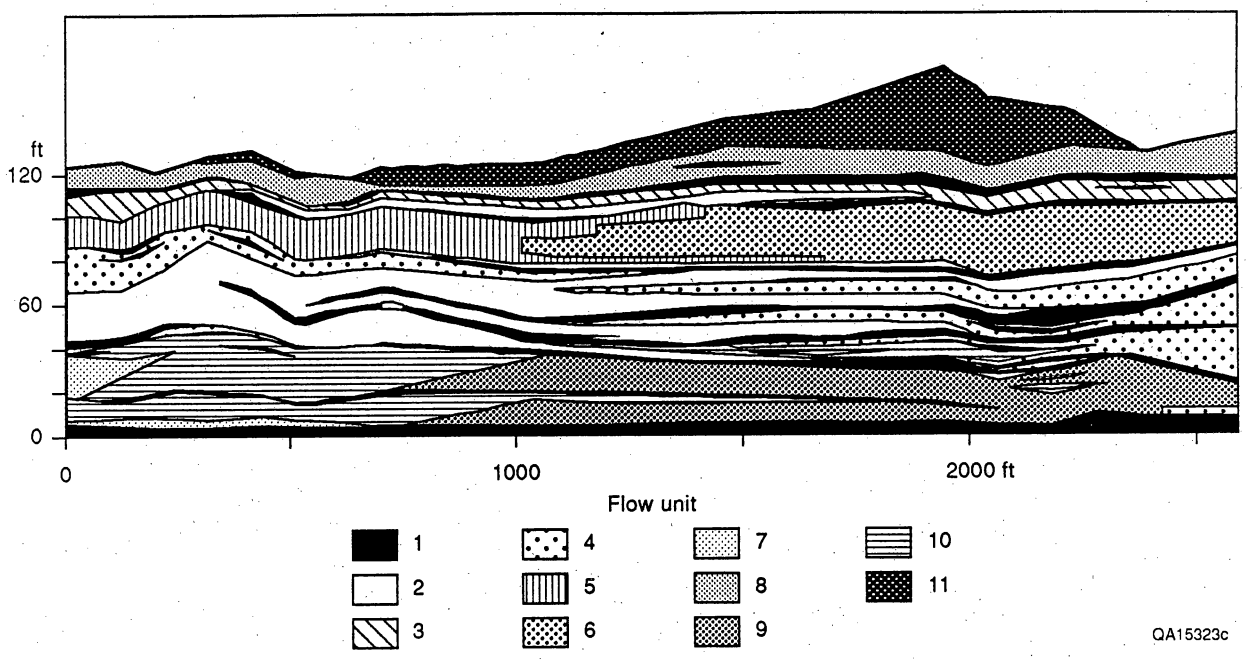

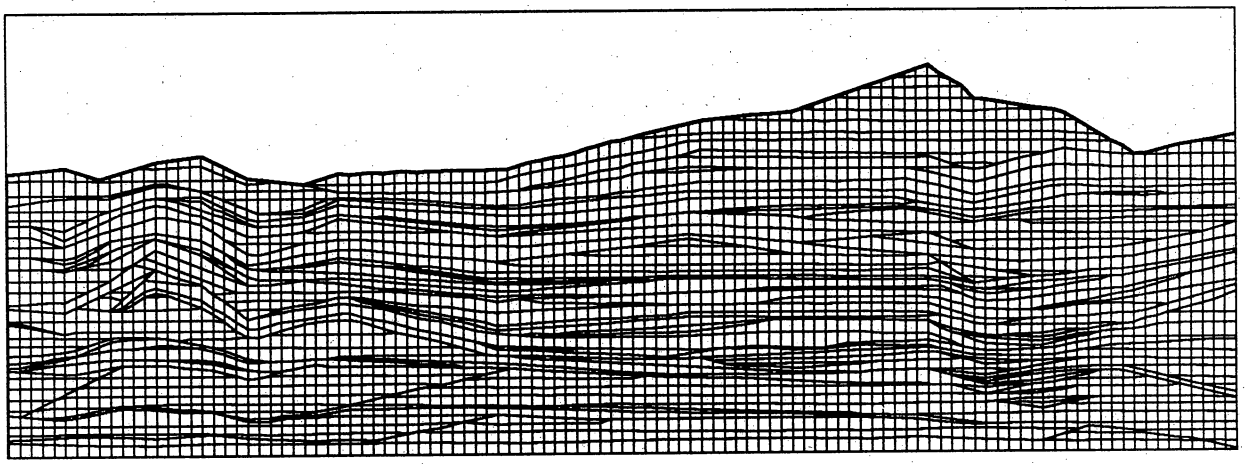

Figure 4. Rock-fabric flow units and finite element grid scheme (4,643 elements and 4,639 node points) generated for flow model of Lawyer Canyon San Andres outcrop.

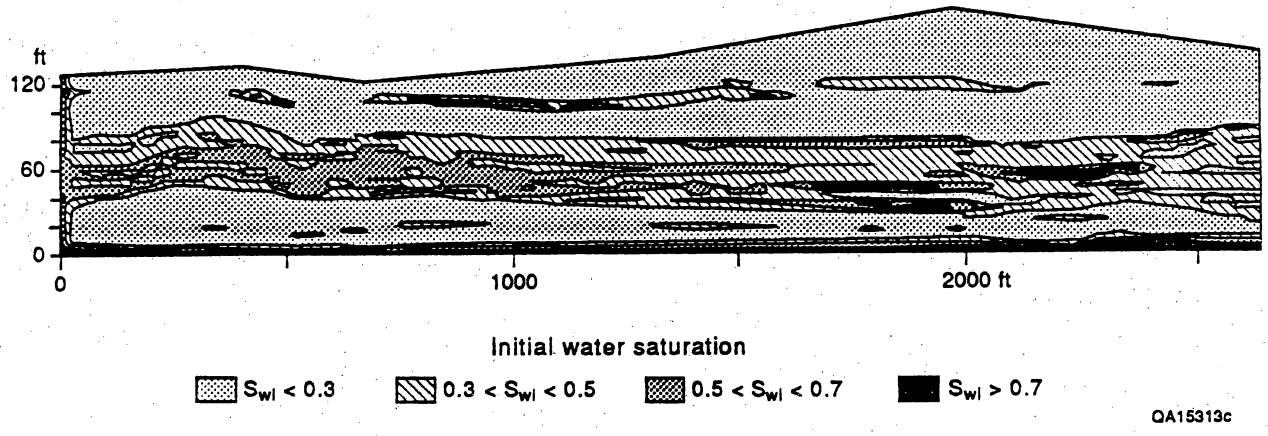

Figure 5. Distribution of initial water saturation.

Table 3. General nomenclature.

L = length, t = time, m = mass, F = force

g	Gravitational constant [=] L / t^2
H	Thickness [=] L
$\overrightarrow{\overrightarrow{k}}$	Permeability tensor [=] L^2
k_r	Relative permeability [=] L^2
L	Length [=] L
M	Mobility ratio
P	Pressure [=] F / L^2
S	Saturation
t	Time [=] t
x,y,z	Simulation coordinate system [=] L
$\vec{u}$	Darcy or superficial velocity [=] L/t
V	Volume [=] L^3

Greek

Δ	Refers to differences
λ_r	Relative mobility [=] $(L^2/F\text{-}t)$
μ	Viscosity [=] $(F/L^2\text{-}t)$
ϕ	Porosity
ρ	Density [=] m/L^3

Subscripts

ri	Relative permeability to phase i
ir	Residual saturation of phase i
T	Total
w	Water
o	Oil

Superscripts

o	End point
~	Effective
$\overrightarrow{\overrightarrow{\ }}$	Tensor
$\rightarrow$	Vector
_	Average

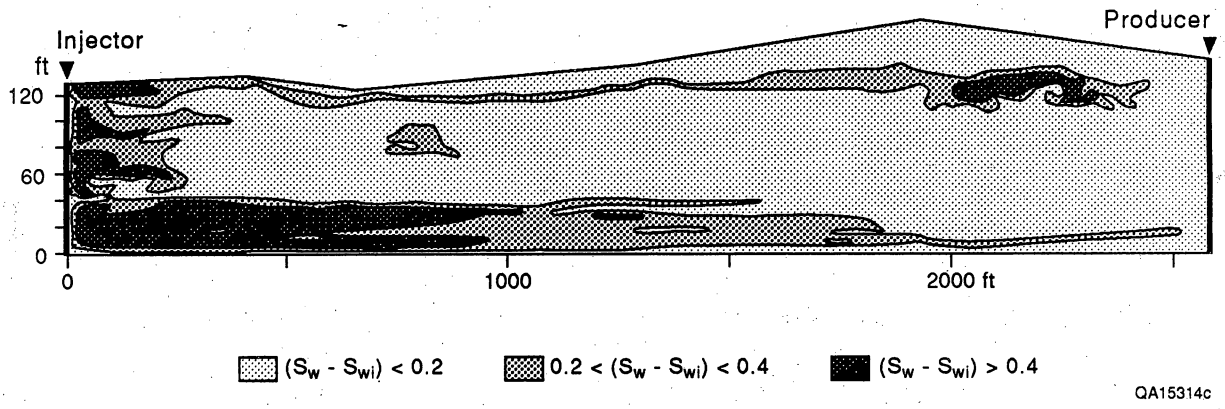

Figure 6. Increase in water saturation at 0.25 mobile fluid volume injected.

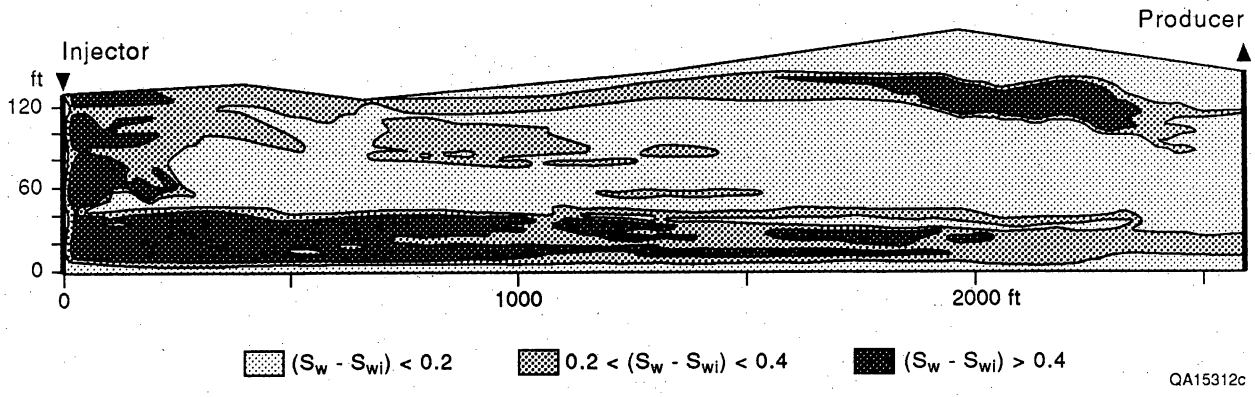

Figure 7. Increase in water saturation at 0.5 mobile fluid volume injected.

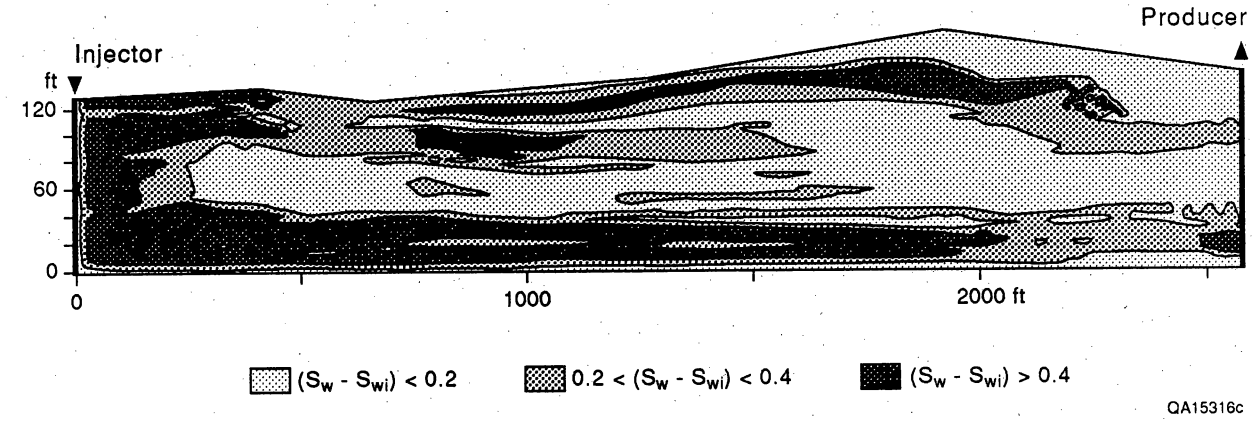

Figure 8. Increase in water saturation at 1.0 mobile fluid volume injected.

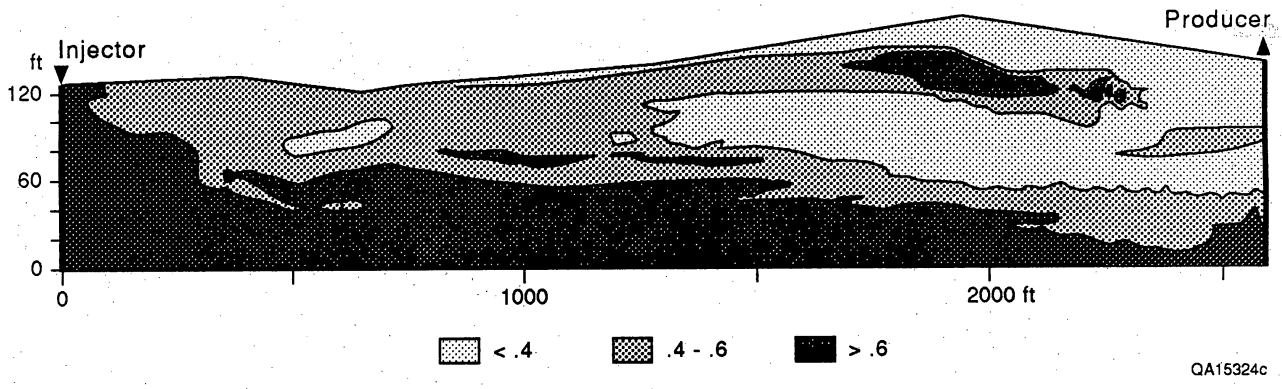

Figure 9. Distribution of water saturation at 1.0 mobile fluid volume injected.

and directing the injected fluid toward the production well. All but the far-right part of the grainstone facies in parasequences 1 and 2 are swept completely, whereas some trapped oil is left in the thickest part of parasequence 9: the only part of the section where there is a gravity effect. This effect is expected because the gravity number (see Discussion of Results) increases linearly with thickness and permeability, and that part of parasequence 9 has the highest permeability and greatest thickness.

Parasequence 7, on the other hand, is swept slowly but steadily. This is probably one reason that the recovery curve shown in figure 10 has not yet leveled off at 1 mobile fluid volume injected. Some crossflow from parasequences 9 through 7 near the thickest part of parasequence 9 can also be seen. The flow of water through the mudstone beds separating parasequence 9 from 7 is unexplained at this time.

Figure 11 shows the effective relative permeabilities generated from the numerical simulation runs. The displacement process has not reached the cutoff point by the time 1 mobile fluid volume has been injected. Figure 12 shows the water-oil ratio at about 2 after 1 mobile volume has been injected. This result indicates that the reservoir will not be abandoned after 1 mobile volume has been injected, and numerical simulation runs need to be extended to determine project life.

Discussion of Results

Gravity and viscous forces compete with one another to dominate this displacement process. Viscous forces are basically a function of injection rate and mobility ratio for given fluid and rock properties, whereas gravity forces are a function of the density difference between displacing and displaced fluids. The gravity number is a good indication of whether the displacement is dominated by gravity or viscous forces.

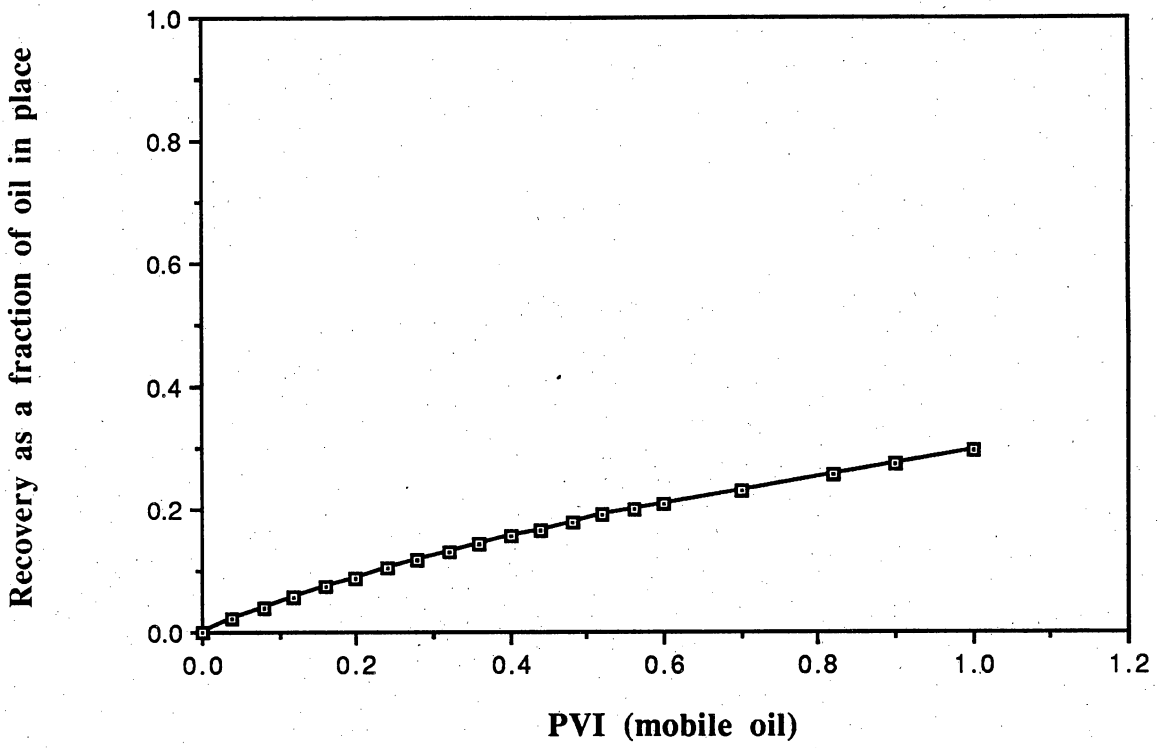

Figure 10. Fractional recovery of oil, from numerical simulation of waterflooding the San Andres outcrop flow model.

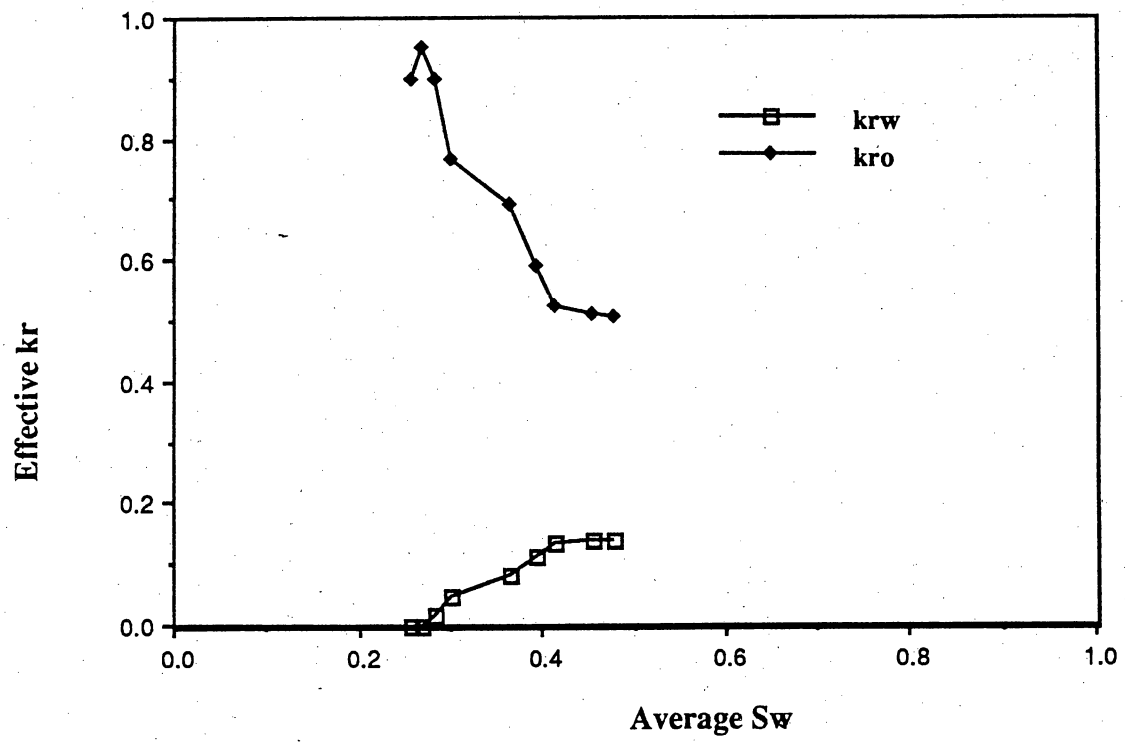

Figure 11. Effective relative permeability curves calculated from the numerical simulation of waterflooding the San Andres outcrop flow model.

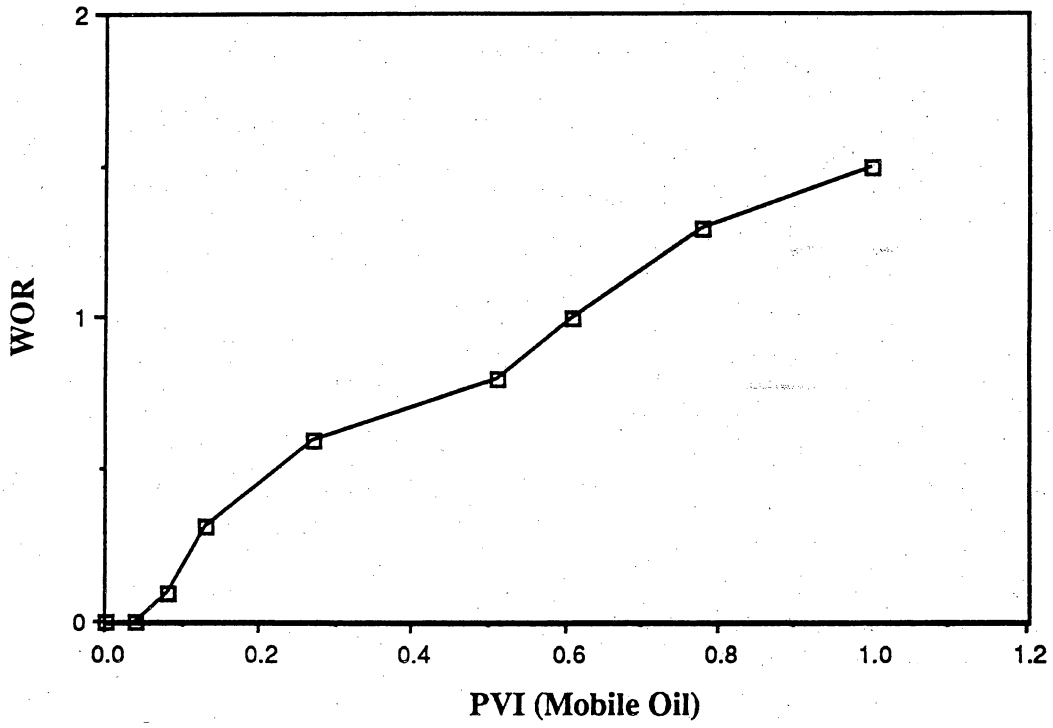

Figure 12. Water/oil ratios (WOR) from the simulated waterflood as a function of dimensionless time.

The gravity number for the horizontal reservoirs given by Shook and Lake (in press) is defined as

$$N_{g2} = \left(\frac{k_h \lambda_{r2}^{o} \Delta\rho\, g}{u_T}\right)\left(\frac{H}{L}\right),$$

where k_h is the permeability in the horizontal direction, λ_{r2}^{o} is the end-point mobility of the resident fluid, u_T is the total superficial velocity, $\frac{H}{L}$ is the aspect ratio, and $\Delta\rho$ is the difference between the fluid densities. For the San Andres outcrop, along with the flow parameters given in table 2, we calculate a gravity number of 0.01875, which, when compared with other calculations (Shook and Lake, in press), indicates that the displacement is dominated strictly by viscous forces. The absence of significant gravity effects is expected in this low-permeability reservoir.

A similar scaling argument, however, indicates that capillary pressure may be important. Capillary pressure varies according to wettability, pore-size distribution and, most important for this study, the inverse square root of the local permeability. Regions containing high permeability in the flow field will contain correspondingly smaller capillary pressures, and vice versa. These differences could either increase sweep efficiency (if lateral transport of fluid is large) or decrease it (if lateral communication is small). On the basis of the pattern of water saturation illustrated in figures 6 through 8, we conclude that the recovery will be increased. However, we cannot estimate the extent of the increase without additional calculations that contain capillary pressure. This will be the subject of future work.

Finally, the calculated recovery may be large because of the two-dimensional nature of the flow. A three-dimensional flow field offers more pathways by which fluids can channel through large permeability regions and accentuates the effects caused by the introduction of fluids though the well point sources. Thus, the absence of three-dimensional flow tends to compensate for the absence of capillary pressure, and vice

versa. However, additional work is needed to assign magnitudes correctly to these effects.

CONCLUSIONS

In this study we simulated a waterflooding process in a vertical cross section of the San Andres outcrop. The flow field is not a real subsurface reservoir, but it is an analog for many subsurface carbonate reservoirs in the Permian Basin. Furthermore, it is deterministic and detailed in the definition of heterogeneity and rock-fabric distribution, even though we ultimately used an average permeability for each facies. Our conclusions only can reflect two-dimensional flow characteristics of incompressible rock and fluids in cases where the displacement is dominated by viscous forces and capillary forces are negligible. Specific conclusions that can be drawn from the above results are:

1. Effect of uncorrelated intraparasequence permeability heterogeneity on sweep efficiency is negligible; therefore, using an average permeability for a facies is justified.
2. Mudstones and fenestral rock-fabric types defining parasequence boundaries act as flow barriers by controlling the flow and minimizing crossflow.
3. Some trapping does occur, even in a vertical cross section, when the thickness of the grainstone bar varies greatly along the cross section, and the thicker part is not in the injection well.

REFERENCES

Arya, A., Hewett, T. A., Larson, R. G. and Lake, L. W., 1988, Dispersion and reservoir heterogeneity: Society of Petroleum Engineers, Reservoir Engineering, February, p. 139–148.

Becker, E. B., Carey, G. F., and Oden, J. T., 1981, Finite elements; introduction to volume I: Englewood Cliffs, New Jersey, Prentice Hall.

Irons, Bruce, and Sohrab, Ahmad, 1980, Techniques of finite elements: New York, Halsted Press, 529 p.

Kasap, Ekrem, 1990, Analytic methods to calculate effective permeability tensor and effective relative permeabilities for cross-bedded flow units: The University of Texas at Austin, Ph.D. dissertation.

Lake, L. W., 1989, Enhanced oil recovery: Englewood Cliffs, New Jersey, Prentice Hall, 550 p.

Lake, L. W., Pope, G. A., Carey, G. F., and Sepehrnoori, Kamy, 1984, Isothermal, multiphase, multicomponent fluid flow in permeable media: In Situ, v. 8, p. 1–40.

Shook, M. G., and Lake, L. W., in press, Scaling fluid-flow problems by inspectional analysis: In Situ.

APPENDIX

Available data sets

A large volume of outcrop and subsurface data was generated for the RCRL project that is not included in this report. The following list summarizes additional retrievable data that are available for interested parties. These data sets are housed in open file at the Bureau of Economic Geology.

Item	Paper Copy	ASC File	Mac Excel	Lotus	Thin Sect.
Outcrop stratigraphic data					
Regional					
Thickness/facies/cycle thickness/water depth	X		X		
Detailed					
XY locations/facies/fabric, Lawyer Canyon upper San Andres window	X	X			
Petrographic, XRD, and core-plug porosity and permeability data					
Lawyer Canyon outcrop					
Cycle 1,2	X				128
Cycle 3–6	X				49
Cycle 7	X				139
Cycle 8,9	X				44
Seminole field, well 2505					
Thin-section descriptions and core-plug data every foot from 5,057 to 5,300 ft	X				240
Anhydrite, particle size, separate vug, total porosity and core-analysis data from 5,057 to 5,300 ft	X			X	
XRD results (dolomite, anhydrite, calcite, quartz) and thin-section point count of anhydrite; 5,057 to 5,406 ft	X			X	
Laboratory results of reanalysis of selected core plugs from whole-core samples	X			X	
Analysis of results of reanalysis of selected core plugs from whole-core samples	X			X	
Thin-section descriptions of selected core plugs taken for reanalysis	X				36

APPENDIX (cont.)

Available data sets

Item	Paper Copy	ASC File	Mac Excel	Lotus	Thin Sect.
Data from outcrop wells					
Algerita 1					
Porosity and permeability	X				
Thin sections					X
Algerita 2					
Porosity and permeability	X				
Thin sections					X
GR Spectral/LDT logs	X				
Algerita 3					
Porosity and permeability	X				
Thin sections					X
GR Spectral/LDT logs	X				
Mechanical field permeameter data					
Lawyer Canyon outcrop data	X	X			
Whole-core samples for reanalysis	X				